LAWRENCE
LIVERMORE
NATIONAL
LABORATORY

UCRL-TR-224997

HPCRM Corrosion Analysis & Modeling Report - Corrosion Resistance of Iron Based Amorphous Metals: SAM2x5 (Fe49.7CR17.7Mn1.9MO7.4W1.6B15.2C3.8Si2.4) and SAM1651 (Fe48M014Cr15Y2C15B6)

J. Farmer, J. Haslam, D. Day, T. Lian, C. Saw, P. Hailey, J.S. Choi, N. Yang, C. Blue, W. Peter, R. Bayles, R. Brown, J. Payer, J. Perepezko, K. Hildal, E. Lavernia, L. Ajdelsztajn, D. J. Branagan, J. Buffa, M. Beardsley, L. Aprigliano, J. Boudreau, L. Kaufman

October 4, 2006

Disclaimer

This work performed under the auspices of the U.S. Department of Energy by Lawrence Livermore National Laboratory under Contract DE-AC52-07NA27344.

UCRL-TR-224997 – October 3rd 2006
DOE-DARPA High Performance Corrosion Resistant Materials Program

HPCRM Corrosion Analysis & Modeling Report

Corrosion Resistance of Two Iron-Based Amorphous Metal Coatings SAM2X5 ($Fe_{49.7}Cr_{17.7}Mn_{1.9}Mo_{7.4}W_{1.6}B_{15.2}C_{3.8}Si_{2.4}$) & SAM1651 ($Fe_{48}Mo_{14}Cr_{15}Y_2C_{15}B_6$) – Evaluated in 5M $CaCl_2$ at 105-120°C & Seawater at 30-90°C

Prepared by:

Joseph Collin Farmer
Lawrence Livermore National Laboratory
7000 East Avenue
Livermore, California 94550

Contributions by:

J. Farmer[1] J. Haslam[1], S. Day[1], T. Lian[1], C. Saw[1], P. Hailey[1], J-S. Choi[1], N. Yang[2], C. Blue[3], W. Peter[3], R. Bayles[4], R. Brown[4], J. Payer[5], J. Perepezko[6], K. Hildal[6], E. Lavernia[7], L. Ajdelsztajn[7], D. J. Branagan[8], J. Buffa[8], M. Beardsley[9], L. Aprigliano[10], J. Boudreau[11] , L. Kaufman[12] and Others

[1]Lawrence Livermore National Laboratory, [2]Sandia National Laboratory, [3]Oak Ridge National Laboratory, [4]Naval Research Laboratory [5]Case Western Reserve University, [6]University of Wisconsin Madison, [7]University of California Davis, [8]The NanoSteel Company, [9]Caterpillar Incorporated, [10]Strategic Analysis Incorporated, [11]BLE Incorporated and [12]CALPHAD

TABLE OF CONTENTS

Section .....Page

INTENTIONALLY LEFT BLANK

FIGURES

INTENTIONALLY LEFT BLANK

TABLES

ABBREVIATIONS AND ACRONYMS

Basic Saturated Water	BSW
Critical Cooling Rate	CCR
Cyclic Polarization:	CP
Corrosion Rate	CR
Defense Advanced Research Projects Agency	DARPA
Fe-Based Amorphous Alloy Designation	DAR__
Defense Sciences Office	DSO
Differential Scanning Calorimetry	DSC
Differential Thermal Analysis	DTA
Department of Energy	DOE
Energy Dispersive X-Ray Spectroscopy	EDS, EDAX
Environmental Scanning Electron Microscopy	ESEM
Equivalent Weight	EW
Yucca Mountain Ground Water Composition	J-13
Conversion Factor	K
Fe-Based Amorphous Alloy Designation	LDAR_X_
Melt-Spun Ribbon	MSR
High Level Waste	HLW
Hardness Rockwell C	HRC
High-Velocity Oxy-Fuel Process:	HVOF
Vickers Hardness Number	HV, VHN
Measuring and Test Equipment	M&TE
Office of Science & Technology International	OSTI
Potential-Step Test	PST
Pitting Resistance Equivalence Number	PREN
Plasma Technology Incorporated	PTI
Physcial Vapor Deposition	PVD
Quality Assurance	QA
Qualified Supplier List	QSL
Structural Amorphous Metal	SAM
Fe-Based Amorphous Alloy Designation	SAM_X_
Simulated Acidified Water	SAW
Scanning Electron Microscopy	SEM
Simulated Concentrated Water	SCW
Simulated Dilute Water	SDW
The NanoSteel Company	TNC
Transmission Electron Microscopy	TEM
Vickers Hardness Number	VHN
X-Ray Diffraction	XRD

DEFINITION OF TERMS USED IN EQUATIONS

Atomic Weight of j-th Component	a_j
Weight Fraction of j-th Component	f_j
Scattering Factor for X-Rays	f_m
Scattering Factor for X-rays	f_n
Scattering Factor for X-rays	f
Corrosion Current Density	i_{corr}
Scattered X-Ray Intensity	$i(k)$
Wave Vector for X-Rays	k
Gram Equivalents of Alloy	n_{alloy}
Inter-atomic distances	r_{mn}
Electrode Area	A
Tafel Parameter	B
Critical Potential:	$E_{critical}$
Open Circuit Corrosion Potential:	E_{corr}
Reversal Potential	E_{rev}
Potential of Anodic Oxidation Peak:	E_{peak}
Repassivation Potential:	E_{rp}
Faraday's Constant (96,484.6 C equiv^{-1})	F
Corrosion Current	I_{corr}
Scattered X-Ray Intensity	I_{eu}
Universal Gas Constant	R
Polarization Resistance	R_p
Temperature	T
Anodic Tafel Slope	β_a
Cathodic Tafel Slope	β_c
Radial Distribution Function	$\rho(r)$
Density of Alloy	ρ_{alloy}
Scattering Angle	θ
Wavelength	λ

1. PURPOSE

1.1 SUMMARY OF MODEL

A conceptual model had been developed and presented for the prediction of corrosion rates for thermal-spray coatings of iron-based amorphous metals. Two iron-based amorphous metal formulations, SAM2X5 and SAM1651, have been developed which exhibit corrosion resistance in some environments comparable to that of Type 316L stainless steel and nickel-based Alloy C-22, including natural seawater at 30, 60 and 90°C, as well as in 5M $CaCl_2$ at 105 and 120°C. This corrosion resistance is achieved by adding chromium, molybdenum and tungsten to the alloys, while maintaining enough boron for glass formation. To determine the suitability of these materials for various repository applications under consideration, a model must be formulated.

The conceptual corrosion model requires specification of the alloy composition, the amorphous alloys crystallization temperature, the maximum temperature that the amorphous metal has seen over its lifetime, the brine composition, pH for the brine or crevice, and brine temperature. Outputs include open circuit corrosion potential, the change in corrosion potential with gamma radiolysis, the critical potential for passive film breakdown, the change in the critical potential with devitrification of the amorphous alloy, the general corrosion rate, and the localized corrosion rate. The model selects the solution pH, based upon whether or not the surface is creviced. If a crevice exists, a lower solution pH is assumed, accounting for the typical acidic conditions known to exist within the crevice. In the case of a thermal-spray coating, a crevice can be formed between contact points with outer surface of the coating, or at the coating-substrate interface in the case of damaged coatings. With the input parameters, and a pH which is selected to represent either crevice or non-crevice conditions, both the corrosion potential and critical potential can be determined. The critical potential is corrected for the effects of devitrificaiton if the maximum temperature that the alloy has experienced exceeds the crystallization temperature. The governing corrosion rate is selected based upon the difference between the corrosion and critical potentials; if the corrosion potential exceeds the critical potential, localized attack is assumed to occur, and the rate of penetration is determined by the expression for localized corrosion; if the corrosion potential is less than the critical potential, general attack is assumed to occur, and the rate of penetration is determined by the expression for general corrosion.

1.2 INTENDED USE OF MODEL

This model is intended to provide a basis for predicting the corrosion performance of new Fe-based amorphous metal coatings developed as part of the science and technology program, supporting the overall objectives of the Office of Civilian and Radioactive Waste Management (OCRWM), which is part of the United States Department of Energy (DOE).

1.3 CORROSION-RESISTANT IRON-BASED AMORPHOUS METALS

As will be discussed in greater detail in a subsequent section of this report, the outstanding corrosion possible with amorphous metals has been recognized for many years. A number of other iron-based amorphous metals have been published, including several with very good corrosion resistance. Examples include: thermally sprayed coatings of Fe-10Cr-10-Mo-(C,B); bulk Fe-Cr-Mo-C-B; and Fe-Cr-Mo-C-B-P. The corrosion resistance of the Fe-Cr-Mo-C-B-P

alloy has been corroborated with laboratory materials by these authors. Nickel-based amorphous metals have also been developed, and exhibit exceptional corrosion performance, even in concentrated acids.

This research has two primary long-term goals, all directed towards development of advanced amorphous-metal thermal-spray coatings with corrosion resistance superior to stainless steel and/or a high-performance nickel alloy. The stainless steel benchmark was selected since one candidate basket material is borated-stainless steel, and since the inner layer of the waste package is Type 316L stainless steel [UNS # S31603]. The nickel-based alloy benchmark was selected since Alloy C-22 [UNS # N06022] has been selected as the corrosion-resistant outer layer of the waste package.

Several Fe-based amorphous metal formulations have been identified that appear to have corrosion resistance comparable to (or better than) that of Ni-based Alloy C-22 (UNS # N06022), based on measurements of breakdown potential and corrosion rate in seawater. Both chromium (Cr) and molybdenum (Mo) provide corrosion resistance, boron (B) enables glass formation, and rare earths such as yttrium (Y) lower critical cooling rate (CCR). SAM1651, which is also known as SAM7 ($Fe_{48.0}Cr_{15.0}Mo_{14.0}B_{6.0}C_{15.0}Y_{2.0}$), has yttrium added, and has a nominal critical cooling rate of only 80 Kelvin per second, while SAM2X5 ($Fe_{49.7}Cr_{17.7}Mn_{1.9}Mo_{7.4}W_{1.6}B_{15.2}C_{3.8}Si_{2.4}$) has no yttrium, and is characterized by relatively high critical cooling rates of approximately 600 Kelvin per second. Data for the SAM2X5 formulation is reported here. Computational materials science has been used to help guide the design these new materials.

The amorphous metals are very attractive as basket materials since the relatively high boron concentration enables neutron absorption. If testing and modeling indicate that these materials have corrosion resistance comparable to borated stainless steels, with acceptable damage tolerance, the use of these materials to fabricate basket assemblies will be viable. To be competitive in such criticality control applications, these materials will have to demonstrate corrosion resistance comparable to borated-stainless steel in the "expected in-package environment." If testing and modeling indicate that these materials have corrosion resistance comparable to Alloy C-22, with acceptable damage tolerance, the application of these materials on the outer surface of the waste package for corrosion protection will be viable.

The use of these materials in repository applications depends upon the demonstrated corrosion resistance of prototypical production samples in a broad range of very harsh environments. The materials must also survive severe mechanical tests. While there are encouraging results from preliminary corrosion tests, much remains to be done. Testing is underway in a much broader range of environments than have been previously explored, including hot concentrated bicarbonate-type brines, chloride brines with various levels of nitrate inhibitor, and acidified brines with very low pH.

Alloy C-22 is an outstanding corrosion-resistant engineering material. Even so, crevice corrosion has been observed with C-22 in hot sodium chloride environments without buffer or inhibitor. SAM2X5 is also expected to experience crevice corrosion under sufficiently harsh conditions.

SAM2X5 and SAM1651 can be applied as coatings with the same corrosion resistance as a fully-dense completely amorphous melt-spun ribbon, provided that its amorphous nature is preserved during thermal spraying, whereas both Alloy C-22 and Type 316L stainless lose much of their corrosion resistance during thermal spraying, due to the formation of deleterious intermetallic phases which deplete the matrix of key alloy elements. Thus, these materials may provide the repository engineer with some unique materials for design enhancement.

SAM1651 has a low critical cooling rate (CCR), due to the addition of yttrium, which enables it to be rendered as a completely amorphous thermal spray coating. It is relatively difficult to atomize, with powders being irregular in shape. This causes the powder to be difficult to pneumatically convey during thermal spray deposition. Gas atomized SAM1651 powder has required cryogenic milling to eliminate irregularities that make flow difficult. SAM2X5 (no yttrium) has a high critical cooling rate, which can lead to devitrification during processing. In contrast to SAM1651, SAM2X5 can be readily gas atomized to produce spherical powders which enable more facile thermal spray deposition.

The hardness of Type 316L Stainless Steel is approximately 150 VHN, that of Alloy C-22 is approximately 250 VHN, and that of HVOF SAM2X5 ranges from 1100-1300 VHN [12-13]. Such hardness makes these materials particularly attractive for applications where corrosion-erosion and wear are also issues. Since SAM2X5 has high boron content, it can absorb neutrons efficiently, and may therefore find useful applications as a criticality control material within the nuclear industry.

This work has was done as part of the High-Performance Corrosion Resistant Material (HPCRM) Program, which was initiated as part of the DARPA DSO Structural Amorphous Metals (SAM) Program.

2. QUALITY ASSURANCE

At the present time, the corrosion testing for the HPCRM Program has been conducted in a manner consistent with the qualified (Q) corrosion testing being conducted with the Yucca Mountain Baseline Program, with the introduction of some new methods not yet used by the baseline program. However, all materials being tested are not qualified (non-Q). Those amorphous metal powders have been produced by industrial partners not yet on the qualified supplier list. Future efforts include work to help those producing amorphous metal powders and thermal spray coatings achieve formal qualified supplier list (QSL) status. The following references are cited to substantiate the non-Q status of the current program.

2.1 CURRENT NON-Q STATUS OF HPCRM PROGRAM

Establishment of Non-Q Status, Reference 1 – Memorandum: United States Department of Energy. Subject: Guidance and Funds to Lawrence Livermore National Laboratory for Tasks from the Office of Civilian Radioactive Waste Management. Date: May 17th 2006. To: David Marks, Office of Field Financial Management, NNSA Service Center, Located in Albuquerque, New Mexico. Reply to: RW-40E.

> "This memorandum has three purposes. First, this memorandum authorizes a change in the quality assurance (QA) pedigree for three of the four tasks listed below at LLNL. Attachment 1 provides specific quality assurance guidance for these tasks. The original guidance and funding memorandum was transmitted on January 23, 2004, and funding was provided in the January j2004 Approved Funding Program."

Second bullet …

> "Fabricate high-velocity oxy-fuel coatings, of various amorphous metal and ceramic compositions. Test these coatings for their corrosion performance, durability (e.g. impact strength) in a repository-relevant environmental conditions, and compatibility (e.g., adhesion) with waste package and drip shield materials. Characterize the relevant microstructure (e.g., interconnected porosity, and size of significant grain boundaries) that governs the measured performance. The end-of-FY deliverable is a report summarizing results to date and describing future plans. $870,000 is targeted to this task, which was begun in FY03 (non-Q). This task was originally issued Q, but is now non-Q because it is a venture to test a variety of coating compositions, in a preliminary way, and hence the vast majority of data will not be used further. Any data or other results that are potentially useful will be repeated in future fiscal years in a way that follows QARD requirements before being applied to Yucca Mountain-related calculations or hardware."
>
> "Some of these efforts are expected to involve collaborations with other institutions, with LLNL as the lead."

Attachment …QA Requirements

> "Tasks that are identified as non-Q are not required to be performed in accordance with an OCRWM approved QA Program. However, the work should be performed in accordance with existing Laboratory QA controls (e.g., DOE Order 414.1A, Quality Assurance, or 10 CFR 830.120, Subpart A, Quality Assurance Requirements."

Establishment of Non-Q Status, Reference 2 – Memorandum: United States Department of Energy. Subject: Initial FY2006 Program Guidance to Lawrence Livermore National Laboratory. Date: January 19th 2006. To: Camille Yuan-Soo Hoo, Manager, Livermore Site Office, Located in Livermore, California. Reply to: RW-40.

> "This initial fiscal year FY 2006 program guidance and funding memorandum provides authorization for LLNL to obligate and expend $4,462K to support the Department of Energy Office of Civilian Radioactive Waste Management for the following Advanced Technologies Targeted Thrust projects: High-Performance Corrosion Materials Testing and Evaluation ($4,462K/Non-Q). Funding for this work was provided in the December 2005 Approved Funding Program (AFP) under B&R Code DF096100, Fund Type TH. Attachment 1 provides specific quality assurance guidance to the above tasks. If you have any questions, please contact Mr. Leroy Stewart at (202) 586-2797."

2.2 QUALITY ASSURANCE CONTROLS USED FOR TESTING

In the current design of the waste package for the Yucca Mountain Project, the material being considered for the corrosion barrier is a primary Ni-based alloy known within the industry as Alloy C-22. The characteristics of this alloy include is its excellent ability to form a protective, corrosion resistant surface film in a broad range of environments. Recent research has focused on alternative materials, principally those that would provide a cost-effective waste package material solution. The focus of this study is to characterize the electrochemical behavior of various coated metal substrates in anticipated repository environments. To understand the degradation modes, it is important to characterize the surface properties of packaging materials under various electrochemical states such as passive film formation (passivation), passive film breakdown, transpassivation and repassivation. Samples of similar compositions will also be prepared for long-term corrosion testing. The purpose of this work is to develop and apply experimental techniques in qualitative and quantitative characterization of materials surfaces under anticipated electrochemical conditions. The principal goal of this work is to scope and investigate possible materials and processing techniques that might provide low cost alternatives with equivalent or improved performance as engineering barrier materials.

2.2.1 Applicable Planning Documents

As previously discussed, this activity has been designated by DOE/RW-40E to be non-Q. Therefore, good science practices will be implemented in the conduct of the testing, analysis, and reporting. Fabrication of the specimens, application of the coatings, and shipping to LLNL for testing has been performed by others. Relevant information will be documented in this scientific notebook. The specimens, therefore, will not be qualified specimens but will be tracked within LLNL using quality procedures. The primary planning tool for the testing being performed under this scope of work will be the scientific notebook initial entry.

2.2.2 Experiment Planning

This work intends to utilize electrochemical polarization measurement techniques and surface analytical techniques, in order to characterize the morphological, physical, and chemical evolution of various metal surface coatings under anticipated long-term repository conditions. The experiment will induce various electrochemical states on the samples using a potentiostat to acquire current-voltage information under controlled conditions. The principle test used to acquire this current-voltage information is the cyclic polarization test, which can provide valuable information on passive film formation, breakdown, repassivation, and susceptibility to localized corrosion. This test also provides insight into the difference between the open circuit potential and the breakdown potential, which can define the span of potentials where the material is resistance to active corrosion. Linear polarization testing can be used to determine in-situ corrosion rates. After electrochemical testing, surface analytical techniques can be used to describe the morphological and chemical characteristics of the surface film.

The experimental techniques and conditions listed in scientific notebooks did not preclude\ the use of additional techniques and conditions. Any modification and addition of experimental procedures were recorded in the scientific notebook.

2.2.3 Electrochemical Testing

2.2.3.1 Categories of Electrochemical Techniques

The electrochemical polarization techniques are used to manipulate the test materials to achieve a desirable electrochemical state. The polarization methods will follow procedures comparable to the following:

1. Cyclic potentiodynamic polarization (ASTM G-61)
2. Potentiodynamic polarization (ASTM G-5)
3. Potentiostatic (or constant potential)
4. Galvanostatic (or constant current)

2.2.3.2 Test Control

All Measuring and Test Equipment (M&TE) must be carefully controlled for purposes of quality assurance.

1. The appropriate Technical Implementing Procedures (TIPS) will be used for calibration of Measurement and Testing Equipment (M&TE).
2. All M&TE will be identified in the Scientific Notebook.
3. M&TE calibration documents and material traceability documents will be maintained in the SN supplemental binder entitled “Supplement to DARPA SN001-V1.”
4. The LLNL M&TE Coordinator will maintain procurement of “Q” calibration services.

2.2.3.3 Measuring and Test Equipment (M&TE)

For electrochemical tests: measuring and test equipment shall be controlled and calibrated in accordance with AP 12.1Q:

1. EG&G potentiostats including models in 263, 273, 283	A
2. Gamry Potentiostats including models in P4-300, DHC-1	A
3. Mettler AT 200 Analytical balance	BU
4. Orion 520A pH meter	BU
5. Keithley 2000 multimeter	A
6. Fluke 8840A/AF	A
7. Fluke 77 multimeter	A
8. Thermocouple Type K	A
9. Fluke TC Module 80TK	A
10. Reference Electrode	A
11. Gilmont Flowmeter	A

Legend: A = Annual; BU = Before Use.

Should other M&TE be required to pursue the investigations documented in this SN, their calibrations will be controlled in the same manners as the above equipment.

2.2.3.4 Calibration and Standards

Calibration of M&TE used for electrochemical tests will be conducted in accordance with relevant procedure and standards described in appropriate TIP documents, by QSL metrology lab approved procedures, and/or through a calibration laboratory on the OCRWM QSL.

2.2.4 Test Materials

2.2.4.1 Categories of Amorphous Metal Thermal Spray Coatings

Coatings of amorphous metal 316L stainless steel will be the primary material focus. However, other materials may be tested as deemed appropriate by the PI. These compositions will be noted in the scientific notebook entries. To study the metallurgical effects, various sample treatments and metallurgical conditions will be used:

1. Base metal
2. As-sprayed (as-applied) coatings
3. Coatings with surface modifications (high-density infrared fusing, laser treatments, and others processing methodologies selected by the Principal Investigator).
4. Thermally aged (intentionally devitrified) amorphous metal coatings
5. Long term samples for immersion corrosion testing

2.2.4.2 Types of Samples

The prospective test specimen shapes will include:

1. Disk shaped flat electrochemical specimen
2. Coated or uncoated thermally treated bars
3. Weight loss and crevice corrosion coupons
4. U-bend samples
5. Other shapes selected at the Principal Investigator's discretion

2.2.4.3 Sample Traceability

Good scientific practice will be followed to assure the specimens are consistent with the alloy intended. Traceability of samples will be processed in accordance with the requirements of LLNL-YMP quality procedure 033-YMP-QP 8.0 current revision and good scientific practices.

2.2.4.4 Sample Control

The control of samples before and after testing is essential for quality assurance.

1. Receipt of samples will be noted in an electronic database (Excel and/or Access) detailing the original manufacturer I.D., the revised sample I.D., alloy composition, specimen dimensions, metallurgical condition, base metal lot number, heat number, base metal certified material test report number, and the P.O. number.
2. Upon receipt, base metal samples are given a unique stamped identifier, if one is required, and this is entered in the database.
3. Shipment to subcontractors and other investigators is noted in the database.
4. All samples are stored in a locked cabinet located in Bldg. 435 Room 2020.

2.2.5 Test Environments

2.2.5.1 Standardized Test Environments

The environments used will focus on the bounding environments relevant to the Yucca Mountain geological horizon. However, a wider range of environments may be appropriate for model development, validation, and parameter identification. Their synthesis shall be appropriately identified in the Scientific Notebook (SN). The following are a list of potential test solutions:

1. Simulated acidified water (SAW)
2. Simulated concentrated water (SCW)
3. Basic saturated water (BSW)
4. Natural seawater (Half Moon Bay Seawater, for example)
5. Substitute ocean water (ASTM practice D 1141-98)
6. Sodium chloride solutions, including sodium chloride-nitrate solutions of various concentrations and at various temperatures
7. Other solution chemistries selected at the Principal Investigator's discretion, including 5M $CaCl_2$ at 105°C

2.2.5.2 Temperature Levels Used for Testing

The electrochemical tests will be conducted in the aforementioned standard electrolytes, at several relevant and standardized temperature levels: 30, 60 and 90ºC. Other temperatures at the Principal Investigator's discretion, and dependent upon the test solution and it's boiling point at atmospheric pressure.

2.2.5.3 Recording Environment Conditions Used in Testing

Any environmental conditions that affect experiments will be noted in the scientific notebook.

2.3 PROCEDURES AND DOCUMENTATION

2.3.1 Technical Implementing Procedures (TIPS)

Applicable TIPS for electrochemical tests are as follows:

1. TIP-CM-04: User Calibration of Mettler AT200 Analytical Balance
2. TIP-CM-05: User Calibration of Fowler Ultra-Cal Mark III Digital Caliper
3. TIP-CM-06: Formulation and Make-Up of Simulated Dilute Water, Low Ionic Content Aqueous Solution
4. TIP-CM-07: Formulation and Make-Up of Simulated Concentrated Water, High Ionic Content Aqueous Solution
5. TIP-CM-08: Formulation and Make-Up of Simulated Acidic Concentrated Water, High Ionic Content Aqueous Solution
6. TIP-CM-10: User Calibration of Analytical Balance
7. TIP-CM-13: User Calibration of Orion 520A pH Meter
8. TIP-CM-14: User Calibration of Reference Electrodes
9. TIP-CM-19: User Calibration & Software Verification of Potentiostats
10. TIP-CM-22: Formulation and Make-Up of Simulated Saturated Water, High Ionic Content Aqueous Solution
11. TIP-CM-42: User Verification of Gamry Potentiostats

Should additional TIPs be required for future activities, they will be referenced in the S/N as they are implemented.

2.3.2 Documentation of Testing

Documentation of testing will be managed in a bound and page numbered scientific notebook that will contain sufficient detail to allow for other similarly trained investigators to repeat the experiment without recourse to the original investigator.

2.3.3 Accuracy, Precision and Sources of Error

The instrumental resolutions will be noted in the Technical Implementation Plans (TIPS) governing each experimental method. Where necessary standard data reduction techniques will be used to determine how representative the results are. Potential sources of error include

improper calibration of test equipment or improper solution preparation. Adequate checks and balances exist within the system to ensure minimum likelihood of this occurring.

2.4 DATA COLLECTION AND STORAGE:

2.4.1 Written Records

All experiment data will be recorded in this scientific notebook or supplemental binders that are identified in this notebook. All experiment data will be also stored in electronic format, and electronic data files will be identified in the notebook whenever data is generated.

The data files will be archived on removable storage media, as well as in a designated location of a network database. The removable data storage media will be secured in a safety vault whose location will be noted in the SN supplemental binder.

2.4.2 Electronic Data Control

1. Original test data files (*.DTA files) are stored on the hard drive of the computer operating the potentiostats under C:\Program Files\Gamry\Framework\Data
2. After each test the electronic data files will be copied to an appropriate LLNL server site. An example of such a site is: "Energy-lan\stcf-server\Disk2\DARPA Farmer\haslam-darpa\Electro Chemical Test Data"

2.5 TRAINING

There are no special training requirements for personnel making entries in this SN other than those required by the YMP QA Training and Personnel Qualification Program.

INTENTIONALLY LEFT BLANK

3. USE OF SOFTWARE

3.1 SUMMARY OF SOFTWARE USED

The software used to run polarization measurements, and to acquire and analyze the measurement data is listed as:

1. EG&G Softcorr III Corrosion Software for EG&G Potentiostats
2. DC105 Corrosion Software for Gamry Potentiostats.

The EG&G Softcorr III and Gamry DC105 Framework software are proprietary products used to operate their potentiostat units. They are exempt from software tracking and baseline qualification.

The verification of EG&G SoftCorr III is covered by TIP-CM-19, and verification of Gamry DC105 corrosion software is covered by TIP-CM-42, or by YMP SRR documents: 10478-SRR-3.20-00.

3.2 EXEMPT SOFTWARE

Microsoft Excel (Table 1) was used for graphing data, adding trend lines to the data, and manipulating data through the use of standard functions included in Excel. Excel is exempt from qualification in accordance with LP-SI.11Q-BSC, Sections 2.1.1, 2.1.2, and 2.1.6. When Excel is used for calculations and plots (Sections 6.6.5, 6.6.6, and 7.5), information required for an independent person to reproduce the work (including formula or algorithm used, listing of inputs, and listing of outputs) is provided.

Table 1 – Required Software for Corrosion Testing

Name	Excel
Version	6.0 or later
Vendor	Microsoft
Address	Redmond, WA
Description	Data plotting
Computer Platform	Mac and/or Windows
Operating System	MacOS and/or Windows NT
Qualification Status	Visual display or graphical representation of data. Qualification not needed, per AP.SI.1Q.
STN	NA
Baseline Date	NA

4. INPUTS

4.1 DIRECT INPUTS – PROCEDURES FOR DETERMINATION

This section of the report discusses those experimental procedures required for the determination of inputs to the corrosion performance model.

4.1.1 Nomenclature for Alloy Designation

In early reports and publications on the development of these Fe-based amorphous metals [1-23], the SAM40 master alloy carried the designation DAR40, the SAM-series alloys were know as the LDAR-series alloys, and the SAM1651 alloy carried either CBCLT or CBCTL prefixes. The "DAR" prefix was used to acknowledge sponsorship of the research program by the Defense Advanced Research Projects Agency, DARPA [12-23]. The "LDAR" prefix was used to acknowledge modifications of the original DAR-type alloys, under sponsorship of the DOE-DARPA High Performance Corrosion Resistant Materials Program, HPCRM Program, at Lawrence Livermore National Laboratory, LLNL [1-8]. The "CBCTL" and "CBCLT" are the initials of those who prepared SAM1651 ingots for the HPCRM Program (C. Blue and C. T. Liu). The "SAM" prefix has been used to begin developing a unified designation for these Fe-based amorphous metals, and acknowledges the DARPA Structural Amorphous Metals (SAM) program that funded early development the DAR, LDAR, and CBCTL/CBCLT alloys.

4.1.2 Melt Spinning Process

The development of an appropriate powder composition for the production of a corrosion-resistant thermal-spray coating requires that the alloy first be tested in a form with no porosity, and with little or no crystalline phases present. Testing of such materials enables determination of the best possible corrosion performance for a given composition. Melt spinning and arc-melting with drop casting have been used as methods to synthesize completely amorphous, Fe-based, corrosion-resistant alloys with near theoretical density, thereby enabling the effects of coating morphology on corrosion resistance to be separated from the effects of elemental composition.

Cooling rates approaching one billion Kelvin per second (10^9 K/s) may be achieved with physical vapor deposition (PVD), and can be used to produce amorphous metal thin films. However, other processes are required to produce free-standing materials and coatings of practical thickness for corrosion and wear resistance. The thickness of PVD films is typically one to five microns (1-5 μm). Maximum cooling rates of one million Kelvin per second (10^6 K/s) have been achieved with melt spinning, and is therefore ideal for producing amorphous metals over a very broad range of compositions. The melt-spun ribbon (MSR) samples produced with this equipment are several meters long, several millimeters wide and approximately 150 microns thick [12, 13]. In contrast, the cooling rate in a typical thermal spray process such as HVOF are on the order of ten thousand Kelvin per second (10^4 K/s). The compositional range of materials that can be rendered as amorphous metals with thermal spray is therefore more restricted.

The melt spinning involves the ejection of a liquid melt onto a rapidly moving copper wheel with a pressure-controlled gas. The liquid melt solidifies onto the wheel, with subsequent separation

from the wheel by thermal contraction and centrifugal force, and collection in a chamber. By changing the tangential velocity of the wheel, as well as other processing parameters, the cooling rate can be controlled over a very broad range. The specific processing parameters for the melt-spinning process can be selected to establish cooling rates that are representative of a given thermal spray process. If a specific cooling rate produces an amorphous, glassy metal during melt spinning, it should also produce a glassy structure during thermal spray. It is therefore possible to use melt spinning to simulate the type of microstructure that can be achievable with thermal spraying, such as the high-velocity oxy-fuel process. Furthermore, an entire series of developmental materials, with different compositions, heat capacities, and thermal conductivity, can be made with the same cooling rates, so that the ease of processing each can be compared.

By exploiting the melt spinning process, several alloy compositions of Fe-based amorphous metals have been produced, characterized, and tested [1-8]. Several of these were compositional modifications of the SAM40 master alloy [12-23], and were prepared by following the general formula: $[(SAM40)_{100-x} + Z_x]$ where Z is the added element, and x is the amount of the addition in atomic percent [12-13]. Additives investigated included nickel, chromium, molybdenum, tungsten, yttrium, titanium and zirconium. The nickel and molybdenum additions are known to greatly influence the electrochemical properties of conventional stainless steel alloys. The yttrium, titanium, and zirconium additions, while not normally added to steels are known to form very stable oxides and are expected to increase the stability and passivity of the oxide film in a variety of environments. The SAM1651 formulation has the same nominal elemental composition as the Y-containing Fe-based amorphous metal formulation discussed in the literature [9-11]. These rare-earth containing materials have been selected with particular emphasis on glass forming ability, thermal stability, hardness, and corrosion resistance, all under conditions of interest.

The melt-spinning process was used to perform a systematic study of various elemental compositions, each based on the Fe-based SAM40 master alloy, with 1, 3, 5, and 7 atomic percent additions of specific elements believed to be beneficial to glass formation or corrosion resistance. The alloy compositions explored during this study are summarized in TableAs 1 and 2. Elemental additions investigated included nickel, molybdenum, yttrium, titanium, zirconium, and chromium. The densities of the amorphous metals prepared with melt spinning were determined, and all were less dense than nickel-based N06022 (Alloy C-22), and therefore offer a weight advantage over such classical corrosion-resistant alloys. The first re-crystallization peak for each of melt-spun ribbons was determined with differential thermal analysis (DTA), and was similar to that of the master alloy (SAM40). The formula with the yttrium additions showed re-crystallization peaks at higher temperatures than achieved with other formulae, corroborating the fact that yttrium additions do indeed promote thermal stability and glass formability. Some formulae exhibited a second re-crystallization process at a higher temperature than the first, with titanium and zirconium based formulations showing these processes at the highest temperatures. All of the “as-cast” amorphous metal formulae produced by the HPCRM Team exhibited hardness far superior to many of the conventional materials of interest, such as Type 316L stainless steel, and nickel-based N06022 (Alloy C-22). Thus, coatings of these materials would also be expected to be less prone to erosion, wear and gouging than conventional engineering alloys. Partially de-vitrified samples of the HPCRM materials exhibited dramatic increases in

hardness. Thus, carefully controlled heat treatment of these materials can be used to achieve dramatic improvements in resistance to erosion, wear and penetration.

4.1.3 Thermal Spray Process

Several thermal spray processes have been developed by industry and include: flame spray, wire-arc; plasma spray; water-stabilized plasma spray; high-velocity oxy-fuel; and the detonation gun. Any of these can be used for the deposition of Fe-based amorphous metals, with varying degrees of residual porosity and crystalline structure. The coatings discussed here were made with the high-velocity oxy-fuel (HVOF) process, which involves a combustion flame, and is characterized by gas and particle velocities that are three to four times the speed of sound (mach 3 to 4). This process is ideal for depositing metal and cermet coatings, which have typical bond strengths of 5,000 to 10,000 pounds per square inch (5-10 ksi), porosities of less than one percent (< 1%) and extreme hardness.

Optimization of the thermal spray process through careful selection of powder size and process temperature, has now yielded coatings of SAM40 (non-optimized elemental coating) that are virtually pore-free, and for all practical purposes, fully dense. These new coating architectures have also been shown, through detailed examination with X-ray diffraction (XRD) and scanning electron microscopy (SEM), to be amorphous. An optimized thermal spray process is now being used to render SAM2X5 and SAM1651 amorphous metal formulations as high-performance corrosion-resistant coatings, with nearly full density, no significant porosity, and good bond strength.

It is noteworthy that ceramic coatings, applied with thermal spray processes such as high-velocity oxy-fuel (HVOF) deposition, have been previously investigated as a means of protecting containers for the transportation, aging and disposal of high-level radioactive wastes and spent nuclear fuel [41-44]. Other applications may include tunnel boring machines and wind mills.

4.1.4 Energy Dispersive Analysis with X-Rays – Composition

Electron microanalysis of melt-spun ribbons was performed on a series of Fe-based formulations and on Alloy C-22 and Type 316L stainless reference materials. Scanning electron microscopy (SEM) was used to image superficial microstructure using both secondary and backscattered electron detectors. Semi-quantitative elemental composition of the melt-spun ribbons was determined with energy-dispersive X-ray spectroscopy (EDS, EDAX).

Segments of each ribbon were imaged using a Quanta Series 200 environmental scanning electron microscope (ESEM). Images were obtained from both sides of the ribbon, using both secondary electron and back-scattered electron detectors. The side of each ribbon that had been in contact with the melt-spinning copper wheel was distinguishable as being noticeably rougher than the non-contact side.

Semi-quantitative elemental composition was determined with EDS. Compositional analysis was performed on the smoother side of each ribbon, as the rougher sides were found in some cases to be contaminated with small amounts of copper, presumably from contact with the copper wheel during the melt spinning process. Quantification of the light elements, such as boron (B) and

carbon (C), was found to be unreliable for these complex sample formulations. The given (formulation) values for these elements were therefore assumed and used in calculating the compositional values for the remaining heavier elements. Microanalysis of each sample was performed at three randomly-selected locations at 10,000X magnification, with the average being reported here.

4.1.5 X-Ray Diffraction – Crystal Structure

The basic theory of X-ray diffraction of amorphous materials is well developed and has been published in the literature [45, 46]. A brief summary is presented here to place experimental data for the Fe-based amorphous metals in proper perspective. For crystalline diffraction, specific x-ray peaks can be observed from a diffraction pattern acquired from x-ray diffractometer for crystalline materials. These peaks are the results of constructive interference of the probing X-ray wave. If the sample is single crystal, these peaks have specific arrangements and orientations. The positions and intensities of these peaks are related to the atomic arrangements in the unit cell of the crystals. Unit cells have 3 axes with 3 angles (called lattice parameters), and they can be grouped into triclinic, monoclinic, orthorhombic, tetragonal, hexagonal, rhombohedral or cubic structures. In general, specific compounds have specific lattice parameters and the compounds can be identified by these parameters. The lattice parameters consist of three axes and three angles.

In an amorphous material, the atoms are not arranged in a periodic fashion such that crystals can be formed. The scattering intensity is then the summation of each individual atom. The time average scattering of non-interacting scattering like mono-atomic gases, the scattering is given by the Debye equation,

$$I_{eu} = \sum_m \sum_n f_m f_n \frac{\sin kr_{mn}}{kr_{mn}}$$

f_m, f_n are the scattering factors, r_{mn} are the inter-atomic distances and k is the wave vector. This equation can be further reduced and converted to an integral,

$$I_{eu} = Nf^2\left[1 + \int 4\pi\rho(r)\frac{\sin kr}{kr}dr\right]$$

Using algebraic manipulation and defining $\rho(r) = [\rho(r) - \rho_o] + \rho_o$, this equation becomes

$$k[i(k)] = 4\pi\int_0^\infty r[\rho(r) - \rho_o]\sin krdr$$

where $i(k) = \dfrac{I_{eu}/N - f^2}{f^2}$.

For simplicity and by using the theorem of Fourier's conversion, we can write the radial distribution function as

$$4\pi r^2 \rho(r) = 4\pi r^2 \rho_o + \frac{2r}{\pi}\int_0^\infty k[i(k)]\sin krdk$$

The above expression provides a means of converting the intensity function, which is in *k* space ($k=4\pi \sin\theta/\lambda$), to the radial distribution function, which is in real space. In this formulation, the atoms are arranged in random fashion with no order. There are broad diffraction peaks, which belong to the amorphous structure. The amorphous state does have structure as defined by the radial distribution function and the partial radial distribution, if it is a multiple elements system. For the present effort, such an analysis is not necessary at the moment. The degree of crystalline structure is correlated to the intensity of each scattering component.

The X-ray diffraction experiment is carried out using the Philip vertical goniometer in the para-focusing or also known as the Bragg-Bretano method. The X-ray optics are self-focusing, and the distance between the X-ray focal point to the sample position is equal to the distance between the sample position and the receiving slit for the reflection mode. Thus, the intensity and resolution are optimized. Parallel vertical slits are also added to improve the scattering signal.

Scintillation detectors are used in most modern X-ray diffractometers. However, the energy resolution is not sufficient to discriminate fluorescence X-rays of certain elements with energy close to the probing X-ray energy. Hence, very often, an analyzing crystal is used after the receiving slit. The choice of the crystal is based on the crystal mosaic, for energy selectivity and the efficiency. The most widely use energy discriminator is usually graphite for efficiency without significantly scarifying X-ray intensity. This is particularly important for the HPCRM because of the iron content in the samples. Iron fluorescence has energy which is close to that of the copper K_α probing X-ray. Sometime X-ray filters are used.

In the present setup, CuK_α is used with a graphite analyzing crystal. Step scan is performed from 20 to 90° (2θ) with step size of 0.02° at 4-10 seconds per point, depending on the amount of sample. The samples are loaded onto low quartz holders. This is because the expected intensity is very low and hence background scattering needs to be minimized.

4.1.6 Thermal Properties

The thermal properties of these Fe-based amorphous metals have been determined by Perepezko et al. [47]. Thermal analysis of these Fe-based amorphous metals, with differential scanning calorimetry (DSC) or differential thermal analysis (DTA), allows determination of important thermal properties such as the glass transition temperature T_g, crystallization temperature T_x and melting interval T_m-T_L. Results from the thermal analysis of amorphous samples provides initial assessment of the glass forming ability of these samples through conventional metrics such as T_{rg} (T_g/T_L), T_x (=T_x-T_g) and γ (=$T_x/(T_g+T_L)$ that can be used to rank alloys based on the expected suitability for thermal spray processing. However, note that the metrics provided by thermal analysis are only initial assessments, and more detailed studies are required to determine the glass formability of a particular alloy. These data are summarized in TableA 3.

Perepezko and his colleagues have also used wedge casting allows accurate determination the cooling rate required to avoid crystallization of the melt upon continuous cooling. A continuous range of cooling rates can be experienced simultaneously by an amorphous metal formulation by casting into a wedge-shaped mold for solidification. Then, examination of the wedge-shaped ingot's microstructure as a function of position reveals the lowest possible cooling rate (correlated with position) that can be used to maintain the material in a glassy state. The cooling rates in the wedge can be predicted with finite element modeling, and can be determined experimental with optical pyrometers (or other comparable methods).

In order to use amorphous coatings in application such as nuclear waste storage, it is crucial to determine the long-term stability of the amorphous phase, as precipitation of crystalline phases such as bcc-Fe will severely reduce the overall corrosion resistance of the coating. A convenient way to visualize thermal stability is the calculation of Time-Temperature-Transformation (TTT) curves that consists of the loci of time-temperature for the onset of nucleation of crystalline phases occurs. A kinetic model as been developed that combines information from wedge casting experiments and isothermal annealing experiments and incorporates these into a heterogeneous nucleation model. Based on this model, TTT-diagrams have been assessed for alloys SAM35 and SAM40, whereas work is in progress (preliminary results are available) for determining the TTT-curves for SAM2X5 and other alloys of interest.

4.1.7 Mechanical Properties

Hardness is an important parameter that has impact on wear resistance, as well as the resistance to erosion-corrosion. Vickers micro-hardness (HV) is the standard approach used to assess the hardness of thermal spray coatings. In the specific case of thermal spray coatings, a 300-gram load is frequently used, since it is believed that this load and the affected area are large enough to produce a measurement that is averaged over any macro-porosity that may be present. These authors also like to report micro-hardness measurements with a 100-gram load, since it is believed that this load and the affected area are smaller, and therefore capable of sampling bulk material properties. Typical ranges of the measured micro-hardness for these HVOF coatings are summarized in TableA 4.

4.1.8 Cyclic Polarization – Passive Film Stability

Spontaneous breakdown of the passive film and localized corrosion require that the open-circuit corrosion potential exceed the critical potential:

$$E_{corr} \geq E_{critical}$$

The resistance to localized corrosion is quantified through measurement of the open-circuit corrosion potential (E_{corr}), the breakdown potential ($E_{critical}$) and the repassivation potential (E_{rp}). The greater the difference between the open-circuit corrosion potential and the repassivation potential (ΔE), the more resistant a material is to modes of localized corrosion such a pitting and crevice corrosion. In integrated corrosion models, general corrosion is invoked when E_{corr} is less than $E_{critical}$ ($E_{corr} < E_{critical}$), and localized corrosion is invoked when E_{corr} exceeds $E_{critical}$ [24].

The data provided in this publication are sufficient to establish when general and localized corrosion occur, and the rates of general corrosion are when general corrosion is invoked. Note that these data only apply for the environments explored during testing.

Cyclic polarization (CP) is used as a means of measuring the critical potential ($E_{critical}$) of corrosion resistant materials, relative to their open-circuit corrosion potential (E_{corr}). In the published scientific literature, different bases exist for determining the critical potential from electrochemical measurements. The critical potential is frequently defined as the point where the passive current density increases during the forward (anodic) scan to a level between 1 to 10 $\mu A/cm^2$ (10^{-6} to 10^{-5} A/cm^2). Alternative definitions of the repassivation potential are used. One definition is the point during the reverse (cathodic) scan where the current density drops to a level indicative of passivity, which is *assumed* to be between 0.1 to 1 $\mu A/cm^2$ (10^{-6} to 10^{-7} A/cm^2). An alternative definition is the point where the forward and reverse scans intersect, a point where the current density being measured during the reverse scan drops to a level *known* to be indicative of passivity. These authors prefer the latter definition.

Definitions of the threshold and repassivation potentials vary from investigator to investigator. Gruss et al. define the repassivation potential as the point where the current density drops to 10^{-6} to 10^{-7} A cm^{-2} [39]. Scully et al. define the threshold potential for crevice corrosion of Alloy 22 as the point during the scan of electrochemical potential in the forward direction where the current density increases to a level of 10^{-6} to 10^{-5} A cm^{-2}. Scully et al. generated CP data with very tight crevices and concentrated electrolytes consisting of 5M LiCl, 0.024 to 0.24M $NaNO_3$, 0.026 to 0.26M Na_2SO_4 and HCl [48]. Testing was conducted at two temperature levels, 80 and 95°C. The crevices were formed with a multiple crevice former, PTFE tape, and an applied torque of 70 inch pounds. Under these circumstances, some electrochemical activity indicative of crevice corrosion was observed at potentials ranging from 71 to 397 mV versus Ag/AgCl, depending upon the composition of the electrolyte. Using a current density criterion for repassivation of 10^{-5} A cm^{-2}, repassivation potentials were determined to be slightly above, but relatively close to the open-circuit corrosion potential.

Cyclic polarization measurements have been based on a procedure similar to ASTM (American Society for Testing and Materials) G 5 standard with slight modification [49-52]. The ASTM G 5 standard calls for a 1N H_2SO_4 electrolyte, whereas synthetic bicarbonate, sulfate-chloride, chloride-nitrate, and chloride-nitrate solutions, with sodium, potassium and calcium cations, as well as natural seawater have been used for this investigation. The chloride anion promotes passive film breakdown, while the nitrate serves as an inhibitor. Furthermore, the ASTM G 5 standard calls for the use of de-aerated solutions, whereas aerated and de-aerated solutions were used here. After a 24-hour hold period, during which the open circuit corrosion potential is determined, the potential is scanned in the positive (anodic) direction from a level slightly more negative than the corrosion potential (cathodic limit), to a reversal potential (E_{rev}) near that required for oxygen evolution (anodic level). During the positive scan, anodic oxidation peaks may be observed (centered at E_{peak}) that have been correlated with the oxidation of molybdenum at the alloy surface (passive film), as well as current excursions that are usually associated with breakdown of the passive film. During the negative (cathodic) scan, a hysteresis loop will be observed in cases where passivity has been lost. As the scan continues, the current density may eventually decrease to a level equivalent to that experienced during the positive scan, and

indicative of reformation of the passive film. The potential at which this occurs is known as the repassivation potential (E_{rp}).

Temperature-controlled borosilicate glass (Pyrex) electrochemical cells were used for cyclic polarization and other similar electrochemical measurements. This cell has three electrodes, a working electrode (test specimen), the reference electrode, and the counter electrode. A standard silver silver-chloride electrode, filled with near-saturation potassium chloride solution, is used as the reference, and communicates with the test solution via a Luggin probe placed in close proximity to the working electrode, thereby minimizing Ohmic losses. Numerical corrections for the reference electrode junction potential have been estimated, and have been found to be insignificant [25]. The electrochemical cell is equipped with a water-cooled junction to maintain reference electrode at ambient temperature, thereby maintaining integrity of the potential measurement, and a water-cooled condenser to prevent the loss of volatile species from the electrolyte. All powder used to produce these coatings was produced by The NanoSteel Company (TNC), and the HVOF coatings used to generate the data in this publication were produced by Plasma Technology Incorporated (PTI). Synthetic brine solutions (5M $CaCl_2$ and others) were prepared at Lawrence Livermore National Laboratory with reagent-grade chemicals and de-ionized water. The natural seawater used in these tests was obtained directly from Half Moon Bay along the northern coast of California, and was transported to the laboratory in a clean polyethylene container. This Half Moon Bay seawater is referred to as natural seawater in this publication.

4.1.9 Cyclic Polarization – Alloy Screening

Cyclic polarization of melt spun ribbons was further used to compare the relative corrosion resistance of a large number candidate alloy compositions in near-boiling natural seawater at 90°C. As previously discussed, the alloy compositions explored during this study are summarized in TableAs 1 and 2. The difference between the open circuit corrosion potential (E_{corr}) and the repassivation potential (E_{rp}) was used as a basis of comprison for the relative corrosion performance of candidate alloys. Several of the candidate alloy compositions had a larger metric value (E_{rp}- E_{corr}) than the reference material, which has been established as nickel-based Alloy C-22, due to its own outstanding corrosion performance. During this early phase of the study, it was concluded that several types of iron-based amorphous metals exist which all have passive film stabilities in seawater at 30°C and 90°C that are comparable to that of the reference material [1-8].

4.1.10 Potentiostatic Step – Threshold for Passive Film Breakdown

Potentiostatic step tests have been used to determine the potential at which the passive film breaks down on the reference material, Alloy C-22, and on the two amorphous metals of primary interest, SAM2X5 and SAM1651. During prolonged periods of at a constant applied potential (potentiostatic polarization), which are typically 24 hours in duration, the current is monitored as a function of time. In cases where passivity is lost, the current increases, and the test sample is aggressively attacked. In cases where passivity is maintained, the current decays to a relatively

constant asymptotic level, consistent with the known passive current density. In these tests, periods of polarization are preceded by one hour at the open circuit corrosion potential.

All were tested in natural seawater heated to 90°C. To eliminate the need for surface roughness corrections in the conversion of measured current and electrode area to current density, the SAM2X5 coatings were polished to a 600-grit finish prior to testing. The constant potential denoted in Figures 40 through 45 and Figures 47 through 52 was applied after 1 hour at the open circuit corrosion potential (OCP).

4.1.11 Relationship Between Thermal Phase Stability and Corrosion Resistance

To assess the sensitivity of these iron-based amorphous metals to devitrification, which can occur at elevated temperature, melt-spun ribbons of Fe-based amorphous metals were intentionally devitrified by heat treating them at various temperatures for one hour. After heat treatment, the samples were evaluated in low temperature seawater (30°C), to determine the impact of the heat treatment on passive film stability and corrosion resistance. The temperatures used for the heat treatment were: 150, 300, 800 and 1000°C. Untreated (as received) ribbons were also tested, and provide insight into the baseline performance.

4.1.12 Determining Corrosion Rate with Linear Polarization

The linear polarization method has been used as a method for determining the corrosion rates of the various amorphous metal coatings, including SAM2X5 and SAM1651. This method is based upon experimental determination of electrokinetic parameters in the classic Tafel equation with a potentiostat. The classic Butler-Volmer expression collapses into the well-known anodic Tafel equation at high anodic potential, where the contribution of the electrochemical reduction (cathodic) reaction to the overall current at the electrode surface becomes insignificant (defined as < 1%). At high cathodic potential, where the contribution of the electrochemical oxidation (anodic metal dissolution) reaction to the net electrode current is insignificant, the Butler-Volmer expression becomes the cathodic Tafel equation. The procedure used for linear polarization testing consists of the following steps: (1) hold the sample for ten (10) seconds at the open circuit potential (OCP); (2) beginning at a potential 20 mV below the OCP (OCP-20 mV), increase the potential linearly at a constant rate of 0.1667 mV per second, to a potential 20 mV above the OCP (OCP+20 mV); (3) record the current being passed from the counter electrode to the working electrode by the potentiostat, as a function of potential relative to the standard/silver silver-chloride (Ag/AgCl) reference electrode; and (4) determine the parameters in the cathodic Tafel line by performing linear regression on the voltage-current data from 10 mV below the OCP (OCP – 10 mV) to 10 mV above the OCP (OCP + 10 mV). The slope of this line is the polarization resistance, *Rp* (ohms), which is defined as [54]:

$$R_P = \left(\frac{\partial E}{\partial I} \right)_{E_{corr}}$$

A parameter (*B*) is defined in terms of the slopes of the anodic and cathodic branches of the Tafel line:

$$B = \frac{\beta_a \beta_c}{2.303(\beta_a + \beta_c)}$$

Values of B are published for a variety of iron-based alloys, and vary slightly from one alloy-environment combination to another [54]. Values for carbon steel, as well as Type 304, 304L and 430 stainless steels, in a variety of electrolytes which include seawater, sodium chloride, and sulfuric acid, range from 19 to 25 mV. A value for nickel-based Alloy 600 in lithiated water at 288°C is given as approximately 24 mV. While no values have yet been developed for the Fe-based amorphous metals that are the subject of this investigation, it is believed that a conservative representative value of approximately 25 mV is appropriate for the conversion of polarization resistance to corrosion current. Given the value for Alloy 600, a value of 25 mV is also believed to be acceptable for converting the polarization resistance for nickel-based Alloy C-22 to corrosion current. The corrosion current, I_{corr} (A) is then defined as:

$$I_{corr} = \frac{B}{R_p}$$

where the parameter B is conservatively assumed to be approximately 25 mV. The corrosion current density, i_{corr} (A cm^{-2}), is defined as the corrosion current, normalized by electrode area, and is:

$$i_{corr} = \frac{I_{corr}}{A}$$

A is the surface area of the sample in square centimeters (cm^2). The corrosion (or penetration) rate of an alloy can be calculated from the corrosion current density with the following formula derived from Jones [55]:

$$\frac{dp}{dt} = \frac{i_{corr}}{\rho_{alloy} n_{alloy} F}$$

where p is the penetration depth, t is time, i_{corr} is the corrosion current density, ρ_{alloy} is the density of the alloy (g cm^{-3}) , n_{alloy} is the number of gram equivalents per gram of alloy, and F is Faraday's constant. The value of n_{alloy} can be calculated with the following formula:

$$n_{alloy} = \sum_j \left(\frac{f_j n_j}{a_j} \right)$$

where f_j is the mass fraction of the jth alloying element in the material, n_j is the number of electrons involved in the anodic dissolution process, which is assumed to be congruent, and a_j is the atomic weight of the jth alloying element. Congruent dissolution means that the dissolution rate of a given alloy element is proportional to its concentration in the bulk alloy. These equations have been used to calculate factors for the conversion of corrosion current density to the penetration rate (corrosion rate). These conversion factors are summarized in Table 2.

An equivalent expression that frequently appears in the literature for calculation of the penetration rate, referred to in this case as the corrosion rate, *CR* (mm y^{-1}), is also given:

$$CR = \left(K \times i_{corr} \times EW\right) / \rho_{alloy}$$

The parameter K is a conversion factor has a value of (3.27×10^{-3} mm·g·μA^{-1}·cm^{-1}·yr^{-1}), the corrosion current density i_{corr} is given in the units (μA cm^{-2}), and *EW* is the equivalent weight of the alloy.

Table 2 – The conversion of the corrosion current density to penetration rate (corrosion rate) requires the parameters summarized in this table. These penetration rates are for an assumed current density of one microamp per square centimeter (1 μA cm^{-2}). If the corrosion rate is 2 μA cm^{-2} instead of the assumed 1 μA cm^{-2}, the penetration rate is simply doubled. The value of Faraday's constant (F) is 96,484.6 C $equiv^{-1}$.

Alloy	ρ_{alloy}	$n_{alloy} = (f_j n_j / a_j)/100$		$(dp/dt) = (i_{corr})/(\rho_{alloy} \times n_{alloy} \times F)$			
	g cm^{-3}			cm sec^{-1}		μm $year^{-1}$	
		Low	High	Low	High	Low	High
316L SS	7.85	3.9049E-02	6.5291E-02	2.0222E-11	3.3811E-11	6.3772	10.6627
C-22	8.69	3.8041E-02	6.7509E-02	1.7667E-11	3.1352E-11	5.5714	9.8872
SAM2X5	7.65	5.4149E-02	7.9309E-02	1.7083E-11	2.5020E-11	5.3872	7.8904
SAM1651	6.18	4.6979E-02	8.0221E-02	2.0906E-11	3.5699E-11	6.5928	11.2579

4.1.13 Effects of Junction Potential on Electrochemical Measurements

It is important to understand the magnitude of the error in the potential measurements due to the junction potential. A correction has been performed based upon the Henderson Equation, as presented by Bard and Faulkner [56].

$$E_j = \frac{\sum_i \frac{|z_i| u_i}{z_i}\left[C_i(\beta) - C_i(\alpha)\right]}{\sum_i |z_i| u_i \left[C_i(\beta) - C_i(\alpha)\right]} \frac{RT}{F} \ln \frac{\sum_i |z_i| u_i C_i(\alpha)}{\sum_i |z_i| u_i C_i(\beta)}$$

where E_j is the potential across the junction connecting the α and β phases, z_i is the valence of the i^{th} ion, u_i is the mobility of the i^{th} ion, $C_i(\alpha)$is the concentration of the i^{th} ion in the α phase, $C_i(\beta)$ is the concentration of the i^{th} ion in the β phase, R is the universal gas constant, T is the absolute temperature, and F is Faraday's constant. The calculated junction for several test solutions have been estimated with ionic properties used in the calculation were also taken from Bard and Faulkner. These corrections are not very large, with the largest being less than approximately 10 mV. This value corresponds to the junction potential for SSW at 90°C. It is concluded that insignificant error results from neglecting to correct for the junction potential.

4.1.14 Validation with Salt Fog Testing

The corrosion resistance of the amorphous metal coatings was verified during salt fog testing. As previously discussed, the salt fog test was used to compare various wrought ant thermal-spray alloys, melt-spun ribbons, arc-melted drop-cast ingots, and thermal-spray coatings for their susceptibility to corrosion by salt sprays, like those that might be encountered aboard naval ships [57]. This test is also known as the salt spray test. The most recent tests have focused on reference materials, including the SAM40 master alloy, and the SAM2X5 and SAM1651 amorphous metal formulations, in the form of arc-melted drop-cast ingots, melt-spun ribbons, and high-velocity oxy-fuel coatings with no significant porosity and near theoretical density. In contrast, the first tests focused on early thermal-spray coatings, which had residual porosity and crystalline structure, and lower resistance to corrosion.

Both salt fog tests were conducted according to the standard General Motors (GM) salt fog test, identified as GM9540P, which is similar to the standard American Society for Testing and Materials (ASTM) salt fog test, which is identified as ASTM B117 and entitled "Standard Test Method of Salt Spray (Fog) Testing." The test protocol for GM9540P is summarized in Table 3. Samples of iron-based amorphous-metal thermal spray coatings and several reference samples were evaluated with the GM9540P test protocol. The four reference samples included Type 316L stainless steel, nickel-based Alloy C-22 (N06022), Ti Grade 7, and the 50:50 nickel-chromium binary.

Table 3 – A description of the standard GM9540P Salt Fog Test is summarized here. Note that the salt solution mists (denoted with asterisks) consisted of 1.25% solution containing 0.9% sodium chloride, 0.1% calcium chloride, and 0.25% sodium bicarbonate.

24-Hour Test Cycle for GM9540P Accelerated Corrosion Test		
Shift	**Elapsed Time (hrs)**	**Event**
Ambient Soak	**0**	**Salt solution mist for 30 seconds, followed by ambient exposure at 13-28°C (55-82°F)**
	1.5	**Salt solution mist for 30 seconds, followed by ambient exposure at 13-28°C (55-82°F)**
	3	**Salt solution mist for 30 seconds, followed by ambient exposure at 13-28°C (55-82°F)**
	4.5	**Salt solution mist for 30 seconds, followed by ambient exposure at 13-28°C (55-82°F)**
Wet Soak	**8 to 16**	**High humidity exposure for 8 hours at 49 ± 0.5°C (120 ± 1°F) and 100% RH, including a 55-minute ramp to wet conditions**
Dry Soak	**16 to 24**	**Elevated dry exposure for 8 hours at 60 ± 0.5°C (140 ± 1°F) and less than 30% RH, including a 175-minute ramp to dry conditions**

4.1.15 Composition of Amorphous Metals

Several Fe-based amorphous metals were systematically explored during this investigation, with the compositions of the yttrium-containing variants summarized in Table 4. Additions of molybdenum (Mo), chromium (Cr) and tungsten (W) were added to enhance passivity; boron (B) was added to enable glass formation; and yttrium (Y) was added to lower critical cooling rate (CRR). The compositions of melt-spun ribbon samples were verified with energy dispersive X-ray spectroscopy (EDAX), as shown in Figures 1 through 14, and summarized in Table 5.

The EDS data shown in Figure 1 provides the relative abundance of yttrium in a SAM3X1 melt-spun ribbon, which was prepared by adding one atomic percent (1 at. %) yttrium to SAM40 (master alloy). Similarly, the EDS data shown in Figures 2 through 6 provides the relative abundance of yttrium and these other alloying elements in SAM3X1, SAM3X3, SAM3X5, SAM3X7, SAM7 (SAM1651) and SAM8 melt-spun ribbons, which were prepared by adding three, five and seven atomic percent (3, 5 and 7 at. %) yttrium to SAM40, respectively. SAM7 (SAM1651) and SAM8 provide very good corrosion resistance in extremely aggressive environments, and can be readily processed due to their relatively low critical cooling rates. Figure 7 compares the EDAX spectra of SAM7 and SAM8, with a relatively coarse energy scale. Figure 8 has an expanded energy scale, with a maximum of approximately 4 keV.

The EDS data shown in Figures 9 through 14 provides the relative abundance of molybdenum in a SAM2X1 melt-spun ribbon, which was prepared by adding one atomic percent (1 at. %) molybdenum to SAM40 (master alloy). The chromium and tungsten were also added to contribute to passivity. Similarly, the EDS data shown in Figures 9 through 12 provides the relative abundance of molybdenum in SAM2X3, SAM2X5 and SAM2X7 melt-spun ribbons, which were prepared by adding three, five and seven atomic percent (3, 5 and 7 atomic %) molybdenum to SAM40, respectively. The SAM2X5 composition appears to provide adequate corrosion resistance, and is a formulation that can still be processed with relative ease. The SAM2X7 composition has a higher calculated pitting-resistance equivalence number (PREN) than the alloys with less molybdenum, and slightly better corrosion resistance than SAM2X5, but is somewhat more difficult to make. Figure 13 is a comparison of the spectra shown in Figures 9 through 12. Similarly, Figure 14 is a comparison of the spectra shown in Figures 9 through 12, but with an expanded energy scale, with a maximum energy being approximately 4 keV. The molybdenum peak is presented with greater clarity by using the expanded scale.

4.2 DIRECT INPUTS – SUMMARY OF EXPERIMENTAL RESULTS

This section of the report discusses those experimental procedures required for the determination of inputs to the corrosion performance model.

4.2.1 Structural Characterization of Melt-Spun Ribbons – SAM1651

Melt-spun ribbons prepared by The NanoSteel Company (TNC) were also characterized with XRD. Figure 15a shows X-ray diffraction (XRD) data for melt-spun ribbon (MSR) samples of Type 316L stainless steel and nickel-based Alloy C-22. The strong peaks are indicative of the crystalline nature of these materials. Figure 15b shows X-ray diffraction data for melt-spun ribbon (MSR) samples of iron-based amorphous metals identified as: (a) SAM40; (b) SAM7,

which is also known as SAM1651; and (c) SAM8 are completely amorphous, as expected. Figure 16 shows a scanning electron micrograph of the original SAM40 Fe-based amorphous metal shows clear evidence of crystallization after annealing at 800°C for 1 hour. Figure 17 shows a scanning electron micrograph of the SAM1651 (SAM7) Fe-based amorphous metal with yttrium shows no evidence of crystallization after annealing at 800°C for 1 hour.

4.2.2 Structural Characterization of Melt-Spun Ribbons – SAM2X5

Figure 18a shows the resulting diffraction patterns of melt-spun ribbons of two austenitic alloys, nickel-based Alloy C-22 and Type 316L stainless steel, which clearly indicate that both of these materials are indeed crystalline, and that the melt spinning process cannot capture the amorphous meta-stable state for these compositions Figure 18b shows X-ray diffraction data for melt-spun ribbon (MSR) samples of iron-based amorphous metals identified as: (a) SAM40; (b) SAM2X1; (c) SAM2X3; (d) SAM2X5; and (e) SAM2X7. These data are clearly indicative of amorphous structure, and a complete lack of crystalline structure, which is attributed to the relatively high concentrations of boron.

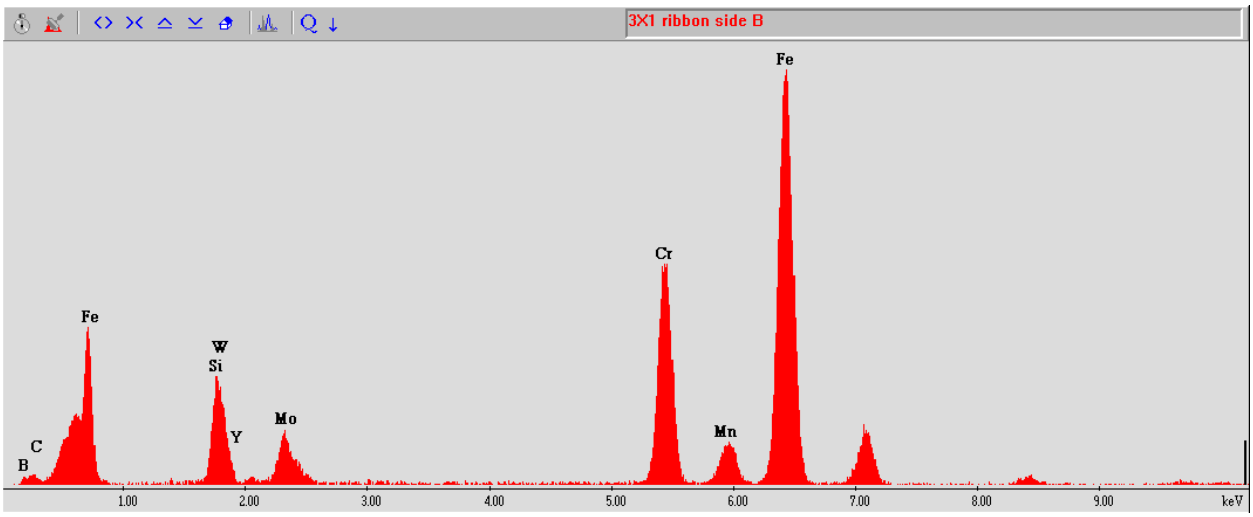

Figure 1 – This figure shows the energy-dispersive x-ray (EDS) spectrum from the smooth side of melt-spun ribbon SAM3X1. Semi-quantitative analysis yields the approximate elemental composition of the melt-spun ribbon. Compositional data for this sample is in agreement with the initial formula.

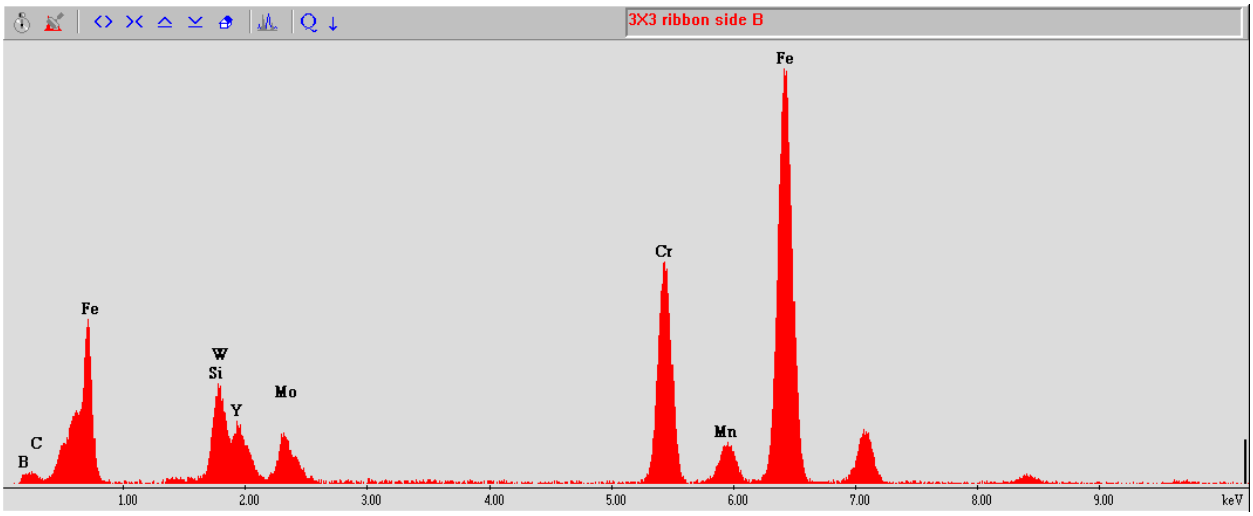

Figure 2 – This figure shows the energy-dispersive x-ray (EDS) spectrum from the smooth side of melt-spun ribbon SAM3X3. Semi-quantitative analysis yields the approximate elemental composition of the melt-spun ribbon. Compositional data for this sample is in agreement with the initial formula.

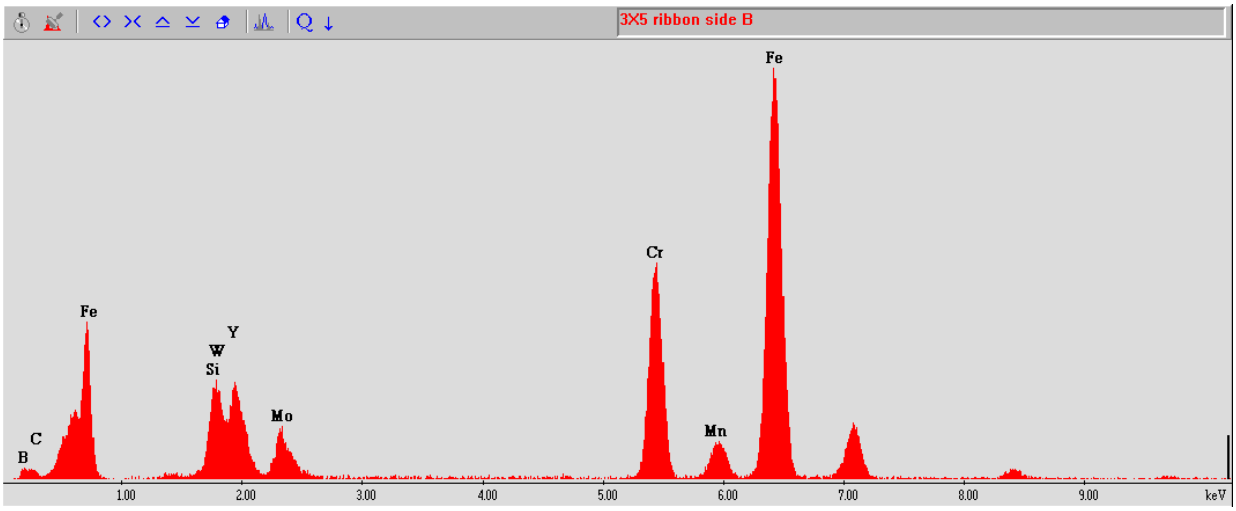

Figure 3 – This figure shows the energy-dispersive x-ray (EDS) spectrum from the smooth side of melt-spun ribbon SAM3X5. Semi-quantitative analysis yields the approximate elemental composition of the melt-spun ribbon. Compositional data for this sample is in agreement with the initial formula.

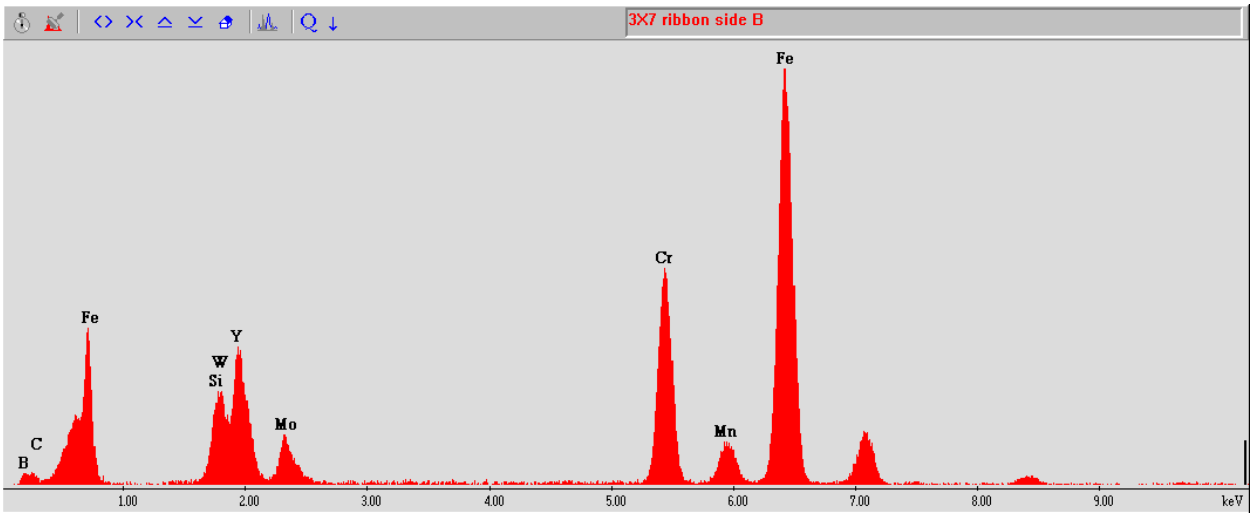

Figure 4 – This figure shows the energy-dispersive x-ray (EDS) spectrum from the smooth side of melt-spun ribbon SAM3X7. Semi-quantitative analysis yields the approximate elemental composition of the melt-spun ribbon. Compositional data for this sample is in agreement with the initial formula.

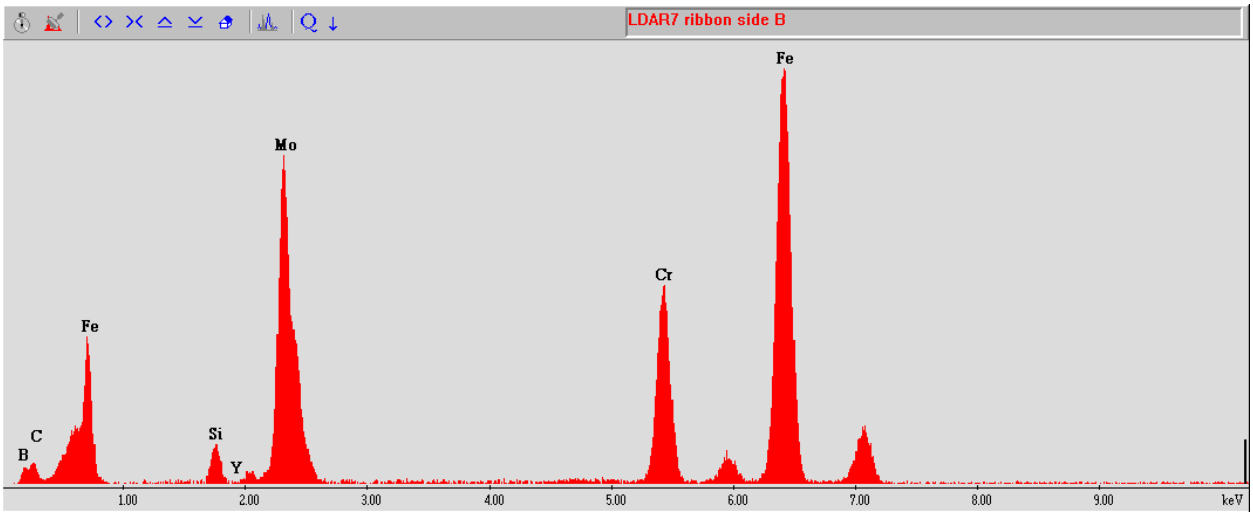

Figure 5 – This figure shows the energy-dispersive x-ray (EDS) spectrum from the smooth side of melt-spun ribbon LDAR7 (SAM-1651). Semi-quantitative analysis yields the approximate elemental composition of the melt-spun ribbon. Compositional data for this sample may indicate less yttrium (Y) than expected, which should be present at 2.0 at. %. Furthermore, silicon (Si) is detected at 1.6 at. %, when in fact it should not be present in this sample.

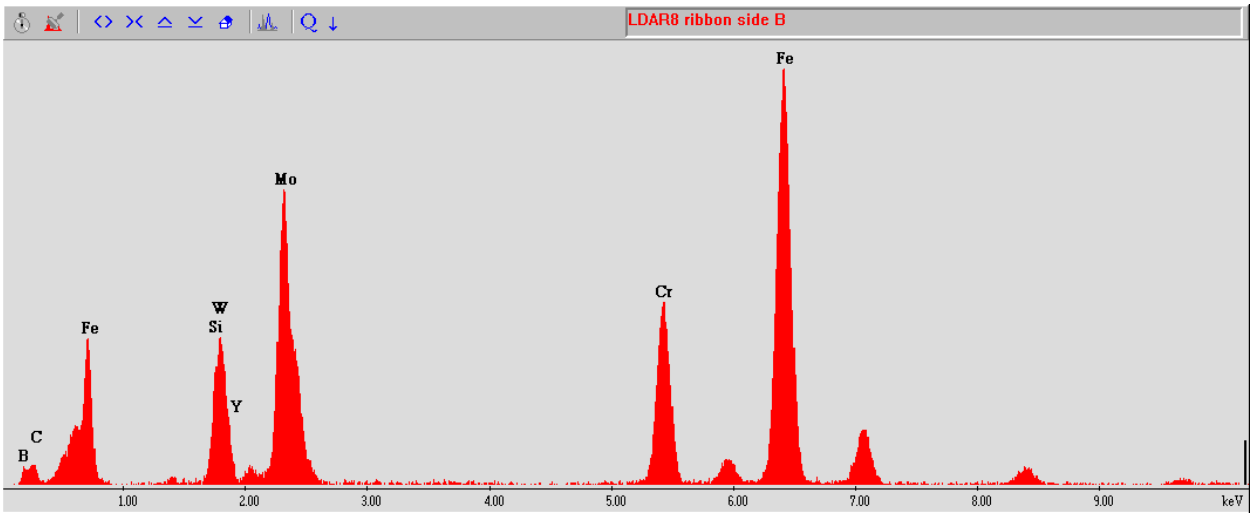

Figure 6 – This figure shows the energy-dispersive x-ray (EDS) spectrum from the smooth side of melt-spun ribbon LDAR8. Semi-quantitative analysis yields the approximate elemental composition of the melt-spun ribbon. Compositional data for this sample may indicate less yttrium (Y) than expected, which should be present at 1.9 at. %. Furthermore, silicon (Si) is detected at 1.7 at. %, when in fact it should not be present in this sample.

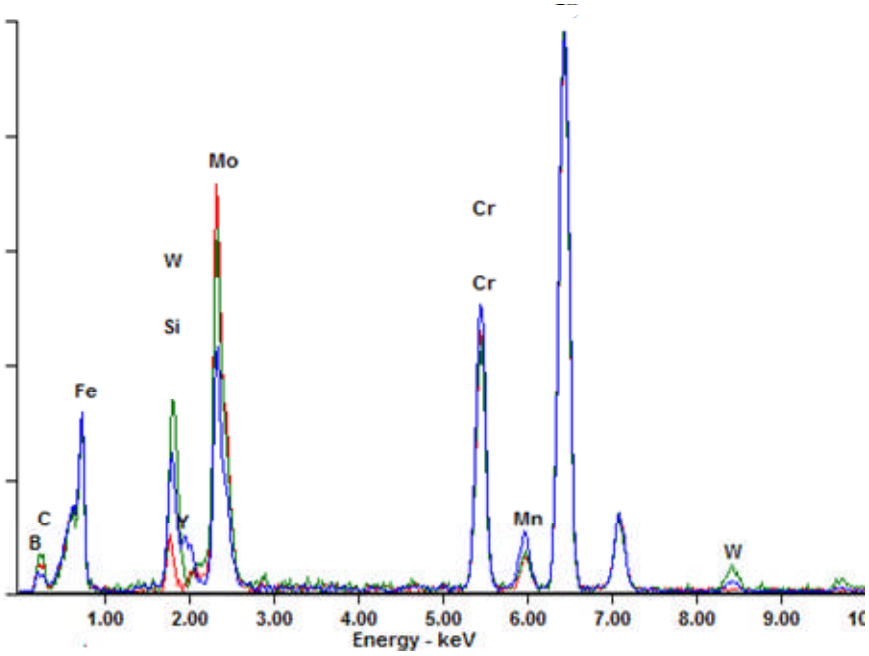

Figure 7 – This figure shows energy-dispersive X-ray spectroscopy (EDS) of SAM1651 (SAM7) and the SAM3X-serics of melt-spun ribbons, and reveals the abundance of various alloying elements.

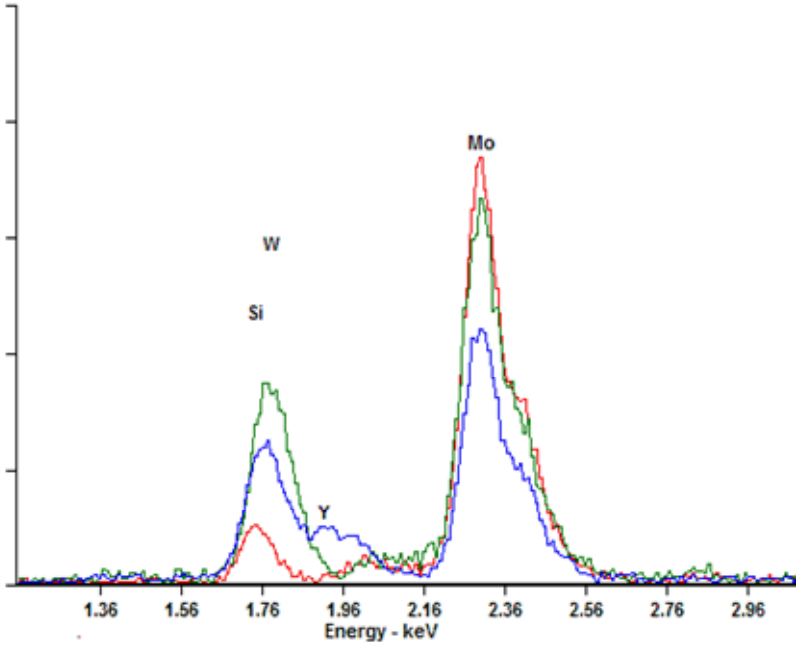

Figure 8 – This figure shows energy-dispersive X-ray spectroscopy (EDS) of SAM1651 (SAM7) and the SAM3X-serics of melt-spun ribbons, and reveals the abundance of various alloying elements. This figure has an expanded energy scale, with energies below 3 keV.

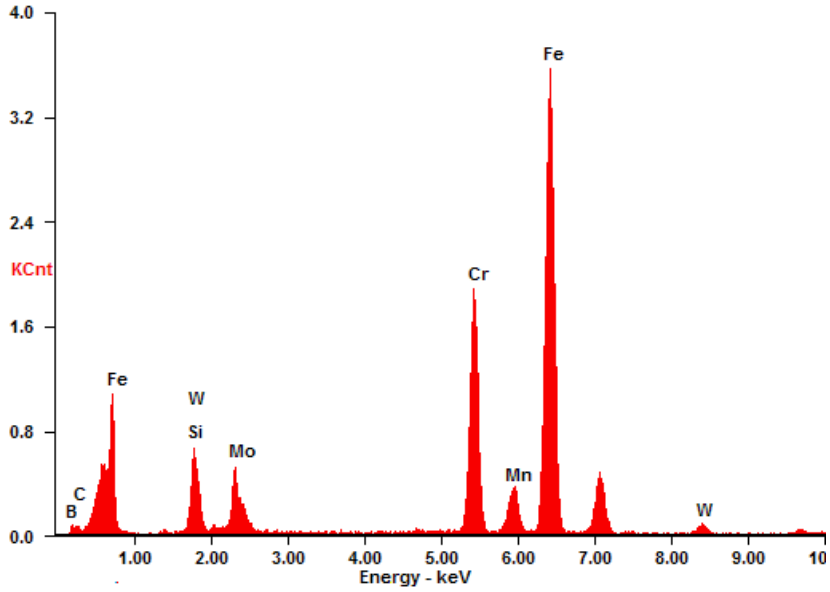

Figure 9 – This energy dispersive spectroscopy (EDS) data shows the relative abundance of molybdenum in a SAM2X1 melt-spun ribbon, which was prepared by adding one atomic percent (1 at. %) molybdenum to SAM40 (master alloy). The chromium and tungsten were also added to contribute to passivity.

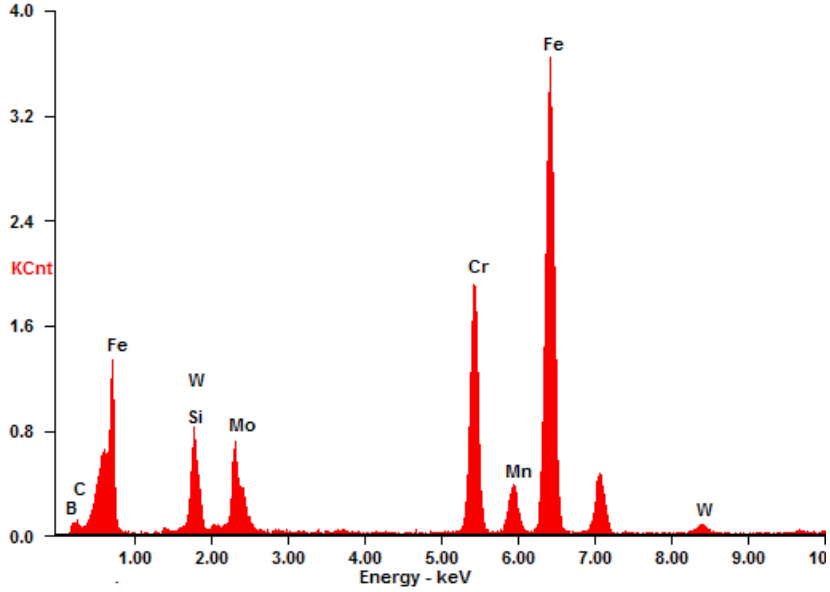

Figure 10 – This energy dispersive spectroscopy (EDS) data shows the relative abundance of molybdenum in a SAM2X3 melt-spun ribbon, which was prepared by adding one atomic percent (3 at. %) molybdenum to SAM40 (master alloy).

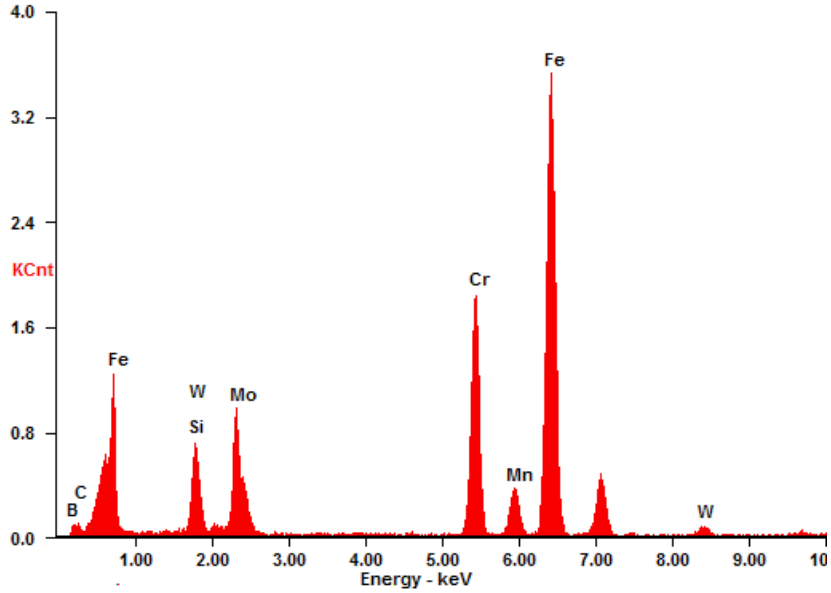

Figure 11 – This energy dispersive spectroscopy (EDS) data shows the relative abundance of molybdenum in a SAM2X5 melt-spun ribbon, which was prepared by adding five atomic percent (5 at. %) molybdenum to SAM40 (master alloy). This composition appears to provide adequate corrosion resistance, with a formulation that can still be processed with relative ease.

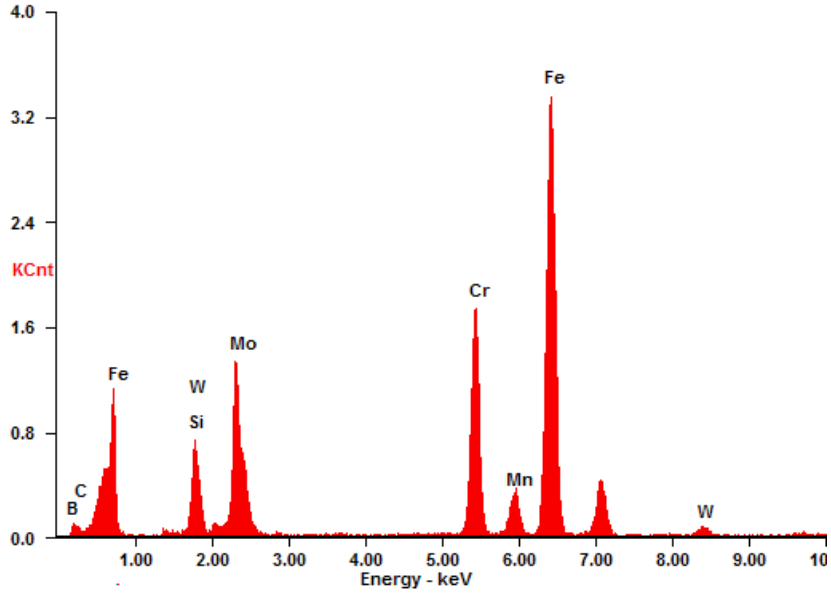

Figure 12 – This energy dispersive spectroscopy (EDS) data shows the relative abundance of molybdenum in a SAM2X7 melt-spun ribbon, which was prepared by adding seven atomic percent (7 at. %) molybdenum to SAM40 (master alloy). This composition has a high calculated pitting-resistance equivalence number (PREN), and slightly better corrosion resistance than SAM2X5, but is somewhat more difficult to make.

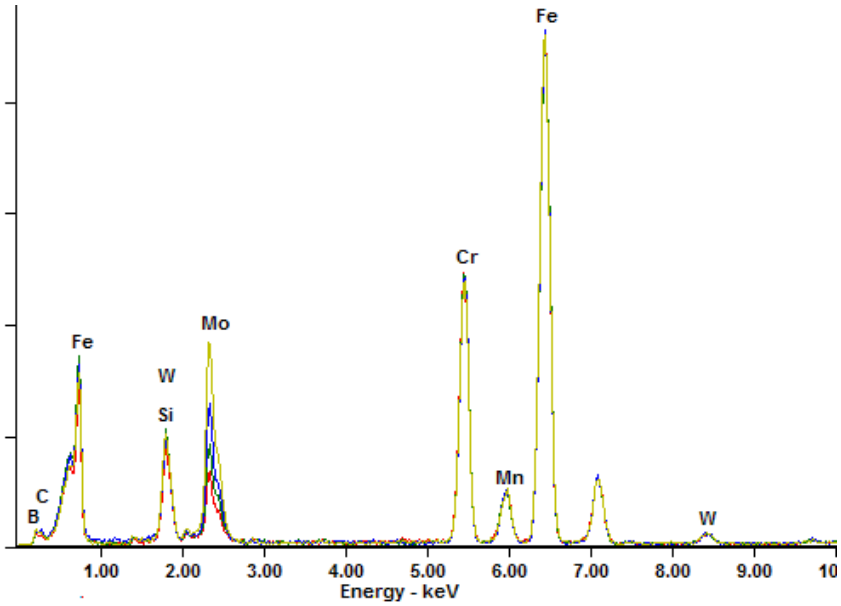

Figure 13 – This energy dispersive spectroscopy (EDS) data shows the relative abundance of molybdenum in the entire SAM2X series of iron-based amorphous metal alloys. Each spectrum was shown individually in Figures 9 through 12 and compared in this figure.

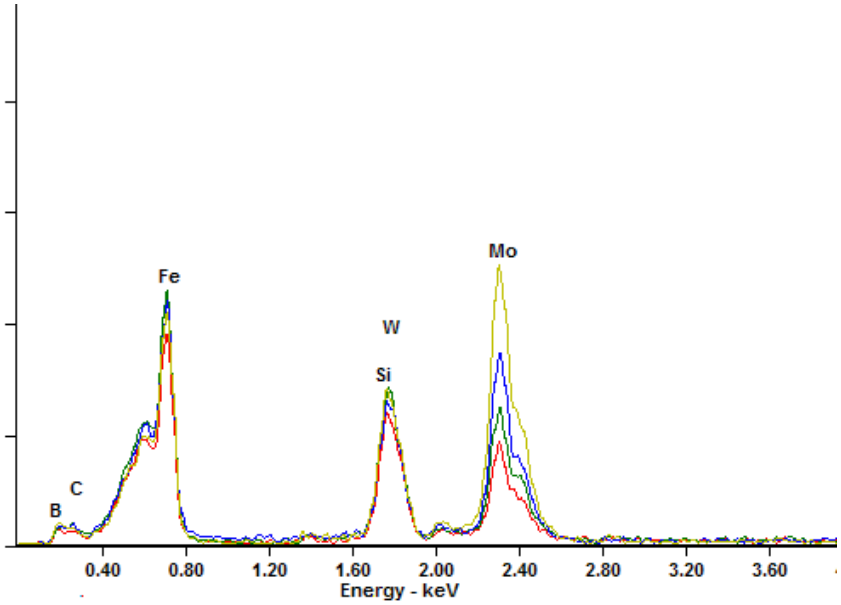

Figure 14 – This energy dispersive spectroscopy (EDS) data shows the relative abundance of molybdenum in the entire SAM2X series of iron-based amorphous metal alloys. Each spectrum was shown individually in Figures 9 through 12 and compared in this figure. In this case, the energy scale has been expanded, with the maximum energy being approximately four thousand electron volts, to show the molybdenum peak with greater clarity.

Table 4 – The melt-spinning process was used to perform a systematic study of various elemental compositions, each based on the Fe-based DAR40 composition, with 1, 3, 5, and 7 atomic percent additions of specific elements believed to be beneficial to glass formation or corrosion resistance. Elemental additions investigated included nickel (Ni), molybdenum (Mo), yttrium (Y), titanium (Ti), zirconium (Zr) and chromium (Cr). The two formulations of greatest interest at the present time, based upon corrosion resistance and ease of processing are SAM2X5 ($Fe_{49.7}Cr_{17.7}Mn_{1.9}Mo_{7.4}W_{1.6}B_{15.2}C_{3.8}Si_{2.4}$), which has a relatively high critical cooling rate (CCR), and yttrium-containing SAM1651 ($Fe_{48.0}Cr_{15.0}Mo_{14.0}B_{6.0}C_{15.0}Y_{2.0}$), which has a relatively low CCR.

Nominal Composition in Atomic Percent - Used to Prepare Samples														
Alloy	**Specification / Formula**	**Fe**	**Cr**	**Mn**	**Mo**	**W**	**B***	**C***	**Si**	**Y**	**Ni**	**P***	**Co**	**Total**
316L	**UNS S31603**	**68.0**	**18.0**	**1.5**	**1.5**	**0.0**	**0.0**	**0.0**	**1.0**	**0.0**	**10.0**	**0.0**	**0.0**	**100**
C-22	**UNS N06022**	**4.0**	**25.0**	**0.1**	**8.0**	**1.4**	**0.0**	**0.0**	**1.0**	**0.0**	**60.0**	**0.0**	**0.5**	**100**
SAM40	$Fe_{52.3}Mn_2Cr_{19}Mo_{2.5}W_{1.7}B_{16}C_4Si_{2.5}$	**52.3**	**19.0**	**2.0**	**2.5**	**1.7**	**16.0**	**4.0**	**2.5**	**0.0**	**0.0**	**0.0**	**0.0**	**100**
SAM2X1	$(SAM40)_{99} + Mo_1$	**51.8**	**18.8**	**2.0**	**3.5**	**1.7**	**15.8**	**4.0**	**2.5**	**0.0**	**0.0**	**0.0**	**0.0**	**100**
SAM2X3	$(SAM40)_{97} + Mo_3$	**50.7**	**18.4**	**1.9**	**5.4**	**1.6**	**15.5**	**3.9**	**2.4**	**0.0**	**0.0**	**0.0**	**0.0**	**100**
SAM2X5	$(SAM40)_{95} + Mo_5$	**49.7**	**18.1**	**1.9**	**7.4**	**1.6**	**15.2**	**3.8**	**2.4**	**0.0**	**0.0**	**0.0**	**0.0**	**100**
SAM2X7	$(SAM40)_{93} + Mo_7$	**48.6**	**17.7**	**1.9**	**9.3**	**1.6**	**14.9**	**3.7**	**2.3**	**0.0**	**0.0**	**0.0**	**0.0**	**100**
SAM3X1	$(DAR40)_{99} + Y_1$	**51.8**	**18.8**	**2.0**	**2.5**	**1.7**	**15.8**	**4.0**	**2.5**	**1.0**	**0.0**	**0.0**	**0.0**	**100**
SAM3X3	$(DAR40)_{97} + Y_3$	**50.7**	**18.4**	**1.9**	**2.4**	**1.6**	**15.5**	**3.9**	**2.4**	**3.0**	**0.0**	**0.0**	**0.0**	**100**
SAM3X5	$(DAR40)_{95} + Y_5$	**49.7**	**18.1**	**1.9**	**2.4**	**1.6**	**15.2**	**3.8**	**2.4**	**5.0**	**0.0**	**0.0**	**0.0**	**100**
SAM3X7	$(DAR40)_{93} + Y_7$	**48.6**	**17.7**	**1.9**	**2.3**	**1.6**	**14.9**	**3.7**	**2.3**	**7.0**	**0.0**	**0.0**	**0.0**	**100**
SAM1651	$Fe_{48}Mo_{14}Cr_{15}Y_2C_{15}B_6$	**48.0**	**15.0**	**0.0**	**14.0**	**0.0**	**6.0**	**15.0**	**0.0**	**2.0**	**0.0**	**0.0**	**0.0**	**100**

Table 5 – The actual compositions of several samples used in this study were determined with energy dispersive X-ray spectroscopy (EDS), and are summarized here. The measurements were done for wrought samples of Type 316L stainless steel and nickel-based Alloy C-22; melt-spun ribbons of SAM40, SAM2X1, SAM2X3, SAM2X5 and SAM2X7; and a drop-cast ingot of SAM1651.

Actual Compositions in Atomic Percent - Determined by Energy Dispersive X-Ray Spectroscopy														
Alloy	**Specification / Formula**	**Fe**	**Cr**	**Mn**	**Mo**	**W**	**B***	**C***	**Si**	**Y**	**Ni**	**P***	**Co**	**Total**
316L	**UNS S31603**	67.6	18.7	1.3	1.2	0.0	0.0	0.0	1.2	0.0	10.0	0.0	0.0	100
C-22	**UNS N06022**	3.9	25.2	0.1	7.8	1.4	0.0	0.0	1.1	0.0	60.0	0.0	0.5	100
SAM40	$Fe_{52.3}Mn_2Cr_{19}Mo_{2.5}W_{1.7}B_{16}C_4Si_{2.5}$	51.9	19.2	2.6	2.5	1.5	16.0	4.0	2.2	0.0	0.0	0.0	0.0	100
SAM2X1	$(SAM40)_{99} + Mo_1$	52.0	19.1	2.7	2.9	1.6	15.8	4.0	1.9	0.0	0.0	0.0	0.0	100
SAM2X3	$(SAM40)_{97} + Mo_3$	49.3	17.9	2.6	5.3	2.5	15.5	3.8	3.1	0.0	0.0	0.0	0.0	100
SAM2X5	$(SAM40)_{95} + Mo_5$	48.8	17.6	2.4	7.2	2.5	15.0	3.7	2.7	0.0	0.0	0.0	0.0	100
SAM2X7	$(SAM40)_{93} + Mo_7$	46.9	16.9	2.3	10.0	2.5	14.9	3.7	2.9	0.0	0.0	0.0	0.0	100
SAM3X1	$(DAR40)_{99} + Y_1$	49.1	19.2	1.8	3.1	3.0	15.8	4.0	2.9	1.0	0.0	0.0	0.0	100
SAM3X3	$(DAR40)_{97} + Y_3$	49.4	18.9	1.7	3.0	2.8	15.5	3.9	1.9	2.9	0.0	0.0	0.0	100
SAM3X5	$(DAR40)_{95} + Y_5$	48.8	18.4	1.5	2.6	2.6	15.2	3.8	2.2	4.8	0.0	0.0	0.0	100
SAM3X7	$(DAR40)_{93} + Y_7$	47.3	17.8	2.1	2.5	2.6	14.9	3.7	2.2	6.8	0.0	0.0	0.0	100
SAM1651	$Fe_{48}Mo_{14}Cr_{15}Y_2C_{15}B_6$	49.1	14.6	0.0	13.9	0.0	5.9	14.0	0.3	1.9	0.2	0.0	0.0	100

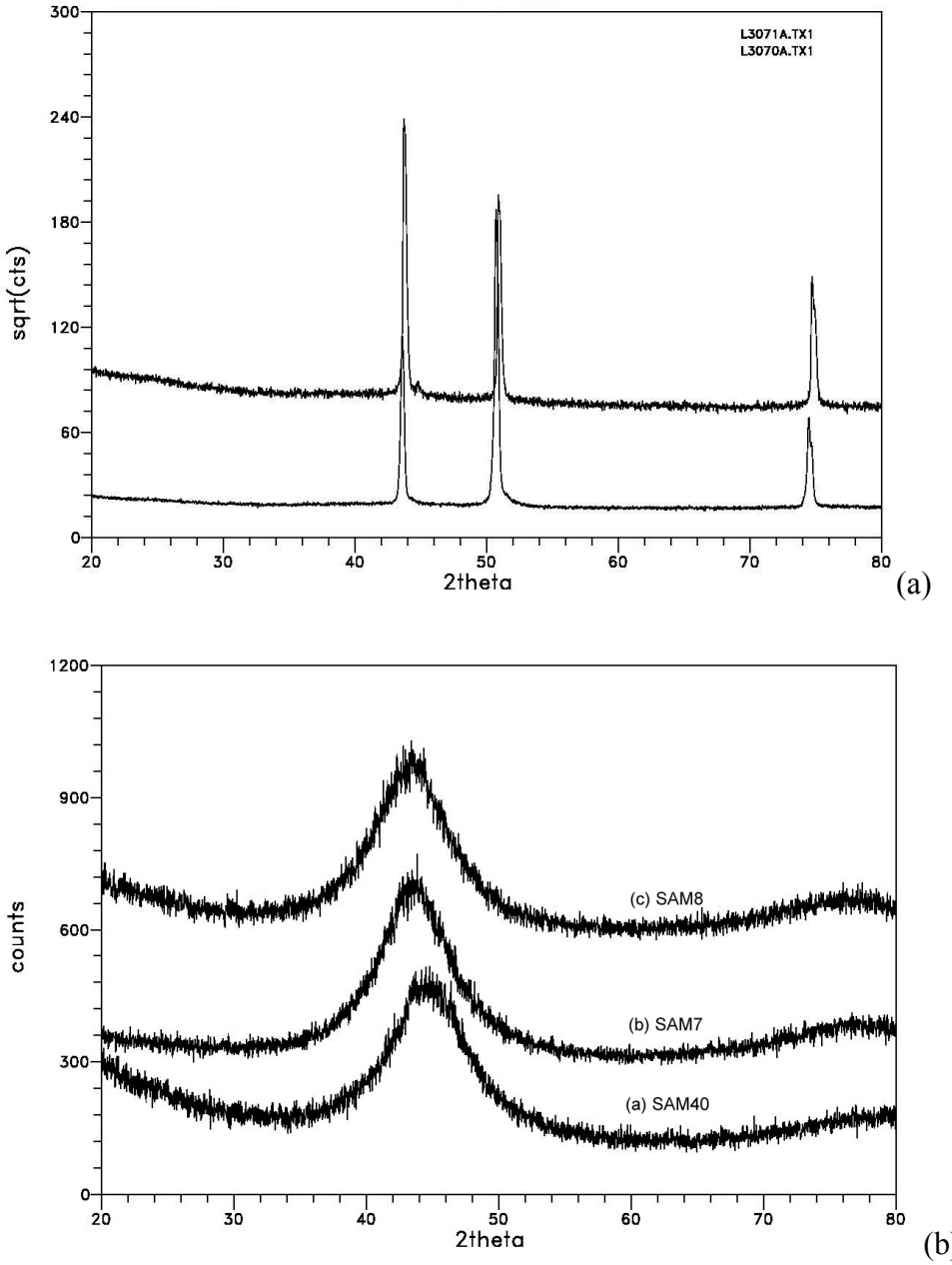

Figure 15 – (a) This figure shows X-ray diffraction data for melt-spun ribbon (MSR) samples of Type 316L stainless steel and nickel-based Alloy C-22. The strong peaks are indicative of the crystalline nature of these materials. (b) This figure shows X-ray diffraction data for melt-spun ribbon (MSR) samples of iron-based amorphous metals identified as: (a) SAM40; (b) SAM7, which is also known as SAM1651; and (c) SAM8. These MSR samples are completely amorphous.

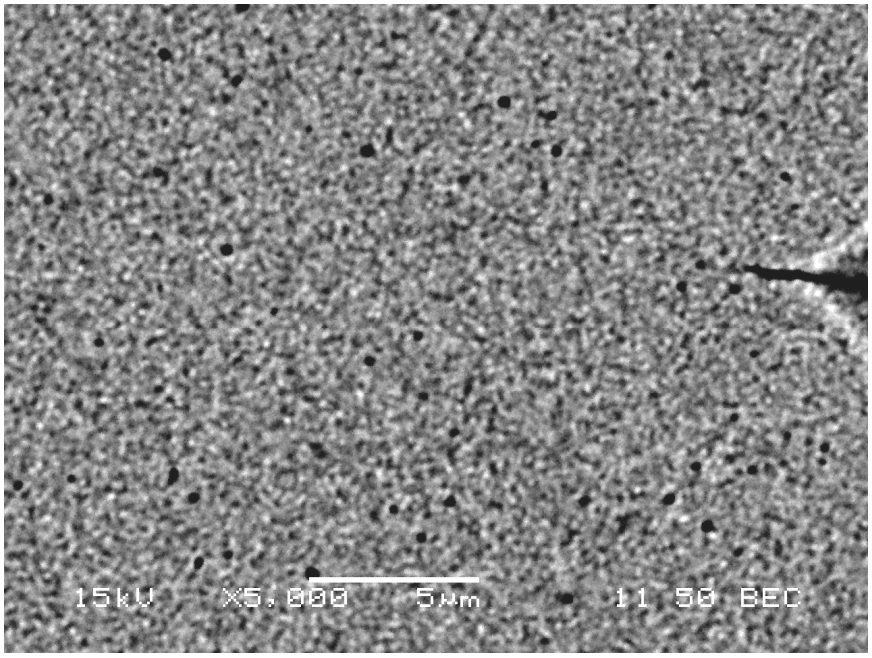

Figure 16 – This scanning electron micrograph of the original SAM40 Fe-based amorphous metal shows clear evidence of crystallization after annealing at 800°C for 1 hour.

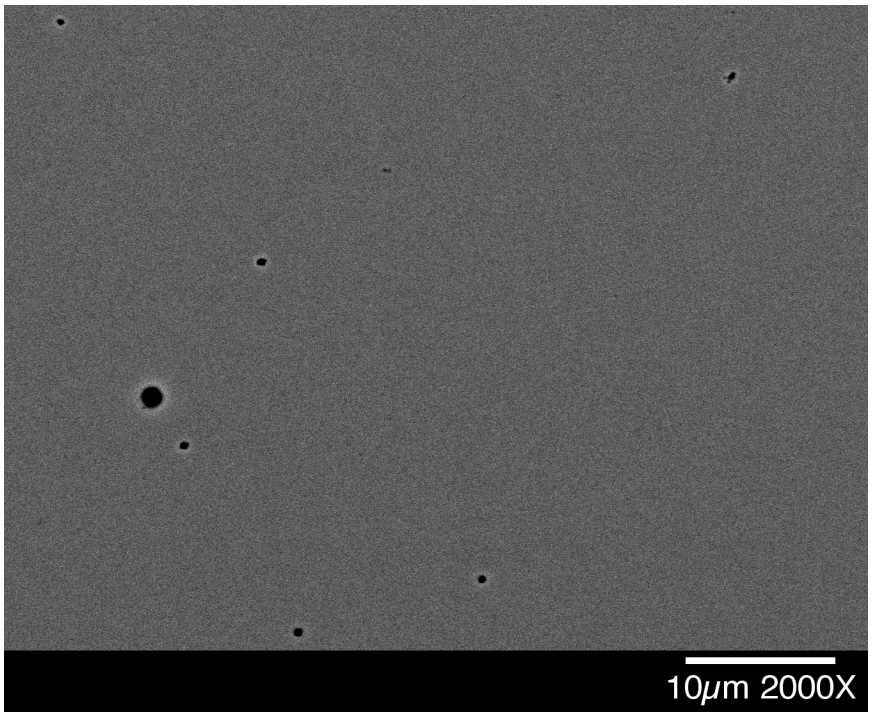

Figure 17 – This scanning electron micrograph of the SAM1651 (SAM7) Fe-based amorphous metal with yttrium shows no evidence of crystallization after annealing at 800°C for 1 hour.

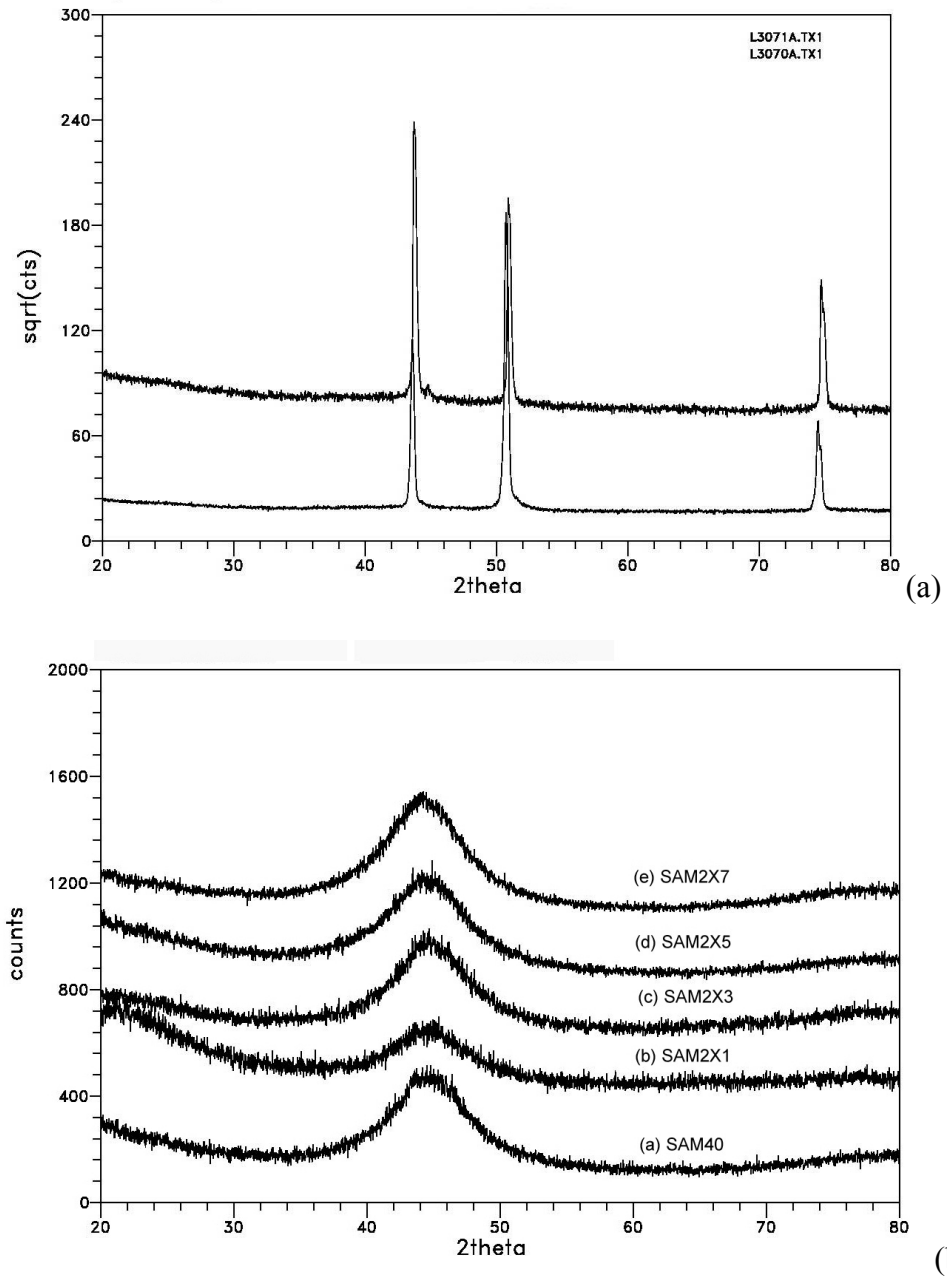

Figure 18 – (a) This figure shows X-ray diffraction data for melt-spun ribbon (MSR) samples of Type 316L stainless steel and nickel-based Alloy C-22. The strong peaks are indicative of the crystalline nature of these materials. (b) This figure shows X-ray diffraction data for melt-spun ribbon (MSR) samples of iron-based amorphous metals identified as: (a) SAM40; (b) SAM2X1; (c) SAM2X3; (d) SAM2X5; and (e) SAM2X7. All ribbons were completely amorphous.

4.2.3 Characterization of Gas Atomized Powders Used in Testing – SAM1651

Figure 19 shows scanning electron micrographs of gas-atomized SAM1651 (SAM7) powder, and reveal asymmetric particle morphology, with a number of ligaments (comet tails). The filaments are attributed to the increased melt viscosity with the rare-earth (yttrium addition). This irregular powder morphology complicates the pneumatic conveyance of the powder in thermal spray processes, and makes thermal spray deposition relatively difficult. Even with this irregular morphology, these powders have been used to render high-performance corrosion-resistant coatings of SAM1651. A research effort is underway to render this formulation as a spherical powder that can flow more easily. Figure 20 shows XRD data of the powder shown in Figure 19. In contrast to SAM2X5, which has no yttrium, these powders are amorphous over a very broad range of particle sizes. The thermal spray coatings produced with these powders were also found to be completely amorphous.

4.2.4 Characterization of Gas Atomized Powders Used in Testing – SAM2X5

The absence of crystalline structures is generally believed to be one factor that contributes to the corrosion resistance of amorphous alloys [28-31]. It was hypothesized that a relationship may exist between powder size, residual crystallinity, mechanical properties and corrosion resistance. A portion of this investigation was directed towards the proof or disproof of this hypothesis. The crystalline structure of powders can vary with particle size, since different cooling rates are experienced by particles with different sizes. Particle size sensitivity is explored in this publication, in regard to the residual crystalline phases present in powders and coatings, as well as in regard to the impact of those crystalline phases on the corrosion resistance of coatings. A correlation has been observed between the formation of substantial amounts of deleterious crystalline phases, such as ferrite, in Fe-based amorphous metals, and the susceptibility to corrosion in chloride-containing environments [1].

Due to the relatively high critical cooling rate of SAM2X5 in comparison to that of SAM1651, technological challenges had to be overcome to produce completely amorphous powder with this high-boron Fe-based amorphous metal. It has been found that particular care must be paid to the control of raw material feedstock, conditions within the atomization process. Through careful control of these variables, completely amorphous powders have been produced with the SAM2X5 high-boron composition. It should be noted that the particle size distribution of powders typically used as feedstock for HVOF deposition processes lies between 15 and 53 microns (–53/+15 μm). To explore the impact of particle size on the residual crystalline content of coatings, as well as the corrosion resistance of these coatings, a larger number of particle size distributions have been explored. Thus, this work provide unique insight into the relationship between particle size, as it effects the critical cooling rate along the radius of the particles, residual crystalline structure in the produced coatings, and the corresponding corrosion resistance.

The corrosion performance of thermal spray coatings of iron-based amorphous metals depends upon the quality of the powder used to produce the coating. In general, completely amorphous

powders are required for the deposition of completely amorphous coating with the desired level of corrosion resistance. Note that the powders are usually softened during thermal spray, and not remelted, so the original degree of crystalline or amorphous structure is preserved. Substantial experience has now been gained with a wide range of powders, having various levels of residual crystalline phase present. XRD data (intensity verses diffraction angle 2θ) for SAM2X5 powder (Lot # 05-079), showing devitrification and formation of deleterious crystalline phases, including bcc ferrite and Cr_2B, is given in Figure 21. Similar XRD data for an earlier batch of very fine SAM2X5 powder (Lot # 04-191), with a particle size distribution below 15 microns, is given in Figure 22. Clearly, this lot of powder was completely amorphous nature. XRD data for an earlier batch of coarser SAM2X5 powder (Lot # 04-199), with particles between 15 and 30 microns, is shown in Figure 23, and indicates that this powder is also completely amorphous. XRD data for an earlier batch of even coarser batches of SAM2X5 powder (Lots # 04-200 and # 04-193), with particles greater than 30 microns, show residual crystalline phases present, increasing in abundance with increasing powder size. XRD data for a recent batch of standard SAM2X5 powder sized for HVOF deposition (Lot # 06-015), which had particle sizes between 15 and 53 microns, indicates that the powder is completely amorphous and is shown in Figure 24.

A comparison of the XRD data for several lots of SAM2X5 amorphous-metal powder is shown in Figure 25, and revealed the relationship between particle size distribution and processing conditions to the formation of devitrified microstructure. During gas atomization, the powder lots with small particle sizes (Lots # 04-191 and 04-199) cooled at a rate above the critical cooling rate, and therefore maintained an amorphous microstructure. The particle sizes covered by these two lots of powder were below 30 microns. However, larger particles cooled slower, and with some points within the particles cooling below the critical cooling rate, thereby causing localized devitrification (Lots # 04-200 and # 04-193). The particle sizes covered by these lots of powder were above 30 microns. Attempts to re-melt and gas atomize this formulation causes devitrification in powders of all particle size, and is therefore undesirable (Lot # 05-079).

Differential thermal analysis (DTA) curves for various lots of SAM2X5 powder, including Lot # 04-265 (substantially amorphous), Lot # 05-079 (devitrified), Lot # 05-263 (substantially amorphous) and Lot # 06-015 (completely amorphous) are shown in Figure 26. The absence of peaks in the DTA scan for the Lot # 05-079 lot is indicative of complete devitrification, and is consistent with the XRD data shown in Figure 25. The top two curves were laboratory gas atomization runs using re-melted Lot # 05-079 feedstock powder and atomizing with helium and argon respectively, showing potential for recycling material with helium. The bottom four curves represent commercial production lots atomized with argon. A more recent lot of SAM2X5 powder, designated as Lot # 06-015 has the least crystalline content of any SAM2X5 produced to date. Recycling powder with re-melting is undesirable, as it produces a devitrified microstructure, and undesirable corrosion performance.

A scanning electron micrograph (SEM) image of SAM2X5 iron-based amorphous-metal powder is presented in Figure 27, and shows spherical morphology, which is essential for good flow characteristics in thermal spray processes.

4.2.5 Characterization of Thermal Spray Coatings Used in Testing – SAM2X5

XRD data for a HVOF coating of SAM2X5 on nickel-based Alloy C-22 substrate, and deposited with with a JP5000™ thermal-spray gun (Praxair TAFA JP5000 System), is shown in Figure 28. This coating had substantial residual crystalline phases present, and was prepared with Lot # 05-079 powder, which had a broad range of particle sizes (–53/+15μm). Recall that the XRD data for the corresponding SAM2X5 powder (Lot # 05-079) also showed substantial devitrification and formation of deleterious crystalline phases, including bcc ferrite and Cr_2B, over the entire range of particle sizes (refer Figure 21).

Similar XRD data for a HVOF coating of SAM2X5 on a Type 316L stainless steel substrate, and deposited with a JP5000 thermal-spray gun, is shown in Figure 29. This coating also had residual crystalline phases present, and was prepared with Lot # 04-265 powder, which had a similarly broad range of particle sizes (–53/+15μm). However, there was less bcc ferrite than present in the coatings prepared with Lot # 05-079 powder. Recall from the thermal analysis data shown in Figure 26 that this lot of powder was amorphous, unlike the devitrified batch identified as Lot # 04-265.

XRD data for a HVOF coating of SAM2X5 on Type 316L stainless steel substrate, deposited with the JK2000™ thermal spray gun (Deloro Stellite JetKote JK2000 System), is shown in Figure 30. This coating was prepared with Lot # 04-200 powder which had a broad range of particle sizes (–53/+15μm), typically used for HVOF processes.

XRD data for a HVOF coating of SAM2X5 on Type 316L stainless steel substrate, deposited with JK2000 thermal spray gun is shown in Figure 31. This coating was prepared with Lot # 04-199 powder which had a broad range of particle sizes (–30/+15μm).

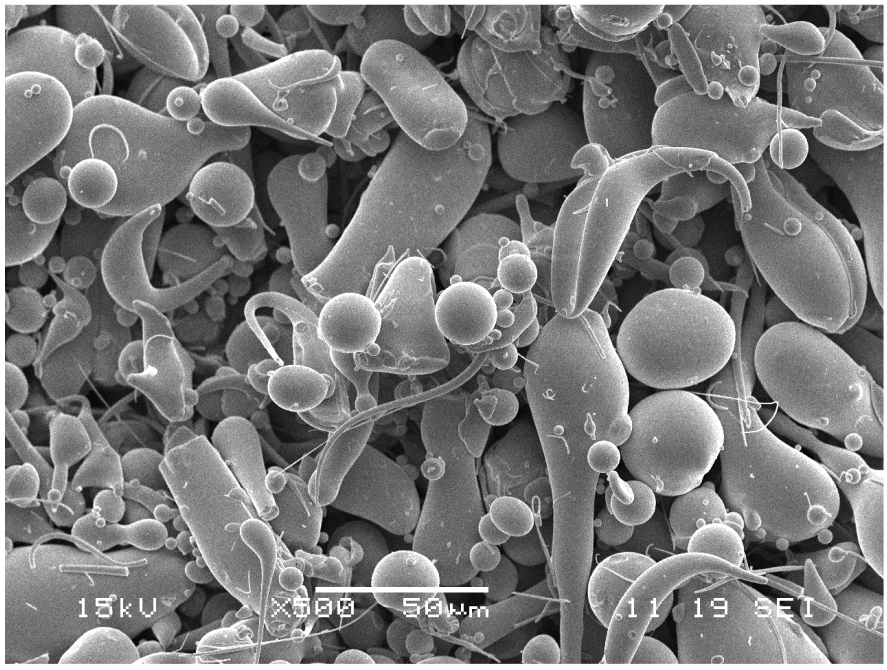

(a)

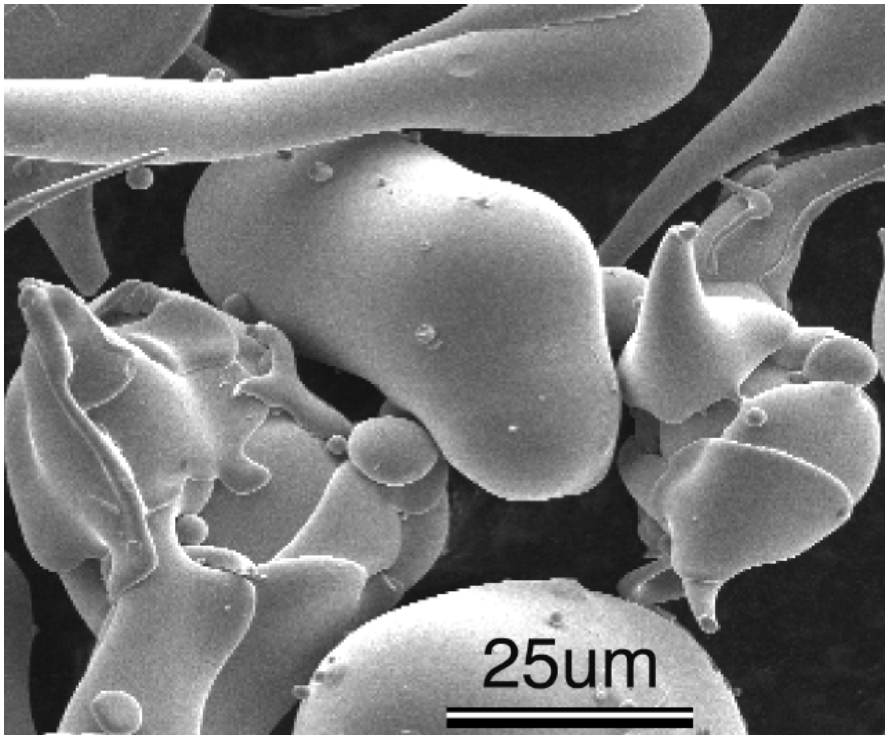

(b)

Figure 19 – These scanning electron micrographs of gas-atomized SAM1651 (SAM7) powder show the asymmetric non-spherical morphology, which results from the increased melt viscosity with the rare-earth (yttrium addition). This irregular powder morphology complicates the pneumatic conveyance of the powder in thermal spray processes, and makes thermal spray deposition relatively difficult. A research effort is underway to render this formulation as a spherical powder that can flow more easily.

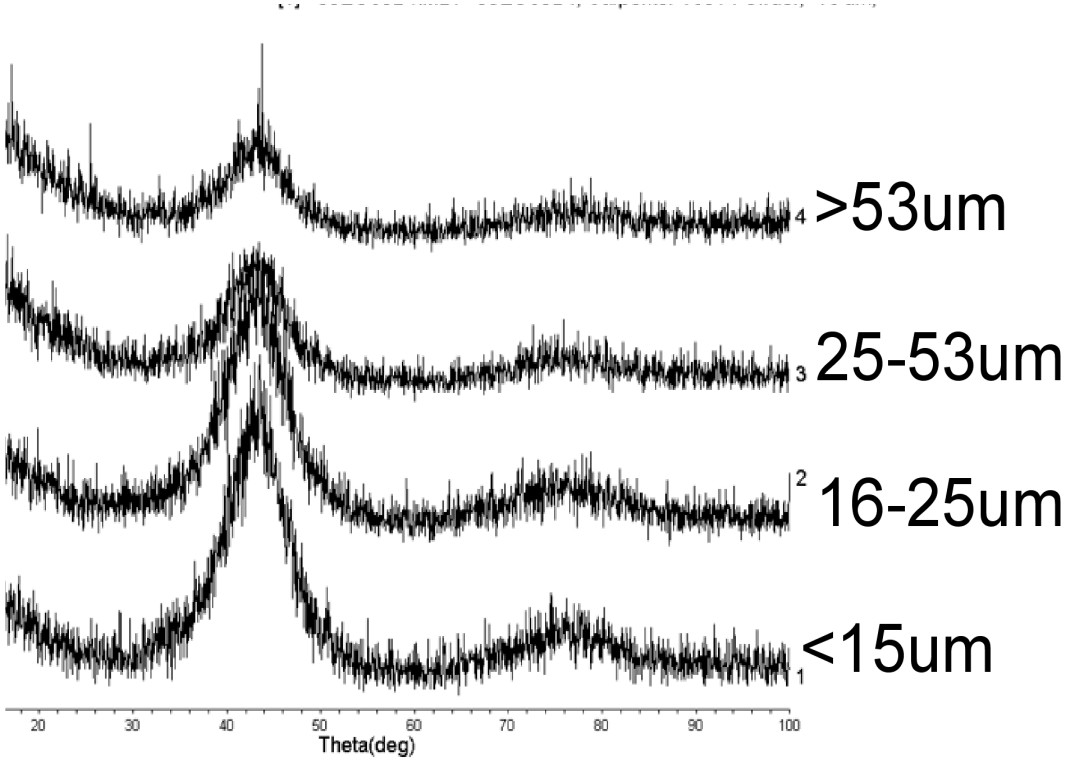

Figure 20 – This figure shows X-ray diffraction data of the powder shown in Figure 19. In contrast to SAM2X5, these powders are amorphous over a very broad range of particle sizes. SAM1651.

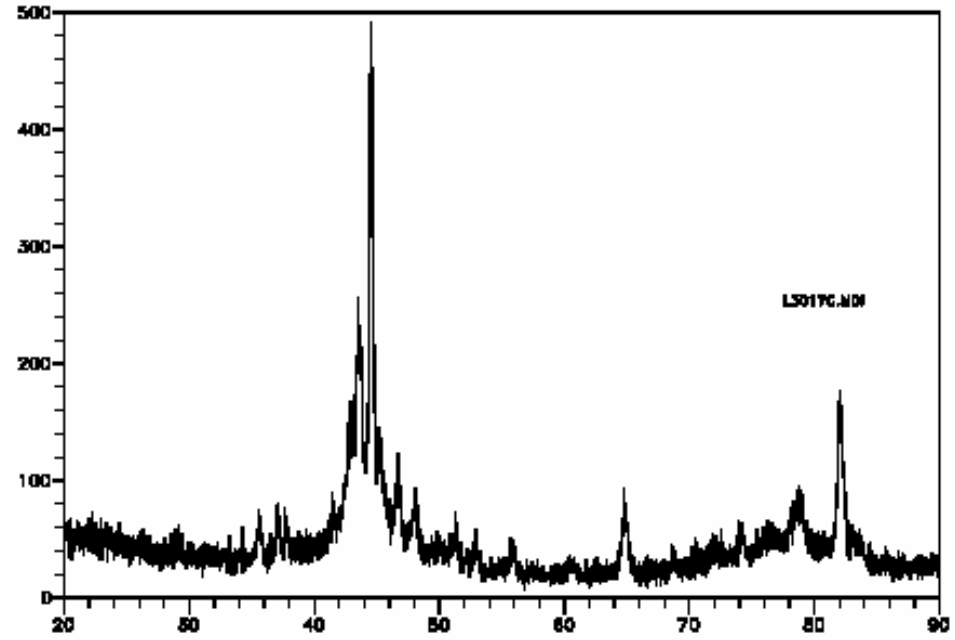

Figure 21 – XRD data (intensity verses diffraction angle 2θ) for Lot # 05-079 SAM2X5 Powder, shows devitrification and the formation of deleterious crystalline phases, including bcc ferrite and Cr_2B.

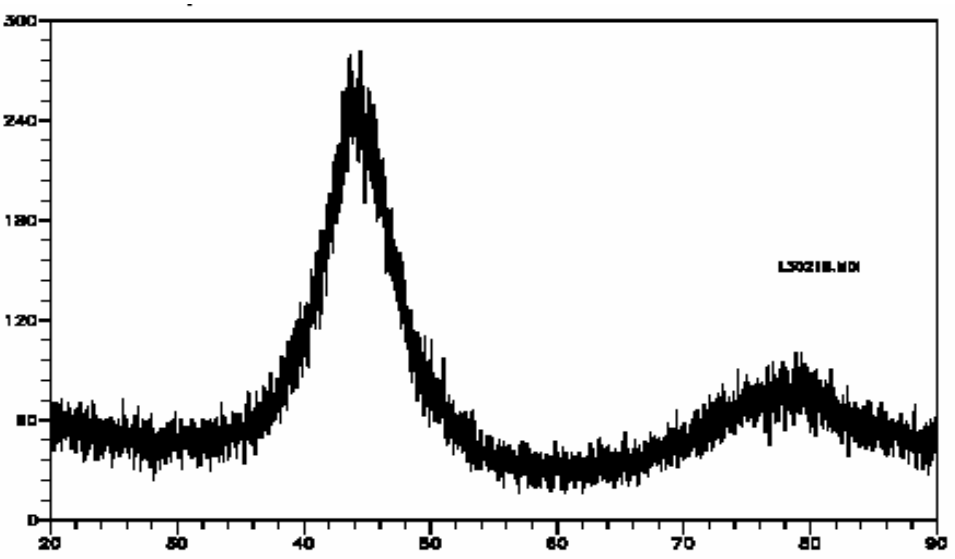

Figure 22 – XRD data (intensity verses diffraction angle 2θ) for Lot # 04-191 SAM2X5 Powder, with a particle size distribution lying below 15 microns, indicates that the material is completely amorphous.

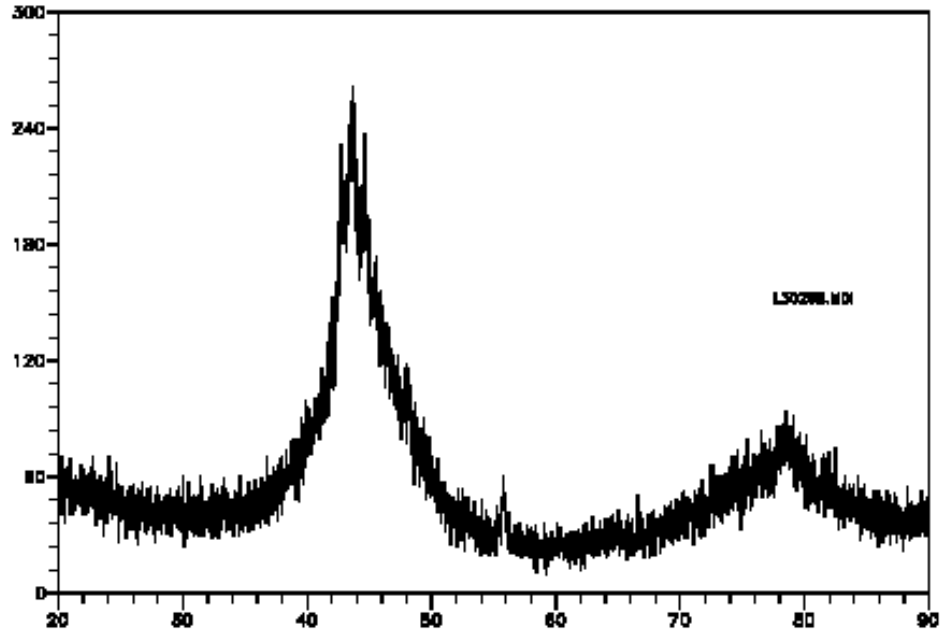

Figure 23 – XRD data (intensity verses diffraction angle 2θ) for Lot # 04-199 SAM2X5 Powder, with a particle size distribution lying between 15 and 30 microns, indicates that the material is completely amorphous.

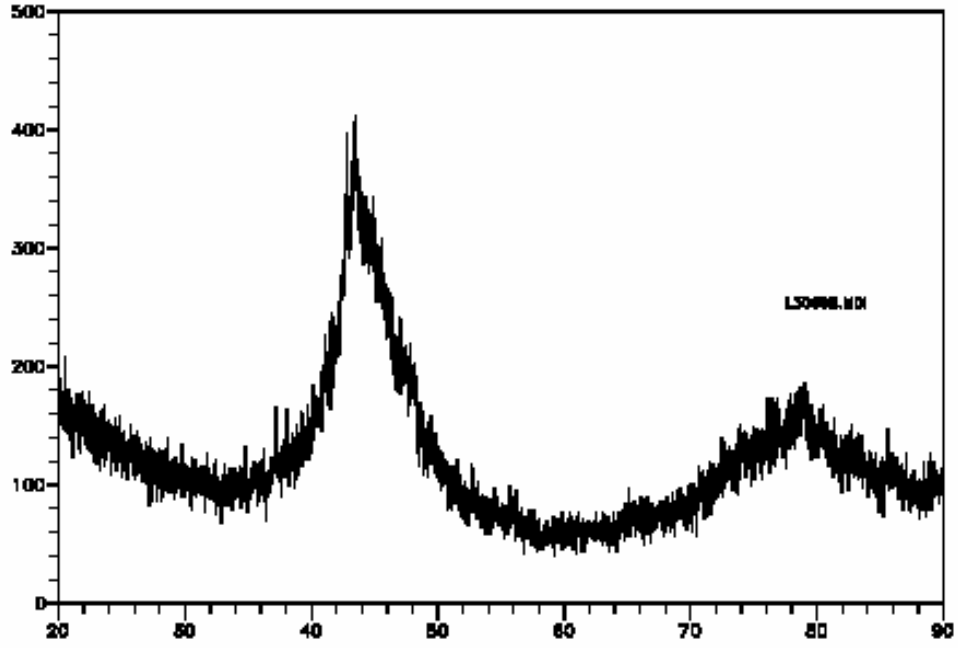

Figure 24 – XRD data (intensity verses diffraction angle 2θ) for Lot # 06-015 SAM2X5 Powder, with a broad particle size distribution lying between 15 and 53 microns, indicates that this material is completely amorphous. This material is amorphous over a much broader range of particle sizes than any previously measured lot of powder.

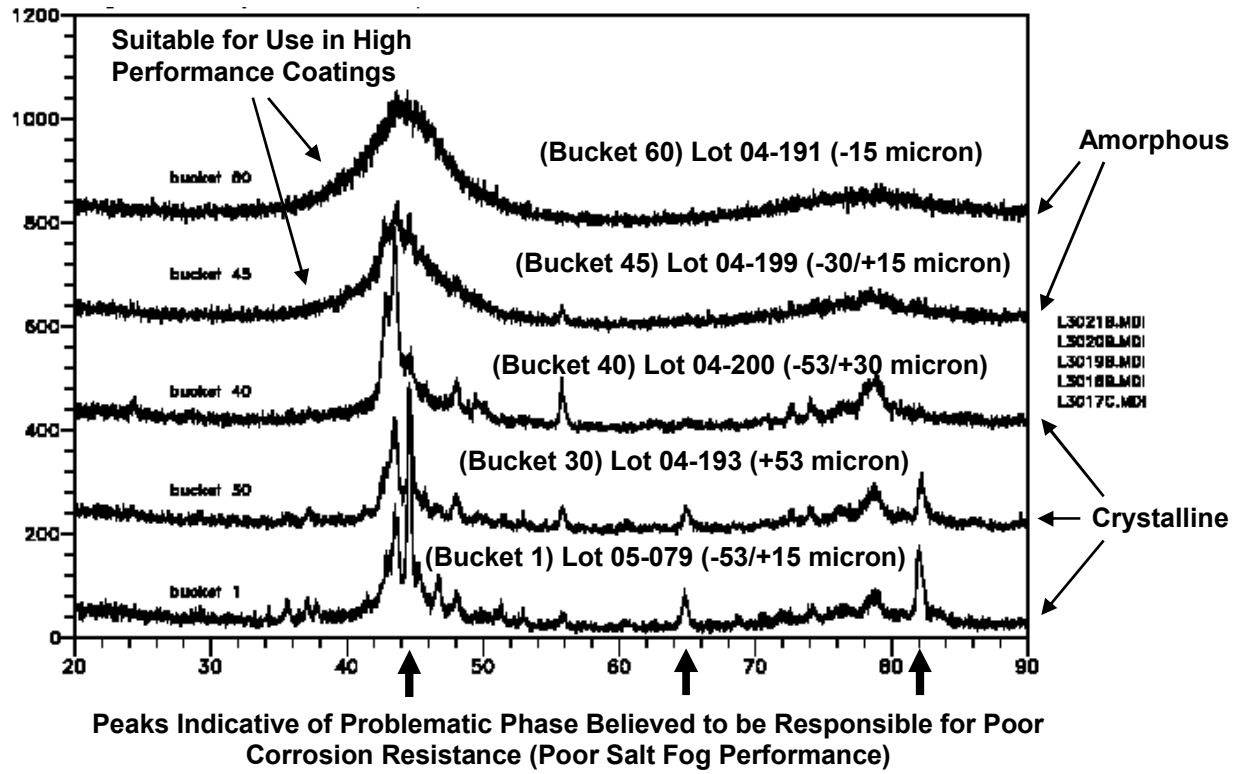

Figure 25 – This figure is a comparison of the XRD data (intensity verses diffraction angle 2θ) for several lots of SAM2X5 amorphous metal powder, revealing the relationship between particle size distribution and processing conditions to the formation of devitrified microstructure. During gas atomization, the powder lots with small particle sizes (Lots # 04-191 and 04-199) cooled at a rate above the critical cooling rate, and therefore maintained an amorphous microstructure. The particle sizes covered by these two lots of powder were below 30 microns. However, larger particles cooled slower, and with some points within the particles cooling below the critical cooling rate, thereby causing localized devitrification (Lots # 04-200 and # 04-193). The particle sizes covered by these lots of powder were above 30 microns. Attempts to re-melt and gas atomize this formulation causes devitrification in powders of all particle size, and is therefore undesirable (Lot # 05-079).

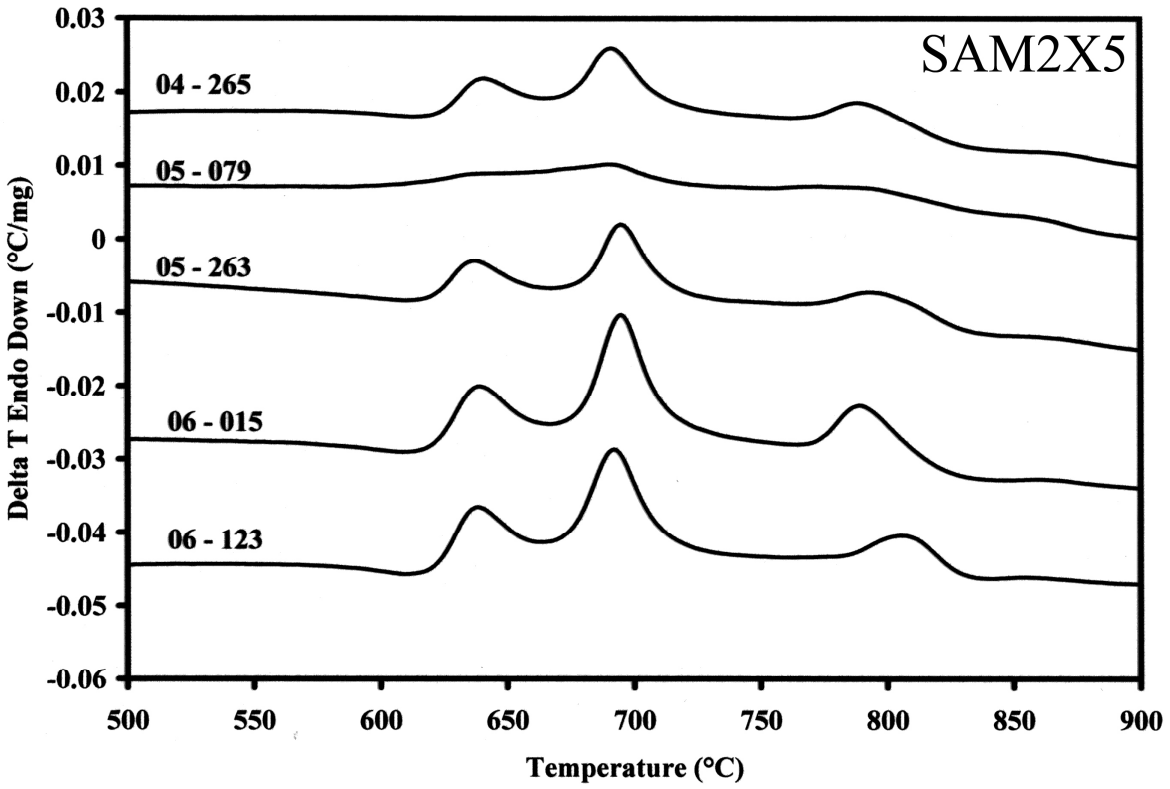

Figure 26 – Differential thermal analysis (DTA) curves for various lots of SAM2X5 powder, including Lots # 04-265, 05-079 (devitrified), 05-263 and 06-015. The absence of peaks in the DTA scan for the Lot # 05-079 lot is indicative of complete devitrification, and is consistent with the XRD data shown in Figure 25. The top two curves were laboratory gas atomization runs using re-melted Lot # 05-079 feedstock powder and atomizing with helium and argon respectively, showing potential for recycling material with helium. The bottom four curves represent commercial production lots atomized with argon. A more recent lot of SAM2X5 powder, designated as Lot # 06-015 has the least crystalline content of any SAM2X5 produced to date. Recycling powder with re-melting is undesirable, as it produces a devitrified microstructure, and undesirable corrosion performance.

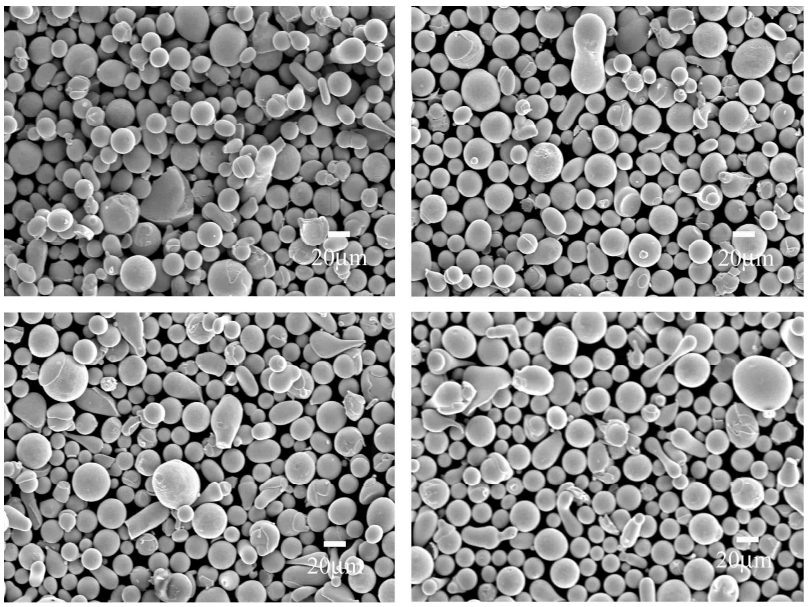

(a)

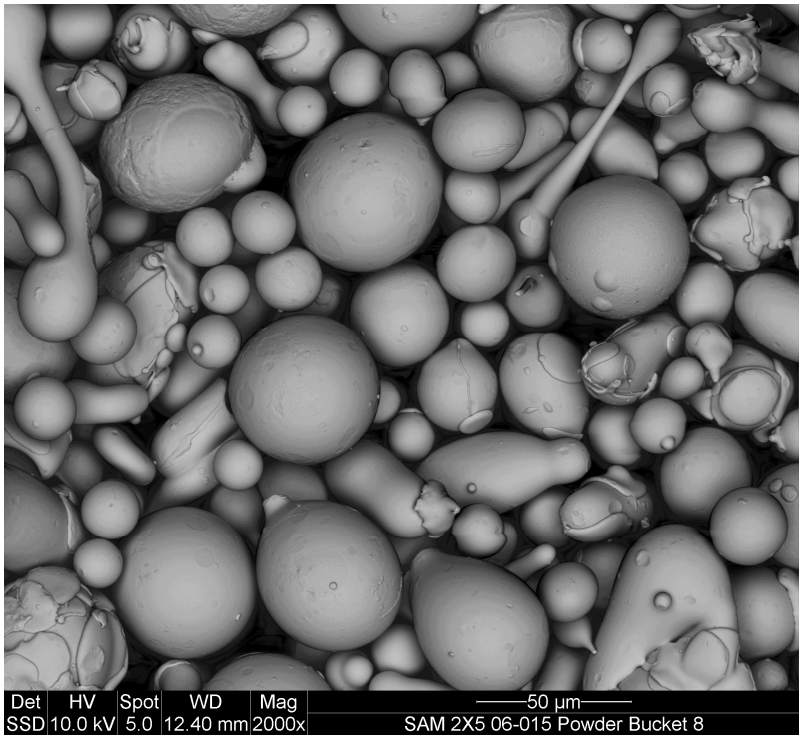

(b)

Figure 27 – Electron micrographs are shown for two lots of SAM2X5 powder produced over a span of two years: (a) Lot # 04-265; and (b) Lot # 06-123. These powders have predominantly spherical morphology, which is essential for good flow characteristics in thermal spray processes.

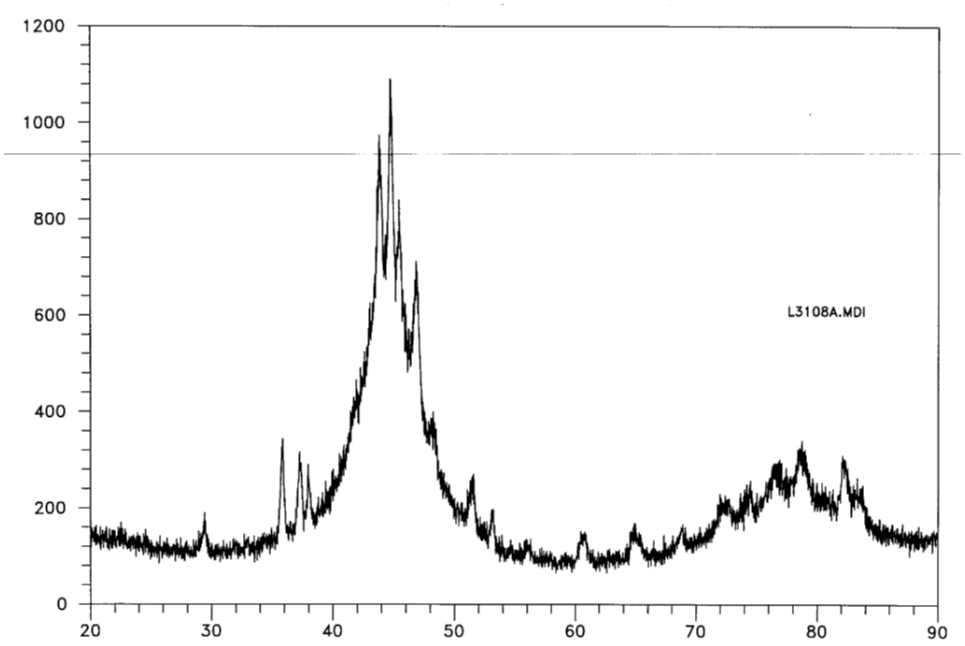

Figure 28 – XRD data (intensity verses diffraction angle 2θ) for high-velocity oxy-fuel (HVOF) coating of SAM2X5 on nickel-based Alloy C-22 substrate, deposited with a JK2000 thermal-spray gun. This coating was prepared with Lot # 05-079 powder, which had a broad range of particle sizes (–53/+15μm).

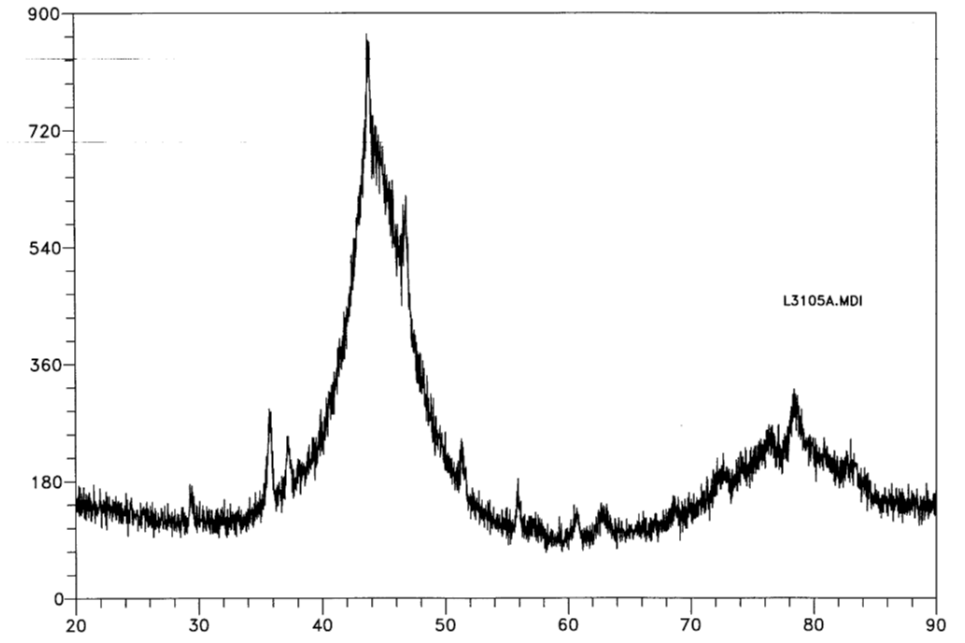

Figure 29 – XRD data (intensity verses diffraction angle 2θ) for high-velocity oxy-fuel (HVOF) coating of SAM2X5 on Type 316L stainless steel substrate prepared with JP5000 thermal spray gun. This coating was prepared with Lot #04-265 powder, which had a broad range of particle sizes (–53/+15μm).

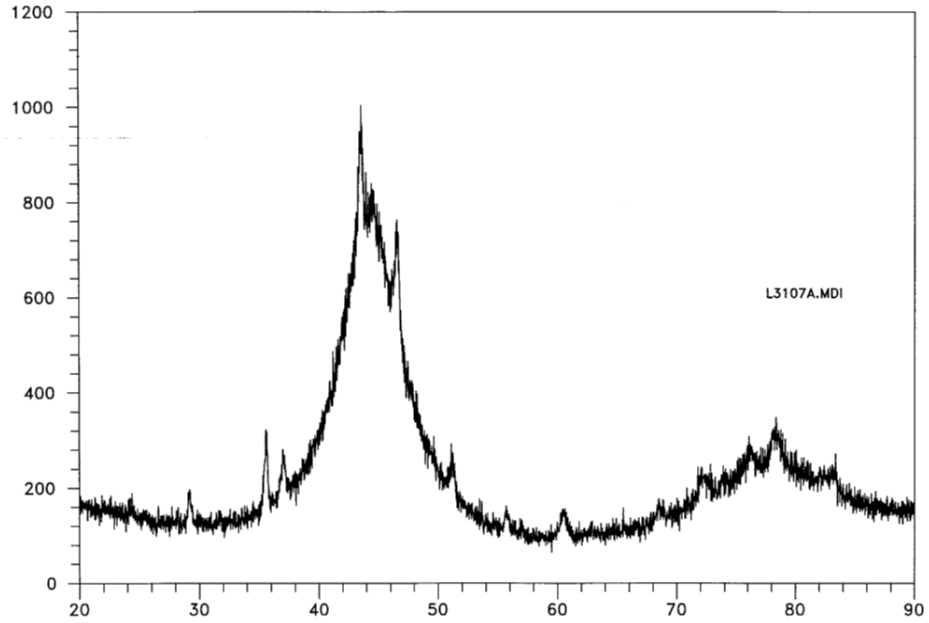

Figure 30 – XRD data (intensity verses diffraction angle 2θ) for high-velocity oxy-fuel (HVOF) coating of SAM2X5 on a Type 316L stainless steel substrate, and deposited with a JK2000 thermal-spray gun at Plasma Tech Incorporated (PTI). The feed powder was Lot # 04-200 powder, which had a relatively coarse range of particle sizes (–53/+30μm).

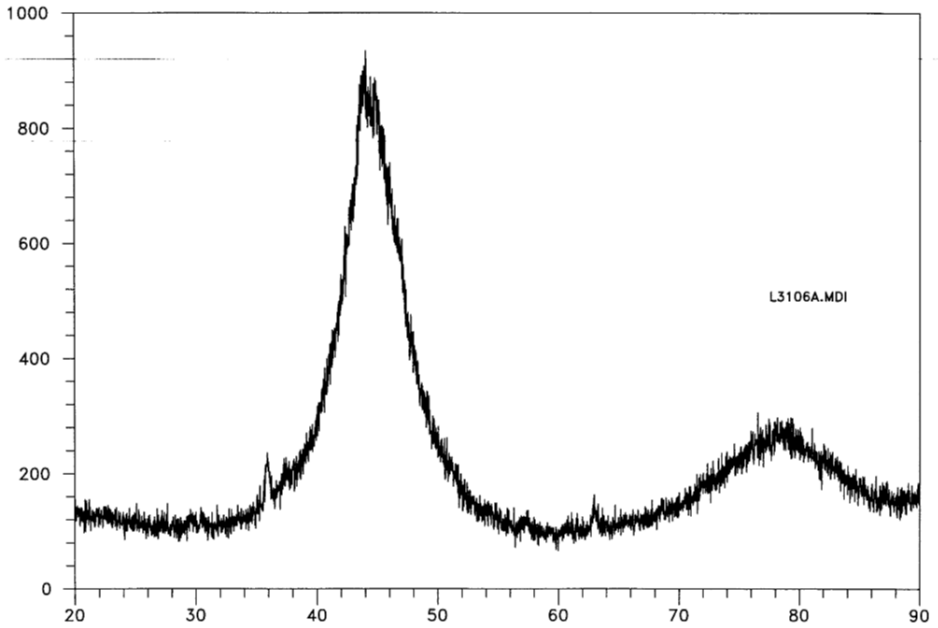

Figure 31 – XRD data (intensity verses diffraction angle 2θ) for high-velocity oxy-fuel (HVOF) coating of SAM2X5 on a Type 316L stainless steel substrate, deposited with a JK2000 thermal-spray gun at Plasma Tech Incorporated (PTI). The feed powder was Lot # 04-199 powder, which had a relatively fine range of particle sizes (–30/+15μm), and is a standard HVOF distribution.

4.2.6 Thermal Properties – SAM1651

The thermal properties of these Fe-based amorphous metals have been determined by Perepezko et al. [47]. SAM3X1 has a glass transition temperature of ~560°C, a crystallization temperature of ~614°C, a melting point of ~1108°C, and a reduced glass transition temperature of ~0.52. SAM3X5, which has significantly more yttrium than SAM3X1, has a glass transition temperature of ~590°C, a crystallization temperature of ~677°C, a melting point of ~1143°C, and a reduced glass transition temperature of 0.52. In contrast, the yttrium-containing SAM1651 (SAM7) formulation has a glass transition temperature of ~584°C, a crystallization temperature of ~653°C, a melting point of ~1121°C, and a reduced glass transition temperature of ~0.55. The critical cooling rate of SAM1651 has been determined to be ≤ 80 K per second, which is significantly less than other corrosion-resistant iron-based amorphous metals such as SAM2X5. Clearly, the yttrium additions in SAM1651 enhance glass-forming ability of these materials. Table 6 summarizes these thermal properties for SAM3X1 through SAM3X7, SAM7 (SAM1651), and SAM8.

4.2.7 Thermal Properties – SAM2X5

SAM2X5 has a glass transition temperature of ~579°C, a crystallization temperature of ~628°C, a melting point of ~1133°C, and a reduced glass transition temperature of ~0.57 (with a value of 0.6 being ideal). SAM2X7, an alloy in the same family as SAM2X5, has a glass transition temperature of ~573°C, a crystallization temperature of ~630°C, a melting point of ~1137°C, and a reduced glass transition temperature of 0.57. In contrast, the yttrium-containing SAM1651 formulation has a glass transition temperature of ~584°C, a crystallization temperature of ~653°C, a melting point of ~1121°C, and a reduced glass transition temperature of ~0.55. The critical cooling rates for SAM2X7 and SAM1651, have been determined to be ~ 610 and ≤ 80 K per second, respectively. Clearly, the yttrium additions in SAM1651 enhance glass-forming ability of these materials. The data for the SAM2X-series of alloys is summarized in Table 6.

Table 6 – Thermal analysis data (DTA or DSC) for Fe-based glass forming alloys suitable for thermal spray deposition as summarized in this table. The two formulations of greatest interest at the present time are SAM2X5 ($Fe_{49.7}Cr_{17.7}Mn_{1.9}Mo_{7.4}W_{1.6}B_{15.2}C_{3.8}Si_{2.4}$), which has a relatively high CCR, and yttrium-containing SAM1651 ($Fe_{48.0}Cr_{15.0}Mo_{14.0}B_{6.0}C_{15.0}Y_{2.0}$), which has a relatively low CCR. These selections are based upon their good corrosion resistance and relative ease or processing.

Alloy	T_g (°C)	T_x (°C)	T_m (°C)	T_L (°C)	T_{rg}
SAM40	**568-574**	**623**	**1110**	**1338**	**0.53**
SAM2X1	**575**	**620**	**1124**	**1190-1210**	**0.57**
SAM2X3	**578**	**626**	**1131**	**1190-1210**	**0.57**
SAM2X5	**579**	**628**	**1133**	**1190-1210**	**0.57**
SAM2X7	**573**	**630**	**1137**	**1190-1210**	**0.57**
SAM3X1	**560**	**614**	**1108**	**min. 1320**	**0.52**
SAM3X3	**573**	**659**	**1138**	**min. 1380**	**0.51**
SAM3X5	**590**	**677**	**1143**	**min. 1400**	**0.52**
SAM3X7	**not clear**	**697**	**1164**	**min. 1420**	
SAM1651	**584**	**653**	**1121**	**1290**	**0.55**

4.2.8 Hardness – SAM1651 & SAM2X5

Hardness is an important parameter that has impact on wear resistance, as well as the resistance to erosion-corrosion. Vickers micro-hardness (HV) is the standard approach used to assess the hardness of thermal spray coatings. In the specific case of thermal spray coatings, a 300-gram load is frequently used, since it is believed that this load and the affected area are large enough to produce a measurement that is averaged over any macro-porosity that may be present. These authors also like to report micro-hardness measurements with a 100-gram load, since it is believed that this load and the affected area are smaller, and therefore capable of sampling bulk material properties. Typical ranges of the measured micro-hardness for these HVOF coatings are summarized in Tables 7 and 8.

Table 7 – Measurements of the micro-hardness of Fe-based amorphous metal thermal spray coatings.

	Measured Vickers Micro-Hardness (kg mm^{-2})	
Loading Conditions	**As-Sprayed HVOF-Coating**	**Devitrified at 700°C for 10 Minutes**
HV100 (100-gram load)	**1050-1200**	**1300-1500**
HV300 (300-gram load)	**1000-1100**	**1200-1350**

Table 8 – The hardness (kg mm^{-2}) for as-sprayed SAM1651 HVOF coatings is summarized here.

HV100									
Indentation	**HV1**	**HV2**	**HV3**	**HV4**	**HV5**	**HV6**	**HV7**	**HV8**	**HV9**
1	**1046**	**1191**	**840**	**1232**	**1097**	**955**	**1048**	**1183**	**931**
2	**1129**	**1103**	**1181**	**1175**	**1121**	**988**	**1202**	**1140**	**903**
3	**1004**	**1022**	**978**	**1130**	**979**	**1089**	**1155**	**1035**	**827**
4	**861**	**1059**	**1104**	**1033**	**1120**	**1075**	**1160**	**1105**	**893**
5	**883**	**1115**	**1154**	**1075**	**1043**	**975**	**1205**	**1058**	**979**
Average	**985**	**1098**	**1051**	**1129**	**1072**	**1016**	**1154**	**1104**	**907**
Std. Dev.	**112**	**64**	**142**	**79**	**61**	**61**	**64**	**60**	**56**
HV300									
Indentation	**HV1**	**HV2**	**HV3**	**HV4**	**HV5**	**HV1**	**HV2**	**HV3**	**HV4**
1	**919**	**994**	**910**	**985**	**894**	**987**	**992**	**908**	**856**
2	**789**	**1038**	**889**	**861**	**876**	**870**	**1058**	**1024**	**908**
3	**784**	**1005**	**848**	**848**	**887**	**944**	**965**	**1050**	**921**
4	**892**	**1004**	**1011**	**977**	**886**	**837**	**970**	**911**	**880**
5	**901**	**943**	**854**	**810**	**917**	**876**	**971**	**924**	**894**
Average	**857**	**997**	**902**	**896**	**892**	**903**	**991**	**963**	**892**
Std. Dev.	**65**	**34**	**66**	**80**	**15**	**61**	**39**	**68**	**25**

4.2.9 Cyclic Polarization Polarization – SAM1651

Cyclic polarization data for three drop-cast ingots of SAM1651 (SAM7) Fe-based amorphous metal with yttrium in three different environments is shown in Figure 32: seawater at 90°C; 3.5 molal NaCl at 90°C; and 5M $CaCl_2$ at 105°C. All three cyclic polarization curves show outstanding passivity.

Cyclic polarization data for a wrought prism of nickel-based Alloy C-22, a drop-cast ingot of iron-based SAM7 (SAM1651) amorphous metal, and a melt-spun ribbon of SAM8 (SAM1651 or SAM7 + 3 atomic percent tungsten), all obtained with 5M $CaCl_2$ at 105°C is shown in Figure 33. Both the SAM7 (SAM1651) and SAM8 showed passive film stability comparable to (or better than) Alloy C-22. The addition of 3 atomic-percent tungsten to the SAM7 (SAM1651) enhanced the passive film stability, and also yielded more ductile and damage-tolerant amorphous metal ribbons.

4.2.10 Cyclic Polarization Polarization – SAM2X5

Potential-current data obtained during the cyclic polarization (CP) of a SAM40 melt-spun ribbon (MSR) in natural seawater at 30°C is shown in Figure 34. The OCP was –0.296 V verses Ag/AgCl, and the current density measured between OCP and 0.9 volts was below 1 $\mu A/cm^2$, which is indicative of passivity, with a distinct anodic oxidation peak was observed at approximately 0.5 V, which is believed to be due to the oxidation of molybdenum in the passive film.

Potential-current data obtained during the CP of a SAM2X3 MSR (master alloy) in natural seawater at 30°C is shown in Figure 35a. The OCP was –0.136 V verses Ag/AgCl, and the current density measured between OCP and 0.9 volts was less than approximately 1-5 $\mu A/cm^2$, which is indicative of passivity. A distinct anodic oxidation peak was observed at approximately 0.6 V, and is believed to be due to the oxidation of molybdenum in the passive film. Figure 35b shows similar data for a SAM2X5 MSR in natural seawater at 90°C. The OCP was ~–0.211 V verses Ag/AgCl, and the current density measured between OCP and 0.8 volts was less than approximately 1-5 $\mu A/cm^2$, which is indicative of passivity. A distinct anodic oxidation peak was observed at approximately 0.5 V, and is believed to be due to the oxidation of molybdenum in the passive film.

Potential-current data obtained during the cyclic polarization (CP) of a SAM2X7 MSR in natural seawater at 30°C is shown in Figure 36a. The OCP was –0.282 V verses Ag/AgCl, and the current density measured between OCP and 0.9 volts was less than approximately 1-5 $\mu A/cm^2$, which is indicative of passivity. In this case, only a slight anodic oxidation peak was observed at approximately 0.5 V, and is also believed to be due to the oxidation of molybdenum in the passive film. Figure 36b shows similar data for a SAM2X7 MSR in natural seawater at 90°C. The OCP was ~–0.182 V verses Ag/AgCl, and the current density measured between OCP and 0.8 volts was less than approximately 1-5 $\mu A/cm^2$, which is indicative of passivity. A distinct anodic oxidation peak was observed at approximately ~0.45 V, and is believed to be due to the oxidation of molybdenum in the passive film.

Potential-current data for two wrought Alloy C-22 samples and a SAM2X7 MSR in natural seawater at 30°C is shown in Figure 37. In general, the measured current densities for the SAM2X series of iron-based amorphous-metal melt-spun ribbons were less than those measured for wrought samples of Alloy C-22, indicating better passivity of the amorphous metals. The anodic oxidation peaks for SAM2X7 (see previous figure) and Alloy C-22 are believed to be due to the oxidation of molybdenum.

Potential-current data for two wrought Alloy C-22 samples, and an as-sprayed HVOF coating of SAM2X5, which was deposited on a Type 316L stainless steel substrate, in natural seawater at 90°C is shown in Figure 38. In general, the measured current density for the iron-based amorphous-metal thermal-spray coating in heated seawater was less than those measured for wrought samples of Alloy C-22, indicating better passivity of HVOF SAM2X5 coating in this particular environment. The distinct anodic oxidation peaks for Alloy C-22, and the faint peak for the SAM2X5 thermal spray coating, are all believed to be due to the oxidation of molybdenum.

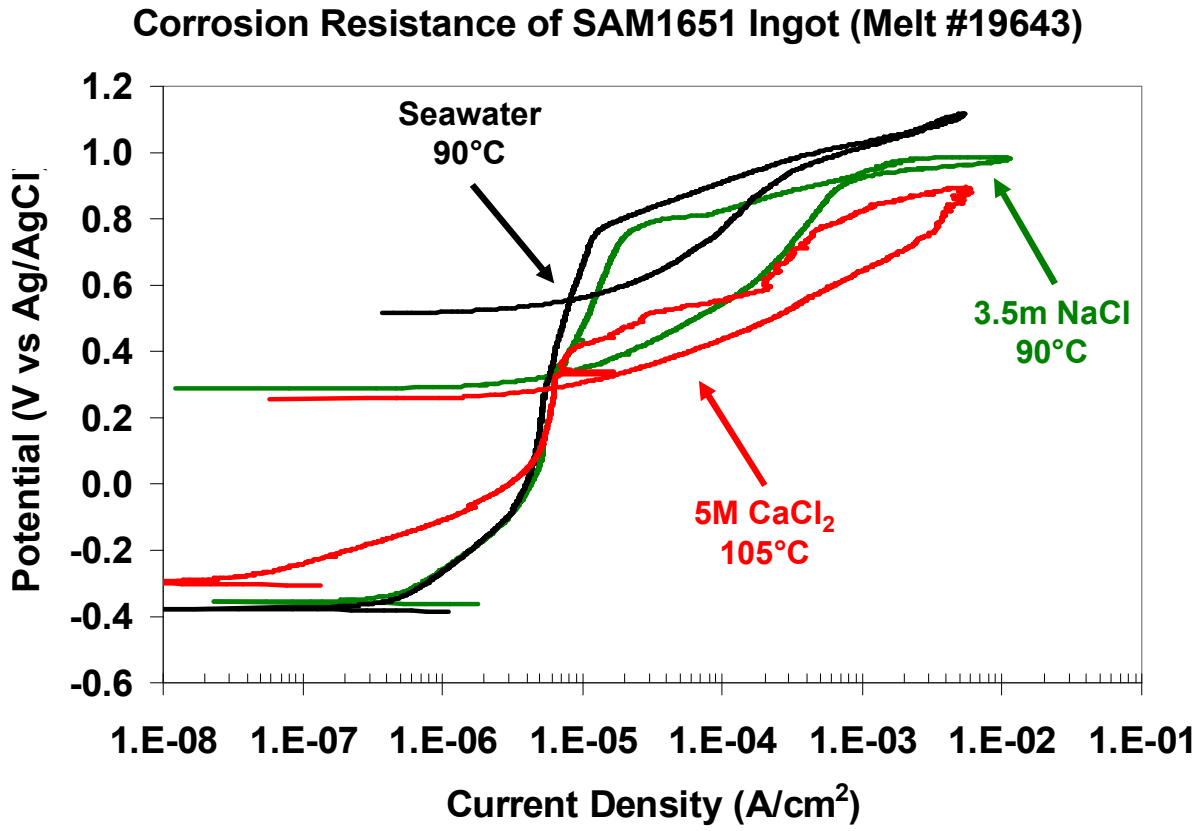

Figure 32 – Cyclic polarization data for three drop-cast ingots of SAM1651 (SAM7) Fe-based amorphous metal with yttrium in three different environments: seawater at 90°C; 3.5 molal NaCl at 90°C; and 5M $CaCl_2$ at 105°C. All three cyclic polarization curves show outstanding passivity.

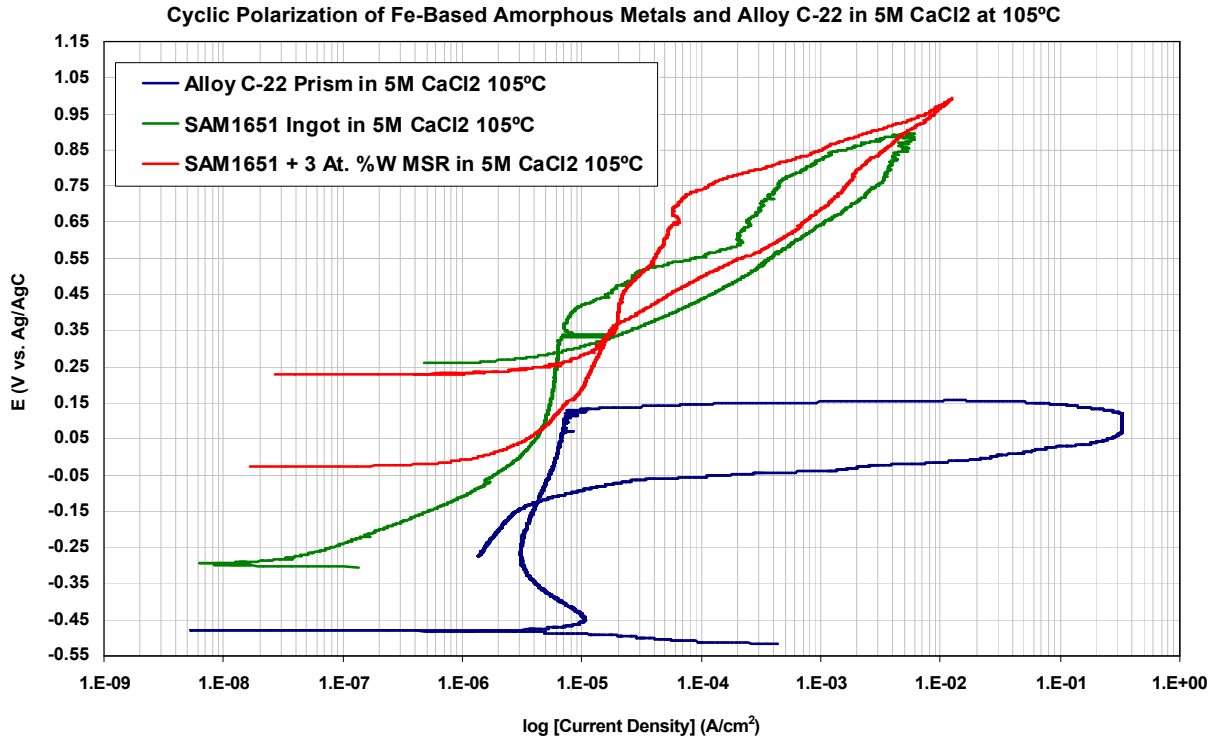

Figure 33 – Cyclic polarization data for a wrought prism of nickel-based Alloy C-22, a drop-cast ingot of iron-based SAM7 (SAM1651) amorphous metal, and a melt-spun ribbon of SAM8 (SAM1651 (SAM7) + 3 atomic percent tungsten), all obtained with 5M $CaCl_2$ at 105°C. Both the SAM7 and SAM8 showed passive film stability comparable to (or better than) Alloy C-22. The addition of 3 atomic-percent tungsten to the SAM1651 (SAM7) enhanced the passive film stability, and also yielded more ductile and damage-tolerant amorphous metal ribbons.

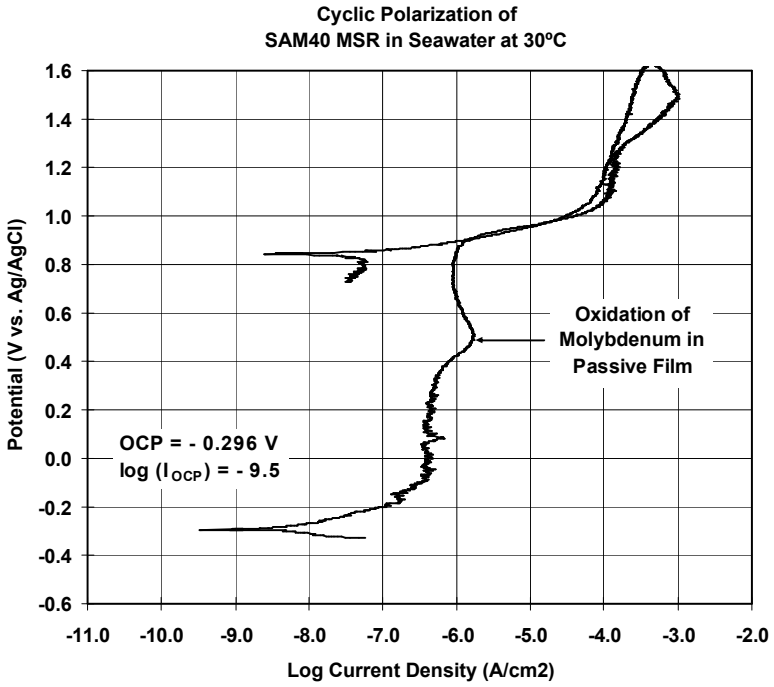

Figure 34 – This figure shows potential-current data obtained during the cyclic polarization (CP) of a SAM40 melt-spun ribbon (MSR) in natural seawater at 30°C. The OCP was –0.296 V verses Ag/AgCl, and the current density measured between OCP and 0.9 volts was below 1 μA/cm2, which is indicative of passivity, with a distinct anodic oxidation peak was observed at approximately 0.5 V, which is believed to be due to the oxidation of molybdenum in the passive film.

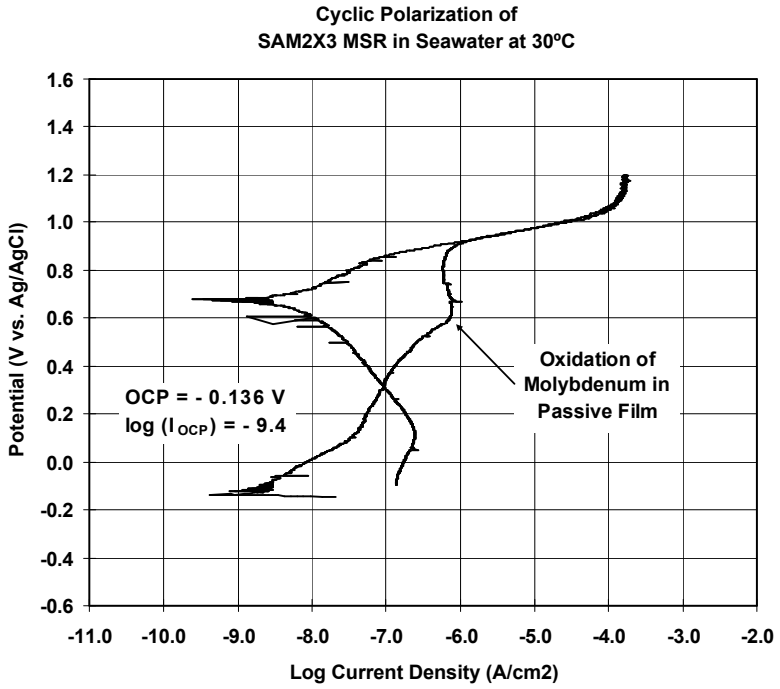

(a)

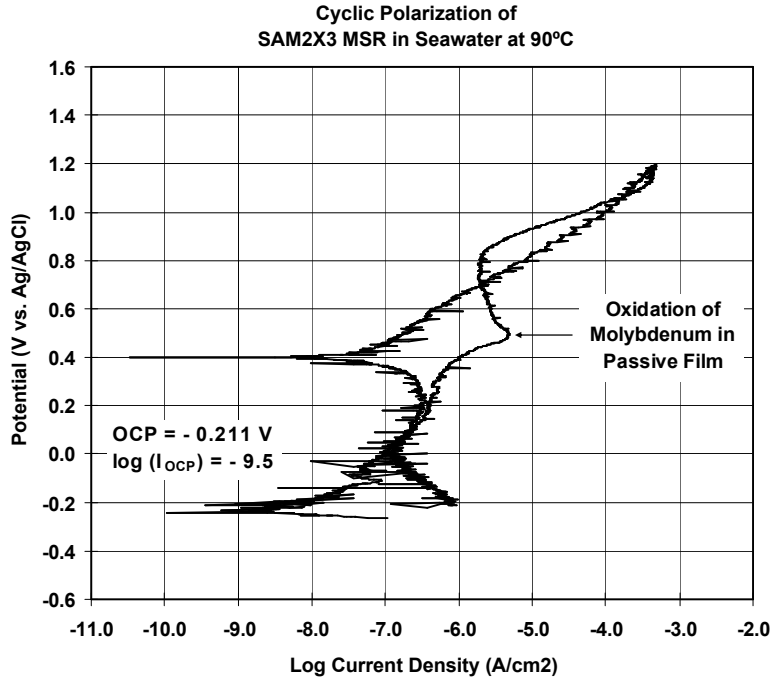

(b)

Figure 35 – (a) This figure shows potential-current data obtained during the cyclic polarization (CP) of a SAM2X3 MSR (master alloy) in natural seawater at 30°C. (b) This figure shows potential-current data obtained during the cyclic polarization (CP) of a SAM2X3 MSR in natural seawater at 90°C.

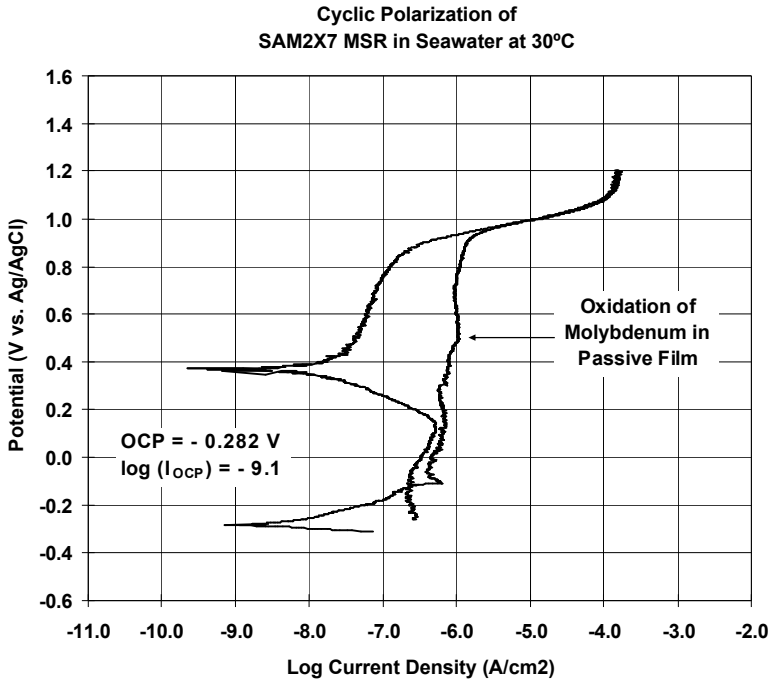

(a)

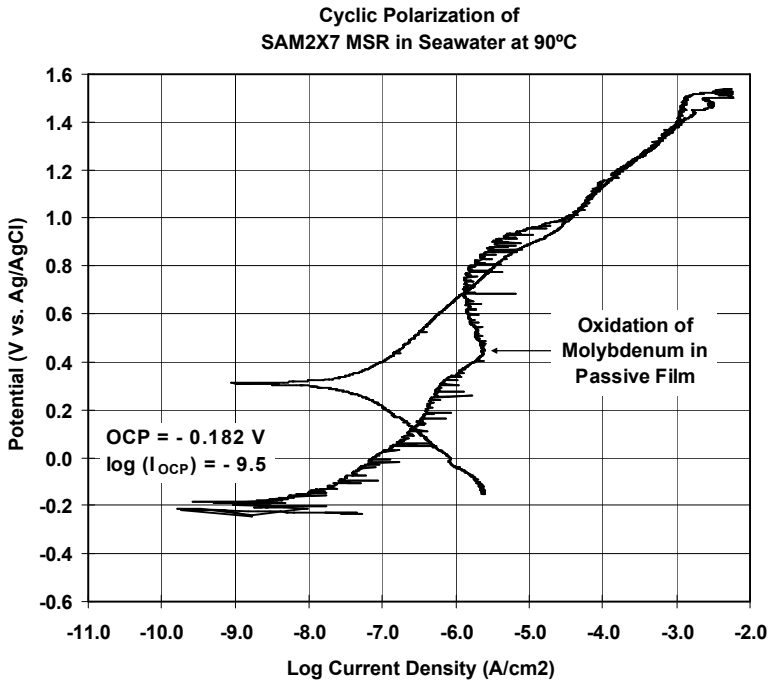

(b)

Figure 36 – (a) This figure shows potential-current data obtained during the cyclic polarization (CP) of a SAM2X7 MSR in natural seawater at 30°C. (b) This figure shows potential-current data obtained during the cyclic polarization (CP) of a SAM2X7 MSR in natural seawater at 90°C.

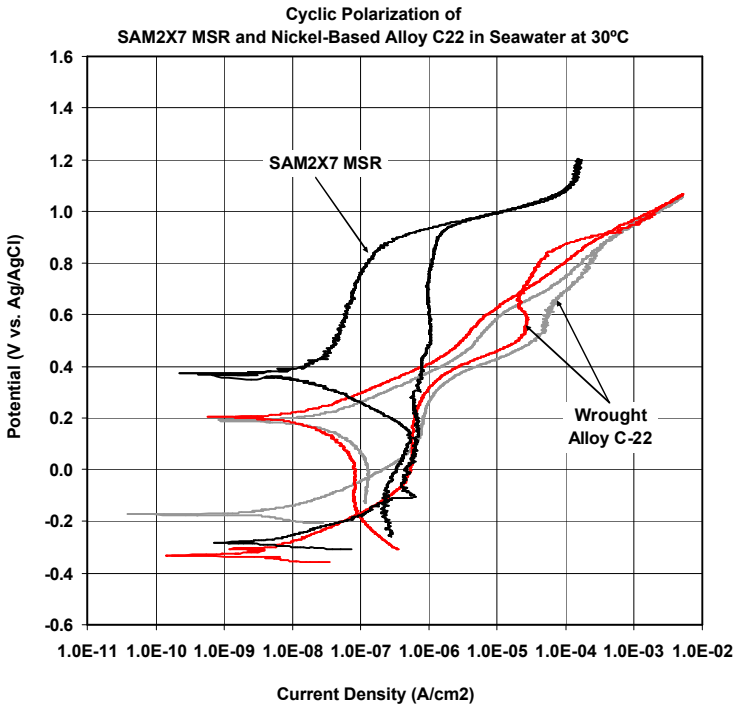

Figure 37 – This figure shows potential-current data for two wrought Alloy C-22 samples, and a SAM2X7 MSR in natural seawater at 30°C.

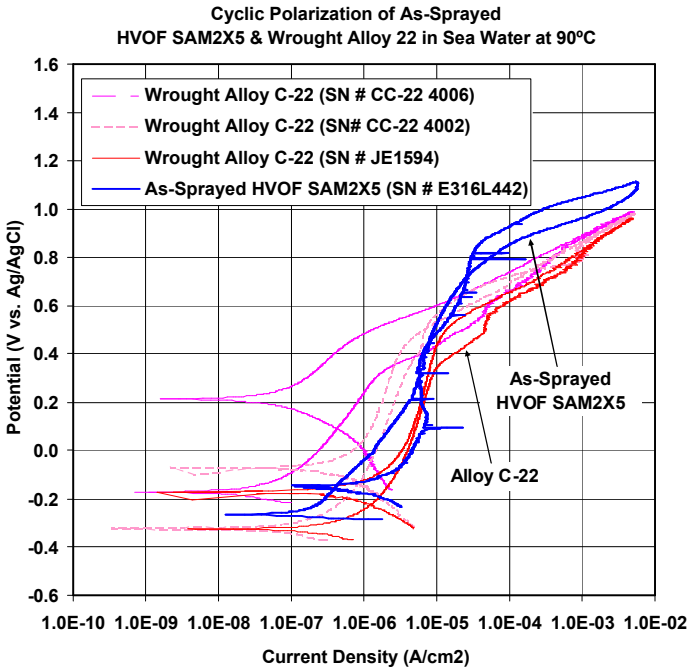

Figure 38 – This figure shows potential-current data for two wrought Alloy C-22 samples, and an as-sprayed HVOF coating of SAM2X5, which was deposited on a Type 316L stainless steel substrate, in natural seawater at 90°C.

4.2.11 Potentiostatic Data – 5M $CaCl_2$ at 105°C – SAM1651

Potential-step testing has been performed on HVOF coatings of SAM1651 (SAM7) on Type 316L stainless steel (serial number E316L475) in extremely aggressive 5M $CaCl_2$ heated to 105°C, as shown in Figure 39. Tests were also performed on the reference material, Alloy C-22, in both wrought and thermally sprayed condition (serial numbers CC-22-4008 and E316L256, respectively). To eliminate the need for surface roughness corrections in the conversion of measured current and electrode area to current density, the SAM1651 (SAM7) coating was polished to a 600-grit finish prior to testing. The curves represent the asymptotic current density reached after 24 hours at the corresponding potential. In this series of experiments, the passive film on wrought Alloy C-22 also commences breakdown at a potential of only 240 mV above the open circuit corrosion potential, with evidence of repassivation at potentials above 400 mV. Even with the repassivation at higher potential, the window of vulnerability between 240 to 400 mV is problematic for the reference material (Alloy C-22). Passive film breakdown on the HVOF coating of SAM1651 (SAM7) occurred at a significantly higher applied potential, between 360 and 400 mV, where breakdown of the passive film on thermally sprayed Alloy C-22 was virtually spontaneous. The new SAM1651 (SAM7) coating provides clear advantages for operation in hot concentrated chloride brines with aggressive divalent cations such as calcium.

Current transients wee measured at various levels of constant applied potential (100 to 450 mV vs. OCP) in 5M $CaCl_2$ at 105°C, for a polished SAM1651 (SAM7) HVOF coating on a Type 316L stainless steel (serial number E316L475), and are shown in Figure 40. These transients are indicative of good passive film stability, which is superior to that of wrought Alloy C-22 in this very aggressive environment. To eliminate the need for surface roughness corrections in the conversion of measured current and electrode area to current density, the SAM1651 (SAM7) coating was polished to a 600-grit finish prior to testing. Passive film breakdown on the HVOF coating of SAM1651 (SAM7) occurred at an applied potential between 360 and 400 mV vs. OCP, with a clear loss of passivity at 450 mV.

Current transients were measured at various levels of constant applied potential ranging (100 to 550 mV vs. OCP) in 5M $CaCl_2$ at 105°C, for wrought Alloy C-22 (serial number CC-22 4008), and are shown in Figure 41. These transients show complete breakdown of the passive film in two potential regimes, one regime located between 300-400 mV vs. OCP (350 mV), and the second located above 500 mV vs. OCP (550 mV). Like the polished SAM1651 (SAM7) coating, this reference was also polished to a 600-grit finish.

Current transients were measured at various levels of constant applied potential (100 to 350 mV vs. OCP) in 5M $CaCl_2$ at 105°C, for an as-sprayed (unpolished) Alloy C-22 HVOF coating on Type 316L stainless steel (serial number E316L256), and are shown in Figure 42. This as-sprayed HVOF coating of Alloy C-22 appears to be passive at 100-150 mV vs. OCP, but has a clear loss of passivity at potentials above 200 mV vs. OCP (250-350 mV).

4.2.12 Potentiostatic Data – Natural Seawater at 90°C – SAM1651

Potential-step testing in deaerated seawater heated to 90°C has been performed with SAM1651 (SAM7) and Alloy C-22 thermal spray coatings, as well as wrought Alloy C-22, as shown in Figure 43. The natural seawater used in these tests was obtained directly from Half Moon Bay along the northern coast of California. Tests were also performed on the reference material, Alloy C-22, in both wrought and thermally sprayed condition. To eliminate the need for surface roughness corrections in the conversion of measured current and electrode area to current density, the SAM1651 (SAM7) coating was polished to a 600-grit finish prior to testing. The Alloy C-22 thermal spray coating was tested in the as-sprayed condition, so a roughness factor must be applied to convert the apparent current density into actual current density. The curves represent the asymptotic current density reached after 24 hours at the corresponding potential. In this series of experiments, the passive film on wrought Alloy C-22 also commences breakdown at a potential of approximately 600 mV above the open circuit corrosion potential. Passive film breakdown on the HVOF coating of SM1651 occurred at an applied potential between 500 and 600 mV, where breakdown occurred at approximately 400 mV for the Alloy C-22 HVOF coating. In near-boiling seawater, the passive film stability of SAM1651 (SAM7) is comparable to that of Alloy C-22, but inferior to that of SAM2X5.

Current transients at various levels of constant applied potential ranging from (100 to 1000 mV vs. OCP) in deaerated seawater at 90°C, for wrought nickel-based Alloy C-22 (serial number CC-22 4007), and are shown in Figure 44. These measured transients are indicative of good passive film stability at the lower applied potentials. This sample was polished to a 600-grit finish, and has a surface area of approximately one square centimeter. At 700 to 800 mV vs. OCP, the current, which is close in value to the current density, rose to a point where the material was losing passivity (greater than 10 $\mu A/cm^2$).

Current transients were measured at various levels of constant applied potential (100 to 800 mV vs. OCP) in seawater at 90°C, for a 600-grit polished SAM1651 (SAM7) HVOF coating on Type 316L stainless steel (serial number E316L409), and are shown in Figure 45. These measured transients are indicative of good passive-film stability, which is comparable to that of wrought Alloy C-22. To eliminate the need for surface roughness corrections in the conversion of measured current and electrode area to current density, the SAM1651 (SAM7) coating was polished to a 600-grit finish prior to testing. Passive film breakdown on the HVOF coating of SM1651 occurred at an applied potential between 500 and 600 mV vs. OCP, with a clear loss of passivity at 700 mV. The coating represented by this figure is one of the first known thermal spray coatings with the SAM1651 (SAM7) composition.

Current transients were measured at various levels of constant applied potential (100 to 500 mV vs. OCP) in seawater at 90°C, for an as-sprayed (unpolished) Alloy C-22 HVOF coating on Type 316L stainless steel (serial number E316L255), and are shown in Figure 46. These measured transients are clearly and unambiguously indicative of a loss of passivity at the highest potential level. Since this Alloy C-22 coating was tested in the as-sprayed condition, a roughness factor must be applied to convert the *apparent* current density into the *actual* current density.

Current transients were measured at various levels of constant applied potential (100 to 736 mV vs. OCP) in seawater at 90°C, for an as-sprayed (unpolished) HVOF coating of SAM1651 (SAM7) on a Type 316L stainless steel (serial number E316L410), and are shown in Figure 47. These measured transients are indicative of good passive-film stability, which is comparable to that of wrought Alloy C-22. Since this as-sprayed SAM1651 (SAM7) coating was tested in the as-sprayed condition, a roughness factor must be applied to convert the *apparent* current density into the *actual* current density. From visual inspection, it was evident that passivity was maintained at higher potentials.

Current transients were measured at various levels of constant applied potential (100 to 615 mV vs. OCP) in seawater at 90°C, for an early as-sprayed (unpolished) HVOF coating of SAM2X5 on a Type 316L stainless steel (serial number E316L445), and are shown in Figure 48. These measured transients are indicative of good passive-film stability, which is comparable to that of wrought Alloy C-22. Since this as-sprayed SAM2X5 coating was tested in the as-sprayed condition, a roughness factor must be applied to convert the *apparent* current density into the *actual* current density. While passivity at 315 mV vs. OCP is clear, current transients are observed at 415 mV on this as-sprayed surface that may be indicative of the onset of passive film breakdown. Such breakdown is clearly evident at a slightly higher potential of 515 mV vs. OCP. While this data shows very good corrosion resistance, more recent optimization of the SAM2X5 powder and coating has enabled enhanced performance with this formulation [47].

Current transients were measured at various levels of constant applied potential (100 to 460 mV vs. OCP) in seawater at 90°C, for an early as-sprayed (unpolished) HVOF coating of SAM40XV on Type 316L stainless steel (serial number E316L325), and are shown in Figure 49. These measured transients are indicative of good passive-film stability, which is comparable to that of wrought Alloy C-22. Like the SAM2X-series of alloys, SAM40XV was prepared from the SAM40 master alloy by adding molybdenum. Since this as-sprayed SAM40XV coating was tested in the as-sprayed condition, a roughness factor must be applied to convert the *apparent* current density into the *actual* current density. While passivity at 100 to 244 mV vs. OCP is clear, current transients observed at 460 and 560 mV are clearly indicative of passive film breakdown. The SAM40XV has less molybdenum than SAM2X5, and corresponding less passive film stability.

4.2.13 Potentiostatic Data – Natural Seawater at 90°C – SAM2X5

Potential-step testing has been performed on wrought Alloy C-22 (reference material); fully dense and completely amorphous melt spun ribbons of SAM2X5; optimized HVOF coatings produced with –53/+30 micron powders of SAM2X5; and optimized HVOF coatings produced with –30/+15 micron powders of SAM2X5, as shown in Figure 50. These coatings were produced with SAM2X5 powder supplied by The NanoSteel Company (TNC), and deposited by the University of California in Davis, California (UCD) and Plasma Tech Incorporated (PTI) in Torrance, California. All were tested in natural seawater heated to 90°C. To eliminate the need for surface roughness corrections in the conversion of measured current and electrode area to current density, the SAM2X5 and SAM1651 coatings were polished to a 600-grit finish prior to testing. The curves represent the asymptotic current density reached after 24 hours at the corresponding potential (each data point represents a 24 hour test). The constant potential was

applied after 1 hour at the open circuit corrosion potential (OCP). From previous work presented in the FY04 Annual Report (given in references), it has been found that coatings produced with SAM2X5 powders below a critical size are fully dense and are completely amorphous. The coatings produced with finer powders are therefore expected to have lower porosity and less residual crystalline phases present than those produced with larger particles. These data enable a clear and unambiguous determination of the threshold potentials for passive film breakdown in a non-creviced condition. First, it is clear that the passive film on wrought Alloy C-22 commences breakdown at a potential of approximately 200 mV relative to a standard Ag/AgCl reference electrode (approximately 600 mV above the open circuit corrosion potential), and has the least corrosion resistance of any sample evaluated during this test. Passive film breakdown on the SAM2X5 melt-spun ribbon did not occur until a potential in excess of 1200 mV verses Ag/AgCl (1400 mV above OCP) was applied. Furthermore, the observed passive current density observed with this sample was extremely low. Both HVOF coatings of SAM2X5 (large and small powder sizes) also exhibited outstanding passive film stability, superior to that of the reference material. The passive film on the coating produced with –30/+15 micron powder remained intact until application of 1000 mV verses Ag/AgCl (1200 mV above OCP), with a current density well within the passive range of several microamps per square centimeter. Similar observations were made with the coating produced with –53/+30 micron powders. Any differences in morphology did not have significant impact on corrosion resistance.

Figures 51 through 56 show measured transients in current density at a constant applied potentials of 900, 1000, 1100, 1200, 1300 and 1400 mV verses OCP for several different materials in natural seawater at 90°C. The materials compared in each figure include wrought Alloy C-22 (reference material), a fully dense and completely amorphous melt-spun ribbon (MSR) of SAM2X5, HVOF coatings produced with –53/+30 micron powders of SAM2X5, and HVOF coatings produced with –30/+15 micron powders of SAM2X5. The constant potential was applied after 1 hour at the open circuit corrosion potential (OCP). The passive film on the melt spun ribbon and HVOF coatings of SAM2X5 is more stable than that on wrought nickel-based Alloy C-22 under these conditions, leading to the conclusion that this iron-based amorphous metal has superior corrosion resistance.

Transients in current density at a constant applied potential of 900 mV verses OCP for wrought Alloy C-22 (reference material), a fully dense and completely amorphous MSR of SAM2X5, HVOF coatings produced with –53/+30 micron powders of SAM2X5, and HVOF coatings produced with –30/+15 micron powders of SAM2X5, all in natural seawater heated to 90°C, are compared in Figure 51a. The constant potential was applied after 1 hour at the open circuit corrosion potential (OCP). It should also be noted that the periodic current fluctuations observed during testing of Alloy C-22 are real, and are indicative of the onset of localized corrosion. The HVOF coating prepared with relatively fine (–30/+15 μm) SAM2X5 powder has a temporary loss of passivity at 5×10^4 seconds, but undergoes repassivation at 5×10^4 seconds. In contrast, the coating produced with the standard HVOF cut of powder (–53/+30 μm) appears to be completely stable, as does the melt-spun ribbon. The differences in the corrosion resistance of the SAM2X5 coatings produced with relatively coarse (–53/+30 μm) and relatively fine (–30/+15 μm) powders is not well understood, but may be related to differences in surface area. The passive film on the melt spun ribbon and HVOF coatings of SAM2X5 is more stable than that on wrought nickel-based Alloy C-22 under these conditions, leading to the conclusion that this iron-

based amorphous metal has superior corrosion resistance. Figure 51b is identical to the previous figure, with the exception that in this case the current density scale is logarithmic.

Transients in current density at a constant applied potential of 1000 mV verses OCP for wrought Alloy C-22 (reference material), a fully dense and completely amorphous MSR of SAM2X5, HVOF coatings produced with –53/+30 micron powders of SAM2X5, and HVOF coatings produced with –30/+15 micron powders of SAM2X5, all in natural seawater heated to 90°C, are compared in Figure 52a. The constant potential was applied after 1 hour at the open circuit corrosion potential (OCP). The passive film on the melt spun ribbon and HVOF coatings of SAM2X5 is more stable than that on wrought nickel-based Alloy C-22 under these conditions, leading to the conclusion that this iron-based amorphous metal has superior corrosion resistance. Figure 52b is identical to the previous figure, with the exception that in this case the current density scale is logarithmic.

Transients in current density at a constant applied potential of 1100 mV verses OCP for wrought Alloy C-22 (reference material), a fully dense and completely amorphous MSR of SAM2X5, HVOF coatings produced with –53/+30 micron powders of SAM2X5, and HVOF coatings produced with –30/+15 micron powders of SAM2X5, all in natural seawater heated to 90°C, are compared in Figure 53a. The constant potential was applied after 1 hour at the open circuit corrosion potential (OCP). In this case, the passivity of Alloy C-22 was completely lost, with a dramatic increase in the observed current density to levels between 80 and 90 $\mu A/cm^2$, with dramatic attack of the Alloy C-22. A significant difference was observed between the corrosion resistance of HVOF SAM2X5 coatings produced with coarse (–53/+30 μm) and fine (–30/+15 μm) powders, with the standard coarse powder having better performance. The coating produced with the finer powder (–30/+15 μm) did not exhibit good passivity, defined as a current density less than approximately 5 $\mu A/cm^2$, until 2×10^4 seconds, with fluctuations in current density that may be indicative of localized corrosion phenomena. Passivity appears to have been compromised at 7×10^4 seconds. The coating produced with the coarse (–53/+30 μm) powder and the melt-spun ribbon both maintained exceptional passivity during the entire test. In summary, the passive film on the melt spun ribbon and HVOF coatings of SAM2X5 is more stable than that on wrought nickel-based Alloy C-22 under these conditions, leading to the conclusion that this iron-based amorphous metal has superior corrosion resistance. Figure 53b is identical to the previous figure, with the exception that in this case the current density scale is logarithmic.

Transients in current density at a constant applied potential of 1200 mV verses OCP for wrought Alloy C-22 (reference material), a fully dense and completely amorphous MSR of SAM2X5, HVOF coatings produced with –53/+30 micron powders of SAM2X5, and HVOF coatings produced with –30/+15 micron powders of SAM2X5, all in natural seawater heated to 90°C, are compared in Figure 54a. The constant potential was applied after 1 hour at the open circuit corrosion potential (OCP). The Alloy C-22 samples lost all passivity, while the SAM2X5 HVOF coatings and melt-spun ribbons maintained passivity, with current pulses that may be indicative of incipient localized corrosion phenomena observed during the testing of the coatings produced with the finer (–30/+15 μm) powder. The passive film on the melt spun ribbon and HVOF coatings of SAM2X5 is more stable than that on wrought nickel-based Alloy C-22 under these conditions, leading to the conclusion that this iron-based amorphous metal has superior corrosion

resistance. Figure 54b is identical to the previous figure, with the exception that in this case the current density scale is logarithmic.

Transients in current density at a constant applied potential of 1300 mV verses OCP for wrought Alloy C-22 (reference material), a fully dense and completely amorphous MSR of SAM2X5, HVOF coatings produced with –53/+30 micron powders of SAM2X5, and HVOF coatings produced with –30/+15 micron powders of SAM2X5, all in natural seawater heated to 90°C, are compared in Figure 55a. The constant potential was applied after 1 hour at the open circuit corrosion potential (OCP). Observations here are similar to those discussed in regard to figure 21, with the passive current densities observed with the SAM2X5 HVOF coatings prepared with the coarser powders beginning to exceed those observed with the coatings prepared with the finer powders. The passive film on the melt spun ribbon and HVOF coatings of SAM2X5 is more stable than that on wrought nickel-based Alloy C-22 under these conditions, leading to the conclusion that this iron-based amorphous metal has superior corrosion resistance. Figure 55b is identical to the previous figure, with the exception that in this case the current density scale is logarithmic.

Transients in current density at a constant applied potential of 1400 mV verses OCP for wrought Alloy C-22 (reference material), a fully dense and completely amorphous MSR of SAM2X5, HVOF coatings produced with –53/+30 micron powders of SAM2X5, and HVOF coatings produced with –30/+15 micron powders of SAM2X5, all in natural seawater heated to 90°C, are compared in Figure 56a. The constant potential was applied after 1 hour at the open circuit corrosion potential (OCP). Clearly the passivity on the Alloy C-22 is lost under these aggressive conditions, with the current density pulsing to 10 mA/cm^2 and decaying to 2 mA/cm^2. In contrast, the SAM2X5 samples remained passive with current densities of only 1-5 $\mu A/cm^2$. However, at this high applied potential, the passive current density observed with the coating produced with the coarse (–53/+30 μm) powder, or that observed with the melt-spun ribbon. The passive film on the melt spun ribbon and HVOF coatings of SAM2X5 is more stable than that on wrought nickel-based Alloy C-22 under these conditions, leading to the conclusion that this iron-based amorphous metal has superior corrosion resistance. Figure 56b is identical to the previous figure, with the exception that in this case the current density scale is logarithmic.

Transients in current density at various levels of constant applied potential ranging from 100 to 1400 mV verses OCP for Alloy C-22 in natural seawater at 90°C are shown in Figure 57. This reference material was polished to a 600-grit finish. The constant potential was applied after 1 hour at the open circuit corrosion potential (OCP). Passive film stability is lost above 700 mV verses OCP.

Transients in current density at various levels of constant applied potential ranging from 100 to 1600 mV verses OCP for a melt-spun ribbon of SAM2X5 in natural seawater at 90°C are indicative of good passive film stability, and are shown in Figure 58. The constant potential was applied after 1 hour at the open circuit corrosion potential (OCP). The passive film stability of this SAM2X5 sample is maintained at potentials up to 1500 mV verses OCP, which is approximately 800 mV higher than the critical potential observed with Alloy-C22. At an applied potential of 1600 mV verses OCP, passivity is lost after several hours.

Transients in current density at various levels of constant applied potential ranging from 100 to 1500 mV verses OCP for a recently optimized SAM2X5 HVOF coating (–30/+15 micron powder) in deaerated natural seawater at 90°C are indicative of good passive film stability, and are shown in Figure 59. The constant potential was applied after 1 hour at the open circuit corrosion potential (OCP). To eliminate the need for surface roughness corrections in the conversion of measured current and electrode area to current density, the SAM2X5 coating was polished to a 600-grit finish prior to testing. The curves represent the asymptotic current density reached after 24 hours at the corresponding potential (each data point represents a 24 hour test). The specified fixed potential was applied after 1 hour at the open circuit corrosion potential (OCP). The passive film stability of this SAM2X5 sample is maintained at potentials up to 1400 mV verses OCP, which is approximately 700 mV higher than the critical potential observed with Alloy-C22. At an applied potential of 1500 mV verses OCP, passivity is lost after several hours.

Transients in current density at various levels of constant applied potential ranging from 100 to 1500 mV verses OCP for a recently optimized SAM2X5 HVOF coating (–53/+30 micron powder) in natural seawater at 90°C are indicative of exceptional passive film stability, and are shown in Figure 60. To eliminate the need for surface roughness corrections in the conversion of measured current and electrode area to current density, the SAM2X5 coatings were polished to a 600-grit finish prior to testing. The constant potential was applied after 1 hour at the open circuit corrosion potential (OCP). The passive film stability of this SAM2X5 sample is maintained at potentials up to 1400 mV verses OCP, which is approximately 700 mV higher than the critical potential observed with Alloy C-22. At an applied potential of 1500 mV verses OCP, passivity is lost after several hours.

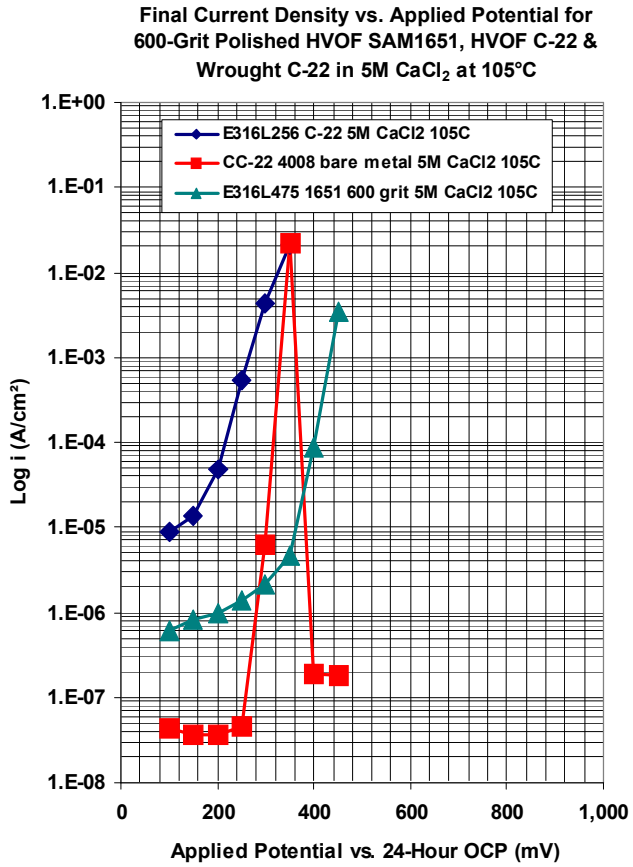

Figure 39 – Potential-step testing has been performed on HVOF coatings of SAM1651 (SAM7) on Type 316L stainless steel (serial number E316L475) in extremely aggressive 5M $CaCl_2$ heated to 105°C. Tests were also performed on the reference material, Alloy C-22, in both wrought and thermally sprayed condition (serial numbers CC-22-4008 and E316L256, respectively). To eliminate the need for surface roughness corrections in the conversion of measured current and electrode area to current density, the SAM1651 (SAM7) coating was polished to a 600-grit finish prior to testing. The curves represent the asymptotic current density reached after 24 hours at the corresponding potential. In this series of experiments, the passive film on wrought Alloy C-22 also commences breakdown at a potential of only 240 mV above the open circuit corrosion potential, with evidence of repassivation at potentials above 400 mV. Even with the repassivation at higher potential, the window of vulnerability between 240 to 400 mV is problematic for the reference material (Alloy C-22). Passive film breakdown on the HVOF coating of SAM1651 (SAM7) occurred at a significantly higher applied potential, between 360 and 400 mV, where breakdown of the passive film on thermally sprayed Alloy C-22 was virtually spontaneous. The new SAM1651 (SAM7) coating provides clear advantages for operation in hot concentrated chloride brines with aggressive divalent cations such as calcium.

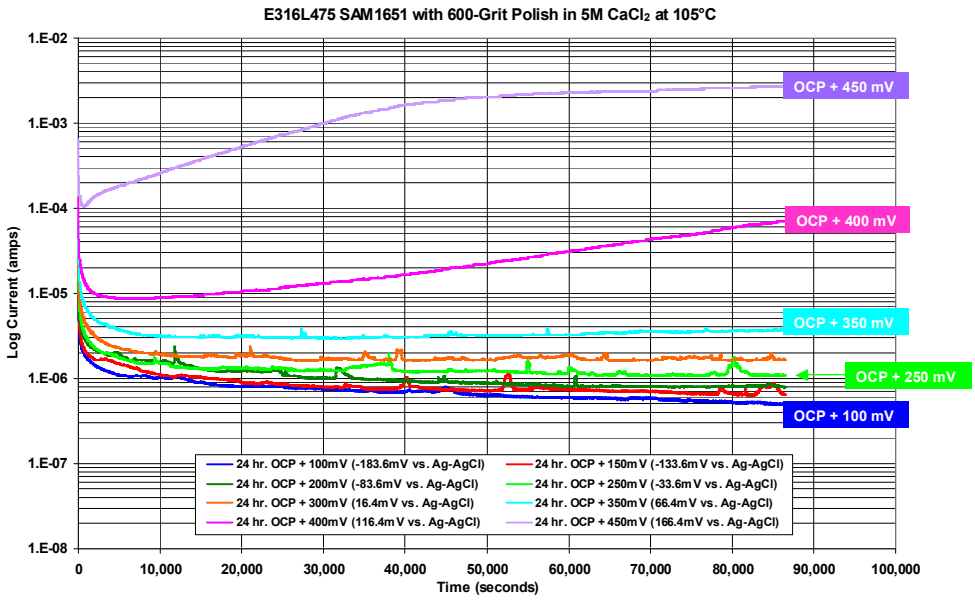

Figure 40 – Current transients wee measured at various levels of constant applied potential (100 to 450 mV vs. OCP) in 5M $CaCl_2$ at 105°C, for a polished SAM1651 (SAM7) HVOF coating on a Type 316L stainless steel (serial number E316L475).

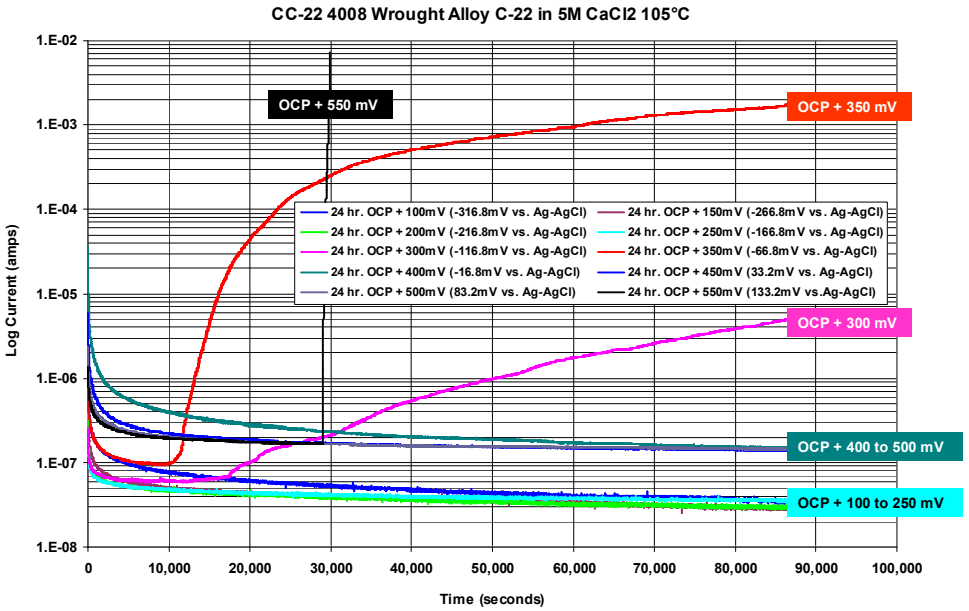

Figure 41 – Current transients were measured at various levels of constant applied potential ranging (100 to 550 mV vs. OCP) in 5M $CaCl_2$ at 105°C, for wrought Alloy C-22 (serial number CC-22 4008).

.

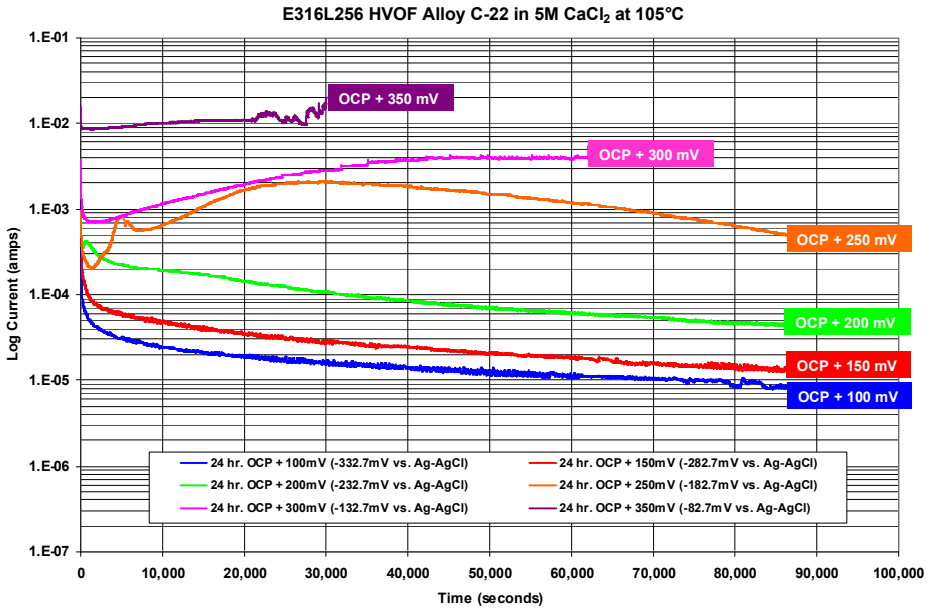

Figure 42 – Current transients were measured at various levels of constant applied potential (100 to 350 mV vs. OCP) in 5M $CaCl_2$ at 105°C, for an as-sprayed (unpolished) Alloy C-22 HVOF coating on Type 316L stainless steel (serial number E316L256).

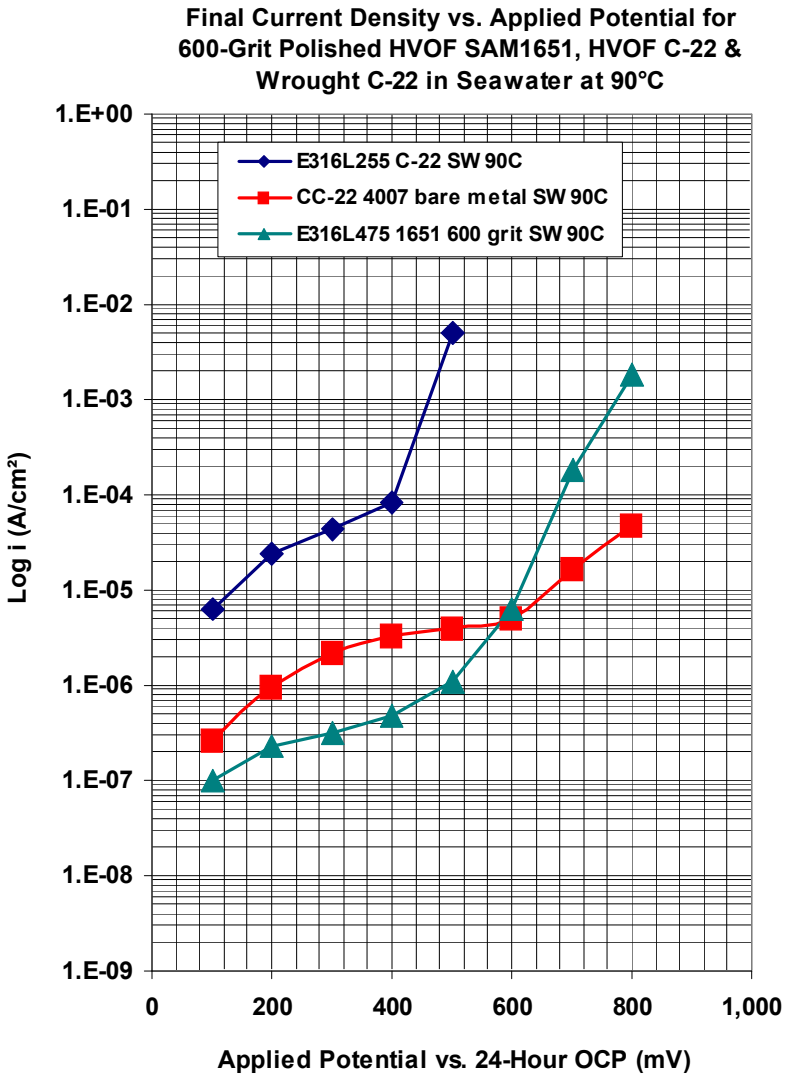

Figure 43 – Potential-step testing in deaerated seawater heated to 90°C has been performed with SAM1651 (SAM7) and Alloy C-22 thermal spray coatings, as well as wrought Alloy C-22. To eliminate the need for surface roughness corrections in the conversion of measured current and electrode area to current density, the SAM1651 (SAM7) coating was polished to a 600-grit finish prior to testing. The Alloy C-22 thermal spray coating was tested in the as-sprayed condition, so a roughness factor must be applied to convert the apparent current density into actual current density. The curves represent the asymptotic current density reached after 24 hours at the corresponding potential. In this series of experiments, the passive film on wrought Alloy C-22 also commences breakdown at a potential of approximately 600 mV above the open circuit corrosion potential. Passive film breakdown on the HVOF coating of SM1651 occurred at an applied potential between 500 and 600 mV, where breakdown occurred at approximately 400 mV for the Alloy C-22 HVOF coating. In near-boiling seawater, the passive film stability of SAM1651 (SAM7) is comparable to that of Alloy C-22, but inferior to that of SAM2X5.

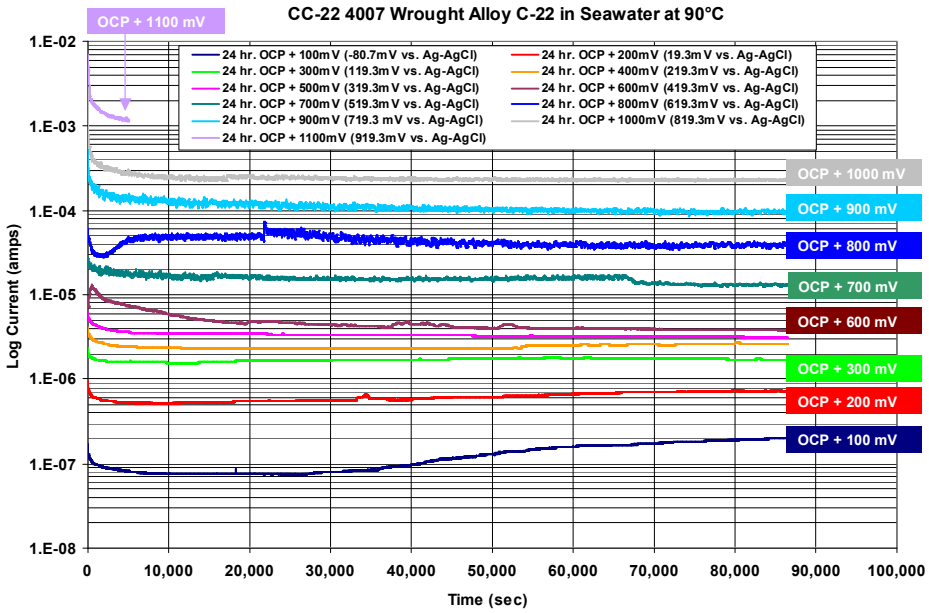

Figure 44 – Current transients at various levels of constant applied potential ranging from (100 to 1000 mV vs. OCP) in deaerated seawater at 90°C, for wrought nickel-based Alloy C-22 (serial number CC-22 4007).

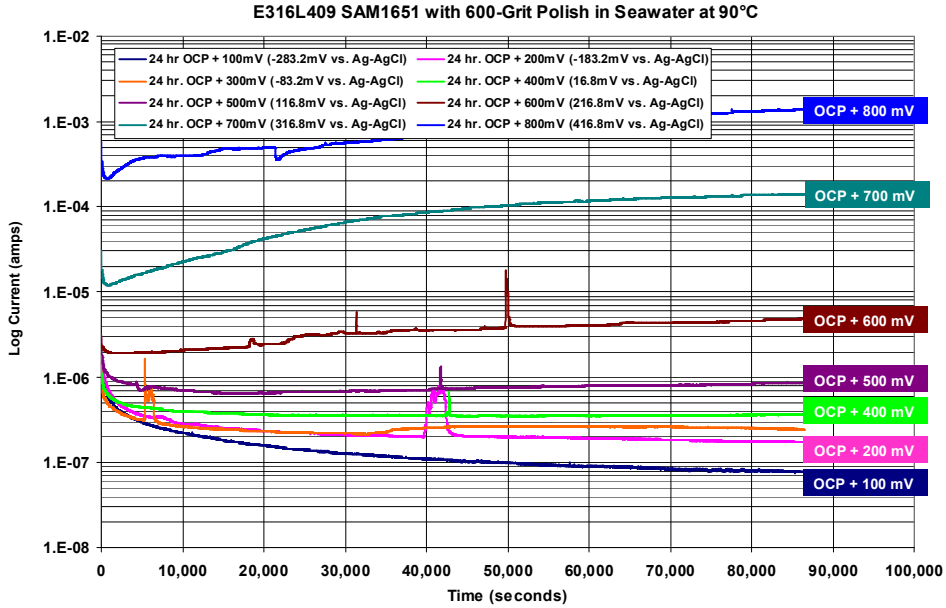

Figure 45 – Current transients were measured at various levels of constant applied potential (100 to 800 mV vs. OCP) in seawater at 90°C for a 600-grit polished SAM1651 (SAM7) HVOF coating on Type 316L stainless steel (serial number E316L409).

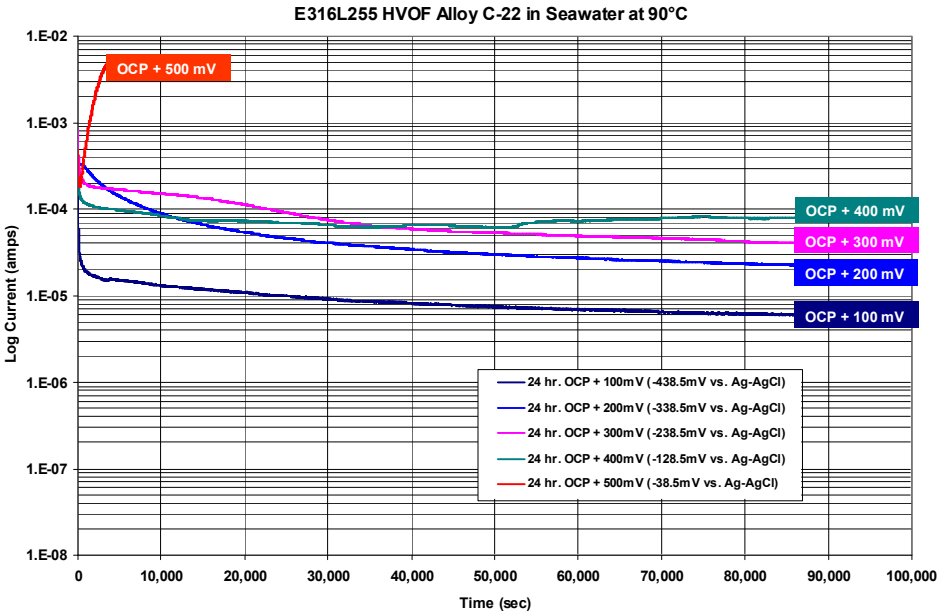

Figure 46 – Current transients were measured at various levels of constant applied potential (100 to 500 mV vs. OCP) in seawater at 90°C, for an as-sprayed (unpolished) Alloy C-22 HVOF coating on Type 316L stainless steel (serial number E316L255).

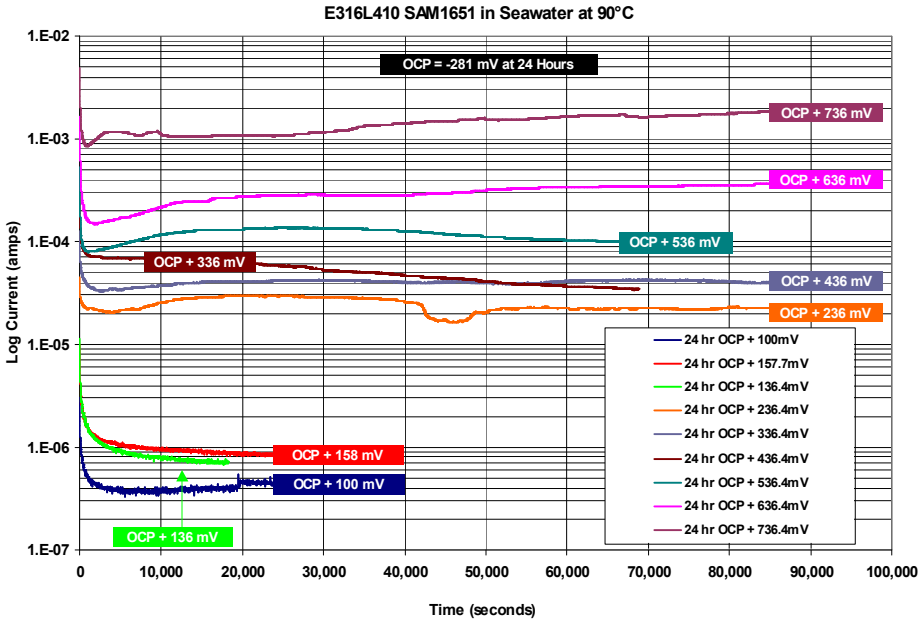

Figure 47 – Current transients were measured at various levels of constant applied potential (100 to 736 mV vs. OCP) in seawater at 90°C, for an as-sprayed (unpolished) HVOF coating of SAM1651 (SAM7) on a Type 316L stainless steel (serial number E316L410).

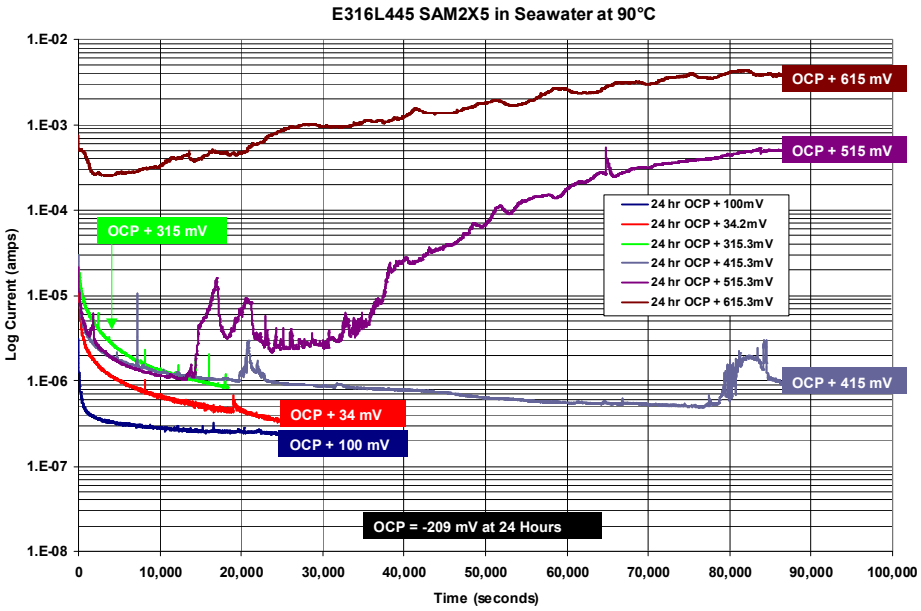

Figure 48 – Current transients were measured at various levels of constant applied potential (100 to 615 mV vs. OCP) in seawater at 90°C, for an early as-sprayed (unpolished) HVOF coating of SAM2X5 on a Type 316L stainless steel (serial number E316L445).

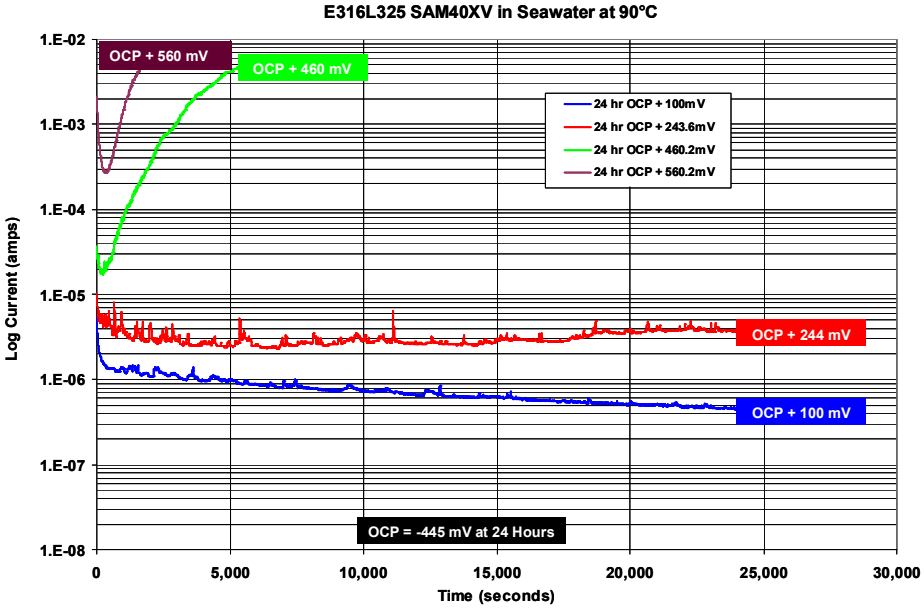

Figure 49 – Current transients were measured at various levels of constant applied potential (100 to 460 mV vs. OCP) in seawater at 90°C, for an early as-sprayed (unpolished) HVOF coating of SAM40XV on Type 316L stainless steel (serial number E316L325).

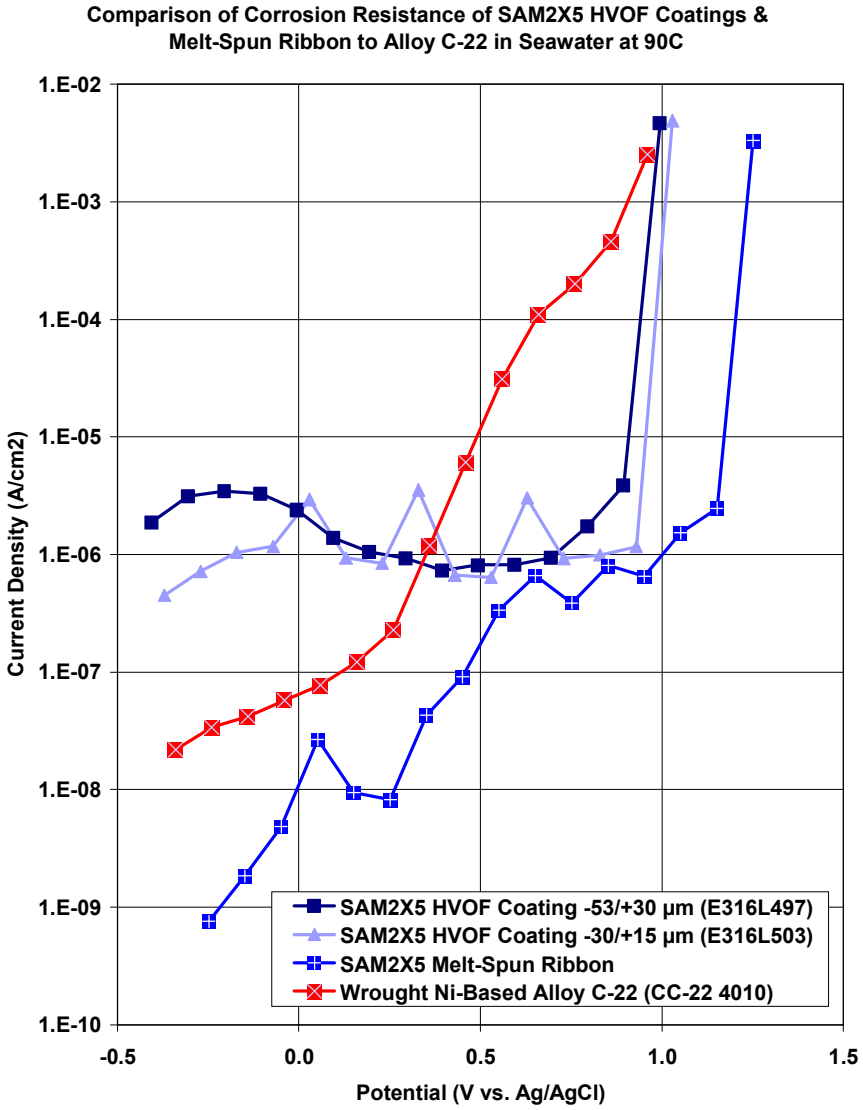

Figure 50 – Potential-step testing has been performed on wrought Alloy C-22 (reference material); fully dense and completely amorphous melt spun ribbons of SAM2X5; optimized HVOF coatings produced with –53/+30 micron powders of SAM2X5; and optimized HVOF coatings produced with –30/+15 micron powders of SAM2X5. All were tested in natural seawater heated to 90°C. To eliminate the need for surface roughness corrections in the conversion of measured current and electrode area to current density, the SAM2X5 and SAM1651 coatings were polished to a 600-grit finish prior to testing. The curves represent the asymptotic current density reached after 24 hours at the corresponding potential (each data point represents a 24 hour test). The constant potential was applied after 1 hour at the open circuit corrosion potential (OCP).

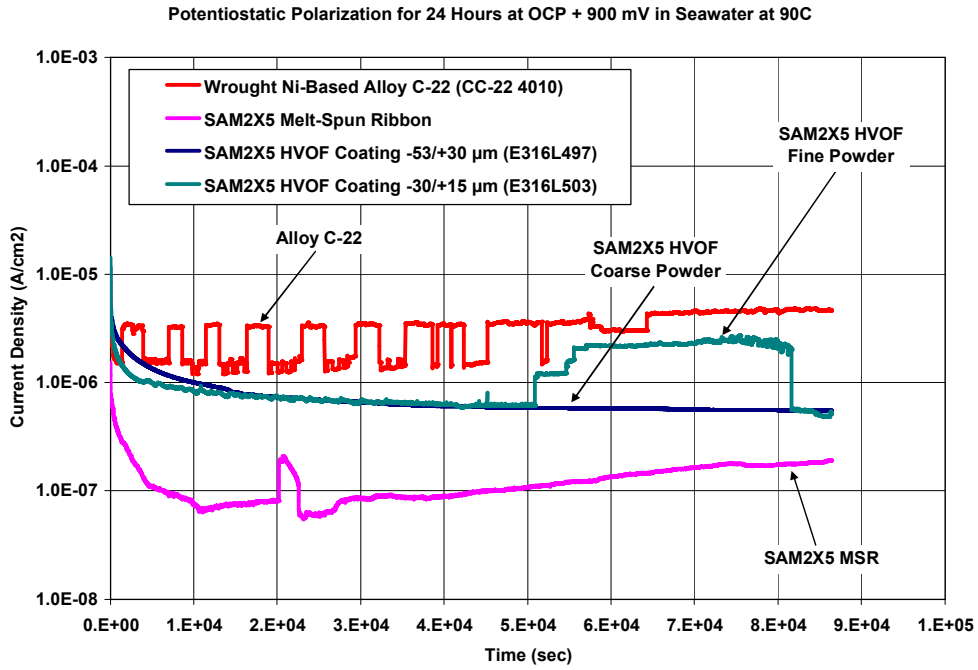

(a)

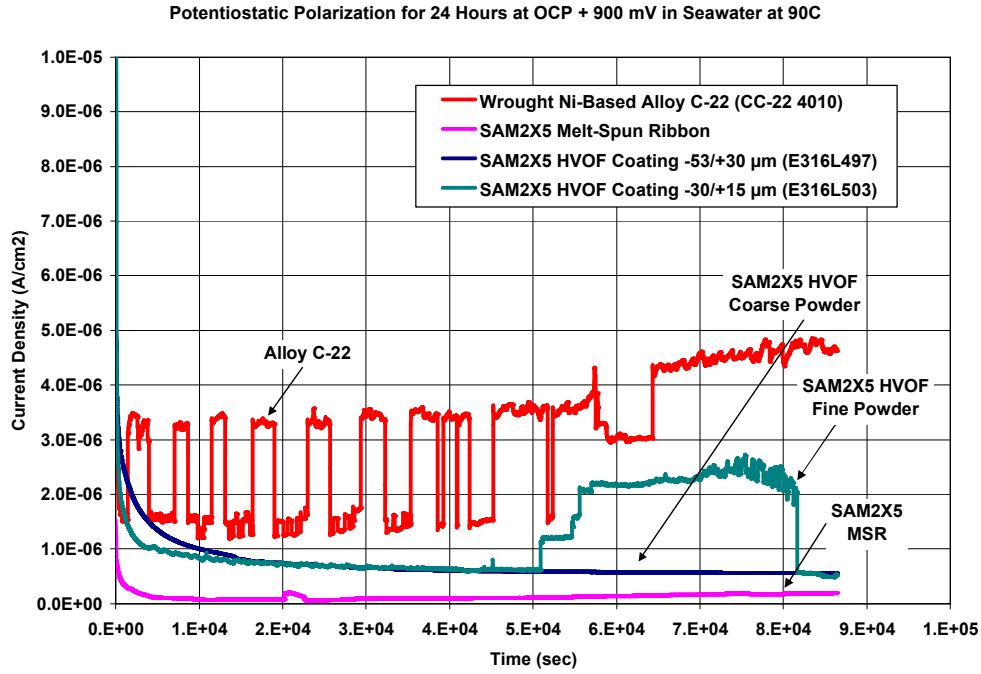

(b)

Figure 51 – (a) Transients in current density at a constant applied potential of 900 mV verses OCP for wrought Alloy C-22 (reference material), a fully dense and completely amorphous melt spun ribbon (MSR) of SAM2X5, HVOF coatings produced with –53/+30 micron powders of SAM2X5, and HVOF coatings produced with –30/+15 micron powders of SAM2X5, all in natural seawater heated to 90°C, are compared. (b) This figure is identical to the previous figure, with the exception that in this case the current density scale is logarithmic.

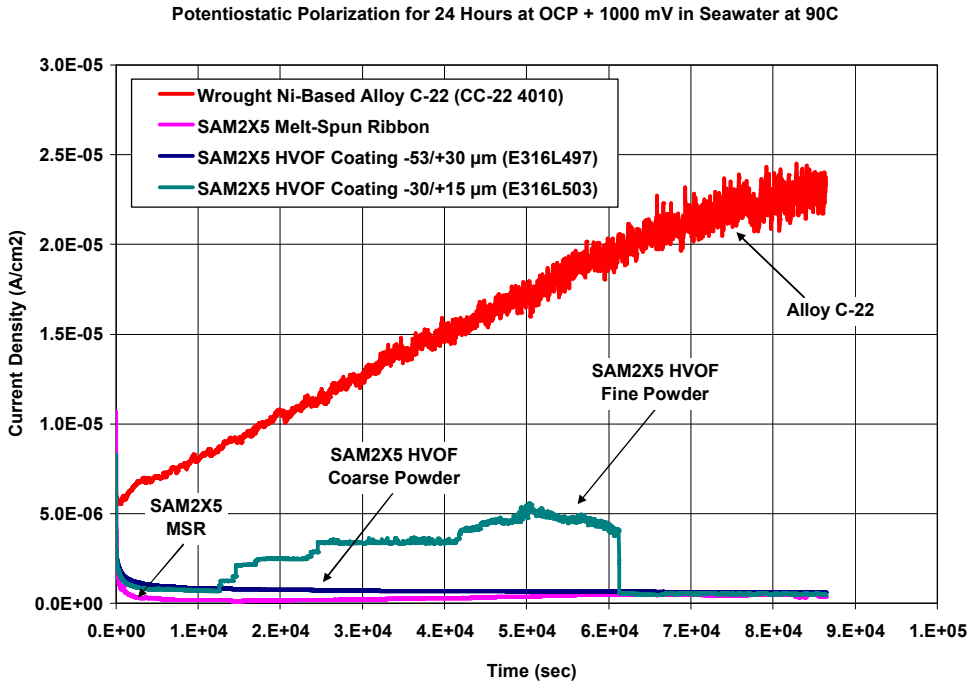

(a)

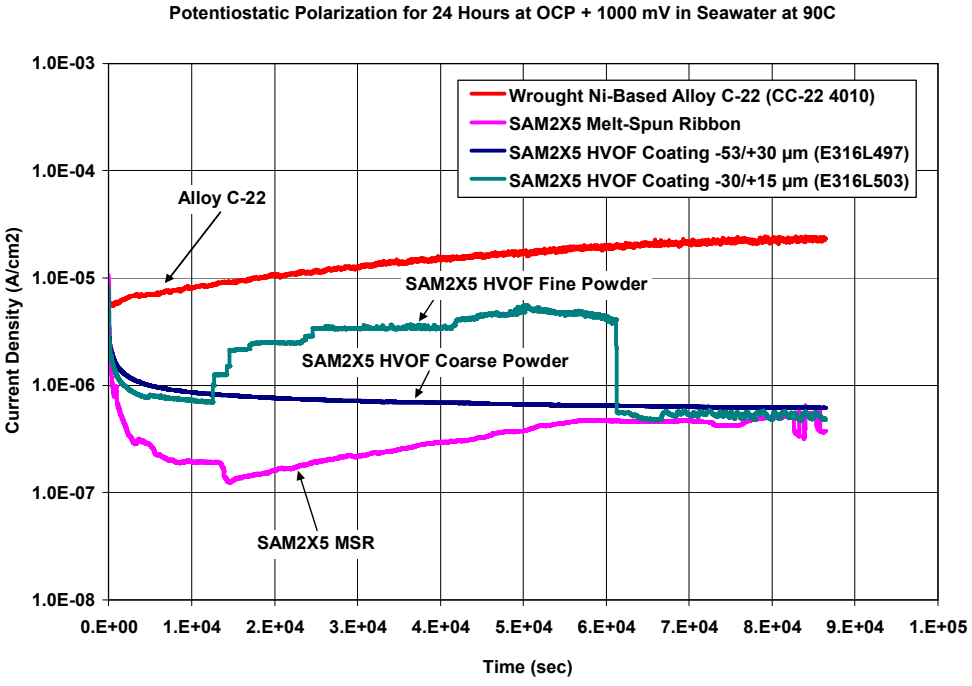

(b)

Figure 52 – (a) Transients in current density at a constant applied potential of 1000 mV verses OCP for wrought Alloy C-22 (reference material), a fully dense and completely amorphous melt spun ribbon (MSR) of SAM2X5, HVOF coatings produced with –53/+30 micron powders of SAM2X5, and HVOF coatings produced with –30/+15 micron powders of SAM2X5, all in natural seawater heated to 90°C, are compared. (b) This figure is identical to the previous FigureA, with the exception that in this case the current density scale is logarithmic.

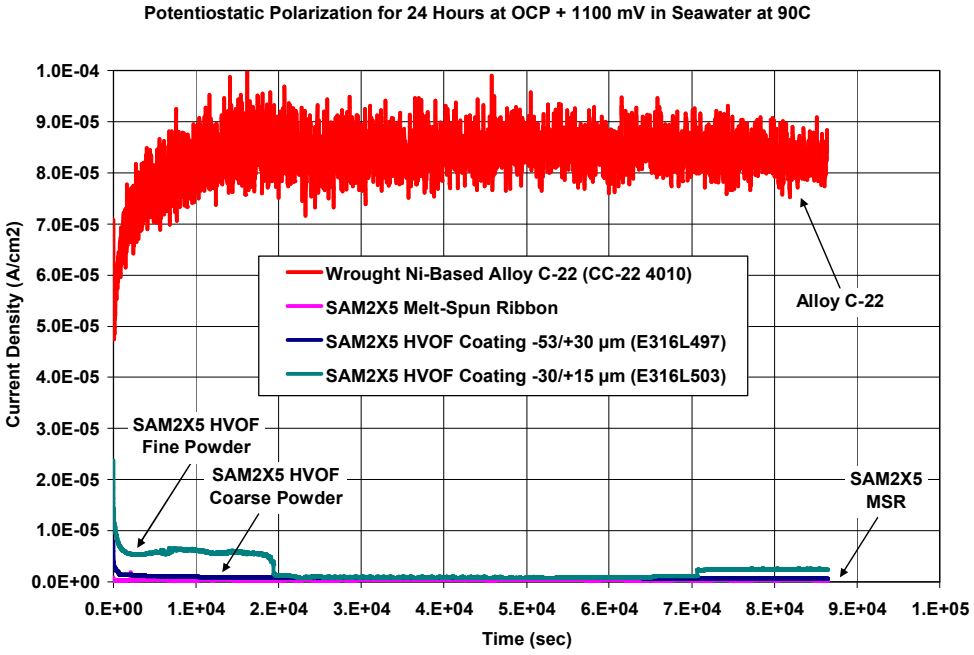

(a)

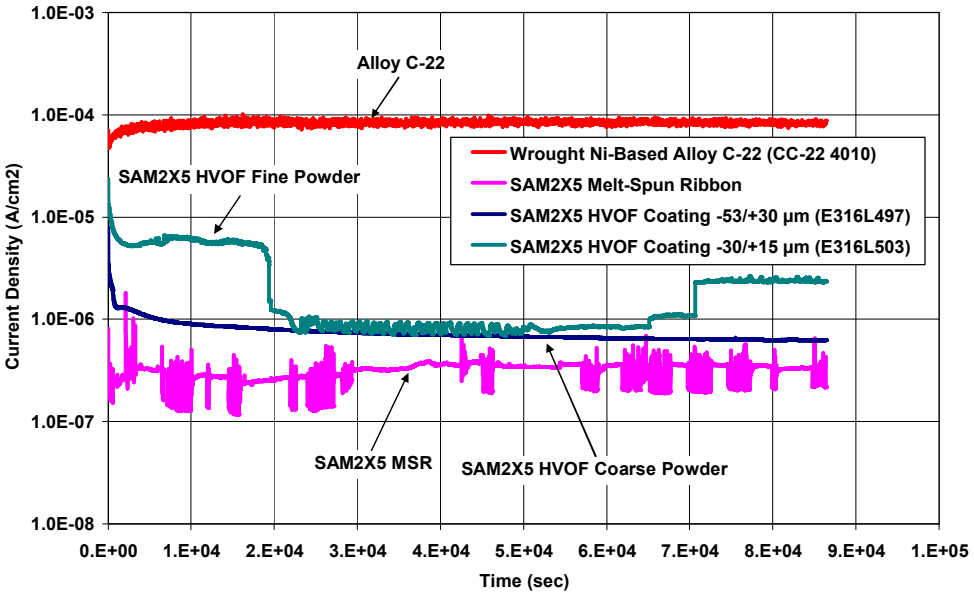

(b)

Figure 53 – (a) Transients in current density at a constant applied potential of 1100 mV verses OCP for wrought Alloy C-22 (reference material), a fully dense and completely amorphous melt spun ribbon (MSR) of SAM2X5, HVOF coatings produced with –53/+30 micron powders of SAM2X5, and HVOF coatings produced with –30/+15 micron powders of SAM2X5, all in natural seawater heated to 90°C, are compared. (b) This FigureA is identical to the previous FigureA, with the exception that in this case the current density scale is logarithmic.

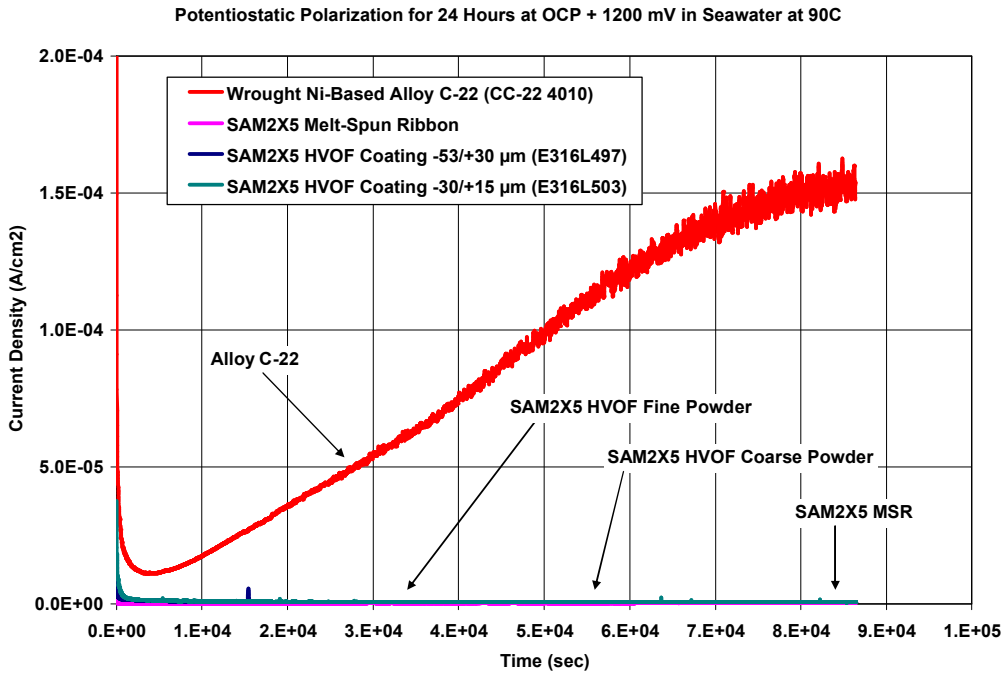

(a)

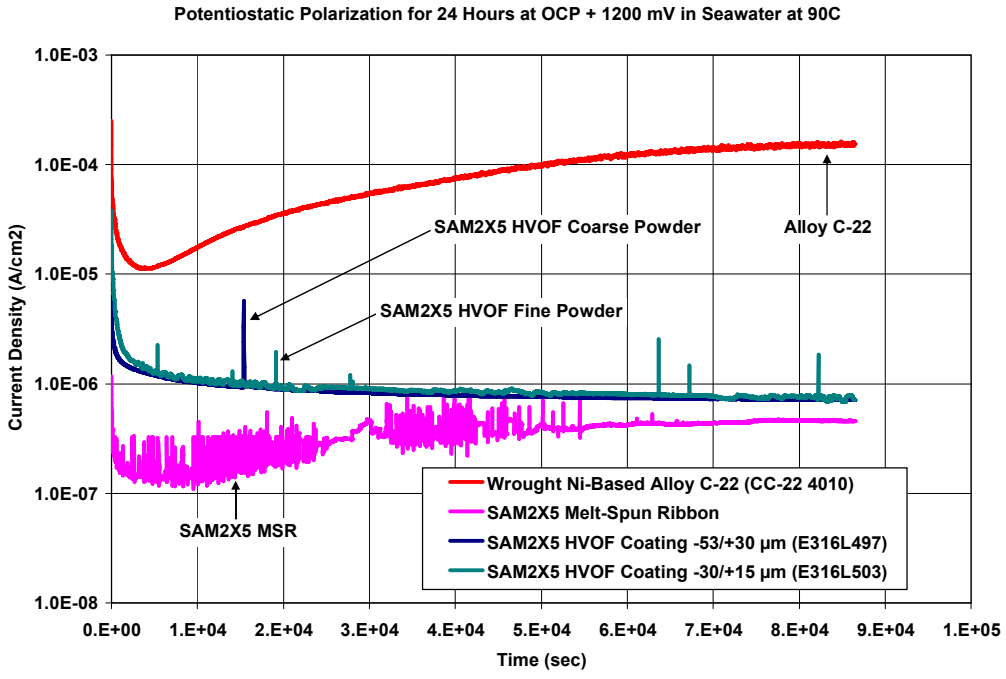

(b)

Figure 54 – (a) Transients in current density at a constant applied potential of 1200 mV verses OCP for wrought Alloy C-22 (reference material), a fully dense and completely amorphous melt spun ribbon (MSR) of SAM2X5, HVOF coatings produced with –53/+30 micron powders of SAM2X5, and HVOF coatings produced with –30/+15 micron powders of SAM2X5, all in natural seawater heated to 90°C, are compared. (b) This FigureA is identical to the previous FigureA, with the exception that in this case the current density scale is logarithmic.

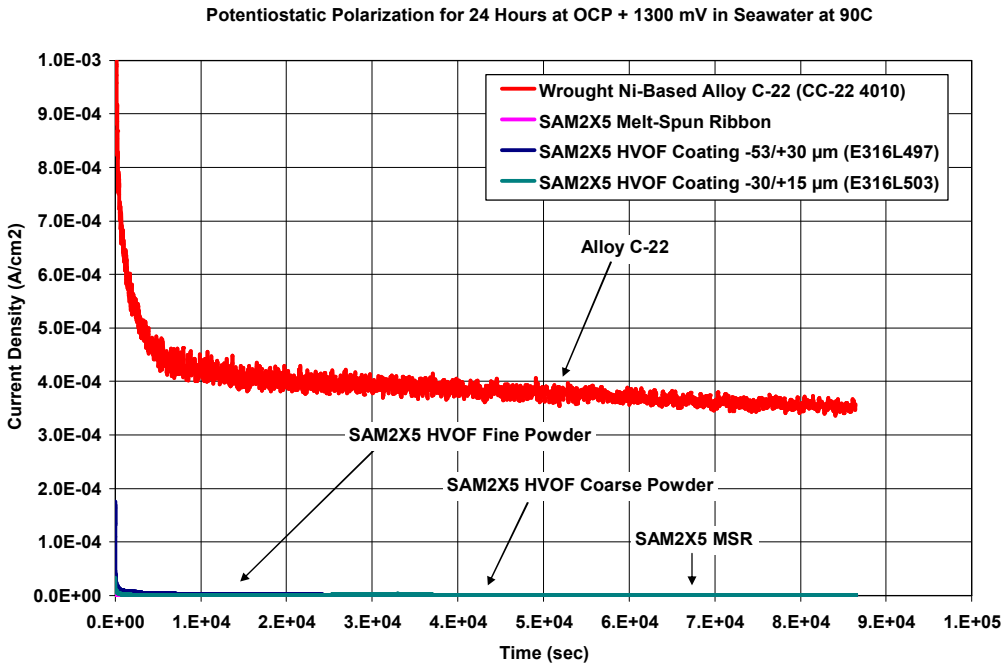

(a)

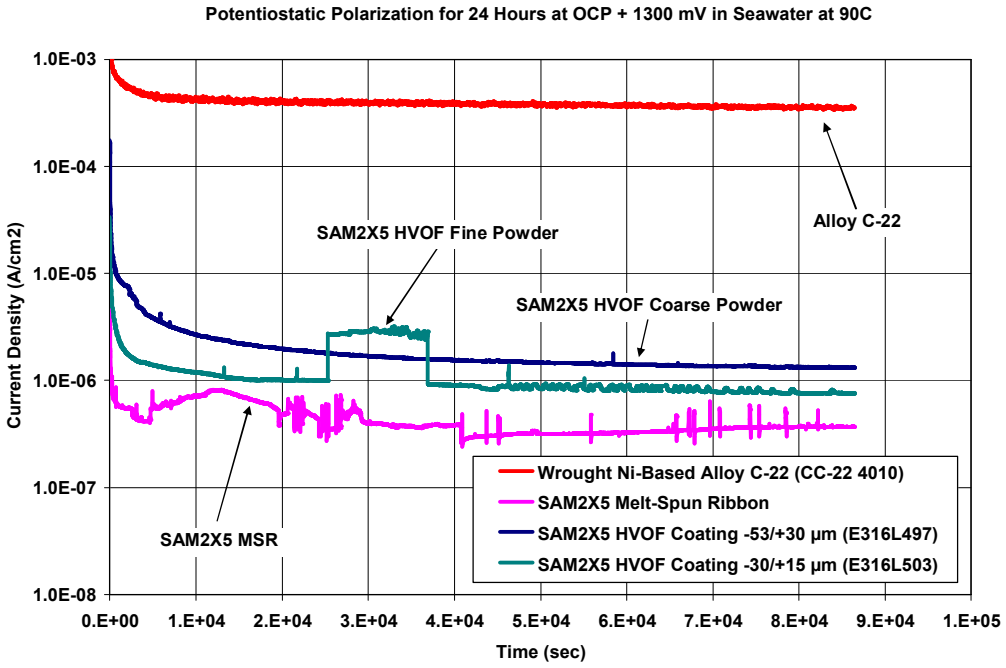

(b)

Figure 55 – (a) Transients in current density at a constant applied potential of 1300 mV verses OCP for wrought Alloy C-22 (reference material), a fully dense and completely amorphous melt spun ribbon (MSR) of SAM2X5, HVOF coatings produced with –53/+30 micron powders of SAM2X5, and HVOF coatings produced with –30/+15 micron powders of SAM2X5, all in natural seawater heated to 90°C, are compared. (b) This figure is identical to the previous figure, with the exception that in this case the current density scale is logarithmic.

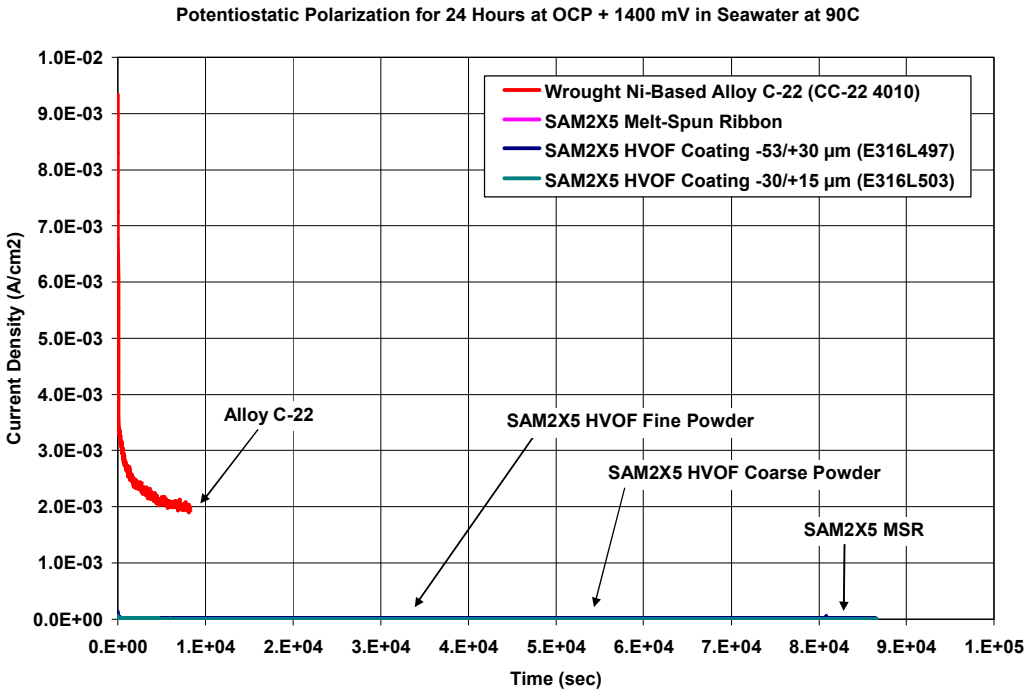

(a)

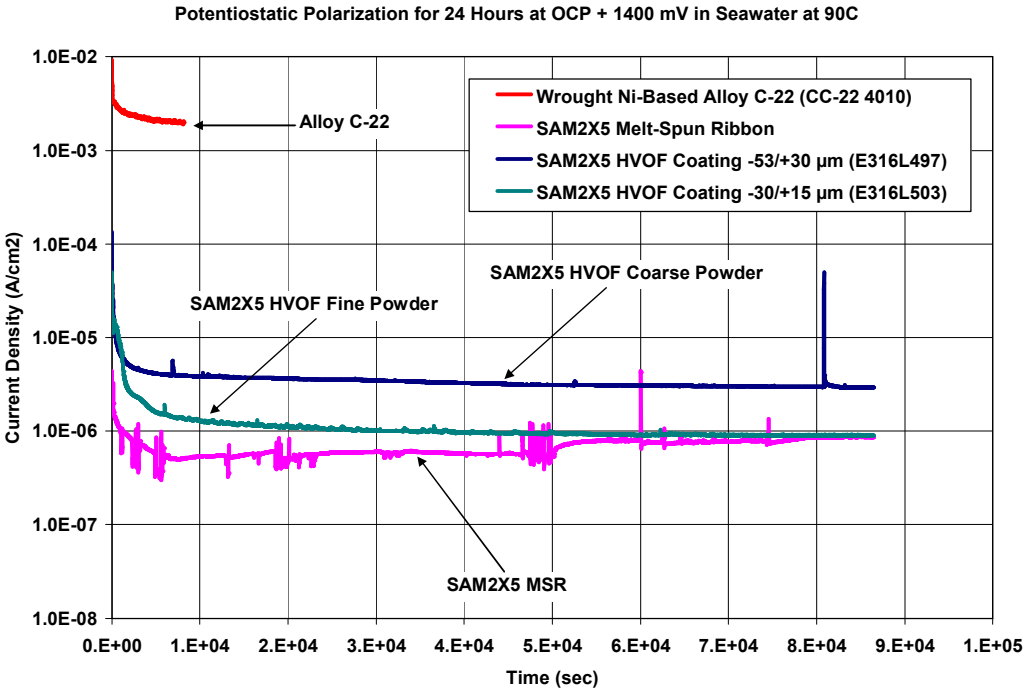

(b)

Figure 56 – (a) Transients in current density at a constant applied potential of 1400 mV verses OCP for wrought Alloy C-22 (reference material), a fully dense and completely amorphous melt spun ribbon (MSR) of SAM2X5, HVOF coatings produced with –53/+30 micron powders of SAM2X5, and HVOF coatings produced with –30/+15 micron powders of SAM2X5, all in natural seawater heated to 90°C, are compared. (b) This figure is identical to the previous figure, with the exception that in this case the current density scale is logarithmic.

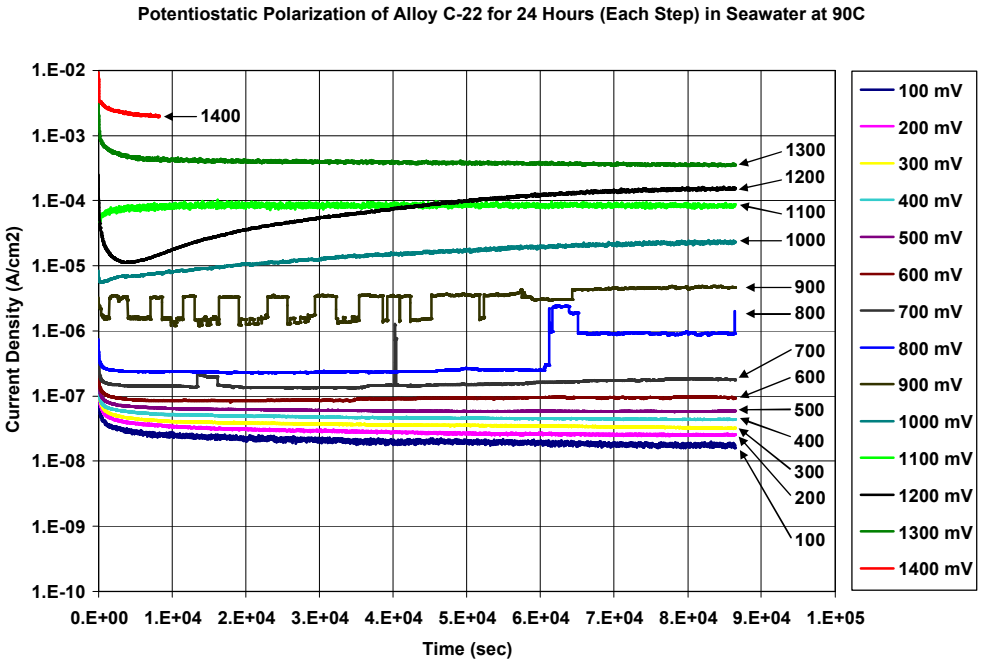

Figure 57 – Transients in current density at various levels of constant applied potential ranging from 100 to 1400 mV verses OCP for Alloy C-22 in natural seawater at 90°C. This reference material was polished to a 600-grit finish.

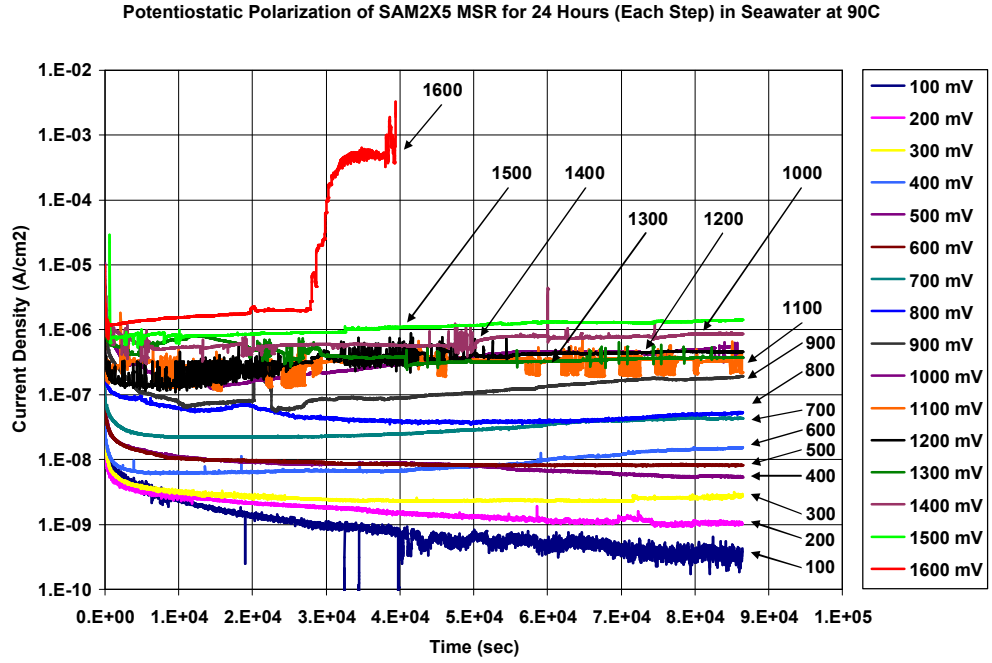

Figure 58 – Transients in current density at various levels of constant applied potential ranging from 100 to 1600 mV verses OCP for a melt-spun ribbon of SAM2X5 in natural seawater at 90°C are indicative of good passive film stability.

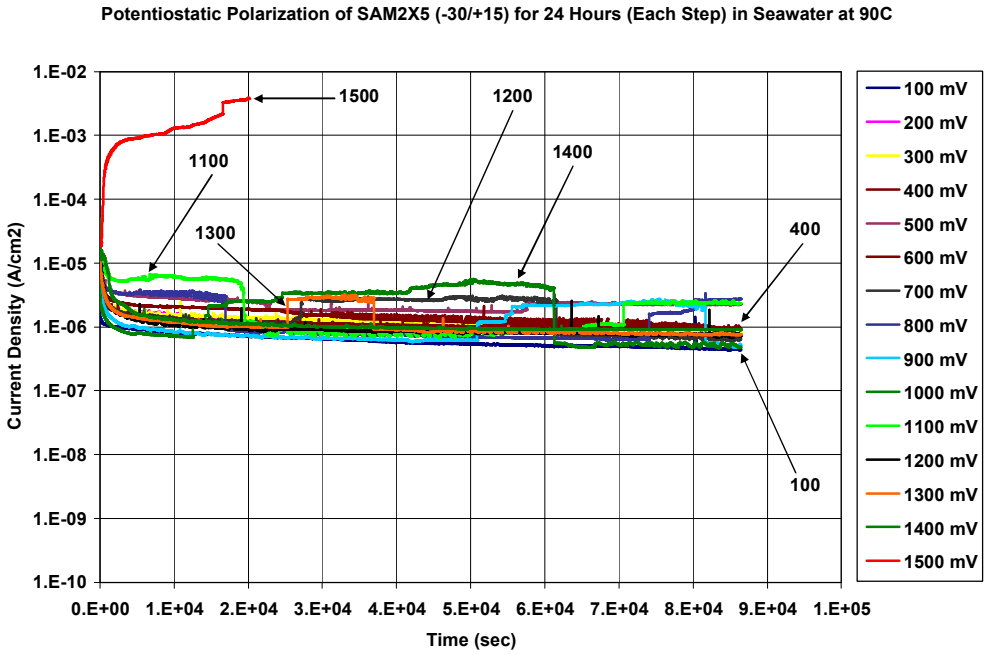

Figure 59 – Transients in current density at various levels of constant applied potential ranging from 100 to 1500 mV verses OCP for a recently optimized SAM2X5 HVOF coating (–30/+15 micron powder) in deaerated natural seawater at 90°C are indicative of good passive film stability.

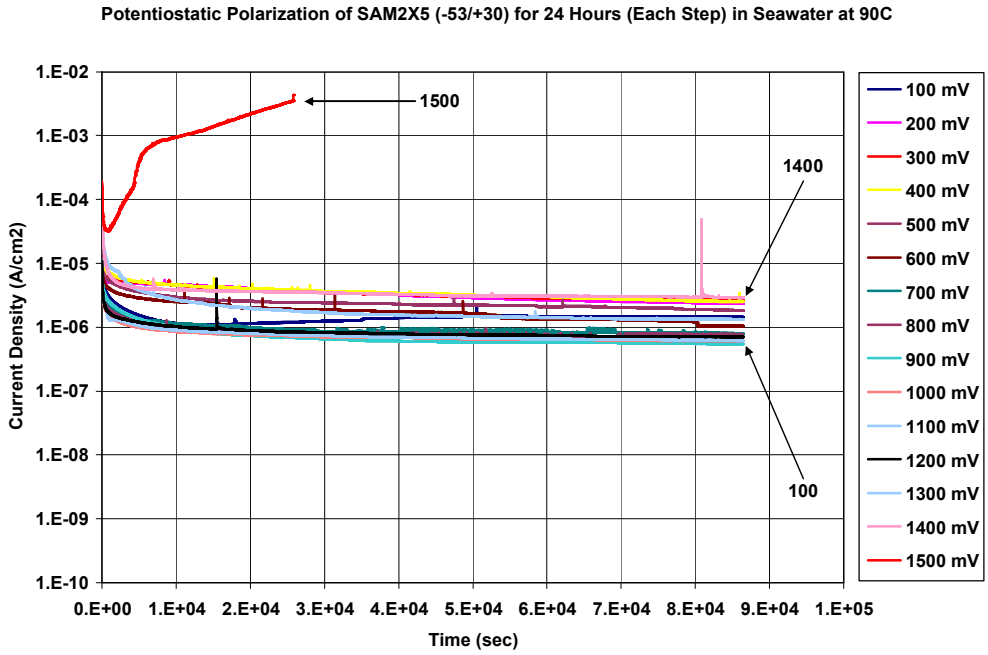

Figure 60 – Transients in current density at various levels of constant applied potential ranging from 100 to 1500 mV verses OCP for a recently optimized SAM2X5 HVOF coating (–53/+30 micron powder) in natural seawater at 90°C are indicative of exceptional passive film stability.

4.2.13 Effects of Thermally-Driven Devitrification – Alloy Stability – SAM2X5

To assess the sensitivity of these iron-based amorphous metals to devitrification, which can occur at elevated temperature, melt-spun ribbons of SAM40 were intentionally devitrified by heat treating them at various temperatures for one hour, as shown in Figure 61. Clearly, heat treatment for one your above the crystallization temperature causes the onset of crystalline phase formation, which has been shown to be deleterious to corrosion resistance. Figure 62 shows X-ray diffraction (XRD) data for SAM40, SAM2X5 and SAM1651 amorphous metal ribbons annealed at various temperature levels up to 800°C. As expected, crystalline peaks appear at temperatures above the crystallization temperature.

The effects devitrification on the electrochemical corrosion behavior of these materials has been investigated, with the results for SAM2X5 reported here. After heat treatment, the samples were evaluated in low temperature seawater (30°C), to determine the impact of the heat treatment on passive film stability and corrosion resistance. The temperatures used for the heat treatment were: 150, 300, 800 and 1000°C. Untreated (as received) ribbons were also tested, and provide insight into the baseline performance. These samples showed no significant hysteresis and change in repassivation potential at heat treatments of 150-300°C, but showed a dramatic loss of corrosion resistance when heat treatments were performed at 800-1000°C, which are above the known crystallization temperature of approximately 600-650°C (623°C) given in Table 6. Both ribbons treated at elevated temperature show large hysterisis loops, which are indicative of passive film breakdown, with a clearly defined repassivation potential near -600 mV verses Ag/AgCl (about 100 mV above the OCP). The operational limit for these materials, when being used for corrosion resistance, appears to be bounded by the crystallization temperature.

Melt spun ribbons of SAM2X5 were also intentionally devitrified by heat treating at 800°C for one hour and then subjected to cyclic polarization in 5M $CaCl_2$ at 105°C. In comparison to the as-received sample, the sample heat-treated at 800°C showed a dramatic loss of corrosion resistance, as shown in Figure 63. As discussed in regard to the preceding figure, this heat-treatment temperature was known to be above the crystallization temperature of approximately 600-650°C (623°C) given in Table 6. The heat-treated ribbon showed a large hysterisis loop in the hot concentrated calcium chloride solution, which is indicative of passive film breakdown, with a clearly defined repassivation potential neat the OCP. The post heat-treatment microstructural characterization with electron microscopy and X-ray diffraction by Yang et al. verify the existence of a completely amorphous material below the crystallization temperature, and the development of crystalline precipitates during heat treatment above this limit. These electron microscopy images may also indicate that the corrosive attack of the precipitated crystalline phases occur to a depth of approximately 10 microns. When being used for corrosion resistance in hot geothermal brines such as calcium chloride, the operational limit also appears to be bounded by the crystallization temperature.

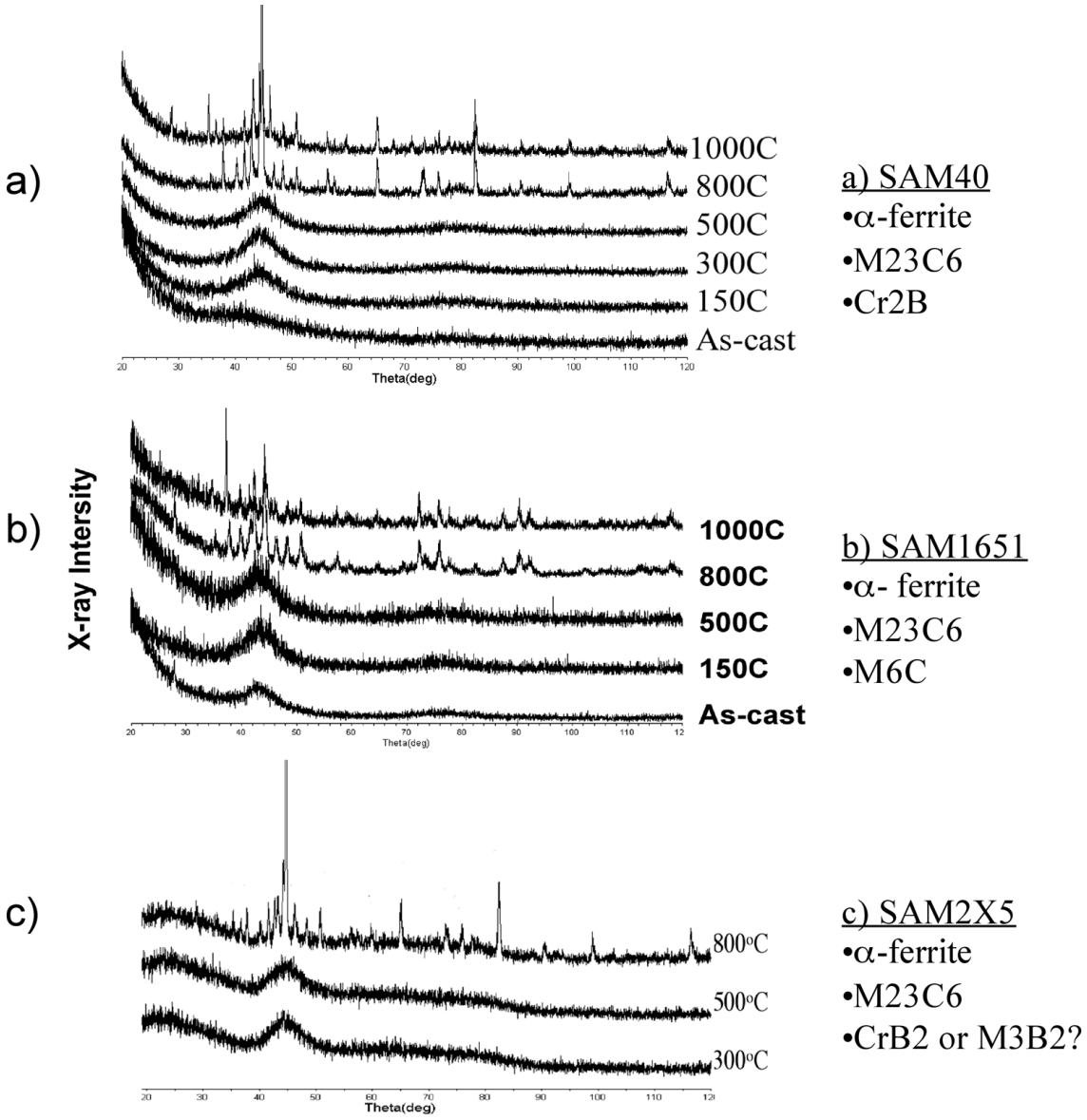

Figure 61 – XRD display broad amorphous halo of the ribbons annealed at and below 500°Cand crystalline peaks of ribbons annealed at 800°C and above; a)SAM40, b)SAM1651, and c) SAM2X5. Note: Tentative Phases identifications for each devitrified ribbon are noted on the right of the XRD.

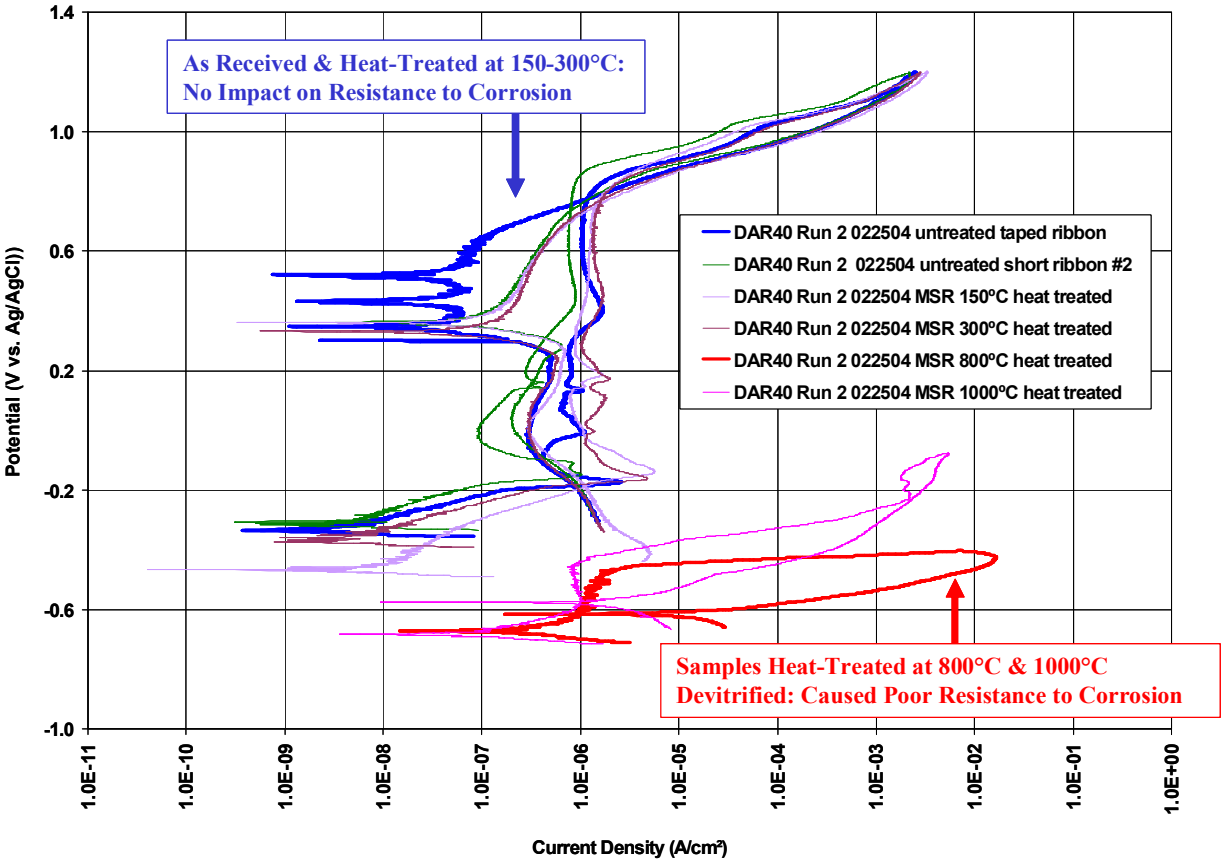

Figure 62 – To assess the sensitivity of these iron-based amorphous metals to devitrification, which can occur at very elevated temperature, melt-spun ribbon of SAM40 (also referred to as DAR40) were intentionally devitrified by heat treating them at various temperatures for one hour. After heat treatment, the samples were evaluated in low temperature seawater (30°C), to determine the impact of the heat treatment on passive film stability and corrosion resistance. The temperatures used for the heat treatment were: 150, 300, 800 and 1000°C. Untreated (as received) ribbons were also tested, and provide insight into the baseline performance. These samples showed no significant hysteresis and change in repassivation potential at heat treatments of 150-300°C, but showed a dramatic loss of corrosion resistance when heat treatments were performed at 800-1000°C, which are above the known crystallization temperature of approximately 600-650°C (623°C) given in Table 6 (Perepezko et al. 2004). Both ribbons treated at elevated temperature show large hysterisis loops, which are indicative of passive film breakdown, with a clearly defined repassivation potential near -600 mV verses Ag/AgCl (about 100 mV above the OCP). The operational limit for these materials, when being used for corrosion resistance, appears to be bounded by the recrystallization temperature.

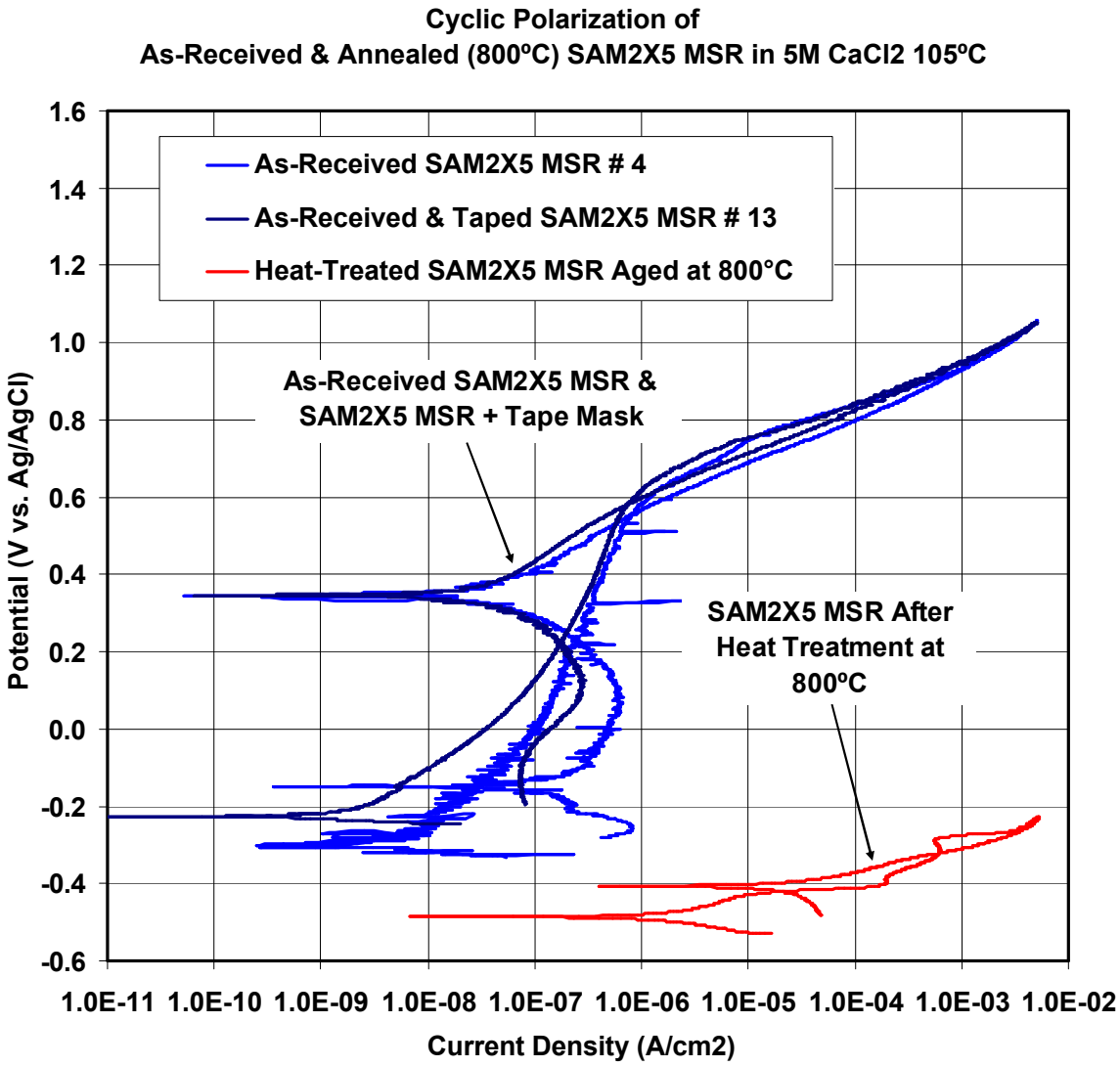

Figure 63 – Melt spun ribbons of SAM2X5 were also intentionally devitrified by heat treating at 800°C for one hour and then subjected to cyclic polarization in 5M $CaCl_2$ at 105°C. In comparison to the as-received sample, the sample heat-treated at 800C showed a dramatic loss of corrosion resistance. As discussed in regard to the preceding figure, this heat-treatment temperature was known to be above the crystallization temperature of approximately 600-650°C (623°C) given in Table 6 (Perepezko et al. 2004). The heat-treated ribbon showed a large hysterisis loop in the hot concentrated calcium chloride solution, which is indicative of passive film breakdown, with a clearly defined repassivation potential neat the OCP. The post heat-treatment microstructural characterization with electron microscopy and X-ray diffraction by Yang et al. verify the existence of a completely amorphous material below the crystallization temperature, and the development of crystalline precipitates during heat treatment above this limit. These electron microscopy images may also indicate that the corrosive attack of the precipitated crystalline phases occur to a depth of approximately 10 microns. When being used for corrosion resistance in hot geothermal brines such as calcium chloride, the operational limit also appears to be bounded by the crystallization temperature.

4.2.15 Linear Polarization Data – Corrosion Rates – SAM1651

Linear polarization was used to determine the approximate corrosion rates of the thermal spray coatings of amorphous metals of interest (HVOF SAM1651 or SAM7 and other coatings) and the reference material (wrought nickel-based Alloy C-22) in three relevant environments, Seawater at two temperature levels, and in hot concentrated calcium chloride (5M $CaCl_2$ at 105°C). Values of the corrosion potential, polarization resistance, corrosion current density, and corrosion rate are summarized in Tables 9 and 10, as well as Figures 64 through 66. In seawater at 30°C, the corrosion rates of HVOF SAM1651 (SAM7) coatings exhibited comparable to slightly higher corrosion rates than either wrought sample of Alloy C-22. As the temperature of the seawater was increased to 90°C, the corrosion rates of HVOF SAM1651 (SAM7) coatings exhibited comparable to slightly lower corrosion rates than either wrought sample of Alloy C-22. In general, corrosion rates trended to higher values with increasing temperature, as expected. In calcium chloride at 105°C, the corrosion rates of HVOF SAM1651 (SAM7) coatings were slightly lower than that of HVOF Alloy C-22; and comparable to slightly greater than those of wrought Alloy C-22. In general, the corrosion rates observed in the hot calcium chloride (105°C) were higher than those observed in the heated seawater (90°C), which was also expected.

4.2.16 Linear Polarization Data – Corrosion Rates – SAM2X5

Linear polarization was used to determine the approximate corrosion rates of the thermal spray coatings of amorphous metals of interest (HVOF SAM2X5 and other coatings) and the reference material (wrought nickel-based Alloy C-22) in three relevant environments, natural seawater at two temperature levels, and in hot concentrated calcium chloride (5M $CaCl_2$ at 105°C). Values of the corrosion potential, polarization resistance, corrosion current density, and corrosion rate are summarized in Tables 9 and 10, as well as Figures 67 through 69. In seawater at both 30 and 90°C, the corrosion rates of HVOF SAM2X5 coatings exhibited slightly lower corrosion rates than either wrought sample of Alloy C-22. The corrosion rates of all materials increased with temperature, as expected. In calcium chloride at 105°C, the corrosion rates of HVOF SAM2X5 coatings were comparable to, or slightly lower than that of wrought Alloy C-22. In general, the corrosion rates observed in the hot calcium chloride (105°C) were higher than those observed in the heated seawater (90°C), which was also expected.

Table 9 – Values of the polarization resistance, corrosion current density, and corrosion rate, measured with linear polarization, are summarized for HVOF coatings of SAM2X5 and Alloy C-22, as well as wrought samples of Alloy C-22. Values of the open circuit corrosion potential are also presented. Values of the corrosion current were determined assuming that the Tafel parameter is approximately 25 mV.

Sample	Parameter	E_{corr}	R_p	i_{corr}	dp/dt
		mV	ohms cm²	A/cm²	μm/yr
30°C Seawater					
HVOF SAM2X5	Average	-87.4	1.633E+06	2.27E-08	0.1789
HVOF SAM2X5	Standard Deviation	5.7	1.366E+06	1.36E-08	0.1071
HVOF SAM1651	Average	-73.4	8.352E+05	3.56E-08	0.4004
HVOF SAM1651	Standard Deviation	4.1	4.672E+05	1.51E-08	0.1705
Wrought Alloy C-22	Average	-163.2	2.744E+06	9.12E-09	0.0901
Wrought Alloy C-22	Standard Deviation	1.5	9.126E+04	3.02E-10	0.0030
Wrought Alloy C-22	Average	-312.4	6.229E+07	5.07E-09	0.0501
Wrought Alloy C-22	Standard Deviation	3.0	1.020E+08	4.40E-09	0.0435
90°C Seawater					
HVOF SAM2X5	Average	-241.0	1.255E+05	2.00E-07	1.580
HVOF SAM2X5	Standard Deviation	7.2	1.036E+04	1.73E-08	0.137
HVOF SAM1651	Average	-227.8	1.761E+05	1.42E-07	1.599
HVOF SAM1651	Standard Deviation	3.0	6.150E+03	5.05E-09	0.057
Wrought Alloy C-22	Average	-318.9	7.685E+04	3.25E-07	3.216
Wrought Alloy C-22	Standard Deviation	0.8	4.950E+02	2.10E-09	0.021
Wrought Alloy C-22	Average	-340.1	7.727E+04	3.24E-07	3.199
Wrought Alloy C-22	Standard Deviation	0.2	1.030E+03	4.29E-09	0.042
Wrought Alloy C-22	Average	-318.2	2.033E+05	1.23E-07	1.216
Wrought Alloy C-22	Standard Deviation	0.7	9.074E+02	5.50E-10	0.005

Table 10 – Values of the polarization resistance, corrosion current density, and corrosion rate, measured with linear polarization, are summarized for HVOF coatings of SAM2X5 and Alloy C-22, as well as wrought samples of Alloy C-22. Values of the open circuit corrosion potential are also presented. Values of the corrosion current were determined assuming that the Tafel parameter is approximately 25 mV.

Sample	Parameter	E_{corr}	R_p	i_{corr}	dp/dt
		mV	ohms cm²	A/cm²	μm/yr
105°C 5M $CaCl_2$					
HVOF SAM2X5	Average	-240.9	7.32E+04	3.42E-07	2.696
HVOF SAM2X5	Standard Deviation	1.8	1.03E+03	4.76E-09	0.038
HVOF SAM1651	Average	-292.6	2.81E+04	8.91E-07	10.027
HVOF SAM1651	Standard Deviation	4.6	2.49E+02	7.92E-09	0.089
Wrought Alloy C-22	Average	-464.3	4.93E+04	5.10E-07	5.040
Wrought Alloy C-22	Standard Deviation	3.0	4.14E+03	4.37E-08	0.433
HVOF Alloy C-22	Average	-347.9	2.14E+03	1.17E-05	115.692
HVOF Alloy C-22	Standard Deviation	4.5	8.94E+01	4.82E-07	4.770

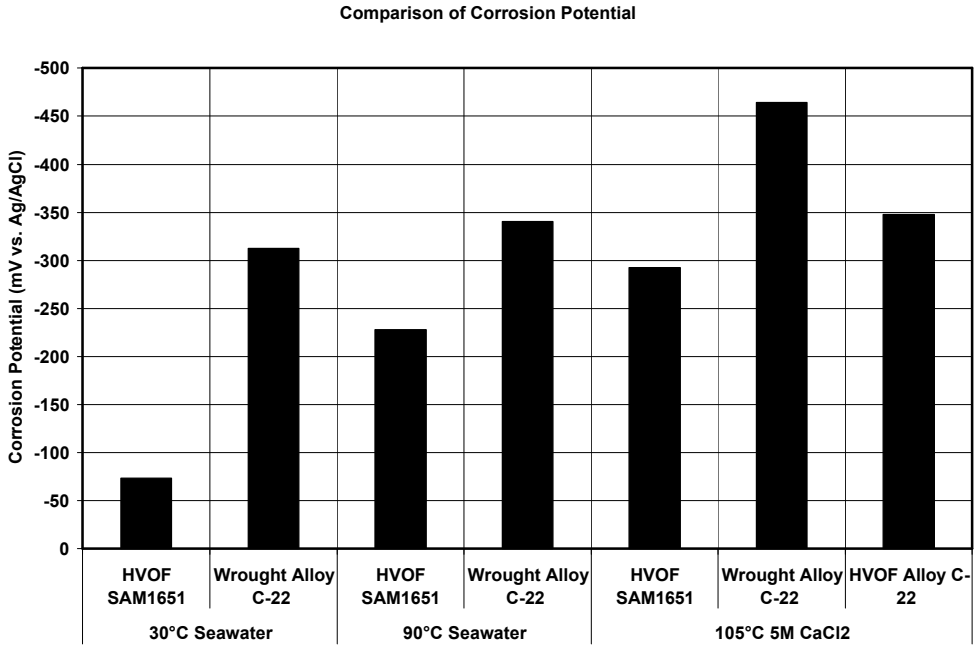

Figure 64 – The corrosion potentials for the thermal spray coatings of SAM1651 and the reference material (wrought nickel-based Alloy C-22) in three relevant environments, Half Moon Bay seawater at two temperature levels, and in hot concentrated calcium chloride (5M $CaCl_2$ at 105°C) are summarized.

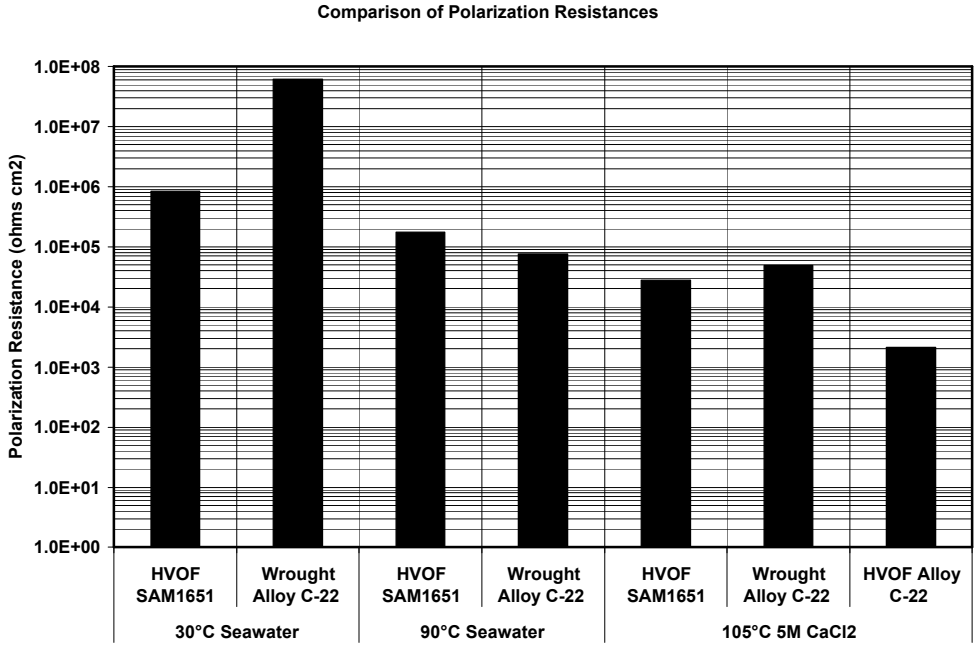

Figure 65 – FigureB 21 – Linear polarization was used to determine the polarization resistance for thermal spray coatings of SAM1651 and the reference material (wrought nickel-based Alloy C-22) in three relevant environments, Half Moon Bay seawater at two temperature levels, and in hot concentrated calcium chloride (5M $CaCl_2$ at 105°C).

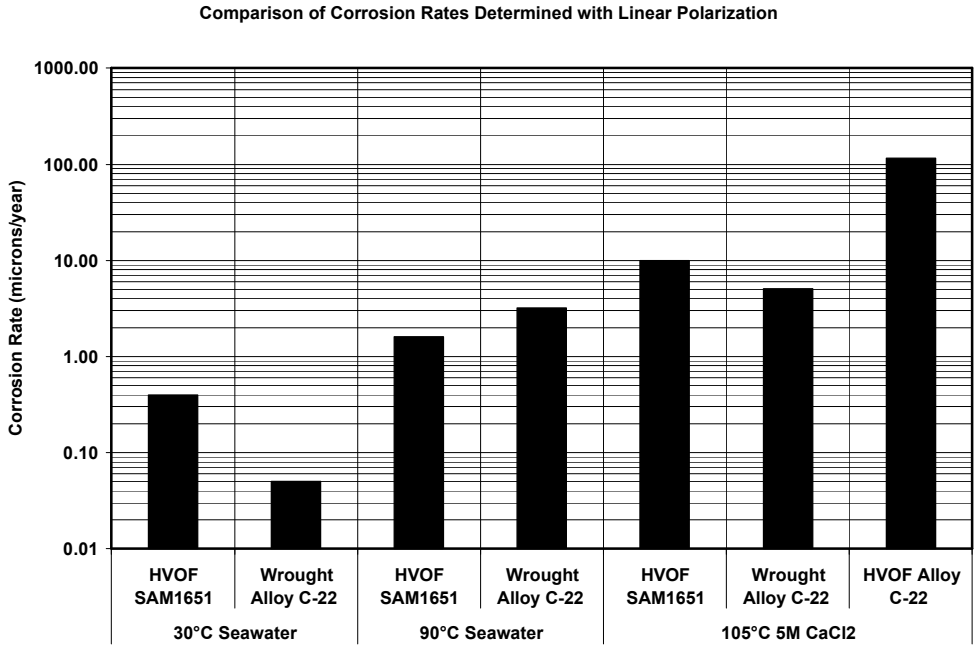

Figure 66 – Values of the polarization resistance shown in Figure 65 were converted to corrosion rates for the thermal spray coatings of SAM1651 and the reference material (wrought nickel-based Alloy C-22) in three relevant environments, natural seawater at two temperature levels, and in hot concentrated calcium chloride (5M $CaCl_2$ at 105°C).

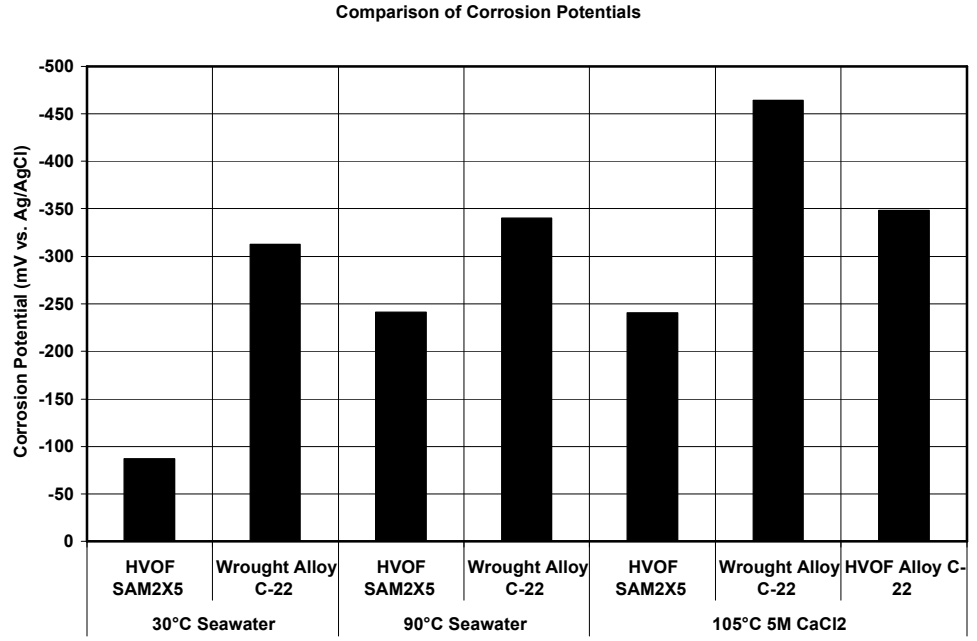

Figure 67 – The corrosion potentials for the thermal spray coatings of SAM2X5 and the reference material (wrought nickel-based Alloy C-22) in three relevant environments, natural seawater at two temperature levels, and in hot concentrated calcium chloride (5M $CaCl_2$ at 105°C) are summarized.

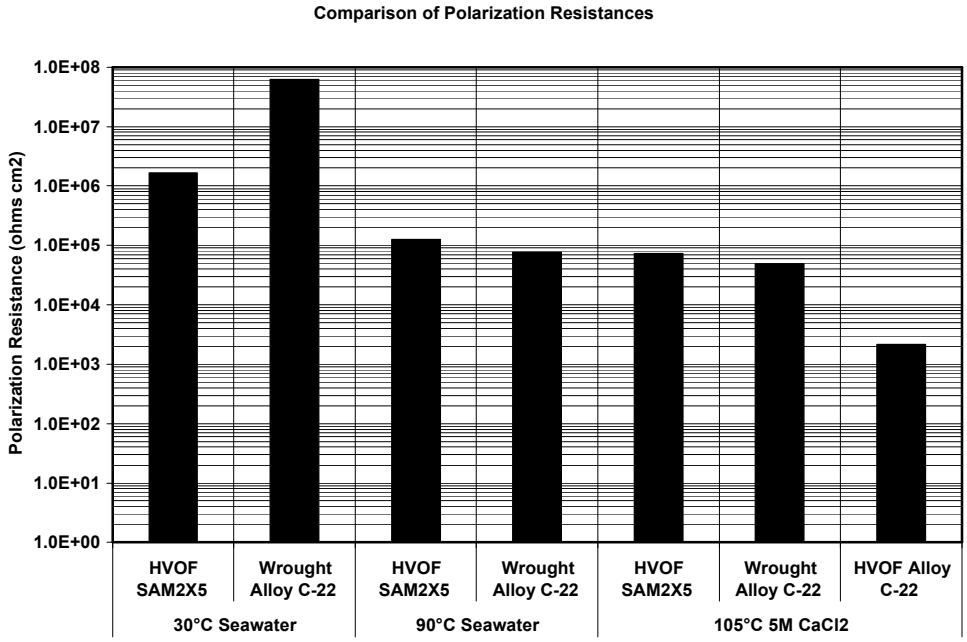

Figure 68 – Linear polarization was used to determine the polarization resistance for thermal spray coatings of SAM2X5 and the reference material (wrought nickel-based Alloy C-22) in three relevant environments, natural seawater at two temperature levels, and in hot concentrated calcium chloride (5M $CaCl_2$ at 105°C).

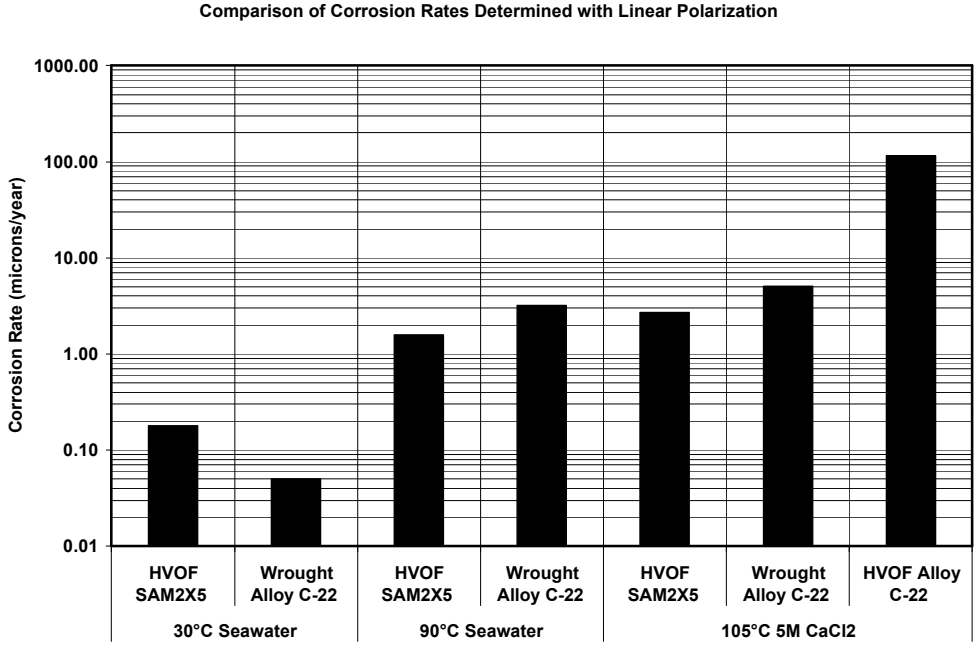

Figure 69 – Values of the polarization resistance shown in Figure 68 were converted to corrosion rates for the thermal spray coatings of SAM2X5 and the reference material (wrought nickel-based Alloy C-22) in three relevant environments, natural seawater at two temperature levels, and in hot concentrated calcium chloride (5M $CaCl_2$ at 105°C).

4.2.17 Salt Fog Testing – Verification of Corrosioin Resistance – SAM1651 and SAM2X5

Salt fog testing was conducted on several thermal spray coatings, including HVOF coatings of Alloy C-22, Type 316L stainless steel, SAM40, SAM1651 and SAM2X5. As shown in Figure 70, fter 30 cycles in the standard GM salt-fog test, the HVOF coating of Alloy C-22 showed slight rusting (not shown), while HVOF coatings of Type 316L stainless steel and SAM40 showed substantial corrosion. In contrast, SAM1651 and SAM2X5 coatings showed no corrosion at 30 cycles. The salt fog testing of SAM1651 and SAM2X5 coatings was continued to almost 60 cycles with no evidence of corrosion on either type of coating. The corrosion of the SAM40 has been attributed to the presence of bcc ferrite and other deleterious crystalline phases.

Type 316L Coating
After Exposure for 13 Cycles

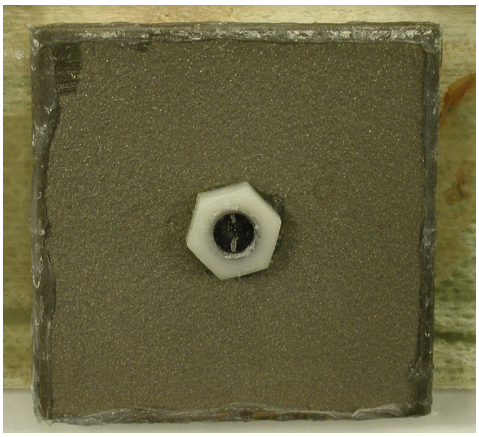

SAM1651 (SAM7) Coating
After Exposure for 30 Cycles
No Corrosion at 60 Cycles

Original SAM40 (DAR40) Coating
After Exposure for 13 Cycles

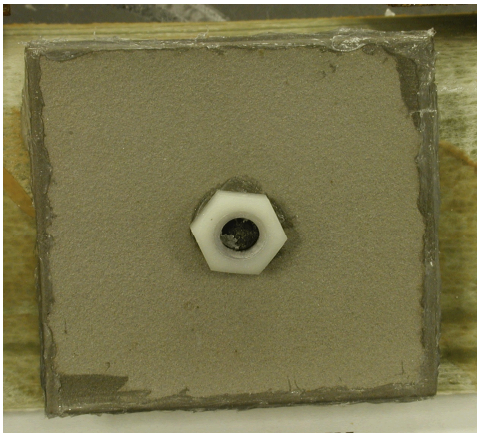

SAM2X5 Coating
After Exposure for 30 Cycles
No Corrosion After 60 Cycles

Figure 70 – Results of salt fog testing with Type 316L stainless steel, SAM40, SAM1651 (SAM7) and SAM2X5 high-velocity oxy-fuel (HVOF) coatings.

4.2 CRITERIA

Technical Work Plan for: Regulatory Integration Modeling and Analysis of the Waste Form and Waste Package (BSC 2004 [DIRS 171583]) has identified the following acceptance criteria (AC) based on the requirements mentioned in *Project Requirements Document* (Curry et al. 2002 [DIRS 157916]) and *Yucca Mountain Review Plan, Final Report* (NRC 2003 [DIRS 163274]): Degradation of Engineered Barriers (NRC 2003 [DIRS 163274], Section 4.2.1.3.1.3; PRD-002/T-015). Specific requirements include describing deterioration or degradation of engineered barriers and modeling degradation processes using data for performance assessment, including TSPA-LA. Consideration of uncertainties and variability in model parameters and alternative conceptual models are also required. To fulfill these requirements, the following acceptance criteria are identified in *Technical Work Plan for: Regulatory Integration Modeling and Analysis of theWaste Form and Waste Package* (BSC 2004 [DIRS 171583]):

4.2.1 Description and Demonstration of Multiple Barriers Acceptance Criteria

The following acceptance criteria are from Section 2.2.1.1.3 of *Yucca Mountain Review Plan, Final Report* (NRC 2003 [DIRS 163274]):

- Acceptance Criterion 1 – Identification of Barriers is Adequate
- Acceptance Criterion 2 – Description of Barrier Capability to Isolate Waste is Acceptable
- Acceptance Criterion 3 – Technical Basis for Barrier Capability is Adequately Presented.

4.2.2 Degradation of Engineered Barriers

The following acceptance criteria are from Section 2.2.1.3.1.3 of *Yucca Mountain Review Plan, Final Report* (NRC 2003 [DIRS 163274]):

- Acceptance Criterion 1 – System Description and Model Integration are Adequate
- Acceptance Criterion 2 – Data Are Sufficient for Model Justification
- Acceptance Criterion 3 – Data Uncertainty is Characterized and Propagated through the Model Abstraction
- Acceptance Criterion 4 – Model Uncertainty is Characterized and Propagated Through the Model Abstraction
- Acceptance Criterion 5 – Model Abstraction Output Supported by Objective Comparisons.

4.3 CODES AND STANDARDS

4.3.1 Standard Test Media

G. E. Gdowski, *Formulation and Make-up of Simulated Dilute Water (SDW), Low Ionic Content Aqueous Solution*, Yucca Mountain Project, Lawrence Livermore National Laboratory, Livermore, CA, TIP-CM-06, Revision CN TIP-CM-06-0-2, April 4, 1997, Table 1, p. 3. (Gdowski 1997a)

G. E. Gdowski, *Formulation and Make-up of Simulated Concentrated Water (SCW), High Ionic Content Aqueous Solution*, Yucca Mountain Project, Lawrence Livermore National Laboratory, Livermore, CA, TIP-CM-07, Revision CN TIP-CM-07-0-2, April 4, 1997, Table 1, pp. 3–4. (Gdowski 1997b)

G. E. Gdowski, *Formulation and Make-up of Simulated Acidic Concentrated Water (SAW), High Ionic Content Aqueous Solution*, Yucca Mountain Project, Lawrence Livermore National Laboratory, Livermore, CA, TIP-CM-08, Revision CN TIP-CM-08-0-2, April 4, 1997, Table 1, p. 3. (Gdowski 1997c)

4.3.2 Cyclic Polarization Measurements

Standard Practice for Conventions Applicable to Electrochemical Measurements in Corrosion Testing, Designation G 3-89, 1997 Annual Book of ASTM Standards, Section 3, Vol. 3.02, pp. 36–44. (ASTM 1997b)

Standard Test Method for conducting Cyclic Potentiodynamic Polarization Measurements for Localized Corrosion Susceptibility of Iron-, Nickel-, or Cobalt-Based Alloys, Designation G 61-86, 1997 Annual Book of ASTM Standards, Section 3, Vol. 3.02, pp. 231–235. (ASTM 1997c)

Standard Reference Test Method for Making Potentiostatic and Potentiodynamic Anodic Polarization Measurements, Designation G 5-94, 1997 Annual Book of ASTM Standards, Section 3, Vol. 3.02, pp. 54–57. (ASTM 1997d)

Standard Reference Test Method for Making Potentiostatic and Potentiodynamic Anodic Polarization Measurements, Designation G 5-87, 1989 Annual Book of ASTM Standards, Section 3, Vol. 3.02, pp. 79–85. (ASTM 1989)

4.3.3 Document Review Policy & Procedures

J. Boudreau, L, Aprigliano, R. Bayles, J. Farmer, A. Meike, E. Christman, R. Sampson, J. Kirkwood, *HPCRM Document Review Policy and Procedures*, UCRL-AM-224117, August 31, 2006, Lawrence Livermore National Laboratory, Livermore, California, 51 pages (2006).

4.3.3 General Corrosion Measurements

Standard Practice for Preparing, Cleaning, and Evaluating Corrosion Test Specimens, Designation G 1-90, 1997 Annual Book of American Society for Testing and Materials (ASTM) Standards, Section 3, Vol. 3.02, pp. 15–21. (ASTM 1997)

Standard Practice for Preparing, Cleaning, and Evaluating Corrosion Test Specimens, Designation G 1-81, 1987 Annual Book of ASTM Standards, Section 3, Vol. 3.02, pp. 89–94, Subsection 8 – Calculation of Corrosion Rate, Appendix X1 – Densities for a Variety of Metals and Alloys. (ASTM 1987)

Standard Test Methods for Pitting and Crevice Corrosion Resistance of Stainless Steels and Related Alloys by Use of Ferric Chloride Solution, Designation G 48-92, 1997 Annual Book of ASTM Standards, Section 3, Vol. 3.02, pp. 181–186. (ASTM 1997)

4.3.4 Technical Implementing Procedures

TIP-CM-04: *User Calibration of Mettler AT200 Analytical Balance*

TIP-CM-05: *User Calibration of Fowler Ultra-Cal Mark III Digital Caliper*

TIP-CM-06: *Formulation and Make-Up of Simulated Dilute Water, Low Ionic Content Aqueous Solution*

TIP-CM-07: *Formulation and Make-Up of Simulated Concentrated Water, High Ionic Content Aqueous Solution*

TIP-CM-08: *Formulation and Make-Up of Simulated Acidic Concentrated Water, High Ionic Content Aqueous Solution*

TIP-CM-10: *User Calibration of Analytical Balance*

TIP-CM-13: *User Calibration of Orion 520A pH Meter*

TIP-CM-14: *User Calibration of Reference Electrodes*

TIP-CM-19: User *Calibration & Software Verification of Potentiostats*

TIP-CM-22: *Formulation and Make-Up of Simulated Saturated Water, High Ionic Content Aqueous Solution*

TIP-CM-42: *User Verification of Gamry Potentiostats*

INTENTIONALLY LEFT BLANK

5. ASSUMPTIONS

5.1 DRY OXIDATION

It is assumed that dry oxidation rates are similar to those for Type 316L stainless steel.

5.2 AQUEOUS PHASE CORROSION

5.2.1 Representative Environments

It is assumed that the performance of these materials in natural seawater at 30, 60 and 90°C, and 5M $CaCl_2$ at 105 and 120°C is representative of the performance under repository conditions. Additional expected environments were not considered in this initial AMR, but should be included in versions.

5.2.2 Temperature Dependence

It is assumed that the temperature dependences of the open circuit corrosion potentials and the general corrosion rates are accounted for with simple linear regression equations. This simplification was adopted due to the limited availability of data, with data at only two temperature levels. It is recognized that better functional forms may be found as additional data is obtained.

5.2.3 Lowered pH in Crevices

It is assumed that crevice corrosion can be accounted for by simply assuming that a lower pH exists inside the crevice. Clearly, the localized environment is much more complicated, and can ultimately be dealt with through the application of detailed reactive transport models.

5.2.4 Other Crevice-Like Occluded Regions

It is assumed that the thermal spray coatings are pore free. However, the surface of the amorphous metal coating may have some degree of porosity and other morphological features that might behave as pits and crevices, with localized acidification within the pores. Acidification inside these features could lead to localized attach that is not accounted for by the simplified conceptual model presented here.

5.2.5 Corrosion at Crystalline Phases in Amorphous Matrix

It is assumed that the surface of the amorphous metal coating is homogenous, with uniform corrosion properties. However, in some cases crystalline phases may be present at the coating-environment interface, and be much more susceptible to corrosion than the amorphous phase.

INTENTIONALLY LEFT BLANK

6. MODEL DISCUSSION

6.1 MODEL OVERVIEW

6.1.1 Goal of Model

The goal of this model is the prediction of corrosion rates for thermal-spray coatings of iron-based amorphous metals developed as part of the DARPA and DOE co-sponsored HPCRM Program.

6.1.2 Background

Two iron-based amorphous metal formulations have been developed which exhibit corrosion resistance comparable to that of Type 316L stainless steel and nickel-based Alloy C-22 in several aggressive test environments, including natural seawater at 30, 60 and 90°C, as well as in 5M $CaCl_2$ at 105 and 120°C. This corrosion resistance is achieved by adding chromium, molybdenum and tungsten to the alloys, while continuing to maintain enough boron for glass formation. To determine the suitability of these materials for various repository applications under consideration, a model must be formulated.

6.2 MODEL FORMULATION

6.2.1 Background and Methodology

The conceptual corrosion model is shown in Figure 72 and requires inputs of: (1) alloy composition; (2) crystallization temperature; (3) the maximum temperature that the amorphous metal has seen over its lifetime; (4) brine composition; (5) pH for the brine or crevice; (6) and brine temperature. The conceptual model has outputs of: (1) open circuit corrosion potential; (2) change in corrosion potential with gamma radiolysis; (3) critical potential for passive film breakdown; (4) the change in the critical potential with devitrification of the amorphous alloy; (5) general corrosion rate; and (6) localized corrosion rate. The model selects the solution pH, based upon whether or not the surface is creviced. If a crevice exists, a lower solution pH ($pH_{crevice}$) is assumed, accounting for the typical acidic conditions known to exist within the crevice. In the case of a thermal-spray coating, a crevice can be formed between contact points with outer surface of the coating, or at the coating-substrate interface in the case of damaged coatings. With the input parameters, and a pH which is selected to represent either crevice or non-crevice conditions, both the corrosion potential and critical potential can be determined. The critical potential is corrected for the effects of devitrificaiton if the maximum temperature that the alloy has experienced exceeds the crystallization temperature. The governing corrosion rate is selected based upon the difference between the corrosion and critical potentials; if the corrosion potential exceeds the critical potential, localized attack is assumed to occur, and the rate of penetration is determined by the expression for localized corrosion (R_{LC}); if the corrosion potential is less than the critical potential, general attack is assumed to occur, and the rate of penetration is determined by the expression for general corrosion (R_{GC}).

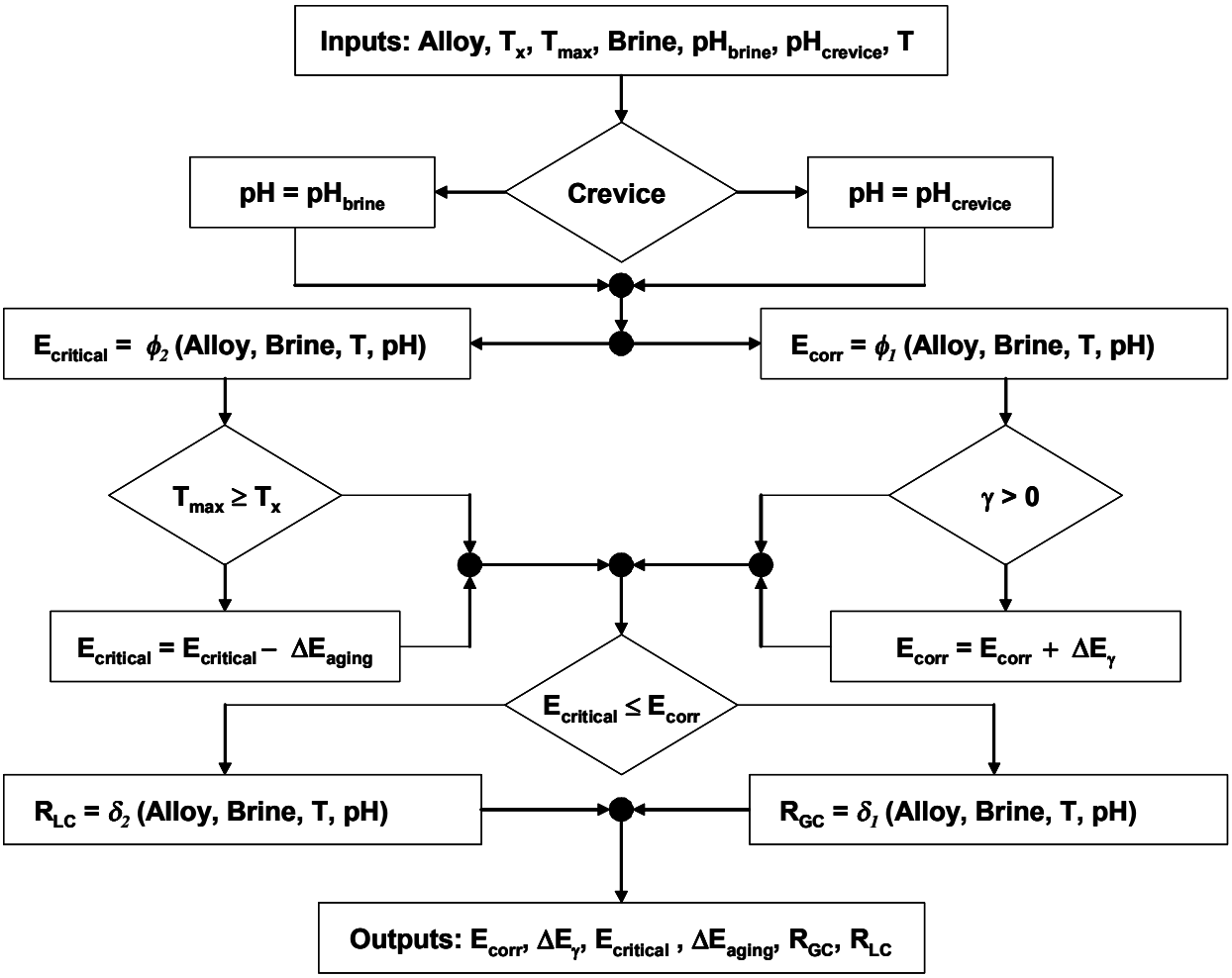

Figure 71 – Conceptual corrosion model for the corrosive attack of iron-based amorphous metal coatings applied with thermal spray.

6.2.2 Atmospheric Corrosion

While the attack of these new materials have been investigated with salt-fog testing, as described in other sections of the report, quantitative data on the atmospheric corrosion of these materials in contact with humid air, with the effects of dust deliquescence, have not yet been investigated.

6.2.3 General Aqueous-Phase Corrosion

As previously discussed, the governing corrosion rate is selected based upon the difference between the corrosion and critical potentials; if the corrosion potential exceeds the critical potential, localized attack is assumed to occur, and the rate of penetration is determined by the expression for localized corrosion (R_{LC}); if the corrosion potential is less than the critical potential, general attack is assumed to occur, and the rate of penetration is determined by the expression for general corrosion (R_{GC}). The temperature-dependent corrosion rates for Alloy C-22, HVOF SAM1651 and HVOF SAM2X5 are shown in Figures 73 through 75. Additional data is given in this report for the general corrosion rates of these materials in very aggressive test environments, such as 5M $CaCl_2$ at 105°C.

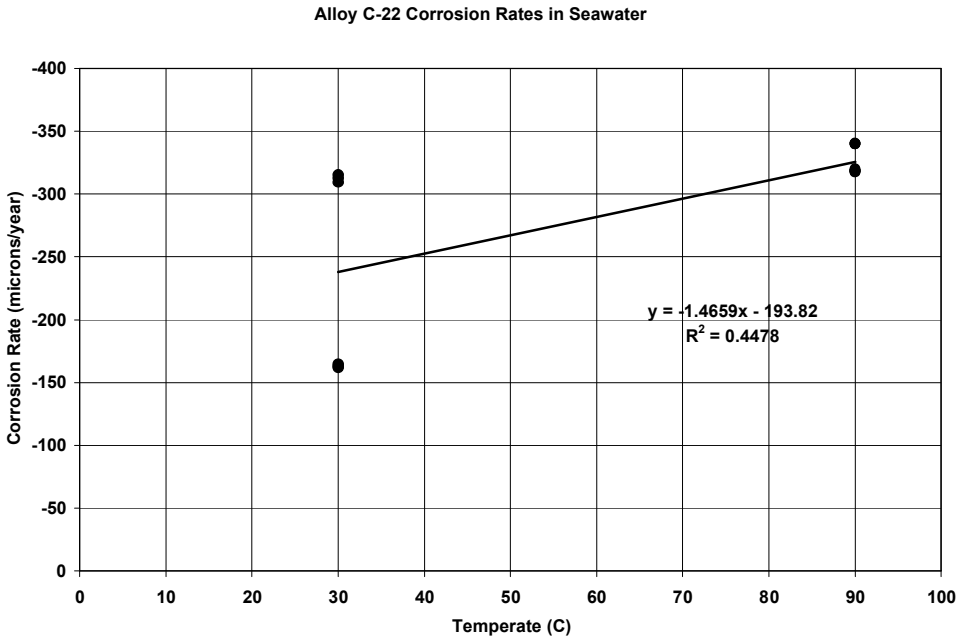

Figure 72 – General corrosion rates of wrought nickel-based Alloy C-22 in natural seawater as a function of temperature, which were determined with linear polarization.

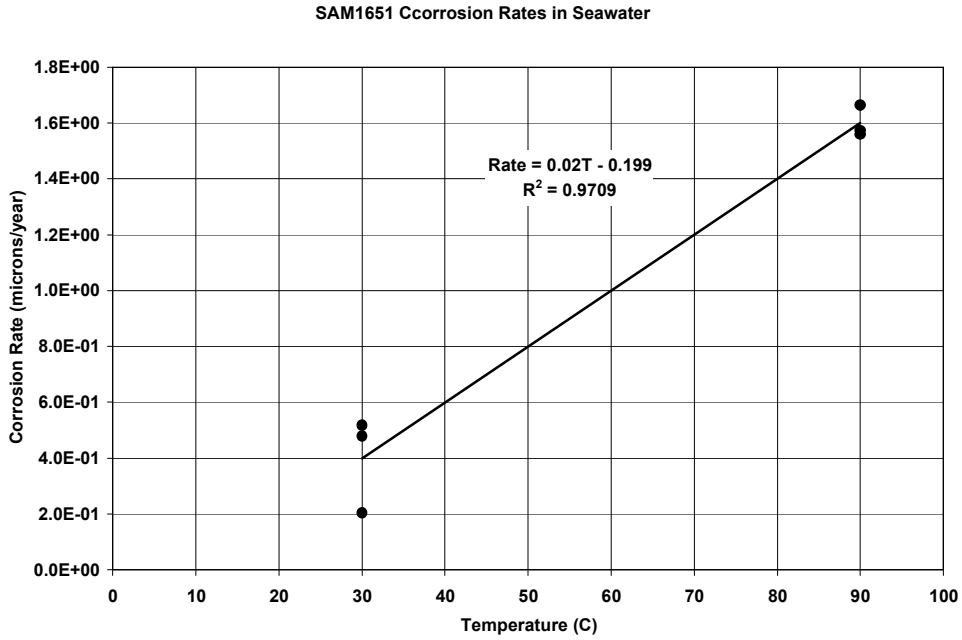

Figure 73 – General corrosion rates of yttrium-containing iron-based HVOF SAM1651 amorphous metal in natural seawater as a function of temperature, which were determined with linear polarization.

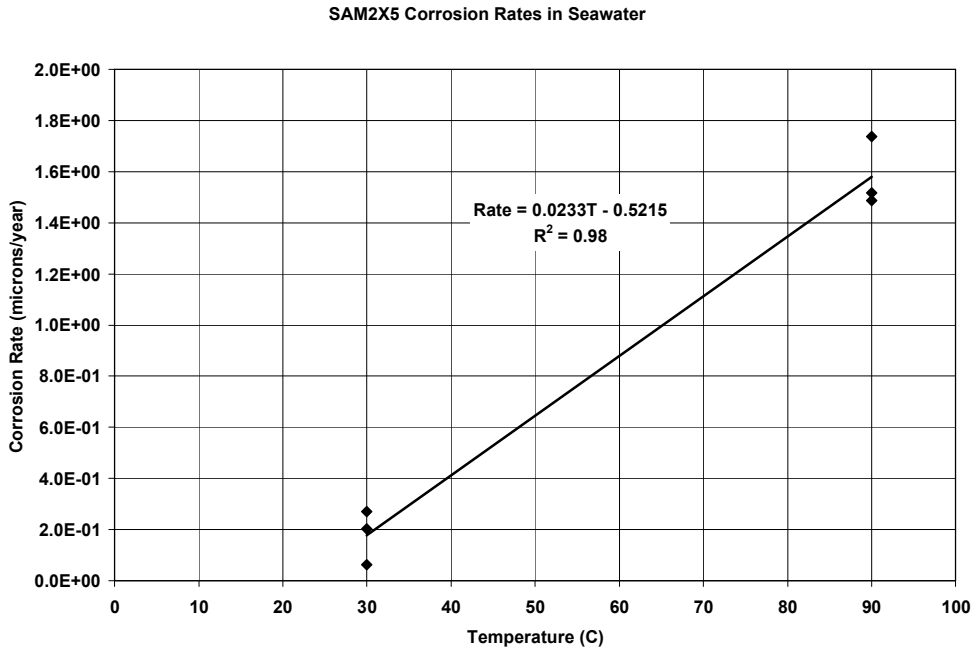

Figure 74 – General corrosion potential rates of high-boron iron-based HVOF SAM2X5 amorphous metal in natural seawater as a function of temperature, which were determined with linear polarization.

6.2.4 Passive Film Breakdown

The temperature-dependent corrosion potentials for wrought Alloy C-22, HVOF SAM1651, and HVOF SAM2X5 are shown in Figure 76 through 78. Based upon earlier work, which determined the effects of gamma radiolysis on the open-circuit corrosion potential of stainless steel, and the effect of hydrogen peroxide on the open circuit corrosion potential of Alloy C-22, it is assumed that gamma radiolysis will increase the open circuit corrosion potential of the iron-based amorphous metals by approximately 200-300 mV. Note that hydrogen peroxide is the primary radiolysis product formed from gamma irradiation of water, is a very strong oxidant, and is primarily responsible for increasing the open-circuit corrosion potential.

The critical potential determined by cyclic or potentiostatic polarization can be deduced from the data provided in the sections of the report that describe electrochemical corrosion testing. Preliminary investigations of the repassivation potential of melt-spun ribbions were conducted with cyclic polarization and are presented in Figures 79 and 80. The potentiostatic polarization data discussed in the section on electrochemical testing requires more time and is more difficult to obtain, but provides much greater confidence in passive film stability. Thus, work is being conducted to acquire such data in a variety of environments, with both creviced and fully exposed (un-creviced) surfaces. While most of the early test data with SAM2X5 and SAM1651 was obtained with natural seawater or concentrated calcium chloride, other environments have been investigated. Now that promising alloy compositions have been identified, future corrosion testing will be directed towards tests in a broader range of environments, with systematic exploration of the competing effects of chloride and nitrate at various temperature levels.

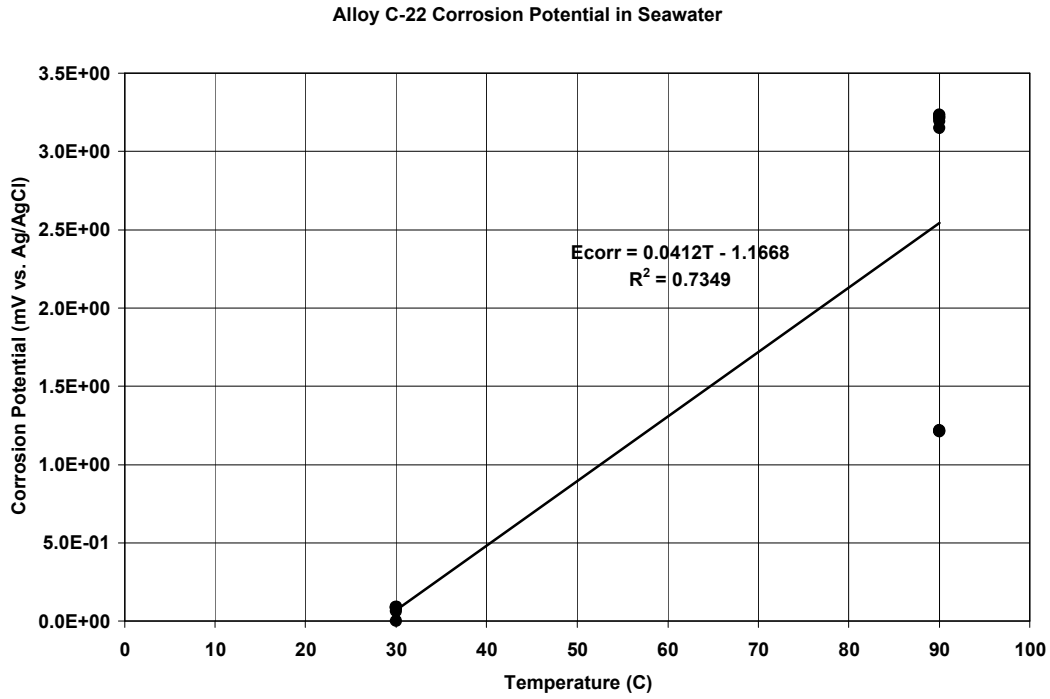

Figure 75 – Corrosion potential of wrought nickel-based Alloy C-22 in natural seawater as a function of temperature.

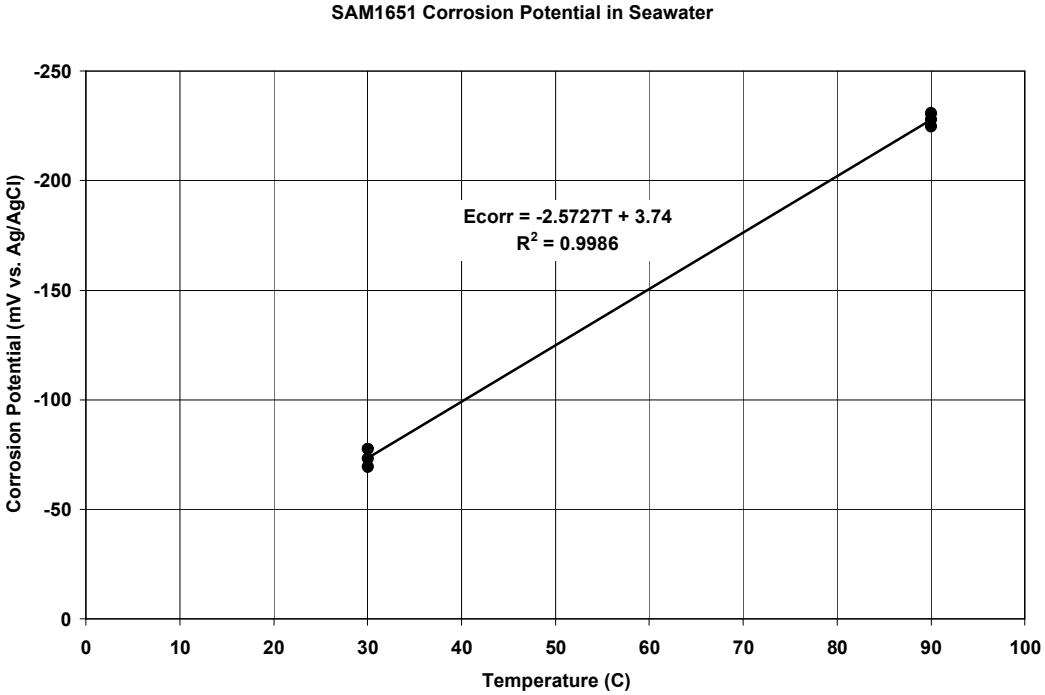

Figure 76 – Corrosion potential of yttrium-containing iron-based HVOF SAM1651 amorphous metal in natural seawater as a function of temperature.

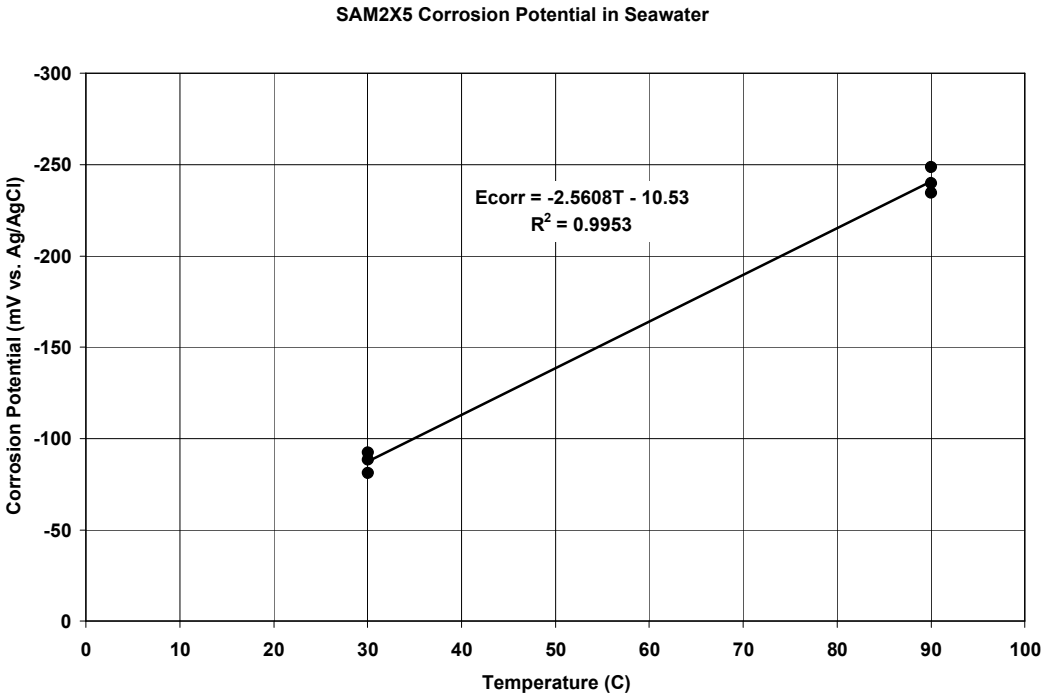

Figure 77 – Corrosion potential of high-boron iron-based HVOF SAM2X5 amorphous metal in natural seawater as a function of temperature.

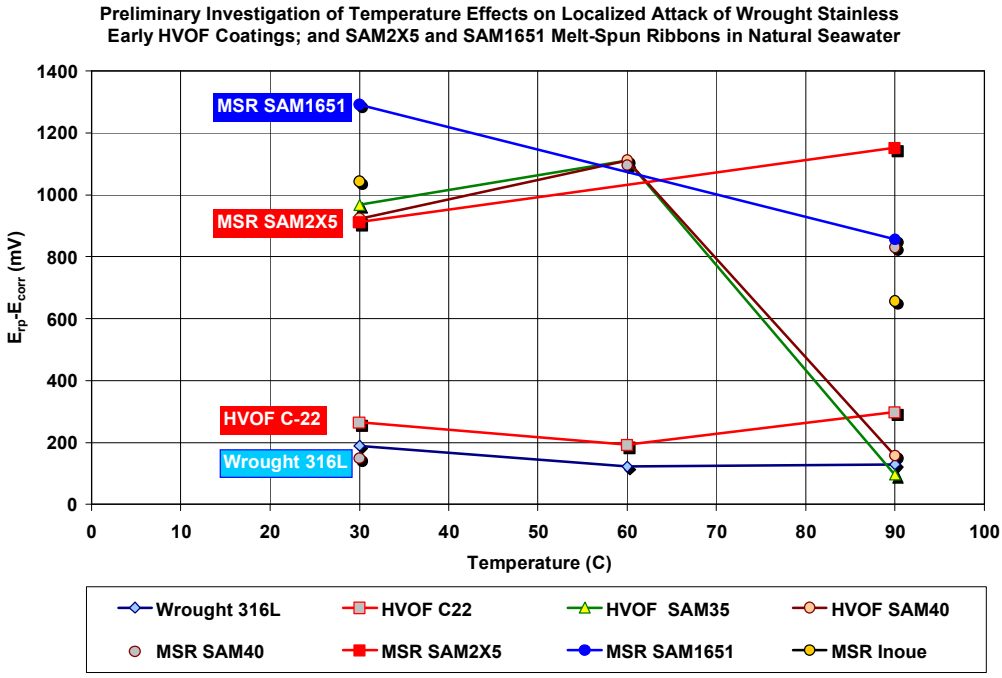

Figure 78 – Difference between the repassivation and open-circuit corrosion potentials for melt-spun ribbon samples of Fe-based amorphous metals in natural seawater at 30, 60 and 90°C.

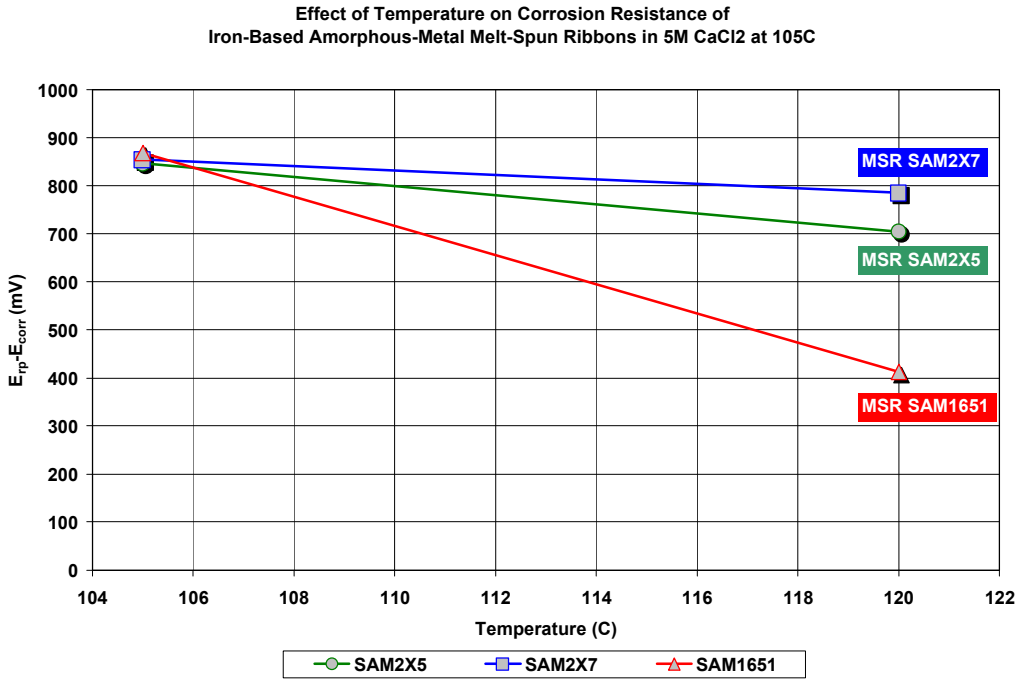

Figure 79 – Difference between the repassivation and open-circuit corrosion potentials for melt-spun ribbon samples of Fe-based amorphous metals in 5M $CaCl_2$ at 105 and 120°C.

6.3 MODEL RESULTS

This model provides the framework for predictive corrosion modeling of thermal spray amorphous metal coatings, but has not yet been applied to quantitative predictions.

6.4 FEATURES, EVENTS AND PROCESSES (FEPS) INCLUDED IN MODEL

No Features, Events and Processes (FEPS) are yet included in this early non-Q developmental model. FEPS will be discussed in future versions of this report.

6.5 CONSIDERATION OF ALTERNATIVE CONCEPTUAL MODELS

6.5.1 Accommodating Alternative Environments

The model presented here only includes parameters for natural seawater at 30, 60 and 90°C, and 5M $CaCl_2$ at 105 and 120°C. Additional expected environments were are not considered in this initial AMR, but should be included in versions.

6.5.2 Simplified Temperature Dependence of Corrosion Potentials and Rates

Furthermore, the temperature dependences of the open circuit corrosion potentials and the general corrosion rates are accounted for with simple linear regression equations. This simplification was adopted due to the limited availability of data, with data at only two temperature levels. It is recognized that better functional forms may be found as additional data is obtained.

6.5.3 Prediction of Overly Conservative Corrosion Rates with Linear Polarization

Note that the corrosion rates determined with linear polarization, for both the amorphous metals and nickel-based Alloy C-22, are viewed as highly conservative, and may be substantially higher than those experienced in some immersion tests. These rates may be most appropriate for a comparison of the relative corrosion rates of different materials. Thus, corrosion rates for iron-based amorphous metals, determined with linear polarization and reported here, could be normalized with the corrosion rates for Alloy C-22, also determined with linear polarization, and used to scale the waste package corrosion rates obtained during multi-year tests.

6.5.4 Detailed Reactive Transport Model for Crevice Corrosion

At the present time, crevice corrosion is being accounted for by simply assuming that a lower pH exists inside the crevice. Clearly, the localized environment is much more complicated, and can ultimately be dealt with through the application of detailed reactive transport models.

At points of contact between the HVOF coating and other solid objects, crevices form occluded geometries, which lead to differential aeration of the crevice solution (electrolyte). Crevices may also form between the coating and the substrate at sites of impact damage. Dissolved oxygen can become depleted deep within the crevice, while the oxygen concentration near the crevice mouth

remains relatively high. Cathodic reduction of dissolved oxygen at the crevice mouth may create a sufficiently high electrochemical potential to drive anodic processes inside the crevice, thereby causing an anodic current to flow along the crevice towards the crevice mouth. The potential at the mouth of a crevice is expected to be well below the threshold for localized attack, as determined with CP measurements. Anodic processes inside the crevice are, therefore, expected to occur at a rate that corresponds to the local passive current density. Two primary electrochemical processes can lead to acidification of the solution in a passive crevice, (1) the preferential transport of anions into the crevice from the mouth driven by the electric field that accompanies the crevice current and (2) hydrolysis reactions of dissolved metal cations. Additional experimental work is required to determine the local environment inside crevices formed with iron-based amorphous-metal thermal-spray coatings.

The hydrolysis of dissolved metal in crevices can lead to the accumulation of H^+ and the corresponding suppression of pH. For example, pH < 2 has been observed in crevices made of stainless steel. Metal ions produced by anodic dissolution are assumed to undergo the following hydrolysis reactions.

Precipitation of hydroxides is favored at more alkaline pH levels. In the case of Alloy 22, the hydrolysis of other dissolved metals such as molybdenum and tungsten ions may be important. The Oldfield-Sutton model does not account for the role of HCl in the crevice on destabilization of the passive film.

Chloride anion will be driven into the crevice by the potential gradient, as discussed in the literature. Field-driven electromigration of Cl^- (and other anions) into crevice must occur to balance cationic charge associated with H^+ ions, as well as the charge associated with Fe^{2+}, Ni^{2+}, Cr^{3+}, and other cations. If such conditions do develop inside Alloy 22 crevices, the stage might be set for an accelerated attack of this material by localized corrosion or stress corrosion cracking (SCC).

A detailed deterministic model has been developed to calculate the spatial distributions of electrochemical potential and current density in WP crevices, as well as transient concentration profiles of dissolved metals and ions. These quantities are calculated with the transport equations, which govern electromigration, diffusion, and convective transport. In cases with strong supporting electrolyte, electromigration can be ignored. First, the axial current density along the length of the crevice is calculated by integrating the wall current density. The electrode potential along the length of the crevice can then be calculated from the axial current density. This technique is similar to that employed in other models. Such models show that the electrochemical potential decreases with increasing distance into the crevice. Therefore, the potential should never be more severe (closer to the threshold for localized corrosion) than at the crevice mouth. The partial differential equations that define transient concentrations in the crevice require determination of the potential gradient, as well as the local generation rates for dissolved species. The concentrations of dissolved metals at the crevice mouth are assumed to be zero. Computations are facilitated by assuming that the crevices are symmetric about a mirror plane where the flux is zero. This model has been used to estimate the extent of pH suppression in crevices due to the simultaneous hydrolysis and transport of dissolved iron, nickel, chromium, molybdenum and tungsten.

6.5.5 Other Crevice-Like Occluded Regions

The surface of the amorphous metal coating may have some degree of porosity and other morphological features that might behave as pits and crevices, with localized acidification within the pores. Acidification inside these features could lead to localized attach that is not accounted for by the simplified conceptual model presented here.

6.5.6 Corrosion at Crystalline Phases in Amorphous Matrix

The surface of the amorphous metal coating is assumed to be homogenous, and have uniform corrosion properties. However, in some cases crystalline phases may be present at the coating-environment interface, and be much more susceptible to corrosion than the amorphous phase. Phases of particular interest in regard to devitrified (thermally aged) iron-based amorphous metals include bcc ferrite and chromium boride (Cr_2B). Models to account for the presence of such phases have not yet been considered, but should be.

6.6 MODEL UNCERTAINTY AND CONFIDENCE

6.6.1 Model Uncertainty

The greatest uncertainty in integrated corrosion models used for the prediction of materials performance over the post-closure period of the repository at Yucca Mountain, which extends over several thousand years, are believed to be due to imperfect knowledge of the evolving environment over such extreme periods of time. At the present time, tests have been conducted in a relatively narrow range of natural environments, including seawater and 5M $CaCl_2$ at elevated temperatures. Additional data is needed to determine important model parameters as a function of the concentrations of various ionic species that are expected to be present in the repository or inside the waste package in the case of criticality control applications, so that the materials performance model can be applied to any predicted environment. This work is in progress.

6.6.1.1 Experimental Uncertainty

Experimental contributions to the uncertainty in electrochemical potentials and corrosion rates, determined by linear polarization, are captured in the form of calculated standard deviations and regression coefficients.

6.7 SUMMARY OF MODEL

In summary, a conceptual model had been developed and presented for the prediction of corrosion rates for thermal-spray coatings of iron-based amorphous metals.

Two iron-based amorphous metal formulations, SAM2X5 and SAM1651, have been developed which exhibit corrosion resistance comparable to that of Type 316L stainless steel and nickel-based Alloy C-22 in several aggressive test environments, including natural seawater at 30, 60 and 90°C, as well as in 5M $CaCl_2$ at 105 and 120°C. This corrosion resistance is achieved by adding chromium, molybdenum and tungsten to the alloys, while continuing to maintain enough boron for glass formation. To determine the suitability of these materials for various repository applications under consideration, a model must be formulated.

The conceptual corrosion model requires specification of the alloy composition, the amorphous alloys crystallization temperature, the maximum temperature that the amorphous metal has seen over its lifetime, the brine composition, pH for the brine or crevice, and brine temperature. Outputs include open circuit corrosion potential, the change in corrosion potential with gamma radiolysis, the critical potential for passive film breakdown, the change in the critical potential with devitrification of the amorphous alloy, the general corrosion rate, and the localized corrosion rate. The model selects the solution pH, based upon whether or not the surface is creviced. If a crevice exists, a lower solution pH is assumed, accounting for the typical acidic conditions known to exist within the crevice. In the case of a thermal-spray coating, a crevice can be formed between contact points with outer surface of the coating, or at the coating-substrate interface in the case of damaged coatings. With the input parameters, and a pH which is selected to represent either crevice or non-crevice conditions, both the corrosion potential and critical potential can be determined. The critical potential is corrected for the effects of devitrificaiton if the maximum temperature that the alloy has experienced exceeds the crystallization temperature. The governing corrosion rate is selected based upon the difference between the corrosion and critical potentials; if the corrosion potential exceeds the critical potential, localized attack is assumed to occur, and the rate of penetration is determined by the expression for localized corrosion; if the corrosion potential is less than the critical potential, general attack is assumed to occur, and the rate of penetration is determined by the expression for general corrosion.

7. VALIDATION

A model has been developed to (1) determine whether or not the mode of corrosive attack is uniform or localized and (2) the rate of penetration.

7.1 CRITERIA

Confidence Building During Model Development to Establish Scientific Basis and Accuracy for Intended Use – Section 2.2.1 of Technical Work Plan for: Regulatory Integration Modeling and Analyses of the Waste Form and Waste Package (BSC 2004 [DIRS 171583]) specifies several steps for confidence building during model development. The model will contain documentation of decisions and activities implemented during the model development process to build confidence and verify a reasonable, credible, technical approach using scientific and engineering principles. The development of the model should be documented in accordance with AP-SIII.10Q (Section 5.3.2(b)) requirements. The development of the corrosion model has been conducted according to these criteria, as follows:

1. Selection of input parameters and/or input data, and a discussion of how the selection process builds confidence in the model. (AP-SIII.10Q, 5.3.2(b) (1); AP-2.27Q, Attachment 3 Level I (a)).

   Input parameters and data have been identified for the model that enable the determination of the mode of corrosive attack, as well as the rate of general uniform corrosion. Thus, this criterion is met.

2. Description of calibration activities, and/or initial boundary condition runs, and/or run convergences, simulation conditions set up to span the range of intended use and avoid inconsistent outputs, and a discussion of how the activity or activities build confidence in the model. Inclusion of a discussion of impacts of any non-convergence runs. (AP-SIII.10Q, 5.3.2(b)(2); AP-2.27Q, Attachment 3, Level I (e)).

   Several inputs are based upon unambiguous experimental measurements, and therefore provide initial calibration of portions of the model. Thus, this criterion is met.

3. Discussion of the impacts of uncertainties to the model results including how the model results represent the range of possible outcomes consistent with important uncertainties. (AP-SIII.10Q, 5.3.2(b)(3); AP-2.27Q, Attachment 3 Level 1 (d) and (f)).

   The uncertainties associated with the model have been identified and discussed. The greatest source of uncertainty is the imperfect knowledge of the environmental conditions that materials will encounter over thousands of years. Experimental uncertainty is captured in standard deviations and regression coefficients. Thus, this criterion is met.

4. Formulation of defensible assumptions and simplifications. (AP-2.27Q, Attachment 3, Level I (b)).

The model is based upon several defensible assumptions, grounded in accepted fact, with rational simplifications to enable predictions. Thus, this criterion is met.

5. Consistency with physical principles, such as conservation of mass, energy and momentum. (AP-2.27Q, Attachment 3 Level I (c))

There is consistency between physical principles. The conversion of the measured corrosion current to penetration rate is a direct application of conservation of charge.

Confidence Building Following Model Development to Support the Scientific Basis of the Model – Specific validation criteria (from AP-SIII.10Q) to be applied to the corrosion model after model development are:

1. Corroboration of model results with data acquired from the laboratory, field experiments, analog studies, or other relevant observations, not previously used to develop or calibrate the model (AP-SIII.10Q, Section 5.3.2).

   The model is being corroborated with data from a long-term immersion test, with the determination of open circuit corrosion potential, polarization resistance, general corrosion rate, and crevice attack in a variety of environments relevant to repository conditions. Such corroboration should be possible within the next twelve months. Thus, this criterion is met.

2. Corroboration with information published in refereed journals or literature (AP-SIII.10Q, Section 5.3.2).

   The corrosion resistance of these iron-based amorphous metals in aggressive environments has been corroborated with published data from several published papers. The effect of alloying additions, such as yttrium, has also been corroborated with published data. Thus, this criterion is met.

7.2 NATURAL ANALOGUES FOR BUILDING CONFIDENCE

The iron-based amorphous metal discussed here are new materials, and the authors are unaware of any suitable natural analogs.

7.3 MODEL VALIDATION ACTIVITIES

The immersion tests that are now underway will enable the validation of the corrosion model presented here. The open circuit corrosion potential, rate of corrosion and crevice attack in various environments of interest will be monitored over a prolonged period of time (as much as one year), with the results compared to predictions for natural seawater. Data for other environments will also be obtained, and used to broaden the models capability.

INTENTIONALLY LEFT BLANK

8. CONCLUSIONS

This research has two primary long-term goals, all directed towards development of advanced amorphous-metal thermal-spray coatings with corrosion resistance superior to Type 316L stainless steel [UNS # S31603] and nickel-based Alloy C-22 [UNS # N06022]. Computational materials science has been used to help guide the design these new materials.

8.1 NOVEL IRON-BASED AMORPHOUS-METAL COATINGS

Several Fe-based amorphous metal formulations have been found that appear to have corrosion resistance comparable to, or better than that of Ni-based Alloy C-22, based on breakdown potential and corrosion rate [1-8]. These formulations use chromium (Cr), molybdenum (Mo), and tungsten (W) to provide corrosion resistance, boron (B) to enable glass formation, and yttrium to lower the critical cooling rate (CRR). SAM1651 ($Fe_{48.0}Cr_{15.0}Mo_{14.0}B_{6.0}C_{15.0}Y_{2.0}$) has yttrium added [9-11], and has a nominal critical cooling rate of only 80 Kelvin per second, while SAM2X5 ($Fe_{49.7}Cr_{17.7}Mn_{1.9}Mo_{7.4}W_{1.6}B_{15.2}C_{3.8}Si_{2.4}$) has no yttrium, and is characterized by relatively high critical cooling rates of approximately 600 Kelvin per second. Note that SAM1651 is also known as SAM7. Corrosion data for the SAM2X5 formulation, which is based upon a master alloy known as either SAM40 or DAR40 [12-23] is reported here.

SAM1651 has a low critical cooling rate (CCR), due to the addition of yttrium (Y), which enables it to be rendered as a completely amorphous thermal spray coating. Unfortunately, it is relatively difficult to atomize, with powders being irregular in shape. This causes the powder to be difficult to pneumatically convey during thermal spray deposition. Gas atomized SAM1651 powder has required exotic milling techniques to eliminate irregularities that make flow difficult. SAM2X5 (no yttrium) has a high critical cooling rate, which has caused problems associated with devitrification. However, in contrast to SAM1651, SAM2X5, and the master alloy used for its preparation, can be readily gas atomized to produce spherical powders which enable more facile thermal spray deposition.

Protective coatings of nickel-based Alloy C-22 and Type 316L stainless can be applied with thermal spray technology [24]. However, their corrosion resistance is lost at the high temperatures required for deposition [1-8]. Based upon extensive studies of these austenitic alloys in wrought form, it is believed that this loss in corrosion resistance may be due to the precipitation of undesirable phases (P, σ, and μ). These precipitated phases deplete the matrix of those alloying elements responsible for passivity [25-27]. In contrast, SAM2X5 and SAM1651 coatings can be applied with thermal spray processes without any significant loss of corrosion resistance [1-8].

It is important to point out that the outstanding corrosion possible with amorphous metals has been recognized for many years [28-31]. A number of other iron-based amorphous metals have been published, including several with very good corrosion resistance. Examples include: thermally sprayed coatings of Fe-10Cr-10-Mo-(C,B) which were explored as early as 1996 by Kishitake et al. [32]; bulk Fe-Cr-Mo-C-B [33]; and Fe-Cr-Mo-C-B-P [34]. The corrosion resistance of the Fe-Cr-Mo-C-B-P alloy [33] was corroborated by these authors [1-8]. Nickel-based materials have also been developed which exhibit exceptional corrosion performance [35].

8.2 OTHER ATTRIBUTES OF FE-BASED AMORPHOUS METAL COATINGS

Such materials are extremely hard, and provide enhanced resistance to abrasion and gouges (stress risers) from backfill operations, and possibly even tunnel boring. The hardness of Type 316L Stainless Steel is approximately 150 VHN, that of Alloy C-22 is approximately 250 VHN, and that of HVOF SAM2X5 ranges from 1100-1300 VHN [12-13]. SAM2X5 and SAM1651 coatings can be applied with thermal spray processes without any significant loss of corrosion resistance.

Both SAM2X5 & SAM1651 have high boron content which should enable them to absorb neutrons and therefore be used for criticality control in baskets. Alloy C-22 and 316L have no neutron absorber, and cannot be used for such functions. Borated stainless steel and Gd-doped Ni-Cr-Mo alloys are being developed but may face limitations related to their availability, cost, corrosion and leach resistance, and mechanical properties. Tests with J-13 well waters have shown that boron can preferentially leach boron, the neutron absorber, from borated stainless steels. Well J-13 water has a typical water chemistry for saturated zone and perched waters at Yucca Mountain and a mean composition that was reported by Harrar et al. [36]. During evaporation of J-13 water, Na^+, K^+, Cl^-, and NO_3^- are concentrated, and HCO_3^-, Ca^{2+} and Mg^{2+} can be removed from solution by the precipitation of calcium and magnesium carbonate.

8.3 IMPORTANCE OF CHROMIUM, MOLYBDENUM AND TUNGSTEN

The importance of chromium, molybdenum and tungsten additions to amorphous metals as a means of enhancing corrosion resistance is discussed in this section. The decision to achieve enhanced corrosion resistance in these Fe-based amorphous metals was initially based upon two considerations. First, substantial enhancements in corrosion resistance had been observed in stainless steels and nickel based alloys by adding molybdenum, as well as other alloying elements. Secondly, this enhancement in localized corrosion resistance can be quantified in the pitting resistance equivalence number, and could be used as a guide to determine the level of molybdenum addition necessary to achieve localized corrosion resistance comparable to nickel-based Alloy C-22, one of the benchmark materials. Branagan et al. used estimates of PREN to determine the maximum molybdenum additions to the series of melt-spun ribbons which include SAM2X1, SAM2X3, SAM2X5 and SAM2X7 [5, 13]. Based upon these calculations, it was believed that the new SAM2X5 and SAM2X7 compositions possessed enough molybdenum to demonstrated passive film stability comparable to nickel-based Alloy C-22. This hypothesis has been tested in this investigation, and found to have merit.

The importance of molybdenum in nickel-based alloys has been recognized for many years. Alloy C-22 (UNS N06022) is now being considered for construction of the outer barrier of the WP. This alloy consists of 20.0-22.5% Cr, 12.5-14.5% Mo, 2.0-6.0% Fe, 2.5-3.5% W, 2.5% (max.) C, and balance Ni [37]. Alloy C-22 is less susceptible to localized corrosion in environments that contain Cl^- than Alloys 825 and 625, materials of choice in earlier designs. The unusual localized corrosion resistance of Alloy C-22 is apparently due to the additions of Mo and W, both of which are believed to stabilize the passive film at very low pH [38]. The oxides of these elements are very insoluble at low pH. Consequently, Alloy 22 exhibits relatively high thresholds for localized attack. High repassivation potentials have been observed by some

[39], while others have found very low corrosion rates in simulated crevice solutions containing 10 wt. % $FeCl_3$ [40].

8.4 CORROSION PERFORMANCE

The hypothesis that the corrosion resistance of Fe-based amorphous metals can be enhanced through application of heuristic principles related to the additions of chromium, molybdenum and tungsten has been tested, and found to have merit. The decision to achieve enhanced corrosion resistance in these Fe-based amorphous metals was initially based upon two considerations. First, substantial enhancements in corrosion resistance had been observed in stainless steels and nickel based alloys by adding molybdenum, as well as other alloying elements. Secondly, this enhancement in localized corrosion resistance can be quantified in the pitting resistance equivalence number, and could be used as a guide to determine the level of molybdenum addition necessary to achieve localized corrosion resistance comparable to nickel-based Alloy C-22, one of the benchmark materials. Electrochemical tests have been used to prove that corrosion performance comparable to wrought and thermally sprayed coatings of nickel-based Alloy C-22 can be achieved with the new Fe-based amorphous metals in hot concentrated calcium chloride and seawater. The passive film on Alloy C-22 in seawater at 90°C begins to breakdown at an applied potential of 200 mV verses OCP, and breaks down catastrophically at 1000 mV verses OCP, whereas SAM2X5 maintains passivity at applied potentials as high as 1400 mV verses OCP in the same environment.

Early HVOF coatings of SAM35, SAM40, SAM40X3 had non-optimal elemental compositions, and were produced with non-optimal thermal spray parameters (powder size, gun pressure, and particle velocity), and exhibited light rusting after 13 cycles in the classic salt fog test. However, optimized elemental compositions of these Fe-based amorphous metals in the form of fully dense pore-free material have shown no corrosion after 24 cycles in this aggressive test. Promising formulations at the present time are believed to be SAM2X5 and SAM1651. Salt-fog testing of HVOF coatings of these materials showed no corrosion after more than 30 cycles (and up to 54 cycles) in the salt fog test. Such performance cannot be achieved with thermally sprayed Type 316L stainless steel, as this material loses most of its desirable corrosion-resistance during the thermal spray process. To a lesser extent, similar difficulties are encountered during the thermal spraying of Alloy C-22.

The second hypothesis tested was that amorphous metals can have better corrosion resistance than comparable, crystalline materials. It is generally believed that the corrosion resistance of amorphous metals is enhanced by the absence of precipitated intermetallic phases which deplete the matrix of those alloying elements responsible for passivity, a large number of grain boundaries intersecting the surface, and passive films with a large number of resulting defects. Defects would be expected to evolve as the passive film grows on an interface with various crystalline faces to the environment. Parts of this hypothesis have been tested by intentionally inducing devitrification in an amorphous metal, known to have good corrosion resistance in the non-crystalline state. Melt-spun ribbons of SAM2X5 and SAM40, the master alloy, were intentionally devitrified by heat treating them at various temperatures for one hour, including levels known to be above the measured crystallization temperature. The samples heat treated for one hour at 800°C, a temperature well above the crystallization temperatures of SAM2X5 and

SAM40, showed a dramatic loss of corrosion resistance in comparison to the as-received samples. It has therefore been proven that such heat treatments and the resultant crystalline phase formation is deleterious to corrosion resistance. Crystalline phase correlated with poor corrosion performance include ferrite.

Furthermore, ingots and melt-spun ribbons of the Fe-based amorphous metals without grain boundaries have shown more corrosion resistance in than crystalline Alloy C-22. It has also been found that it is not been possible to render Alloy C-22 as thermal spray coating with the same corrosion resistance as the wrought alloy, though such possibilities do exist with some of the Fe-based amorphous metal formulations discussed here.

The crystalline structure of powders can vary with particle size, since different cooling rates are experienced by particles with different sizes. Particle size sensitivity is explored in this publication, in regard to the residual crystalline phases present in powders and coatings, as well as in regard to the impact of those crystalline phases on the corrosion resistance of coatings. Corrosion resistance of the SAM1651 amorphous metal alloy is discussed elsewhere [58].

It has been shown that these novel ultra-hard corrosion-resistant materials can be produced as either bulk alloys or coatings. For example, melt spinning and arc melting with drop casting can be used to render these materials as fully dense pore-free bulk alloys. Coatings can be produced with advanced thermal spray processes, or by physical vapor deposition processes such as magnetron sputtering or electron-beam evaporation. The materials can also be rendered as bulk alloys by using HVOF to form large plates on a flat mandrel. Near theoretical density has been achieved through precise control of powder size with atomization and classification.

Given the good performance of the SAM2X5 HVOF coatings in salt fog and seawater environments, these coatings should be able to protect a variety of ships and marine structures, including off-shore drilling platforms. Ultimately, it may be possible to use materials such as these to help protect the outer surface of containers for the transportation, aging, and disposal of spent nuclear fuel, and to protect welds and heat affected zones, thereby preventing exposure to environments that might cause stress corrosion cracking, and as a means of criticality control inside containers [59, 60]. In the future, it may be possible to substitute such high-performance iron-based materials for more-expensive nickel-based alloys, thereby enabling cost savings in a wide variety of industrial applications.

SAM1651 has a low critical cooling rate (CCR), due to the addition of yttrium (Y), which enables it to be rendered as a completely amorphous thermal spray coating. The yttrium addition increases the viscosity of the alloy, thereby slowing the nucleation and growth kinetics of crystalline phases. Unfortunately, such increases in viscosity also make this material relatively difficult to gas atomize, with the powders having irregular shapes. Such non-spherical particle morphology causes pneumatic conveyance of the SAM1651 powder during thermal spray operations to be difficult. The production of nearly spherical gas-atomized SAM1651 powder with acceptable flow characteristics has required extensive particle sorting, exotic and expensive milling to eliminate irregularities, and significant process optimization.

The hypothesis that the corrosion resistance of Fe-based amorphous metals can be enhanced through application of heuristic principles related to the additions of chromium, molybdenum, tungsten and yttrium has been tested with SAM7 (SAM1651) and SAM8 formulations, and found to have merit. The decision to achieve enhanced corrosion resistance in these Fe-based amorphous metals was initially based upon two considerations. First, substantial enhancements in corrosion resistance had been observed in stainless steels and nickel based alloys by adding chromium, molybdenum, tungsten, as well as other alloying elements. Secondly, this enhancement in localized corrosion resistance can be quantified in the pitting resistance equivalence number, and could be used as a guide to determine the level of molybdenum addition necessary to achieve localized corrosion resistance comparable to nickel-based Alloy C-22, one of the benchmark materials. Electrochemical tests have been used to prove that corrosion performance comparable to nickel-based Alloy C-22 can be achieved with the new Fe-based amorphous metals in 5M CaCl2 at 105°C and seawater at 90°C.

Thermal spray coatings produced with early Fe-based amorphous metal formulations (SAM35, SAM40, and SAM40X3) had non-optimal elemental compositions, were produced with non-optimal thermal spray parameters (powder size, gun pressure, and particle velocity), and exhibited rusting after 13 cycles in the standardized salt fog tests. However, dense and pore-free thermal spray coatings produced with improved amorphous metal formulations that have greater concentrations of chromium, molybdenum and yttrium (SAM7, also known as SAM1651) showed no corrosion after more than 30 cycles (and up to 54 cycles) in the salt fog test. Such performance cannot be achieved with thermally sprayed Type 316L stainless steel, as this material loses most of its desirable corrosion-resistance during the thermal spray process. To a lesser extent, similar difficulties are encountered during the thermal spraying of Alloy C-22.

The second hypothesis tested was that amorphous metals can have better corrosion resistance than comparable, crystalline materials. Ingots and melt-spun ribbons of the Fe-based SAM7 (SAM1651) and SAM8 amorphous metals, both free of grain boundaries, have shown much more resistance to corrosion (passive film stability) in aggressive environments such as 5M $CaCl_2$ at 105°C than crystalline Type 316L stainless steel and nickel-based Alloy C-22. It has also been found that it is not been possible to render Alloy C-22 as thermal spray coating with the same corrosion resistance as the wrought alloy, though such possibilities do exist with some of the Fe-based amorphous metal formulations discussed here. Corrosion resistance of Fe-based amorphous metals without yttrium additions, such as SAM2X5, is discussed elsewhere [58].

It has been shown that these novel ultra-hard corrosion-resistant materials can be produced as either bulk alloys or coatings. For example, melt spinning and arc melting with drop casting can be used to render these materials as fully dense pore-free bulk alloys. Coatings can be produced with advanced thermal spray processes, or by physical vapor deposition processes such as magnetron sputtering or electron-beam evaporation. The materials can also be rendered as bulk alloys by using HVOF to form large plates on a flat mandrel. Near theoretical density has been achieved through precise control of powder size with atomization and classification.

Given the good performance of thermal-spray coatings of SAM1651 in salt fog and seawater environments, these coatings should be able to protect a variety of ships and marine structures, including off-shore drilling platforms. The performance in hot calcium chloride may indicate that

this material could be used in processes where hot geothermal brines are involved. Ultimately, it may be possible to use materials such as these to help protect the outer surface of containers for the transportation, aging, and disposal of spent nuclear fuel, and to protect welds and heat affected zones, thereby preventing exposure to environments that might cause stress corrosion cracking, and as a means of criticality control inside containers [59, 60]. In the future, it may be possible to substitute such high-performance iron-based materials for more-expensive nickel-based alloys, thereby enabling cost savings in a wide variety of industrial applications.

8.5 SUMMARY OF DEVELOPED DATASETS

The data used in the development of this report are included in a CD ROM which accompanies the report. Data tracking numbers for the developed datasets will be provided with subsequent versions.

8.6 YUCCA MOUNTAIN REVIEW PLAN ACCEPTANCE CRITERIA

Yucca Mountain Review Plan, Final Report (NRC 2003 [DIRS 163274]) contains Acceptance Criteria that are intended to establish the basis for the review of the material contained in the License Application. While the information included in this report may eventually serve as part of the basis for an amendment of the license application, at the present time it does not serve as the basis for the License Application. Even so, it is important to discuss how the information contained herein could address applicable YMRP Acceptance Criteria.

The YMRP Acceptance Criteria that are applicable to this report are identified in *Technical Work Plan for: Regulatory Integration Modeling and Analysis of the Waste Form and Waste Package* (BSC 2004 [DIRS 171583], Table 3-1). For each applicable criterion, the criterion is found in quotation marks, followed by the authors' discussion in italics, which states how the information in the report addresses the criterion.

8.6.1 System Description and Demonstration of Multiple Barriers

"The following Acceptance Criteria are from Section 2.2.1.1.3 of *Yucca Mountain Review Plan, Final Report* (NRC 2003 [DIRS 163274])."

Discussion in this report may be relevant to a thermally sprayed ground support system, a thermally sprayed drip-shield structure, waste package support pallets, the waste package, transportation-aging-disposal (TAD) containers, and criticality control materials (baskets) inside the waste package. It should also be noted that this information may also be valuable to the Department of Defense, a co-sponsor of this work, for potential naval applications.

Acceptance Criterion 1 - Identification of Barriers Is Adequate

"Barriers relied on to achieve compliance with 10 CFR 63.113(b), as demonstrated in the total system performance assessment, are adequately identified, and are clearly linked to their capability."

Barriers are adequately identified and clearly linked to their capability, and their practical limitations. The thermally-sprayed iron-based amorphous metal coatings described in this report may be useful for the fabrication of relatively low-cost ground support systems, drip shields, waste packages, other spent nuclear fuel storage and transportation containers, and criticality control baskets. Testing has already been done in environments that may ultimately be relevant in the repository, though testing in additional environments is still required, and is underway. The electrochemical potentials where passivity is lost in the environments used in testing thus far have been measured. The rates of general corrosion in these environments, which might ultimately cause penetration of the coatings have been measured, along with experimental uncertainty, and are discussed herein. Effects such as the thermal aging of the amorphous metals during the expected thermal pulse in the repository, and the associated effects of devitrification, have been addressed. It is therefore concluded that good progress has been made in addressing this criterion. Even so, additional work is planned and is being executed to strengthen the work.

Acceptance Criterion 2 - Description of Barrier Capability to Isolate Waste Is Acceptable

"The capability of the identified barriers to prevent or substantially reduce the rate of movement of water or radionuclides from the Yucca Mountain repository to the accessible environment, or prevent the release or substantially reduce the release rate of radionuclides from the waste is adequately identified and described: (1) The information on the time period over which each barrier performs its intended function, including any changes during the compliance period, is provided; (2) The uncertainty associated with barrier capabilities is adequately described; (3) The described capabilities are consistent with the results from the total system performance assessment; and (4) The described capabilities are consistent with the definition of a barrier at 10 CFR 63.2."

The thermal limits for operation of the iron-based amorphous metal coatings in repository applications are clearly established. Above these temperature limits, which correspond to the crystallization temperature of the amorphous alloys, corrosion resistance is lost, and use is not recommended. This temperature limit is above the 350°C temperature limit that is known to exist for zirconium-based cladding on some nuclear fuel rods. See Sections 4.2.6, 4.2.7 and 4.2.13.

The critical potentials and corrosion rates of these thermally sprayed amorphous-metal coatings are provided for two representative, natural brines, natural seawater at 30 to 90°C, and 5M $CaCl_2$ at 105 to 120°C. Natural seawater is the most common brine on the planet, and contains most of the ionic species that will be present at Yucca Mountain, with a concentration of total dissolved solids (TDS) of approximately 3.5 weight percent. Furthermore, a large fraction of published corrosion data for engineering materials exists for seawater tests. Thus, the use of seawater as a test environment provide a means of cross-referencing the data for these newly developed materials to a broad range of well-known and characterized engineering materials. The calcium chloride environment is extremely aggressive, and can cause failure of the passive film on nickel-based Alloy C-22, as shown in this report, as well as published elsewhere. While some believe that the infiltration of calcium-chloride type brines into the repository is improbable, there is sufficient uncertainty regarding the environment that may evolve inside the repository to absolutely eliminate such natural brines from consideration. Scenarios involving the existence of calcium chloride inside the repository have been postulated. These materials

could provide additional "defense in depth" to guard against the evolution of such brines thousands of years into the future. See Sections 4.2.11, 4.2.12, 4.2.13, 4.2.14, 4.2.15 and 4.2.17.

Additional data is required for the thermally sprayed iron-based amorphous metals in a broader range of chloride-nitrate brines, with a broader range of pH, with the effects of gamma radiolysis and thermal aging below the crystallization temperature fully accounted for. The same needs also exist for other engineering materials, such as commercially available Type 316L stainless steel and nickel-based Alloy C-22.

The corrosion rates are comparable to that of other potentially more expensive materials in the repository. It is therefore concluded that these materials may provide suitable waste isolation is some repository applications, thus providing an opportunity for safe waste isolation with cost savings of the repository life cycle. See Sections 4.2.11, 4.2.12, 4.2.13, 4.2.14, 4.2.15 and 4.2.17.

These coatings could also be used to enhance the performance of the existing repository, by enhancing the resistance of closure welds to stress corrosion cracking, by providing a local barrier that separates the closure weld from the local (corrosive) environment which could cause stress corrosion cracking.

Acceptance Criterion 3 - Technical Basis for Barrier Capability Is Adequately Presented

"The technical bases are consistent with the technical basis for the performance assessment. The technical basis for assertions of barrier capability is commensurate with the importance of each barrier's capability and the associated uncertainties."

The technical bases for the performance of the thermally sprayed iron-based amorphous metals are consistent with those that have evolved over the past several years for the engineered barrier system that serves as the basis for the total system performance assessment. For example, the performance of these new materials involves the measurement and quantification of corrosion and critical potentials as a means of determining whether or not the mode of corrosive attack is general or localized corrosion. The corrosion rates which would apply in the event of general corrosion are also determined. Thermal limits for the material, above which corrosion resistance is lost, have been identified. This is analogous to the studies of thermal phase stability of Alloy C-22, with studies of the effects of precipitated TCP phases (P, σ, and μ) on corrosion resistance. Additional models of the phase stability of the amorphous metals are provided in a companion non-Q analysis and modeling report prepared by the HPCRM Program. See Sections 4.2.6, 4.2.7, 4.2.13, 4.2.11, 4.2.12, 4.2.13, 4.2.14, 4.2.15 and 4.2.17.

8.6.2 Degradation of Engineered Barriers

"The following acceptance criteria are from Section 2.2.1.3.1.3 of *Yucca Mountain Review Plan, Final Report* (NRC 2003 [DIRS 163274])."

As previously discussed, the conceptual model and the supporting experimental measurements for these new thermally sprayed iron-based amorphous metal coatings are very similar to the work performed by the Yucca Mountain Program with Type 316L stainless steel and nickel-

based Alloy C-22. Measurements of open-circuit corrosion potential and critical potential are used as the basis of determining whether or not the amorphous metals undergo general or localized corrosion. General corrosion rates have been determined, and will be applied in those cases where environment- and temperature-dependent general corrosion is assumed to occur. Rates of crevice attack will be deduced from long-term exposure tests currently underway at Lawrence Livermore National Laboratory. The effect of thermal aging on the susceptibility to localized corrosion has been determined. These materials have also been exposed to high neutron and gamma radiation at the 1.5 megawatt TRIGA reactor at the McClellan Nuclear Radiation Center. This data is reported in another parallel analysis and modeling report on radiation effects that has been prepared by the HPCRM Program. This criterion has been, and is being met, with the developmental and testing program. As previously discussed, corrosion data is needed in a broader range of environments. An effort is underway to collect this data, and to incorporate the data into a parameterized model that should prove useful to total system performance assessment (TSPA). See Section 6.2.

Acceptance Criterion 1 – System Description and Model Integration are Adequate

"(1) TSPA adequately incorporates important design features, physical phenomena and couplings and uses consistent assumptions throughout the degradation of engineered barriers abstraction processes.

It is believed that appropriate design features and applicable physical phenomena (general and localized corrosion, effects of thermal aging), as well as environmental factors (exposure to hot natural brines) and their coupling (schematic of integrated corrosion model shown in previous section) are addressed within this report. As previously discussed, the need for additional test data over a broader range of conditions is recognized, and is being collected. See Sections 4.2.6, 4.2.7, 4.2.13, 4.2.11, 4.2.12, 4.2.13, 4.2.14, 4.2.15 and 4.2.17 on corrosion phenomena and related testing, and Section 6.2 on Model Development.

"(2) Abstraction uses assumptions, technical bases, data and models that are appropriate and consistent with those used in other abstractions."

As previously discussed, the model abstractions regarding the use of corrosion and critical potentials are entirely consistent with those model abstractions used by TSPA in determining whether or not nickel-based Alloy C-22 undergoes general or localized corrosion. Temperature limits have also been established, above which corrosion resistance is lost. These model abstractions are consistent with those previously used by TSPA for the engineered barrier system which now serves as the baseline for the proposed license application. See Sections 6.2 and 6.5.

"(3) The descriptions of the engineered barriers, design features, degradation processes, physical phenomena, and couplings that may affect the degradation of the engineered barriers are adequate."

The description of engineered barriers, design features, degradation processes, physical phenomena are adequate. See Sections 4.2.1, 4.2.2, 4.2.3, 4.2.5, 4.2.6, 4.2.7 and 4.2.8 on

characterization of the materials. See Sections 4.2.11, 4.2.12, 4.2.13, 4.2.14, 4.2.15 and 4.2.17 on corrosion phenomena and related testing, and Section 6.2 on Model Development.

"(4) Initial and boundary conditions are propagated consistently throughout the abstraction process."

The integrated model (schematic shown in section on modeling), with the linkages shown, allow conditions such as temperature to be carried throughout the corrosion assessment. The same temperature is used for selection of corrosion mode (general or localized corrosion) as used for estimation of the general rate of corrosion. See Sections 6.2.1, 6.2.3, 6.2.4, 6.5.1, 6.5.2, 6.5.3, 6.5.5, and 6.5.6.

"(5) Sufficient technical basis for the inclusion and exclusion of FEPS are provided.

As previously discussed, thermal limits for the material, above which corrosion resistance is lost, have been identified. This is analogous to the studies of thermal phase stability of Alloy C-22, with studies of the effects of precipitated TCP phases (P, σ, and μ) on corrosion resistance. In the future, this analysis and modeling report (AMR), or a subsequent revision, may therefore provide the basis for the exclusion of FEP 2.1.11.06.0A (Thermal sensitization of waste packages) in TSPA-LA (Total System Performance Assessment for the License Application) as discussed in Section 6.6.4. See Sections 4.2.11, 4.2.12, 4.2.13, 4.2.14, 4.2.15 and 4.2.17 of this report..

"(6) Relevance to In-Package Criticality Control"

Both SAM2X5 & SAM1651 have high boron content which should enable them to absorb neutrons and therefore be used for criticality control in baskets. These materials have already been evaluated in the 1.5 megawatt TRIGA reactor at McClellan Nuclear Radiation Center (MNRC), demonstrating the phase stability of these amorphous alloys during exposure in the reactor core to thermal neutrons and gamma rays, with doses equivalent to more than 4,000 years in a PWR waste package at Yucca Mountain. The effects of highly oxidizing radiolysis products, such as hydrogen peroxide, on the open circuit corrosion potential and passive film stability are under investigation and will be reported in a future revision. The neutron absorption cross section (opacity) of these materials has been determined and used in criticality control calculations for a prototype basket assembly, demonstrating that a 1-mm thick coating could lower k-effective by approximately ten percent. These data are presented in a parallel analysis and modeling report (AMR) by the HPCRM Program.

Alloy C-22 and 316L have no neutron absorber, and cannot be used for such functions. Borated stainless steel and Gd-doped Ni-Cr-Mo alloys are being developed but may face limitations related to their availability, cost, corrosion and leach resistance, and mechanical properties. Tests with J-13 well waters have shown that boron can preferentially leach boron, the neutron absorber, from borated stainless steels.

"(7) Guidance in NUREG 1297 and NUREG 1298 [re: Expert Elicitation] are followed."

This is not applicable to this report since no formal expert elicitation was used. However, three formal annual program reviews have been performed (Key West 2004; Pearl Harbor 2005; Key West 2006) and have enabled this work to benefit from the expert opinions of a broad range of professionals.

Acceptance Criterion 2 – Data Are Sufficient for Model Justification

"(1) Parameters used to evaluate the degradation of EBS are adequately justified."

Parameters to evaluate the degradation of the EBS are adequately described and justified. See Sections 4.2.6, 4.2.7, 4.2.13, 4.2.11, 4.2.12, 4.2.13, 4.2.14, 4.2.15 and 4.2.17 on corrosion phenomena and related testing. Also see Sections 6.2.1, 6.2.3, 6.2.4, 6.5.1, 6.5.2, 6.5.3, 6.5.5, and 6.5.6, which describe the integrated model and associated parameters.

"(2) Sufficient data have been collected to establish initial and boundary conditions."

As previously discussed, testing is required in a broader range of environments than discussed in this non-Q AMR to fully characterize the corrosion performance of thermally sprayed iron-based amorphous metal coatings in anticipated repository conditions. However, the test data presented here are relevant, and are encouraging. The test data obtained to date, in heated natural seawater and hot concentrated calcium chloride are described in Sections 4.2.11, 4.2.12, 4.2.14, 4.2.15 and 4.2.1. The effects of thermally driven devitrification, and the impact of such devitrification on corrosion performance is discussed in Sections 4.2.6, 4.2.7, and 4.2.13. The integration of these input data into a coherent predictive model are described in Sections 6.2.1, 6.2.3, 6.2.4, 6.5.1, 6.5.2, 6.5.3, 6.5.5, and 6.5.6, which describe the integrated model and associated parameters.

"(3) Data on the degradation of the engineered barriers (e.g. – general and localized corrosion, microbially induced corrosion, galvanic interactions, hydrogen embrittlement and phase stability) are based on laboratory measurements, site-specific field measurements, industrial and/or natural analogs and tests designed to replicate anticipated conditions. As appropriate, sensitivity or uncertainty analyses are provided and are shown to be adequate."

As previously discussed, testing is required in a broader range of environments than discussed in this non-Q AMR to fully characterize the corrosion performance of thermally sprayed iron-based amorphous metal coatings in anticipated repository conditions. However, the test data presented here are relevant, and are encouraging. The test data obtained to date, in heated natural seawater and hot concentrated calcium chloride are described in Sections 4.2.11, 4.2.12, 4.2.14, 4.2.15 and 4.2.1. The effects of thermally driven devitrification, and the impact of such devitrification on corrosion performance is discussed in Sections 4.2.6, 4.2.7, and 4.2.13. The integration of these input data into a coherent predictive model are described in Sections 6.2.1, 6.2.3, 6.2.4, 6.5.1, 6.5.2, 6.5.3, 6.5.5, and 6.5.6, which describe the integrated model and associated parameters. Model and experimental uncertainty are discussed in Sections 6.6.1 and 6.6.2.

Microbially induced corrosion, galvanic coupling, hydrogen embrittlement and stress corrosion cracking have not yet been adequately dealt with, and are the subject of new investigations that are underway.

"(4) Degradation models for the applicable processes are adequate. For example, general and localized corrosion, microbially induced corrosion, galvanic interactions, hydrogen embrittlement and phase stability are given appropriate consideration and treatment."

As previously discussed, testing is required in a broader range of environments than discussed in this non-Q AMR to fully characterize the corrosion performance of thermally sprayed iron-based amorphous metal coatings in anticipated repository conditions. However, the test data presented here are relevant, and are encouraging. The test data obtained to date, in heated natural seawater and hot concentrated calcium chloride are described in Sections 4.2.11, 4.2.12, 4.2.14, 4.2.15 and 4.2.1. The effects of thermally driven devitrification, and the impact of such devitrification on corrosion performance is discussed in Sections 4.2.6, 4.2.7, and 4.2.13. The integration of these input data into a coherent predictive model are described in Sections 6.2.1, 6.2.3, 6.2.4, 6.5.1, 6.5.2, 6.5.3, 6.5.5, and 6.5.6, which describe the integrated model and associated parameters. Model and experimental uncertainty are discussed in Sections 6.6.1 and 6.6.2.

Microbially induced corrosion (MIC), galvanic coupling, hydrogen embrittlement, and stress corrosion cracking (SCC) have not yet been adequately dealt with, and are the subject of new investigations that are underway.

Acceptance Criterion 3 – Data Uncertainty is Characterized and Propagated through the Model Abstraction

"(1) Models use parameter values, assumed ranges, probability distributions and/or bounding assumptions that are technically defensible, reasonably account for uncertainties and variability, and do not result in under-representation of the risk estimate."

The measurements of corrosion and critical potentials can be used to determine the mode of corrosive attack, thereby bounding the rate of attack in environments similar to those used for testing. Testing in a wider range of environments, including hot concentrated brines with various concentrations of alkali metal cation, chloride and nitrate anion, and radiolysis-generated oxidant are underway. Model and experimental uncertainty are discussed in Sections 6.6.1 and 6.6.2. The largest uncertainty remains precise knowledge of the evolving repository environment over tens or hundreds of thousands of years.

"(2) Appropriate parameters, based on techniques that may include laboratory experiments, field measurements, and industrial analogs are used."

As described in Section 6.2, appropriate parameters, based on techniques that include laboratory experiments and field measurements are being used. Additional work is required to identify suitable natural analogs for the iron-based amorphous metals.

"(3) Assumed range of values and probability distributions for parameters used in conceptual and process-level models are not likely to underestimate the actual degradation and failure of engineered barrier systems."

Testing in extremely aggressive environments, such as 5M $CaCl_2$ at 105 and 120°C, provides a degree of conservatism. Such environments are considered harsh for the baseline engineered barrier system design. The materials are also being subjected to thermal aging conditions in excess of the temperature limits expected in the environment (well above 800°C), which is very conservative. Finally, the materials have been subjected to neutron and gamma irradiation, equivalent to more than 4000 years inside the waste package, with no devitrification. Clearly, additional testing is required, though early results are very encouraging.

The amorphous metals are very attractive as basket materials since the relatively high boron concentration enables neutron absorption. If testing and modeling indicate that these materials have corrosion resistance comparable to borated stainless steels, with acceptable damage tolerance, the use of these materials to fabricate basket assemblies will be viable. To be competitive in such criticality control applications, these materials will have to demonstrate corrosion resistance comparable to borated-stainless steel in the "expected in-package environment." If testing and modeling indicate that these materials have corrosion resistance comparable to Alloy C-22, with acceptable damage tolerance, the application of these materials on the outer surface of the waste package for corrosion protection will be viable.

The use of these materials in repository applications depends upon their corrosion resistance in a broad range of environments. The materials must also survive severe mechanical tests. While there are encouraging results from preliminary corrosion tests, much remains to be done. Testing is underway in a much broader range of environments than have been previously explored, including hot concentrated bicarbonate-type brines, chloride brines with various levels of nitrate inhibitor, and acidified brines with very low pH.

Alloy C-22 is an outstanding corrosion-resistant engineering material. Even so, crevice corrosion has been observed with C-22 in hot sodium chloride environments without buffer or inhibitor. SAM2X5 is also expected to experience crevice corrosion under sufficiently harsh conditions.

SAM2X5 and SAM1651 can be applied as coatings with the same corrosion resistance as a fully-dense completely amorphous melt-spun ribbon, provided that its amorphous nature is preserved during thermal spraying, whereas both Alloy C-22 and Type 316L stainless lose much of their corrosion resistance during thermal spraying, due to the formation of deleterious intermetallic phases which deplete the matrix of key alloy elements. Thus, these materials may provide the repository engineer with some unique materials for design enhancement.

"(4) Non-destructive examination used to evaluate of materials."

Non-destructive evaluation of materials is being conducted, including X-ray diffraction, magnetic susceptibility measurements (detection of ferrite), visual inspection, neutron radiography, ultrasonic evaluation, salt-fog testing of large samples and prototypes, macro

photography and optical microscopy. Data from such NDE evaluation will be available for future revisions of this report.

"(5) Where sufficient data do not exist, the definition of parameter values and conceptual models is based on appropriate use of other sources, such as expert elicitation."

As discussed in this report, testing in a broader range of environments is needed. However, several of the environments, such as the hot calcium chloride are believed to represent some possible bounding worst-case environments. In regard to the general performance of amorphous materials, data on other amorphous metals in corrosive environments has been found in the literature, and is provided in the list of references. No expert elicitation has been used.

Acceptance Criterion 4 – Model Uncertainty is Characterized and Propagated Through the Model Abstraction

"(1) Alternative modeling approaches and methods are being considered and are consistent with available data and current scientific understanding."

Alternative models are discussed in Section 6.5.

"(2) Consideration of conceptual model uncertainty is consistent with available site characterization data, laboratory experiments … and the treatment of uncertainty does not result in under-estimation of the risk estimate."

Model uncertainty is consistent with available laboratory data and is discussed in Section 6.6.

"(3) Alternative modeling approaches, consistent with available data and current scientific understanding, are used and the modeling results are evaluated using tests that are sensitive to the processes modeled."

Alternative modeling approaches are consistent with available data and current scientific understanding, and are discussed in Section 6.5.

Acceptance Criterion 5 – Model Abstraction Output Supported by Objective Comparison

"(1) Models implemented in this total system performance assessment (TSPA) abstraction provide results consistent with output from detailed process-level models and or empirical observations (laboratory and field testing, and/or natural analogs)."

The models implemented in the abstraction model that may ultimately be used by TSPA, will provide results that are consistent with the output from detailed process-level models and the empirical observations on which the process-level models are based. See Section 4.2 entitled "Direct Inputs – Summary of Experimental Results."

"(2) Corrosion models are adequate to predict performance."

Corrosion models are believed to sufficiently comprehensive to predict performance. See Sections 4.2 and 6.2.

"(3) Evidence is sufficient to show that models will not underestimate the actual degradation and failure of engineered barriers."

See response to Acceptance Criterion 3. Testing in extremely aggressive environments, such as 5M $CaCl_2$ at 105 and 120°C, provides a degree of conservatism. Such environments are considered harsh for the baseline engineered barrier system design. The materials are also being subjected to thermal aging conditions in excess of the temperature limits expected in the environment (well above 800°C), which is very conservative. Finally, the materials have been subjected to neutron and gamma irradiation, equivalent to more than 5000 inside the waste package, with no devitrification. Clearly, additional testing is required, though early results are very encouraging.

"(4) Mathematical degradation models are based on the same environmental parameters, material factors, assumptions and approximations shown to be appropriate for closely analogous applications."

The integrated model (schematic shown in section on modeling), with the linkages shown, allow conditions such as temperature to be carried throughout the corrosion assessment. The same temperature is used for selection of corrosion mode (general or localized corrosion) as used for estimation of the general rate of corrosion. See Sections 6.2.1, 6.2.3, 6.2.4, 6.5.1, 6.5.2, 6.5.3, 6.5.5, and 6.5.6.

"(5) Accepted and well documented procedures are used to construct and test the numerical models that simulate the EB chemical environment and degradation of the engineered barrier."

The procedures used for acquiring experimental data, which serve as the basis for constructing numerical process models are described in Sections 2.3 and 4.1. Examples of correlations are shown in Section 6.2.

"(6) Not applicable to the scope of this report."

INTENTIONALLY LEFT BLANK

9. INPUTS AND REFERENCES

9.1 DOCUMENTS CITED

1. J. C. Farmer, J. J. Haslam, S. D. Day, T. Lian, R. Rebak, N. Yang, L. Aprigliano, Corrosion Resistance of Iron-Based Amorphous Metal Coatings, Proceedings of ASME PVP: Pressure Vessels & Piping (PVP) Division Conference, July 23-27, 2006 Vancouver, British Colombia, American Society of Mechanical Engineers, PVP2006-ICPVT11-93835, New York, NY 7 p. (2006).
2. J. C. Farmer, The Development of Next-Generation Materials for Nuclear Energy, UCRL-PRES-219330, Energy and Environment Directorate Review Committee, March 7-9, 2006, Lawrence Livermore National Laboratory, Livermore California, 17 pages (2006).
3. J. C. Farmer, Team FY05 HPCRM Annual Report: High-Performance Corrosion-Resistant Iron-Based Amorphous Metal Coatings, UCRL-SR-219257, January 2006, Contributions by J. C. Farmer, J-S. Choi, J. J. Haslam, S. D. Day, N. Yang, T. Headley, G. Lucadamo, J. L Yio, J. Chames, A. Gardea, M. Clift, C. A. Blue, W. H. Peters, J. D. K. Rivard, D. C. Harper, D. Swank, R. Bayles & E. J. Lemieux, Robert Brown & Theresa M. Wolejsza, L. F. Aprigliano, D. J. Branagan, M. C. Marshall, Brian E. Meacham, E. Joseph Buffa, M. Brad Beardsley, E. J. Lavernia, J. Schoenung, L. Ajdelsztajn, J. Dannenberg, O. A. Graeve, J. J. Lewandowski, John H. Perepezko, Kjetil Hildal, L. P. Kaufman, J. Boudreau, Lawrence Livermore National Laboratory, Livermore, California, 138 pages (2006).
4. J. C. Farmer, J. J. Haslam, S. D. Day, HPCRM Annual Report: High-Performance Corrosion-Resistant Iron-Based Amorphous-Metal coatings: Evaluation of Corrosion Resistance, UCRL-SR-218144, January 2006, Lawrence Livermore National Laboratory, Livermore, California, 68 pages (2006).
5. J. Farmer, C. Earl, C. Doty, D. Spence, J. Walker, F. Wong, J. Payer, G-Q. Lu, D. E. Clark, D. C. Folz, A. Heuer, O. Graeve, D. Branagan, C. Blue, J. Rivard, J. Perepezko, L. Kaufman, N. Yang, E. Lavernia, J. Haslam, E. Lemieux, L. Aprigliano, B. Beardsley, T. Weaver, B. Edwards, B. Brown, Ar. Halter, B Bayles, J. Lewandowski, DARPA-DOE High Performance Corrosion-Resistant Materials (HCPRM) Principal Investigator's Meeting, Turtle Bay Resort, Oahu, Hawaii, January 10-13, 2005, UCRL-PRES-214672, Lawrence Livermore National Laboratory, Livermore, California, 407 pages.
6. J. C. Farmer, J. J. Haslam, S. D. Day, D. J. Branagan, C. A. Blue, J. D. K. Rivard, L. F. Aprigliano, N. Yang, J. H. Perepezko, M. B. Beardsley, Corrosion Characterization of Iron-Based High-Performance Amorphous-Metal Thermal-Spray Coatings, PVP2005-71664, Proceedings of ASME PVP: Pressure Vessels & Piping Division Conference, Grand Hyatt, Denver, Colorado, July 17-21, 2005, American Society of Mechanical Engineers, Three Park Avenue, New York, New York, 7 pages (2005).
7. J. C. Farmer, J. J. Haslam, S. D. Day, D. J. Branagan, M. C. Marshall, B. E. Mecham, E. J. Buffa, C. A. Bue, J. D. K. Rivard, D. C. Harper, M. B. Beardsley, D. T. Weaver, L. F. Aprigliano, L. Kohler, R. Bayles, E. J. Lemieux, T. M. Wolejsza, N. Yang, G. Lucadamo, J. H. Perepezko, K. Hildal, L. Kaufman, A. H. Heuere, F. Ernst, G. M. Michal, H. Kahn, E. J. Lavernia, High-Performance Corrosion-Resistant Materials: Iron-Based Amorphous-Metal Thermal-Spray Coatings, High-Performance Corrosion-Resistant Materials (HPCRM) Annual Report, UCRL-TR-206717, Lawrence Livermore National Laboratory, Livermore, California, 178 pages, September 28 (2004).

8. J. C. Farmer et al., High-Performance Corrosion-Resistant Amorphous Metals, Proc. Global 2003, New Orleans, Louisiana, American Nuclear Society (2003).
9. F. Guo, S. J. Poon, G. J. Shiflet, Metallic Glass Ingots Based on Yttrium, Applied Physics Letters, Vol. 83, No. 13, pp. 2575-2577 (2003).
10. Z. P. Lu, C. T. Liu, W. D. Porter, Role of Yttrium in Glass Formation of Fe-Based Bulk Metallic Glasses, Vol. 83, No. 13, Applied Physics Letters, pp. 2581-2583 (2003).
11. V. Ponnambalam, S. J. Poon and G. Shiflet, J. Mater. Res., 19 (5), 1320, 2004.
12. D. J. Branagan, M. C. Marshall, B. E. Mecham, L. F. Aprigliano, R. Bayles, E. J. Lemieux, T. M. Wolejsza, F. J. Martin, J. C. Farmer, J. J. Haslam, S. D. Day, Wear and Corrosion Resistant Amorphous / Nanostructured Steel Coatings for Replacement of Electrolytic Hard Chromium, UCRL Report, Lawrence Livermore National Laboratory, Livermore, California. 7 pages (2005); Proceedings of the International Thermal Spray Conference and Exposition, American Society of Materials International, Seattle, Washington, May 15-18, 2006 (2006).
13. D. J. Branagan, M. C. Marshall, B. E. Meacham, The NanoSteel Company, Incorporated, Final Report for the Performance of LLNL Subcontract FY05, LLNL-RFP-B550033, High Performance Corrosion Resistant Materials (HPCRM) for Naval Warfighting and Safe Long-Term Storage/Disposal of Spent Nulcear Fuel, Joint DOE-DARPA Program, Institute of Nanomaterials Research and Development, The NanoSteel Company, Idaho Falls, Idaho 84 p. (2005).
14. D. J. Branagan, Highly Active Liquid Melts Used for Form Coatings, United States Patent Application 20040250926, Filed December 16, 2004.
15. D. J. Branagan, Methode of Modifying Iron-Based Glasses to Increase Crystallization Temperature without Changing Melting Temperature, United States Patent Application No. 20040250929, Filed December 16, 2004.
16. D. J. Branagan, Properties of Amorphous/Partially Crystalline Coatings, United States Patent Application No. 20040253381, Filed December 16, 2004.
17. D. J. Branagan, Methods of Forming Hardened Surfaces, United States Patent No. 6,767,419, Filed November 9, 2000, Granted July 27, 2004.
18. D. J. Branagan, Hard Metallic Materials, Hard Metallic Materials, United States Patent Application 20040140017, Filed July 27, 2004.
19. D. J. Branagan, Method for Protecting a Surface, United States Patent Application 20040140021, Filed July 22, 2004.
20. D. J. Branagan, Method for Forming a Hard Metallic Wire, United States Patent Application 20040141868, Filed July 22, 2004.
21. D. J. Branagan, Formation of Metallic Thermal Barrier Coatings, United States Patent Application No. 20050013723, Filed February 11, 2004.
22. D. J. Branagan, Hard Metallic Materials, Hard Metallic Coatings, Methods of Processing Metallic Materials and Methods of Producing Metallic Coatings, United States Patent Application 20030051781, Filed March 20, 2003.
23. D. J. Branagan, Joseph V. Burch, Methods of Forming Steel, United States Patent No. 6,258,185, Filed May 25, 1999, Granted July 10, 2001.
24. D. Chidambaram, C. R. Clayton, M. R. Dorfman, Evaluation of the Electrochemical Behavior of HVOF-Sprayed Alloy Coatings, Surface and Coatings Technology, Vol. 176, pp. 307-317 (2004).
25. J. Farmer, S. Lu, D. McCright, G. Gdowski, F. Wang, T. Summers, P. Bedrossian, J. Horn, T. Lian, J. Estill, A. Lingenfelter, W. Halsey, General and Localized Corrosion of High-

Level Waste Container in Yucca Mountain, Proceedings of the Annual Meeting of the American Society of Mechanical Engineers, Pressure Vessels and Piping, 11 pages, Seattle, Washington, July (2000).

26. J. Farmer, S. Lu, T. Summers, D. McCright, A. Lingenfelter, F. Wang, J. Estill, L. Hackel, H-L. Chen, G. Gordon, V. Pasupathi, P. Andresen, S. Tang, M. Herrera, Modeling and Mitigation of Stress Corrosion Cracking in Closure Welds of High-Level Waste Containers for Yucca Mountain, Proceedings of the Annual Meeting of the American Society of Mechanical Engineers, Pressure Vessels and Piping, 11 pages, Seattle, Washington, July (2000).
27. J. C. Farmer, R. D. McCright, J. C. Estill, S. R. Gordon, Development of Integrated Mechanistically-Based Degradation-Mode Models for Performance Assessment of High-Level Containers, Proceedings of the Symposium on the Scientific Basis for Nuclear Waste Manatement XXII, D. J. Wronkiewicz, J. H. Lee, Eds., Materials Research Society Symposium Series, Warrendale, PA, Vol. 556, pp. 855-862 (1999).
28. M. Telford, The Case for Bulk Metallic Glass, Materials Today, March 2004, Elsevier Ltd., pp. 36-43 (2004).
29. D. E. Polk, B. C. Giessen, Overview of Principles and Applications, Chapter 1, pp. 2-35, Metallic Glasses, J. J. Gilman, H. J. Leamy, Eds., American Society of Metals, Metals Park, Ohio, 348 p. (1978).
30. R. M. Latanison, Corrosion Resistance of Metastable Alloys Processed by Rapid Solidification, Workshop on Amorphous Metals and Semiconductors, Electric Power Research Institute (EPRI), May 12-18, 1985 (1985).
31. J. R. Scully, A. Gerbert, J. H. Payer, Corrosion and Related Mechanical Properties of Bulk Metallic Glasses, Journal of Materials Research, submitted for publication (2006).
32. K. Kishitake, H. Era, F. Otsubo, Characterization of Plasma Sprayed Fe-10Cr-10Mo-(C,B) Amorphous Coatings, Vol. 5, No. 2, pp. 145-153 (1996).
33. S. Pang, T. Zhang, K. Asami, A. Inoue, Materials Transactions, Effects of Chromium on the Glass Formation and Corrosion Behavior of Bulk Glassy Fe-Cr-Mo-C-B Alloys, Vol. 43, No. 8, pp. 2137-2142 (2002).
34. S. J. Pang, T. Zhang, K. Asami, A. Inoue, Synthesis of Fe-Cr-Mo-C-B-P Bulk Metallic Glasses with High Corrosion Resistance, Acta Materialia, Vol. 50, pp. 489-497 (2002).
35. H. Shinimiya, A. Nakazawa, Z. Kato, A. A. El Moneium, Y. Niizeki, K. Asami, K. Hashimoto, Corrosion Resistant Bulk Amrophous Ni-Cr-Ta-Mo-Nb-5P Alloys in Concentrated Hydrochloric Acids, Paper 319, Session on Corrosion and Electrochemistry of Advanced Materials in Honor of Koji Hashimoto, 208th Meeting of the Electrochemical Society, Westing Bonaventure Hotel, Los Angeles, California, October 16-21, 2005, Electrochemical Society, Pennington, New Jersey (2005).
36. J. E. Harrar, J. F. Carley, W. F. Isherwood, E. Raber, Report of the Committee to Review the Use of J-13 Well Water in Nevada Nuclear Waste Storage Investigations, Yucca Mountain Project, UCID-21867, Lawrence Livermore National Laboratory, Livermore, California, 111 pages (1990).
37. Standard Specification for Low-Carbon Nickel-Molybdenum-Chromium, Low-Carbon Nickel-Chromium-Molybdenum, Low-Carbon Nickel-Chromium-Molybdenum-Copper, and Low-Carbon Nickel-Chromium-Molybdenum-Tungsten Alloy Plate, Sheet, and Strip, Designation B 575-94, 1997 Annual Book of American Society for Testing and Materials (ASTM) Standards (1997).

38. H. P. Hack, Crevice Corrosion Behavior of Molybdenum-Containing Stainless Steel in Seawater, Materials Performance, Vol. 22, No. 6, pp. 24–30 (1983).
39. K. A. Gruss, G. A. Cragnolino, D. S. Dunn, N. Sridar, Repassivation Potential for Localized Corrosion of Alloys 625 and C22 in Simulated Repository Environments, Paper 149, *Corrosion 98*, National Association of Corrosion Engineers, Houston, TX, 9 pages (1998).
40. A. I. Asphahani, Corrosion Resistance of High Performance Alloys, Materials Performance, Vol. 19, No. 12, pp. 33–43 (1980).
41. J. C. Farmer et al., Protective Ceramic Coatings for High-Level Radioactive Waste Containers, UCRL-MI-131293, Presented to Ceramic Peer Review Panel, SRI International, Palo Alto, CA, August 17 (1998).
42. J. C. Farmer, K. R. Wilfinger, Process Level Model for Ceramic Coating, UCRL-ID-131899 Rev. 2, November 14 (1998).
43. J. J. Haslam, J. C. Farmer, R. W. Hopper, K. R. Wilfinger, Ceramic Coatings for Corrosion Resistant Nuclear Waste Container Evaluated in Simulated Ground Water at 90C, UCRL-JRNL-206107, Lawrence Livermore National Laboratory, Livermore, California, August 17, 2004 (34 p.); Metallurgical and Materials Transactions A, Volume 36A, May 2005, p. 1085-1095 (2004).
44. K. R. Wilfinger, J. C. Farmer, R. W. Hopper, T. E. Shell, Corrosion Protection of Metallic Waste Packages Using Thermal Sprayed Ceramic Coatings, Proceedings of the Symposium on the Scientific Basis for Nuclear Waste Manatement XXII, D. J. Wronkiewicz, J. H. Lee, Eds., Materials Research Society Symposium Series, Warrendale, PA, Vol. 556, pp. 927-934 (1999).
45. C. K. Saw, X-ray Scattering Techniques for Characterization Tools in the Life Sciences, Nanotechnologies for the Life Science, Edited by Challa Kumar, Wiley-VCH Verlag GmbH & Co., KGaA, Weinheim (2006).
46. C. K. Saw and R. B. Schwarz, Chemical Short-Range Order in Dense Random-Packed Models", Journal of the Less-Common Metals, 140, 385-393 (1988).
47. J. H. Perepezko, K. Hildal, HPCRM Annual Report, Thermal and Kinetic Analysis of Amorphous Fe-Based Alloys for Use in Thermal Spray Processing, Submission to Lawrence Livermore National Laboratory, University of Wisconsin, Madison, Wisconsin, 74 pages, September 9 (2004).
48. J. R. Scully, J. L. Hudson, T. Lunt, G. Ilevbare, B. Kehler, Localized Corrosion Initiation and Transition to Stabilization in Alloys 625 and C-22, Final Report, TRW/DOE YMP Purchase Order Number A10762JM8A, September 30, 1999, 27 pages (1999).
49. Standard Practice for Conventions Applicable to Electrochemical Measurements in Corrosion Testing, Designation G 3-89, 1997 Annual Book of American Society for Testing and Materials (ASTM) Standards, Section 3, Vol. 3.02, pp. 36–44 (1997).
50. Standard Reference Test Method for Making Potentiostatic and Potentiodynamic Anodic Polarization Measurements, Designation G 5-94, 1997 Annual Book of American Society for Testing and Materials (ASTM) Standards, Section 3, Vol. 3.02, pp. 54–57 (1997).
51. Standard Reference Test Method for Making Potentiostatic and Potentiodynamic Anodic Polarization Measurements, Designation G 5-87, 1989 Annual Book of American Society for Testing and Materials (ASTM) Standards, Section 3, Vol. 3.02, pp. 79–85 (1989).
52. Standard Test Method for conducting Cyclic Potentiodynamic Polarization Measurements for Localized Corrosion Susceptibility of Iron-, Nickel-, or Cobalt-Based Alloys, Designation G

61-86, 1997 Annual Book of American Society for Testing and Materials Standards, Section 3, Vol. 3.02, pp. 231–235 (1997).
53. W. T. Kim, K. Clay, C. Small, B. Cantor, Heat Treatment of a Melt Spun Fe70Cr18Mo2B10 Alloy, Journal of Non-Crystalline Solids, Vol. 127, pp. 273-286 (1991).
54. R. S. Treseder, R. Baboian, C. G. Munger, Polarization Resistance Method for Determining Corrosion Rates, NACE Corrosion Engineer's Reference Book, Second Edition, National Association of Corrosion Engineers, 1440 South Creek Drive, Houston, Texas, pp. 65-66 (1991).
55. D. A. Jones, Faraday's Law, Section 3.1.1, Electrochemical Kinetics of Corrosion," Chapter 3, Principles and Prevention of Corrosion, 2nd Edition, Prentice Hall, Upper Saddle River, NJ, Equations 3 and 5, pp. 75–76 (1996).
56. A. J. Bard, L. R. Faulkner, Liquid Junction Potentials, Section 2.3, Potentials and Thermodynamics of Cells, Chapter 2, Electrochemical Methods, Fundamentals and Applications, John Wiley and Sons, New York, NY, 1980, Eqn. 2.3.39, p. 71, Table 2.3.2, p. 67 (1980).
57. L. F. Aprigliano, HPCRM Annual Report, Salt Fog Corrosion Testing at NSWCCD, Submission to Lawrence Livermore National Laboratory, Naval Surface Warfare Center, Carderock Division, 13 pages, November 17 (2005).
58. J. Farmer, J. Haslam, S. Day, T. Lian, C. Saw, P. Hailey, J-S. Choi, N. Yang, C. Blue, W. Peter, R. Bayles, R. Brown, J. Payer, J. Perepezko, K. Hildal, E. Lavernia, L. Ajdelsztajn, D. J. Branagan, J. Buffa, M. Beardsley, L. Aprigliano and J. Boudreau, Corrosion Resistance of Iron-Based Amorphous Metals in Hot Concentrated Calcium Chloride and Seawater: $Fe_{48}Mo_{714}Cr_{15}Y_2C_{15}B_6$, UCRL-TM-224159, August 30, 2006, Lawrence Livermore National Laboratory, Livermore, California, 47 pages (2006).
59. J-S. Choi, J. Farmer, C. Lee, Application of Neutron-Absorbing Structural-Amorphous Metal (SAM) Coatings for Spent Nuclear Fuel (SNF) Container: Use of Novel Coating Materials to Enhance Criticality Safety Controls, UCRL-MI-220385, April 5, 2006, Lawrence Livermore National Laboratory, Livermore, California, 32 pages (2006); Proceedings of CALPHAD Meeting, May 11, 2006, Haifa, Israel (2006).
60. D. J. Branagan, Galen R. Smolik, Advanced Neutron Absorber Materials, Filed February 2, 1999, United States Patent 6,125,912, Granted October 3, 2000.
61. J. Farmer, J. Haslam, S. Day, T. Lian, C. Saw, P. Hailey, J-S. Choi, N. Yang, C. Blue, W. Peter, R. Bayles, R. Brown, J. Payer, J. Perepezko, K. Hildal, E. Lavernia, L. Ajdelsztajn, D. J. Branagan, J. Buffa, M. Beardsley, L. Aprigliano and J. Boudreau, Corrosion Resistance of Iron-Based Amorphous Metals in Seawater: $Fe_{49.7}Cr_{17.7}Mn_{1.9}Mo_{7.4}W_{1.6}B_{15.2}C_{3.8}Si_{2.4}$, UCRL-TM-223298, August 28, 2006, Lawrence Livermore National Laboratory, Livermore, California, 60 pages (2006).

9.2 CODES, STANDARDS, REGULATIONS, AND PROCEDURES

American Society for Testing and Materials (ASTM) 1987. "Calculation of Corrosion Rate," Subsection 8, "Densities for a Variety of Metals and Alloys," Appendix X1, "Standard Practice for Preparing, Cleaning, and Evaluating Corrosion Test Specimens," Designation G 1-81, *1987 Annual Book of American Society for Testing and Materials Standards*, Section 3, Vol. 3.02, pp. 89–94.

ASTM 1989. "Standard Reference Test Method for Making Potentiostatic and Potentiodynamic Anodic Polarization Measurements," Designation G 5-87, *1989 Annual Book of American Society for Testing and Materials Standards*, Section 3, Vol. 3.02, pp. 79–85.

ASTM 1997a. "Standard Specification for Low-Carbon Nickel-Molybdenum-Chromium, Low-Carbon Nickel-Chromium-Molybdenum, Low-Carbon Nickel-Chromium-Molybdenum-Copper, and Low-Carbon Nickel-Chromium-Molybdenum-Tungsten Alloy Plate, Sheet, and Strip," Designation B 575-94, *1997 Annual Book of American Society for Testing and Materials Standards*, Section 2, Vol. 2.04, pp. 409–410, Subsection 7.1 – Weight.

ASTM 1997b. "Standard Practice for Conventions Applicable to Electrochemical Measurements in Corrosion Testing," Designation G 3-89, *1997 Annual Book of American Society for Testing and Materials Standards*, Section 3, Vol. 3.02, pp. 36–44.

ASTM 1997c. "Standard Test Method for conducting Cyclic Potentiodynamic Polarization Measurements for Localized Corrosion Susceptibility of Iron-, Nickel-, or Cobalt-Based Alloys," Designation G 61-86, *1997 Annual Book of American Society for Testing and Materials Standards*, Section 3, Vol. 3.02, pp. 231–235.

ASTM 1997d. "Standard Reference Test Method for Making Potentiostatic and Potentiodynamic Anodic Polarization Measurements," Designation G 5-94, *1997 Annual Book of American Society for Testing and Materials Standards*, Section 3, Vol. 3.02, pp. 54–57.

ASTM 1997e. "Standard Practice for Preparing, Cleaning, and Evaluating Corrosion Test Specimens," Designation G 1-90, *1997 Annual Book of American Society for Testing and Materials Standards*, Section 3, Vol. 3.02, pp. 15–21.

ASTM 1997f. "Standard Test Methods for Pitting and Crevice Corrosion Resistance of Stainless Steels and Related Alloys by Use of Ferric Chloride Solution," Designation G 48-92, *1997 Annual Book of American Society for Testing and Materials Standards*, Section 3, Vol. 3.02, pp. 181–186.

9.3 SOURCE DATA, LISTED BY DATA TRACKING NUMBER

No data tracking numbers have been assigned to non-Q source data.

9.4 OUTPUT DATA, LISTED BY DATA TRACKING NUMBER

No data tracking numbers have been assigned to non-Q output data.

INTENTIONALLY LEFT BLANK

10. ACKNOWLEDGEMENTS

Work was sponsored by the United States Department of Energy (DOE), Office of Civilian and Radioactive Waste Management (OCRWM), and Office of Science and Technology and International (OSTI); and Defense Advanced Research Projects Agency (DARPA), Defense Science Office (DSO). This work was done under the auspices of the U.S. DOE by Lawrence Livermore National Laboratory (LLNL) under Contract No. W-7405-Eng-48. The guidance of Leo Christodoulou at DARPA DSO and of Jeffrey Walker at DOE OSTI is gratefully acknowledged. Thermal spray SAM2X5 coatings used in this investigation were produced by Plasma Tech Incorporated (PTI) in Torrance, California, with amorphous metal powders produced by The NanoSteel Company (TNC).

INTENTIONALLY LEFT BLANK

11. ATTACHMENTS

1. J. C. Farmer, J. J. Haslam, S. D. Day, T. Lian, R. Rebak, N. Yang, L. Aprigliano, Corrosion Resistance of Iron-Based Amorphous Metal Coatings, Proceedings of ASME PVP: Pressure Vessels & Piping (PVP) Division Conference, July 23-27, 2006 Vancouver, British Colombia, American Society of Mechanical Engineers, PVP2006-ICPVT11-93835, New York, NY 7 p. (2006).
2. J. C. Farmer, The Development of Next-Generation Materials for Nuclear Energy, UCRL-PRES-219330, Energy and Environment Directorate Review Committee, March 7-9, 2006, Lawrence Livermore National Laboratory, Livermore California, 17 pages (2006).
3. J. C. Farmer, Team FY05 HPCRM Annual Report: High-Performance Corrosion-Resistant Iron-Based Amorphous Metal Coatings, UCRL-SR-219257, January 2006, Contributions by J. C. Farmer, J-S. Choi, J. J. Haslam, S. D. Day, N. Yang, T. Headley, G. Lucadamo, J. L Yio, J. Chames, A. Gardea, M. Clift, C. A. Blue, W. H. Peters, J. D. K. Rivard, D. C. Harper, D. Swank, R. Bayles & E. J. Lemieux, Robert Brown & Theresa M. Wolejsza, L. F. Aprigliano, D. J. Branagan, M. C. Marshall, Brian E. Meacham, E. Joseph Buffa, M. Brad Beardsley, E. J. Lavernia, J. Schoenung, L. Ajdelsztajn, J. Dannenberg, O. A. Graeve, J. J. Lewandowski, John H. Perepezko, Kjetil Hildal, L. P. Kaufman, J. Boudreau, Lawrence Livermore National Laboratory, Livermore, California, 138 pages (2006).
4. J. C. Farmer, J. J. Haslam, S. D. Day, HPCRM Annual Report: High-Performance Corrosion-Resistant Iron-Based Amorphous-Metal coatings: Evaluation of Corrosion Resistance, UCRL-SR-218144, January 2006, Lawrence Livermore National Laboratory, Livermore, California, 68 pages (2006).
5. J. Farmer, C. Earl, C. Doty, D. Spence, J. Walker, F. Wong, J. Payer, G-Q. Lu, D. E. Clark, D. C. Folz, A. Heuer, O. Graeve, D. Branagan, C. Blue, J. Rivard, J. Perepezko, L. Kaufman, N. Yang, E. Lavernia, J. Haslam, E. Lemieux, L. Aprigliano, B. Beardsley, T. Weaver, B. Edwards, B. Brown, Ar. Halter, B Bayles, J. Lewandowski, DARPA-DOE High Performance Corrosion-Resistant Materials (HCPRM) Principal Investigator's Meeting, Turtle Bay Resort, Oahu, Hawaii, January 10-13, 2005, UCRL-PRES-214672, Lawrence Livermore National Laboratory, Livermore, California, 407 pages.
6. J. C. Farmer, J. J. Haslam, S. D. Day, D. J. Branagan, C. A. Blue, J. D. K. Rivard, L. F. Aprigliano, N. Yang, J. H. Perepezko, M. B. Beardsley, Corrosion Characterization of Iron-Based High-Performance Amorphous-Metal Thermal-Spray Coatings, PVP2005-71664, Proceedings of ASME PVP: Pressure Vessels & Piping Division Conference, Grand Hyatt, Denver, Colorado, July 17-21, 2005, American Society of Mechanical Engineers, Three Park Avenue, New York, New York, 7 pages (2005).
7. J. C. Farmer, J. J. Haslam, S. D. Day, D. J. Branagan, M. C. Marshall, B. E. Mecham, E. J. Buffa, C. A. Bue, J. D. K. Rivard, D. C. Harper, M. B. Beardsley, D. T. Weaver, L. F. Aprigliano, L. Kohler, R. Bayles, E. J. Lemieux, T. M. Wolejsza, N. Yang, G. Lucadamo, J. H. Perepezko, K. Hildal, L. Kaufman, A. H. Heuere, F. Ernst, G. M. Michal, H. Kahn, E. J. Lavernia, High-Performance Corrosion-Resistant Materials: Iron-Based Amorphous-Metal Thermal-Spray Coatings, High-Performance Corrosion-Resistant Materials (HPCRM) Annual Report, UCRL-TR-206717, Lawrence Livermore National Laboratory, Livermore, California, 178 pages, September 28 (2004).

INTENTIONALLY LEFT BLANK

THE END